Powder recycling in laser powder bed fusion of stainless steel 316L : analysis, monitoring and minimization of powder degradation

Timothée Delacroix

▶ To cite this version:

Timothée Delacroix. Powder recycling in laser powder bed fusion of stainless steel 316L : analysis, monitoring and minimization of powder degradation. Materials and structures in mechanics [physics.class-ph]. Université Grenoble Alpes [2020-..], 2022. English. NNT : 2022GRALI073 . tel-04308206

HAL Id: tel-04308206
https://theses.hal.science/tel-04308206

Submitted on 27 Nov 2023

THÈSE

Pour obtenir le grade de

DOCTEUR DE L'UNIVERSITÉ GRENOBLE ALPES

Spécialité : 2MGE : Matériaux, Mécanique, Génie civil, Electrochimie

Arrêté ministériel : 25 mai 2016

Présentée par

Timothée DELACROIX

Thèse dirigée par **Jean-Paul GARANDET**, CEA LITEN, Université Grenoble Alpes
et co-encadrée par **Fernando LOMELLO**, CEA ISAS, Université Paris-Saclay

préparée au sein du **Laboratoire LISL, CEA Paris-Saclay**
dans **l'École Doctorale I-MEP2 - Ingénierie - Matériaux, Mécanique, Environnement, Energétique, Procédés, Production**

Recyclage de la poudre d'acier inoxydable 316L en fabrication additive par fusion laser sur lit de poudre : analyse, suivi et limitation de la dégradation de la poudre

Powder recycling in laser powder bed fusion of stainless steel 316L: analysis, monitoring and minimization of powder degradation

Thèse soutenue publiquement le **21 novembre 2022**,
devant le jury composé de :

Monsieur Eduard HRYHA
PROFESSEUR, Department of Industrial and Materials Science, Chalmers University of Technology, Rapporteur

Monsieur Marc THOMAS
DIRECTEUR DE RECHERCHE, ONERA, Département Matériaux et Structures (DMAS), Rapporteur

Madame Anne-Laure HELBERT
PROFESSEUR DES UNIVERSITES, Polytech Paris-Saclay - Université Paris-Saclay, Examinatrice

Monsieur Jean-Michel MISSIAEN
PROFESSEUR DES UNIVERSITES, Grenoble INP - Phelma, Président

Monsieur Rémi GIRAUD
INGENIEUR DOCTEUR, SAFRAN Additive Manufacturing Campus, Examinateur

Monsieur Jean-Paul GARANDET
DIRECTEUR DE RECHERCHE, CEA-Grenoble, DRT/LITEN/DTNM, Directeur de thèse

"Faire et refaire, c'est toujours travailler"
- Pépé

Acknowledgments

First of all, I would like to thank all the members of the jury for their efforts in evaluating this thesis and especially Eduard Hryha and Marc Thomas who reviewed the manuscript with great expertise, comments and suggestions. Thank you to Jean-Michel Missiaen for being the chairman of this jury and for the enriching comments. Special thanks to Anne-Laure Helbert, in addition to being part of this jury, who gave me the opportunity to follow a double curriculum in the last year of engineering school with a master's degree which directly led to this PhD thesis. Special thanks also to Rémi Giraud for bringing an industrial vision to this jury, as well as for the advice and always relevant remarks over these last years.

I would like to express my deepest gratitude to my supervisors, Jean-Paul Garandet and Fernando Lomello. Jean-Paul, I thank you for your constant availability, your great passion for science and your professionalism. Your critical and constructive mind and your sense of detail are necessary elements that every PhD student should wish to find in their thesis director. Beyond all that, I am grateful for your unconditional support and loyalty, for having always been by my side in somewhat complex situations. Fernando, thank you for your unwavering trust, the freedom you gave me to fully develop my ideas and give the best of myself in this thesis. I am thankful for the connection we have developed over the past 3 years, which made this thesis as well as the Thursdays meetings a success.

I also wish to express my sincere appreciation to Frédéric Schuster, for being the initiator of this innovative topic, and having trusted me and providing me the opportunity to work on this project. I also thank Nihed Chaâbane in this regard, for the confidence granted to me following the Master MET. I gratefully acknowledge the financial support provided by the CEA Cross-Cutting Program on Materials and Processes Skills (PTC-MP), and the international chaire IMPACT. I want to thank Hicham Maskrot and Lionel Gosmain for having welcomed me in the LISL laboratory, and for the great support they have always given me. Hicham, a big thank you for the confidence you gave me at the end of my thesis and the unique opportunity you offered me with the startup project.

I would also like to thank those who introduced me to the additive manufacturing world during my final year's internship with the Safran Additive Manufacturing team, and allowed me to start this thesis with many assets: Aurèle Germain, Rémi, Melina, Elise, Loic, Stéphane... Aurèle, I could not have had a better mentor, our cooperation has been optimal and perfect. It is thanks to the transmission of your passion and the desire to work with you in the future that I did this thesis.

I now address my colleagues and friends who have been part of my daily life during these 3 years at CEA. My thanks go to Nicolas, Pascal, Jérôme, Cécile, Michel, Alexandre, Olivier, Ayoub and Eric B. for all the interactions, trainings and exchanges that have punctuated my days, in the laboratories or the coffee room.

Thanks to all the PhD students, young doctors and interns that were present during my thesis: Cailloux, Vincent, Ulysse, Pouille, Christina, Théo, Gautier, Angélique, Louis, Clément, Marion and all the others. Without this group of friends, the thesis would not have been the same, either on a personal or professional level, as our mutual help have so much contributed to our respective subjects. This experience allowed me to grow professionally and establish friendships and connections that will last a lifetime.

Special thanks to my Mousquetaire brothers, Vincent and Cailloux, I am so grateful to have shared these amazing years with you since 2019. I will obviously remember our conference/trip to California, Sidi Jacqui's marriage, polishing evenings in 391, Beer Garage afterworks (WD-650 and T100-Porter in our hearts, as well as Bohemian Rhapsody and dart performances), and of course the Puzzle's apartment during lockdowns. So many more memories were forged with all of the 6/7 team. Ulysse, fils, thanks you for your daily good mood, our date trip to Porto or the Cali road trip. Keep believing in yourself and know that you always have your toothbrush at home. Pouille, thank you for your cocktails, co-creating FB, our BP victories, our conference in Vienna, the tennis matches and for being the second best meme creator in the building. Also, thank you for challenging me during the thesis writing with your unlimited comments and humor in the 112D. I also think of you Angélique, who has filled with your presence and adventures this office that was once quite empty and isolated.

I would also like to thank my long-time friends who have been there in my personal environment outside of work, as always: thank you Pierre, Noël, Hugo, Aurel, Alexander.

My biggest thought is for you, αγάπη. I am grateful for your support, patience, care and encouragement on a daily basis, and I am proud to be inspired by your journey, courage, and benevolence to become even better.

Lastly, I would like to dedicate this work to my family, for their unconditional love and unwavering support throughout my own journey. Thank you for always being proud of me and accompanying me in my adventures, for setting up a wonderful pot de thèse or as assisting a crazy son and brother on August 15 during a long day of triple effort.

Abstract

Powder-based metal additive manufacturing (AM) has emerged as a competitive, alternative technology to conventional metallurgical processes such as casting or forging for the production of parts used in different industrial sectors, including aerospace, automotive, biomedical and energy. This success is attributed to the almost unlimited design possibilities for the manufacturing of near-net-shape components with excellent mechanical properties. Moreover, one of the main and differentiating advantage of AM technologies from conventional subtractive processes is that substantially smaller amounts of material are needed to build the parts. In the case of laser powder bed fusion (L-PBF), considered as the most mature AM process for the fabrication of complex metallic parts, they are manufactured by successive addition of powder layers on top of each other, with selective consolidation of the material by a laser between each layer. During the process, only a small fraction of the build volume is consolidated as parts, and the economic and ecological efficiency of L-PBF strongly depends on the ability to efficiently reuse un-melted powder. However, the remaining powders recovered at the end of a fabrication can be altered by the process due to the complex interactions between the laser and the powder bed leading to material ejection contaminating the adjacent un-used powder. Besides, the exposition to high temperatures with repeated laser scanning in an imperfectly controlled atmosphere with residual oxygen levels can lead to particles oxidation. This work focuses on the understanding of powder reuse, also referred to as powder recycling, with its impact on the raw material and the manufactured specimens. This PhD thesis also proposes a methodology for the in-situ monitoring of the powder quality during the L-PBF process, as well as an investigation of the influence of manufacturing parameters on powder degradation. In a global perspective, the objective of this thesis is to make powder recycling reliable in L-PBF, and thus reduce material waste in a context of circular economy.

Résumé

La fabrication additive (FA) métallique à base de poudre s'est imposée comme une technologie compétitive alternative aux procédés métallurgiques classiques tels que la fonderie ou le forgeage pour la production de pièces utilisées dans différents secteurs industriels comme l'aérospatial, l'automobile, le biomédical ou les énergies. Ce succès est attribué aux possibilités de conception presque illimitées pour la fabrication de composants proche des cotes avec d'excellentes propriétés mécaniques. En outre, l'un des principaux avantages des technologies de FA par rapport aux procédés soustractifs classiques est le fait que la quantité de matière nécessaire pour fabriquer une pièce donnée est nettement inférieure. Dans le cas de la fusion laser sur lit de poudre (L-PBF), considéré comme le procédé de FA le plus mature pour l'élaboration de pièces métalliques complexes, celles-ci sont fabriquées par ajout successif de couches de poudre les unes au-dessus des autres, avec une consolidation localisée du matériau par un laser après chaque dépôt de couche. De ce fait, lors des fabrications, seule une petite fraction du volume de poudre utilisé est consolidée en tant que pièces, et les coûts et le rendement économique et écologique du procédé L-PBF dépendent fortement de la capacité à réutiliser efficacement la poudre non fondue. Cependant, les poudres récupérées à la fin d'une fabrication peuvent être dégradées par le procédé du fait des interactions complexes entre le laser et le lit de poudre conduisant à l'éjection de matière qui peut contaminer le lit de poudre. Par ailleurs, les particules non fondues peuvent être exposées à de très hautes températures lors des passages successifs du laser, et ce dans une atmosphère imparfaitement contrôlée avec des teneurs résiduelles en oxygène suffisantes pour promouvoir leur oxydation. Ce travail se concentre sur la compréhension des effets de la réutilisation de la poudre, également appelée recyclage de la poudre, et de leur impact sur la matière première et les pièces élaborées. Cette thèse propose également une méthodologie de suivi in-situ de la qualité de la poudre pendant le procédé L-PBF, ainsi qu'une étude de l'influence des paramètres de fabrication sur la dégradation de la poudre. Dans une perspective plus globale, l'objectif de cette thèse est de rendre le recyclage de la poudre plus fiable en technologie L-PBF, et ainsi réduire les déchets de matière première dans un contexte d'économie circulaire.

Contents

List of Figures

List of Tables

Nomenclature

List of Abbreviations

AM	Additive Manufacturing
ANOVA	ANalysis Of VAriance
ASTM	American Society for Testing and Materials
BCC	Body Centered Cubic
BD	Build Direction
BSE	BackScattered Electrons
CAD	Computer Aided Design
CAM	Computer Aided Manufacturing
CCD	Charge-Coupled Device
CIE	International Commission on Illumination
CMOS	Complementary Metal-Oxide Semiconductor
DOE	Design Of Experiments
Dpi	Dots per inch
EBM	Electron Beam Melting
EBSD	Electron BackScattered Diffraction
EDS	Energy-Dispersive x-ray Spectroscopy
FCC	Face Centered Cubic
GD-MS	Glow Discharge Mass Spectrometry
HAGB	High Angle Grain Boundary
HAZ	Heat Affected Zone
ICP-AES	Inductively Coupled Plasma Atomic Emission Spectrometry
IPF	Inverse Pole Figure
IR	InfraRed
ISO	International Organization for Standardization
LBM	Laser Beam Melting
L-PBF	Laser Powder Bed Fusion
MPB	Melt Pool Boundary
NDT	NonDestructive Technique
OM	Optical Microscopy

PSD	Particle Size Distribution
RGB	Red Green Blue
SEM	Scanning Electron Microscopy
SE	Secondary Electrons
SR	Sieved Residues
SS316L	Stainless Steel 316L
STL	STereo-Lithography
UTS	Ultimate Tensile Strength
WD	Working Distance
Wt. %	Weight %
XCT	X-ray Computed Tomography
XRD	X-Ray Diffraction
YS	Yield Strength

List of Symbols

P	Laser power	[W]
v	Laser scanning speed	[mm.s^{-1}]
h	Hatch distance	[mm]
e	Layer thickness	[mm]
d	Laser beam diameter	[mm]
E_{vol}	Volumetric energy density	[J.mm^{-3}]
E_{lin}	Linear energy density	[J.mm^{-1}]
$E_{vol/spot}$	Local volumetric energy density	[J.mm^{-3}]
m	Mass	[g]
ρ	Density	[g.cm^{-3}]
S_a	Areal surface roughness	[µm]
k_p	Parabolic oxidation rate constant	[g^2.cm^{-4}.s^{-1}]
t_{oxide}	Oxide scale thickness	[nm]
M	Molar mass	[g.mol^{-1}]

Introduction

Additive manufacturing (AM) industry is in a continuous growth and maturation, expanding in several sectors such as aerospace, automotive, healthcare or energy [1]. Among the numerous additive manufacturing processes, powder-based metal additive manufacturing is the leading industrial technology for the fabrication of geometrically complex parts [2] and has become an alternative process, competing with more matures and conventional technologies such as casting or forging. This success is attributed to the almost unlimited design possibilities offered by AM, allowing *e.g.* mass reduction of structures with topology optimization, production of integrated assembly resolving joining issues of multiples components, parts functionalization with complex lattices structures. Other advantages are the excellent mechanical properties of elaborated parts that are near-net shape, the fast industrialization time, and the few steps of post-processing operations required. Moreover, one of the main and differentiating benefits of these technologies from conventional subtractive processes is that they require substantially smaller amount of material to build the parts.

Laser powder bed fusion (L-PBF) is the most mature AM technology and is already used industrially. Like any AM process, it allows to manufacture parts by successive addition of material, layer by layer, from a 3D digital file [3]. For L-PBF, fabrication is carried out by spreading thin layers of powder on top of each other, with a selective consolidation of the material by one or multiple lasers between each layer. Many factors impact the process and the resulting parts properties and performances, namely the starting material (metallic powder), the processing parameters and conditions, and the post-treatments. Most of the research efforts have been focused on studying the influence of processing parameters on the printed parts quality. The relationship between the powder attributes and the final components properties is much less studied and understood so far. Yet, costs and resource efficiency of the L-PBF process depends greatly on the ability to reuse powder efficiently.

During the L-PBF process, only a small fraction of the build volume (10 - 50 %) is generally consolidated as parts [4] and material costs are attributed to 5 - 46 % of the total costs [5]. The reuse of the non-melted powder, also referred to as powder recycling, is essential to reduce material waste and improve the process sustainability. However, the remaining powders recovered at the end of a manufacturing process, although not solidified as part on the build platform, may undergo an alteration of their attributes. While the laser interacts with the powder bed, a melt pool is created and complex interactions lead to instabilities and material ejection contaminating the adjacent un-used powder. In addition, the powder bed is exposed to high temperatures with cyclic heating of the parts with successive laser scanning, in an imperfectly controlled environment with residual oxygen levels sufficient to oxidize the particles. This degradation of powder quality adds an uncertainty to the process that can create variations in the elaborated parts properties. In order to avoid risks and to ensure the repeatability of the process, the un-melted powder is not necessarily reused for future fabrications.

A better understanding of the phenomena and conditions of degradation during processing and with successive powder recycling, as well as the influence on the properties of the final components, is necessary to achieve a reliable and efficient reuse of the powder in L-PBF. This knowledge, combined with a better control and monitoring of the powder quality during the process, would ensure the proper implementation of the L-PBF powder reuse practice.

The objectives and aims of this thesis are related to the presented issues, and will seek to address the following research questions:

- How does powder recycling in L-PBF affect the quality of the powder feedstock and the final parts properties ?
- How can powder degradation be monitored during powder recycling in L-PBF ?
- How do the process atmosphere and build characteristics influence powder degradation in order to minimize it ?

These questions were explored using a standard material, which is commonly used in the additive manufacturing community and the energy industry, namely Stainless Steel 316L.

Three chapters will be addressing these research questions, with the aims of understanding powder recycling in L-PBF, implementing a monitoring of powder degradation, and minimizing this degradation with an optimization of the parameters. The research approach of this thesis is schematically summarized in figure 0.1, with these objectives being grouped into the *Analysis*, *Monitoring* and *Optimization* boxes. The *analysis* of powder recycling will focus on a study of the influence of successive powder reuse on both the powder feedtock and the manufactured parts properties. The *monitoring* will be developed on the basis of an ex-situ correlation between the colors of the particles and their oxygen content, and the implementation of a methodology for in-line control of the powder bed. Finally, the *optimization* will focus on a study of the influence of the build strategy on powder degradation, including the process atmosphere and parts characteristics such as their volume fraction, spacing and height.

The manuscript is divided into 5 main chapters. The first chapter (chapter 1) presents a literature review, firstly describing the field of additive manufacturing and the laser powder bed fusion process, as well as the stainless steel 316L material. Then, laser powder bed fusion is presented in more detail with the influential factors on the process, focusing on the effects of the powder and the processing parameters. This is followed by a state of the art on powder recycling in L-PBF, with the different studies dealing with the influence on powders and elaborated parts. Finally, the monitoring of the L-PBF implemented in the literature is addressed, with respect to the various controlled features.

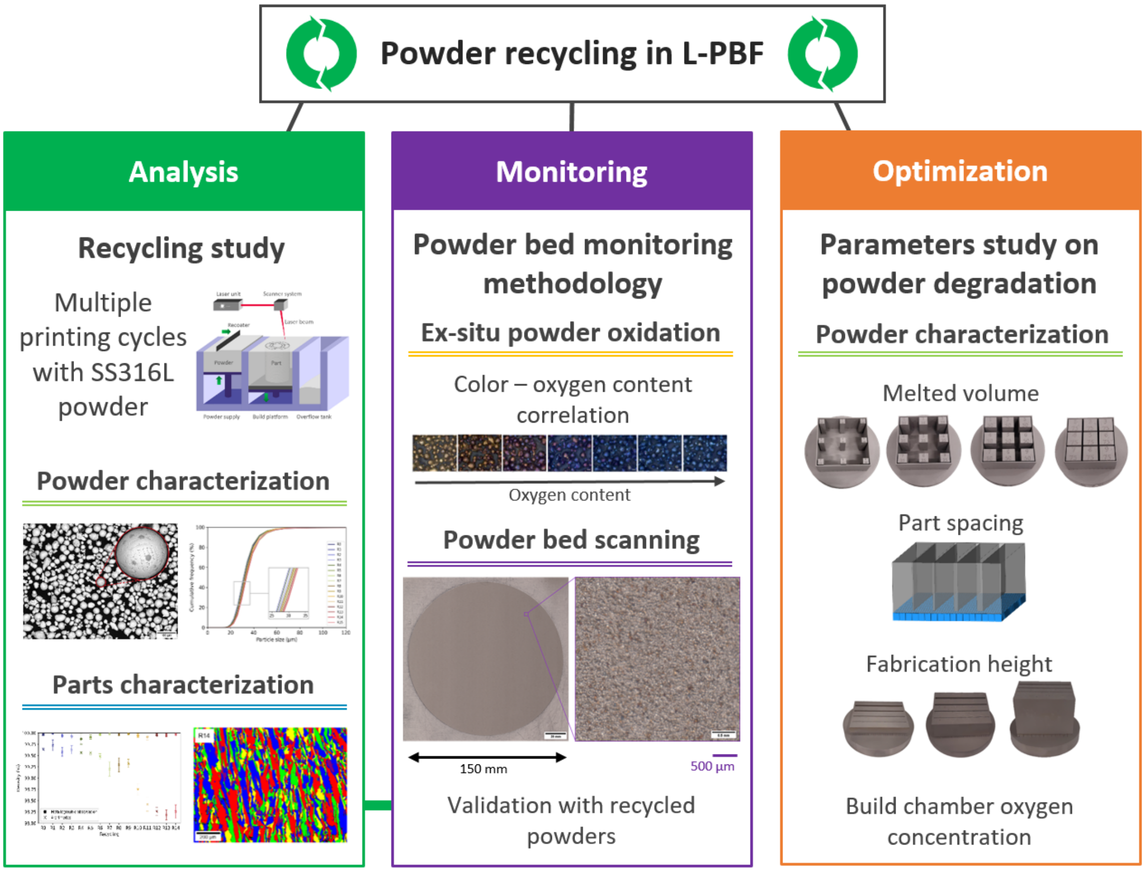

Figure 0.1 – Schematic illustration of the research approach of the thesis.

The second chapter (chapter 2) describes the different experimental techniques and methods employed to produce and characterize the samples. Characteristics and operating conditions of the L-PBF machine used for this work are detailed first. Then, techniques for material characterization are presented, including the microstructural characterization techniques common to powders and parts, followed by the specific methods of characterization of the powders and the elaborated components. At last, the experimental setup for the development of a powder monitoring methodology is introduced.

Chapter 3 deals with the *Analysis* box of the chart in figure 0.1. A powder recycling study on an industrial L-PBF machine is carried out and presented, with the successive fabrication and powder reuse leading to the production of 15 L-PBF builds without addition of virgin powder. A thorough investigation of the evolution of powder feedstocks attributes and the effects on the printed parts properties is conducted.

Chapter 4 proposes a new methodology to monitor in-situ the quality of the powder in L-PBF, regarding its oxygen content. Based on a preliminary ex-situ oxidation study, the colors of oxidized particles are correlated to their oxygen content. Measurement of powder beds oxygen content is performed by image analysis with powder bed scanning at high resolution using an instrumented L-PBF platform. The development of the methodology is detailed, as well as validation results carried out with recycled powder samples collected from the recycling study of chapter 3.

An analysis of the influence of process parameters and build characteristics on the kinetics of powder degradation is presented in the last chapter (chapter 5). Build chamber oxygen concentration, but also less studied parameters such as parts spacing, height and volume fraction in the print are investigated in order to understand their impact during the process, and minimize powder degradation in L-PBF.

The manuscript is then completed by a synthesis and proposal of perspectives.

Chapter 1

Literature Review

1.1 Additive Manufacturing Laser Powder Bed Fusion

1.1.1 Overview

History of Additive Manufacturing

As early as the 1860s, photosculpture allowed duplication of three-dimensional objects with simultaneous photographs of it from different perspectives. Topography, in 1890, introduced the concept of a layered method for topographical reliefs maps [6]. Layerwise creation of a part and manufacturing from a 3D model are the essences of additive manufacturing.

In 1971, french inventor Pierre Ciraud [7] proposed one of the first method with similarities to current additive manufacturing processes, with powder deposition by gravity and an energy beam to heat the particles and form a continuous layer, as shown in figure 1.1 (a).

In 1979, Ross F. Housolder [8] patented a new molding process for forming a three-dimensional article in layers, with sequential deposition of material in planar layer and selective solidification of each layer by using heat (see figure figure 1.1 (b)).

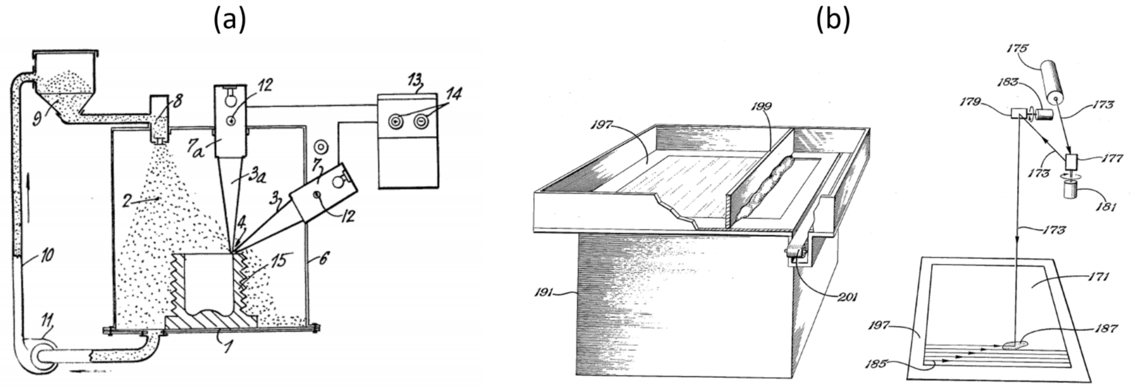

Figure 1.1 – Processes patented by (a) P. Ciraud (1971) and (b) R.F. Housholder (1979).

It is in the 1980s that additive manufacturing really started, with the first machines and commercial uses. Japanese researcher Hideo Kodama was the first to apply for a patent for a rapid prototyping device. Because of funding issues, he was not able to file the full patent specification before the one-year deadline and the application never went through. Nevertheless, he published two papers about his method for automatic fabrication of a three-dimensional plastic model by stacking cross-sectional layers, using liquid photo-hardening polymer solidified by ultraviolet rays [9, 10].

Then in France in July 1984, Alain Le Méhauté, Olivier de Witte and Jean-Claude André filed a patent for the stereolithography process [11]. The patent was granted but the idea of this 3D printer was not supported and payment of patent annuities was discontinued [12].

In the mean time in America, three weeks after the patent application by the french team, Charles Hull filed for his own stereolithography technology [13]. He founded the company 3D Systems which produced in 1987 the first commercial 3D printer in the world, the SLA-1 machine, in which layers are added by hardening photopolymers with a concentrated beam of ultraviolet light. Charles Hull also developed the file format .stl allowing to communicate 3D modeled design to the rapid prototyping system [14].

A set of new and promising technologies were then developed in the early 1990s, producing objects by adding material. These processes involved different kinds of materials and first attempts of classification and standardization started [15, 16].

Firstly used to quickly manufacture prototypes, additive manufacturing technologies were subsequently also employed for rapid tooling, enabling to reduce development and production time. With increased knowledge and improved processes, additive manufacturing is now allowing direct production of parts [17].

Definition

Additive Manufacturing (AM) is nowadays the general term for all the processes that create parts from 3D model data by successive additions of material, usually layer upon layer, as opposed to subtractive manufacturing, according to ISO - ASTM 52900-15 [3]. Processes differ in physical form of starting material, modes of matter input and energy source. However, all of them follow the same path from the digital product to the real product, as schematized in figure 1.2 [18]. First, the part is modeled with a CAD (Computer-Aided Design) software then converted into suitable format called .stl, which translate surface geometry into triangles meshing. The file is then uploaded to a CAM (Computer-Aided Manufacturing) software where the part is divided into multiple layers (slicing) corresponding to the different manufacturing strata. Finally, heat source manufacturing paths are generated and all data are sent to the printer as a program in order to start the build.

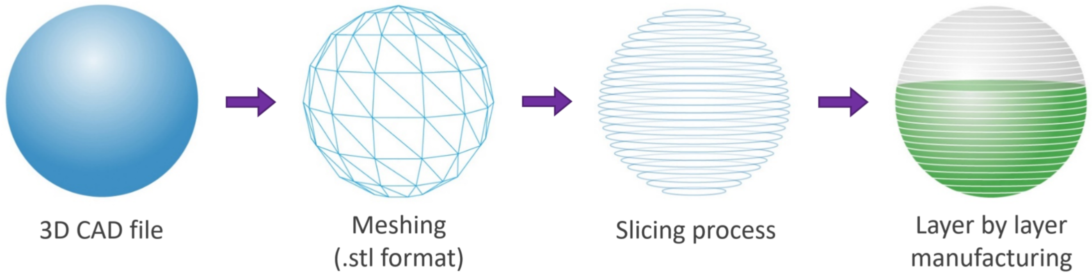

Figure 1.2 – Digital chain of Additive Manufacturing [18].

Other terms are often used to describe AM, although some of them appear a bit reductive: 3D printing, Rapid Prototyping, Rapid Manufacturing, Additive Freeform Fabrication.

There are different ways to categorize the numerous AM processes. Standardization groups (ISO, ASTM) classified all processes into seven categories [19, 20]. Figure 1.3 recalls the standard names of these categories and briefly describes their principle. Processes differ in terms of ways to deposit layers and how the latter are bonded together. Other types of classification has also been used in the literature, including a division of processes into four categories depending on the state of starting material used : liquid, powder, filament/paste or solid sheet [21, 22].

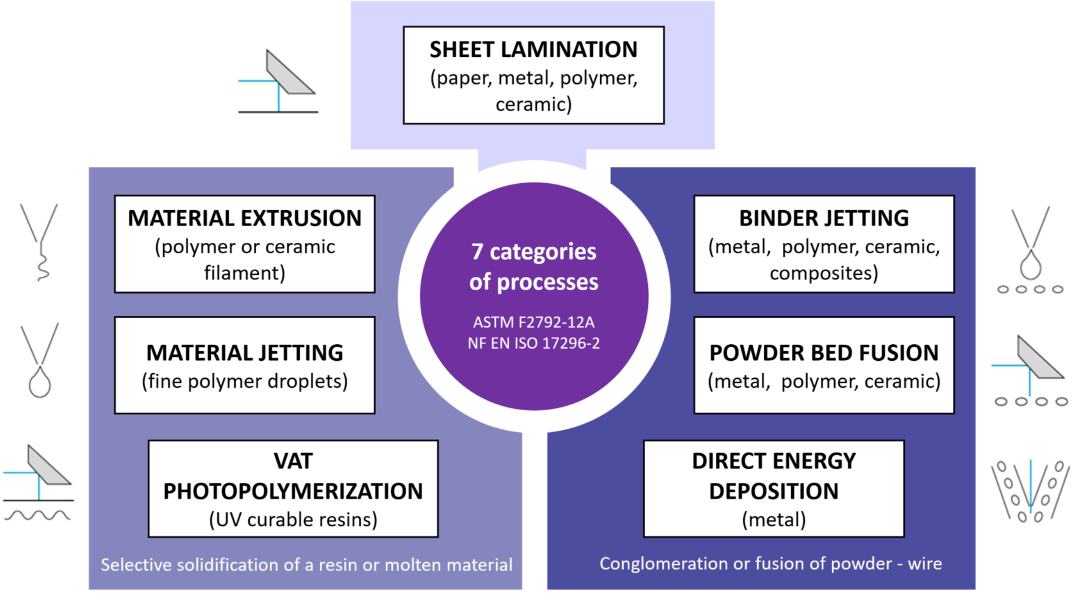

Figure 1.3 – Standard names of AM process categories, adapted from [23].

From now on, the focus will be mainly on metallic additive manufacturing.

Growth

For metallic materials, AM offers alternatives to conventional processes such as casting or forging due to its greater design possibilities [24]. With a higher degree of geometrical freedom, it allows mass reduction with topology optimization and the realization of complex structures. Parts elaborated are near-net shape and machining and assembly steps can therefore be eliminated or at least strongly reduced, making production times shorter. Besides, the a priori possibility to save raw materials as processes only use the right amount of material needed to build the parts is also an asset for production costs reduction. Various additive manufacturing processes and applications have been detailed in the literature over the years [15, 21, 22, 24, 25].

The understanding of these technologies, and the associated possibilities attracted the interest of both academics and industrials to this emergent field. Research in additive manufacturing has been accelerating over the past few years, as reflected by the increased number of publications in the literature on the topic (see figure 1.4 (a)). Many industrial sectors such as aerospace, biomedical, or automotive are now active in the AM field. In 2022, the number of pending patents is very close to the number of granted patents still in effect, representing almost 40 % of the total amount of patents related to AM (including expired patents), as illustrated in figure 1.4 (b).

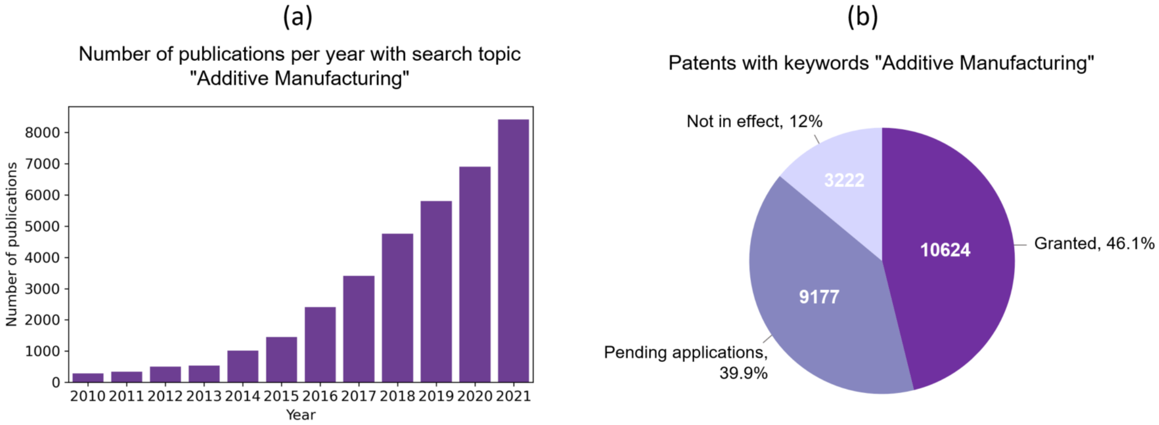

Figure 1.4 – (a) Number of publications (WebOfScience) and (b) patents (Orbit) with keywords ”Additive manufacturing”, April 2022.

The growth of 3D printing industry is outstanding. Wohlers Report 2019 [26] highlighted an annual increase of revenue from metallic materials of more than 40% over the past 5 years. After a slower growth in the AM market in 2020 due to the COVID-19 pandemic, the industry recovered and grew by 19.5 % in 2021 [1]. In the same year, according to AMPOWER Report 2022 [2], machine sales revenue of all AM technologies is dominated by metal powder bed fusion, with a share of 40 %.

AM processes continue to shift from rapid prototyping to rapid tooling and direct parts manufacturing. Wohlers Report 2022 [1] indicated that the production of final parts now represents 33.7 % of all AM applications. However, it is still difficult to replace conventional processes in a near future, in particular for markets with high-volume production of simple parts [27]. To go further and bring AM to the next level, many challenges remain. Huang et al. [28] pointed out four essential technology elements and system integration to make additive manufacturing sustainable, schematized in figure 1.5.

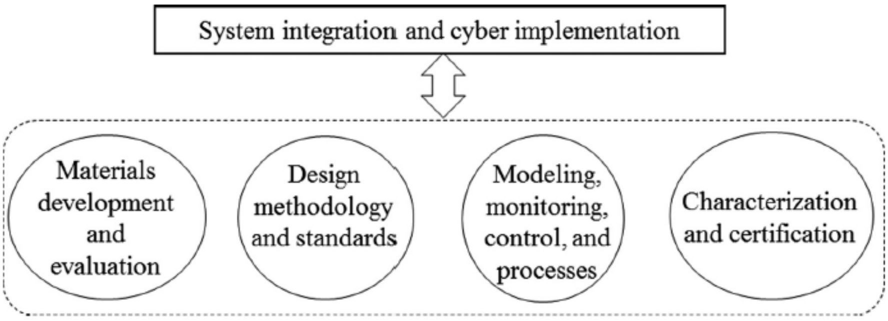

Figure 1.5 – Four essential technology elements and system integration for viable AM [28].

Frazier [29] drew the same conclusions on the technical challenges to widespread adoption of AM. Among them, qualification and certification methods specific to these processes, and integrated in-process monitoring and controls have been repeatedly identified.

1.1.2 Laser Powder Bed Fusion

Definition

Laser Powder Fusion (L-PBF) is one of the most widely used AM technology, also referred as Selective Laser Melting (SLM) or Laser Beam Melting (LBM)[1], being part of the powder bed fusion AM category (figure 1.3). This process is very attractive for production of high-density metallic components with complex structures directly from CAD models. A wide range of materials can be processed by L-PBF: stainless steels, maraging steels, nickel superalloys, titanium alloys, aluminum alloys, cobalt chrome alloys, copper alloys [29, 30].

The general operation of this process is illustrated figure 1.6. The process starts with the spreading by a recoater of a fine metal powder layer (20 - 90 µm)[2] upon a build platform (a substrate metal plate). Then, one or multiple high-power laser beams melt the powder selectively and the molten metal solidifies rapidly. The build platform is lowered by a height equal to the powder layer thickness and the cycle starts over, with a new powder layer spread on top of the previous one [30, 31].

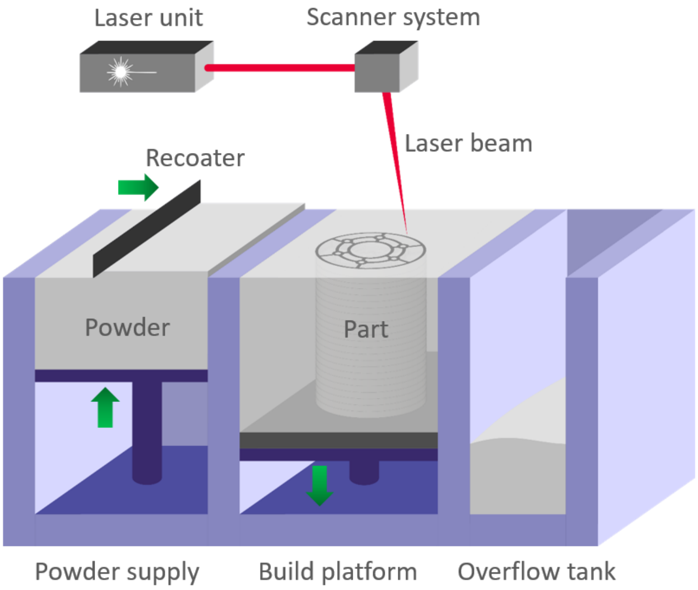

Figure 1.6 – Schematic of Laser Powder Bed Fusion Process.

Manufacturing takes place under protective atmosphere (commonly argon or nitrogen) to avoid oxidation of parts and limit powder degradation. The lasers used are usually infrared radiation (IR) lasers, operating in continuous mode. Some researches are trying the use of lasers with lower wavelength, like green lasers to improve absorption for some materials. Laser beam diameters are between 30 and 150 µm, and laser powers are between 50 and 1000 watts. Along with Electron Beam Melting (EBM, the second metallic powder bed fusion process), L-PBF is the technology that allows the highest input energy density, with this combination of high power and very small laser spot. Some new machines are equipped with multiple lasers to reduce production times. Laser scanning is accomplished by rotating mirrors.

---

[1] Even though the designation SLM is still widely used in the AM domain, the latter is a trademark, and L-PBF terminology will be used in the following, as defined by the norm.

[2] In this section, characteristic values should be taken as indicators.

L-PBF is a complex process involving numerous phenomena. Figure 1.7 describe some of the issues which occur during rapid melting and solidification process (all scales are not necessarily satisfied). The laser interacts with the powder bed to form a melt pool (typical dimensions of 10^{-2} mm^3). Because of rapid movement of the laser (between 0.2 and 3 m.s^{-1}), cooling rates are much higher than in conventional solidification processes, say in the 10^5-10^7 K.s^{-1} range [32]. This results in a fine microstructure quite typical to all selective laser melted parts, that significantly improves strength and toughness [33]. However, microstructure and properties tend to be anisotropic due to temperature gradient [34].

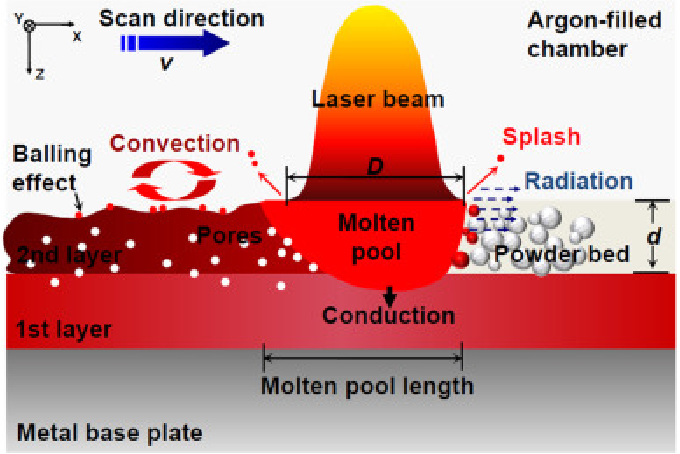

Figure 1.7 – Schematic overview of the interaction zone between laser and powder bed [35].

The quality of parts manufactured by L-PBF depends on the process parameters, mainly laser power, scanning speed, hatch distance (spacing between two laser tracks) and layer thickness. These parameters are strongly influenced by the starting powders properties and characteristics, such as the chemical composition, particle size distribution, shape, density, etc. Inappropriate processing parameters and conditions, like oxygen content in the fabrication chamber lead to defects such as porosity, internal stress, cracks, etc. [35]

Benefits and Limits

Metallic additive manufacturing in general, and L-PBF differs from traditional casting or forging processes in several aspects [31]:

- The design freedom allows manufacturing of complex parts, to resolve joining issues by replacing several parts by one integrated assembly, and also the possibility to add functions (e.g. thermal regulation channels, lattices structures for oil separators).
- Mass reduction of structures is favored, with the use of topology optimization.
- Mechanical properties are equivalent or better compared to parts elaborated by conventional processes due to the really fast cooling rates and resulting fine microstructure.
- This technology does not require a lot of tooling.

- It consumption of energy and resources is low, due to the a priori small amount of material lost. Indeed, the unmelted powder can be recovered, sieved and then re-injected, even though things are not so obvious in practice, as the present thesis will show.
- It is considered a near-net-shape technology.
- A low number of post-processing operations is required, resulting in time saving.
- Production can be on demand, therefore limiting stocks and associated costs.

However, although some parts created by AM are already being industrialized, there are still several obstacles or limitations to the development of the L-PBF to enable mass production of functional parts:

- Build rates of the parts are still quite low, rarely exceeding 30 cm^3/h [36], but this issue is being worked on with the development of multi-laser machines, allowing build rates higher than 100 cm^3/h when using a quite large layer thickness (*e.g.* around 90 µm) [37].
- Implementation costs are relatively high due to high machine cost per part [38]. Combined with above mentioned low build rates, it does not favor mass production for parts with low added value.
- The size of the parts is limited by small build chambers, usually around 20 - 64 dm^3, up to 160 cm^3 [37].
- Structures are generally necessary to allow mechanical support and laser heat dissipation. It can lead to complication in terms of design and the removal of the support structures induces poor surface finishes at interfaces [39].
- Surface roughness of parts is limited by the melt pool characteristic dimensions, and even though reduced as mentioned above, post-treatments are often needed (usually sand-blasting, electropolishing).
- Several metallurgical defects can occur during manufacturing : porosity, internal stress, hot cracking and anisotropy [40]. This points to the need of adapted nondestructive testing (NDT) and in-line diagnostic techniques as mentioned in section 1.1.1.
- Repeatability and reproducibility are critical issues, one of the key parameter being the powder properties. The use of recycled powders can lead to important powder properties variation which directly influence properties of parts, hence repeatability [41].

1.1.3 Stainless Steel 316L

Overview

Stainless steel 316L (SS316L) is an iron-based alloy with chromium and nickel as main additions. It has very good corrosion resistance due to its high chromium content ($> 16\%$). The latter allows formation of a passivating film of chromium oxide Cr_2O_3 on the surface of the parts. "L" stands for "Low carbon", with a content limit of 300 wppm. This feature allows to reduce significantly the formation of chromium carbides and to avoid chromium depletion at the grain boundaries. Nickel stabilizes the austenitic structure γ at room temperature. SS316L crystallizes in FCC system (face-centered cubic) and presents remarkable ductility and very good weldability [42].

Table 1.1 presents the chemical composition requirements of SS316L according to the ASTM ASTM F3184 norm [43].

Table 1.1 – Chemical composition of 316L stainless steel (wt.%).

Fe	Cr	Ni	Mn	Mo	Si	C	P	S
Bal.	16-18	10-14	< 2	2-3	< 1	< 0.03	< 0.045	< 0.03

Austenitic stainless steel 316L is one grade of stainless steel widely used in different fields such as marine, pharmaceutical, chemical, nuclear, petrochemical and construction industries. Several norms and designations exist across the globe and are summarized Table 1.2.

Table 1.2 – Designation of 316L stainless steel.

Europe EN 10088-3	France AFNOR	Germany DIN	USA AISI
X2CrNiMo17-12-2	Z2CND17-12	1.4404	316L

In stainless steel welds, the solidification mode is often predicted by the chromium to nickel equivalencies ratio. The chromium equivalence (Cr_{eq}) regroups δ-ferrite stabilizing elements and nickel equivalence (Ni_{eq}) is the term for cumulative effects of γ-austenite stabilizers. The ratio ($Cr_{eq}/(Ni_{eq})$), based on the chemical composition of the alloy, has been evaluated by different methods and reported by Korinko et al. [44]. For example, the Schaeffler expression $Cr_{eq} = Cr + Mo + 1.5Si + 0.5Nb$; $Ni_{eq} = Ni + 0.5Mn + 30C$ is often used to calculate the ratio, the symbols being the composition of the element in weight percent. The value of the ratio determines the solidification mode. In view of the starting composition, solidification from high temperature liquid should in principle follow the sequence $L \rightarrow L + \delta \rightarrow L + \delta + \gamma \rightarrow \gamma + \delta \rightarrow \gamma$. However, a completely austenitic microstructure is not guaranteed as some residual ferrite may remain due to rapid solidification in welding or AM. The higher the equivalencies ratio is, the larger the ferrite-forming tendency [45]. Differences in chemical composition can therefore result in different amounts of body-centered cubic (BCC) δ-ferrite in stainless steels materials.

L-PBF Microstructure

SS316L parts elaborated by L-PBF have a heterogeneous and hierarchical structure that can be studied in macro, micro and nano-scales, depending on the observation means [46]. The structure is quite different depending on the observation plane, whether it is along the build direction (parallel to z axis) or perpendicular to it.

The macro-scale is that of the melt pool tracks generated by the scanning of the laser beam and of the crystallographic grains. Figure 1.8 is a cross section of a 316L cubic specimen observed by optical microscopy after etching. Melt pool boundaries are revealed in bright. Melt pools width and height depend on the process parameters, such as laser power and scanning speed. The geometry of these melt pools is important and is linked with the heat transfer phenomena associated with laser motion. The latter partly controls the size and shape of the grains [47].

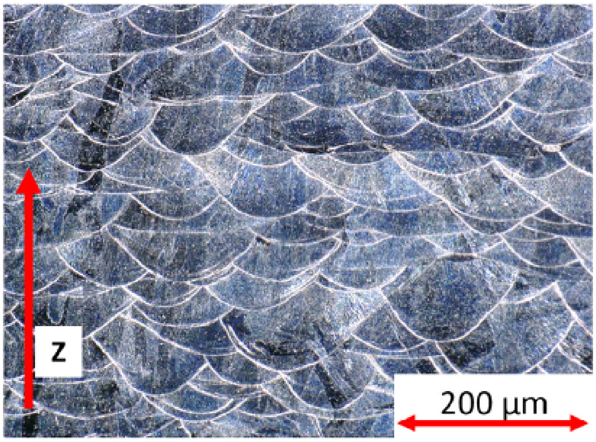

Figure 1.8 – Optical microscopy of L-PBF 316L melt pools [48].

Still at the macro-scale, the crystallographic grains are elongated and columnar, roughly aligned with the building direction, often extending across several melt pools. When the laser is scanning the layer, adjacent and underlying previously formed melt tracks are partially re-melted. Cooling rates are different between the center and the boundaries of the melt pools. Heat extraction creates a temperature gradient, and the columnar grains grow in the direction of the latter. The grain size range is between 10 - 100 µm. Samples exhibit a strong epitaxial orientation, mostly in the $\langle 101 \rangle$ or $\langle 001 \rangle$ along the build direction [49], as illustrated in figure 1.9. This texture is typical of the L-PBF process and is common to other materials such as nickel, titanium or aluminum alloys [50].

Upon higher magnification, at the micro-scale, a fine cellular network is present within the grains. This intragranular sub-structure has a cell diameter around 1 µm and is formed because of extremely high cooling speed of the L-PBF process [46]. The cellular structure can also be observed as bar-like depending on the orientation of the large columnar grains containing the sub-structure. The forming mechanisms of these cellular networks will be discussed later in section 1.2.2.

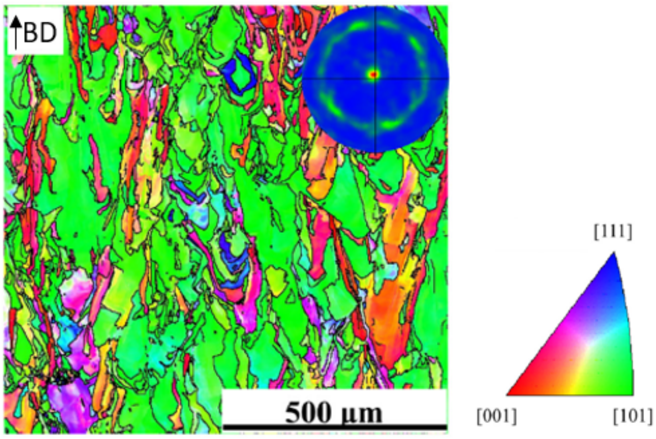

Figure 1.9 – Orientation imaging microscopy using EBSD and pole figure of L-PBF 316L [51].

Figure 1.10 presents this overview of multi-scales structures features in L-PBF SS316L with schematic drawings and corresponding SEM micrographs. As we can see, elongated grains delimited by high angle grain boundaries (HAGB) cross several melt pool boundaries (MPB). Inside the grains, the fine cellular structure is observed.

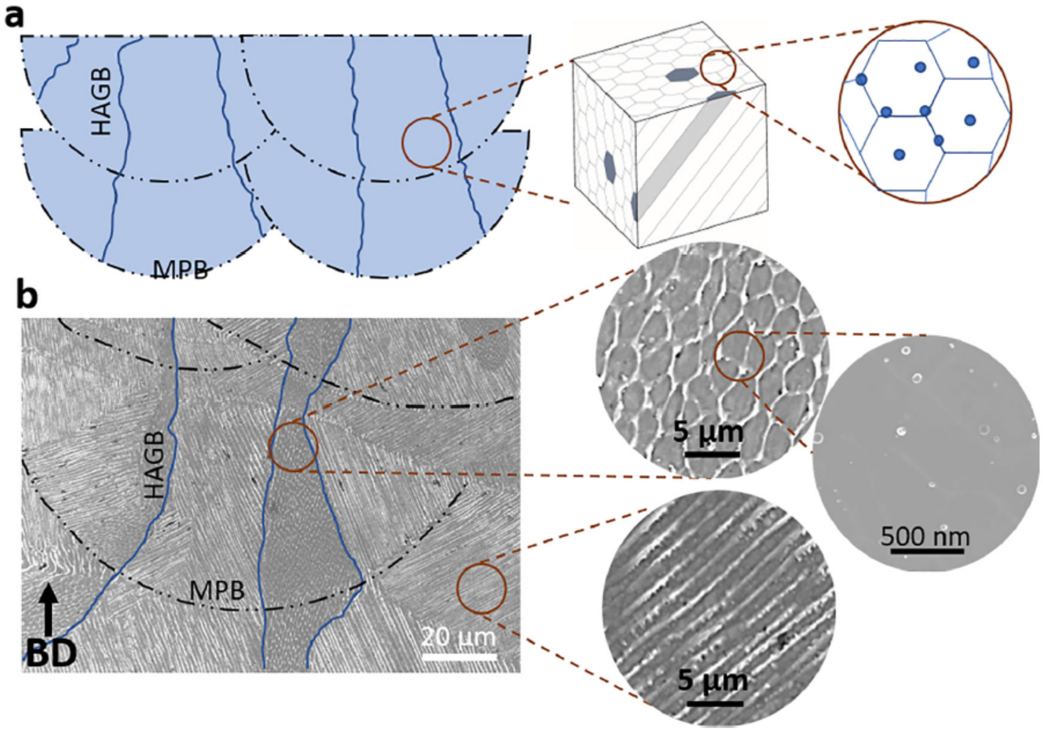

Figure 1.10 – Overview of the general micostructure of L-PBF parts [52].

At the nano-scale, spherical and amorphous oxide nano-inclusions (between several tens to several hundred nanometers) are present, randomly distributed both inside the matrix and at cells boundaries [53]. They are mostly nano-oxides of silicon and chromium reacting at high temperature with residual oxygen during the process.

Properties compared to conventional processes

Several research works in the literature have been performed regarding the comparison between the mechanical properties of SS316L fabricated using L-PBF process and samples manufactured with conventional methods.

Yield strength is significantly improved with the L-PBF process, attributed to the fine microstructure [54]. When comparing to casting and hot pressing, Bartolomeu et al. [55] highlights also better yield strength, as well as ultimate tensile strength and hardness. However, elongation at break is lowered, but still acceptable for various applications (greater than 30% in most cases). Similar conclusions are made by Song et al. [56] and Tolosa et al. [57], comparing to wrought products. They showed a Vickers hardness for L-PBF samples around 240 HV. Riemer et al. [58] investigated the fatigue behavior. Under cycling loading, SS316L showed fairly good fatigue performance, similar to those of traditionnally manufactured products, even without any post-processing operations.

Wang et al. [59] presented their values of L-PBF 316L tensile properties compared to those of cast and wrought materials of numerous authors. Figure 1.11 (a) is the stress-strain curves, and (b) summarizes yield stress versus elongation of their work, high performance materials (strenghtened by nanotwin bundles and bimodal grain), annealed materials and strengthened through plastic deformation materials.

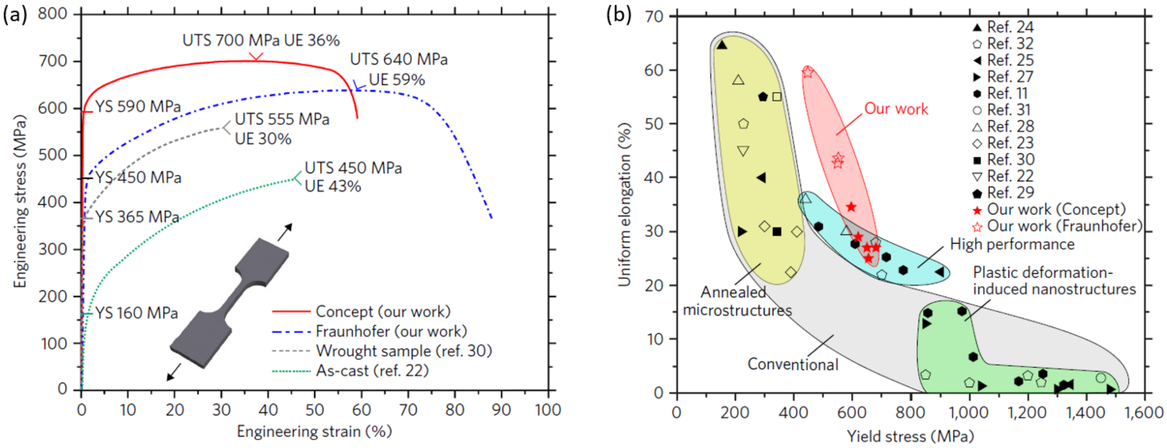

Figure 1.11 – Tensile properties of L-PBF 316L [59].

Stainless steel parts elaborated by laser powder bed fusion display outstanding combination of strength and ductility, making this process very attractive for various applications.

Even if the properties of parts elaborated by L-PBF are equivalent or superior compared to those of conventional processes, a number of parameters needs to be accounted for. The influential factors on laser powder bed fusion, powder and process-related, will be presented in the following section.

1.2 Influential factors on Laser Powder Bed Fusion

Different characteristics and parameters influence L-PBF parts. Spears and Gold [60] listed 50 key process variables that impact the ultimate quality of the finished products. A non-exhaustive list of influential factors is illustrated figure 1.12.

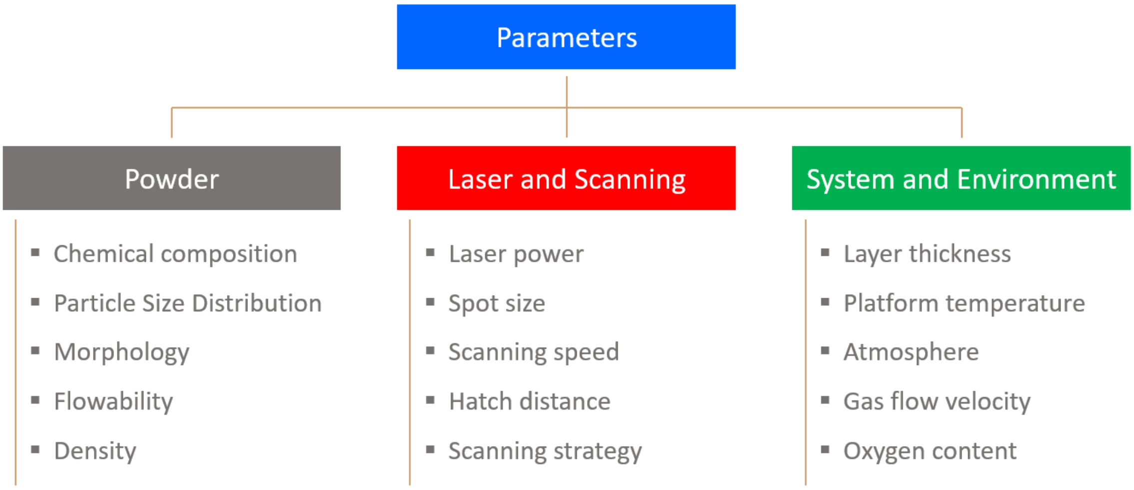

Figure 1.12 – Influential factors of L-PBF process (non-exhaustive list).

Control of the powder material with the understanding of the powder characteristics and impacts is the first step in order to improve the reliability of the L-PBF process.

1.2.1 Powders

Production processes

Several methods for powder production exist: atomization processes, mechanical processes, chemical processes, etc. These different methods will lead to variability in terms of powder characteristics and costs [61]. Powder bed fusion requires high quality metal powders without contaminants. Atomization processes are convenient to produce powders suitable for AM and are the most used commercialized methods.

Atomization is two-steps process. First, molten metal is sheared into small liquid particles due to high-velocity gas jets, water jets, plasma jets or centrifugal action [62]. In order to minimize their surface energy, these liquid particles tend to assume a spherical shape, but cooling kinetics and other phenomena (*e.g.* collisions) may prevent that achievement. According to the system used to disintegrate the liquid metal, there are three well-known atomization processes : gas atomization, water atomization and plasma atomization [62].

- **Gas atomisation** is the most common powder production technique for AM. Figure 1.13 represents the gas atomization process. A gas atomizer contains a furnace where the metal is melted under inert gas or vacuum. Molten metal is forced through a nozzle and dispersed into small droplets by a high-velocity gas jet. It forms mostly fine powders with a globally spherical shape.

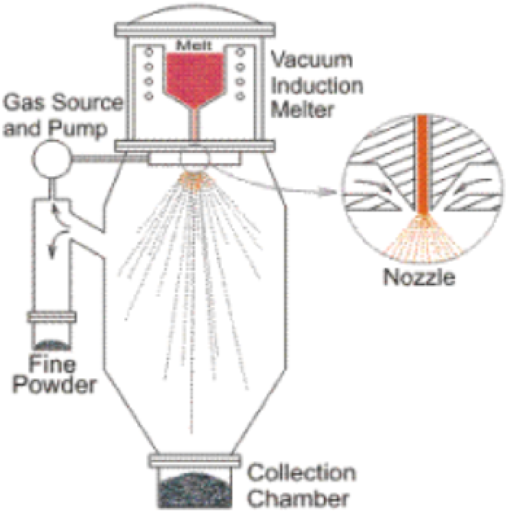

Figure 1.13 – Schematic of gas atomization [63].

- Similar to gas atomization, **water atomization** uses a water jet to disintegrate the molten metal stream. It is used for high production rates at lower cost but the particles produced have irregular shapes [64].
- **Plasma atomization** allows to produce powders with high purity. One or more plasma torches are used to transform metal wire into metal droplets. Melted material solidifies without contacting any crucible and the full process takes place inside the inert atmosphere. Hence, powders produced present a very low level of impurities [61]. If powder of high specific surface are fed in as a raw material, plasma process will yield sphereoidized powders.

Figure 1.14 presents the shape of the particles produced by these three atomization techniques.

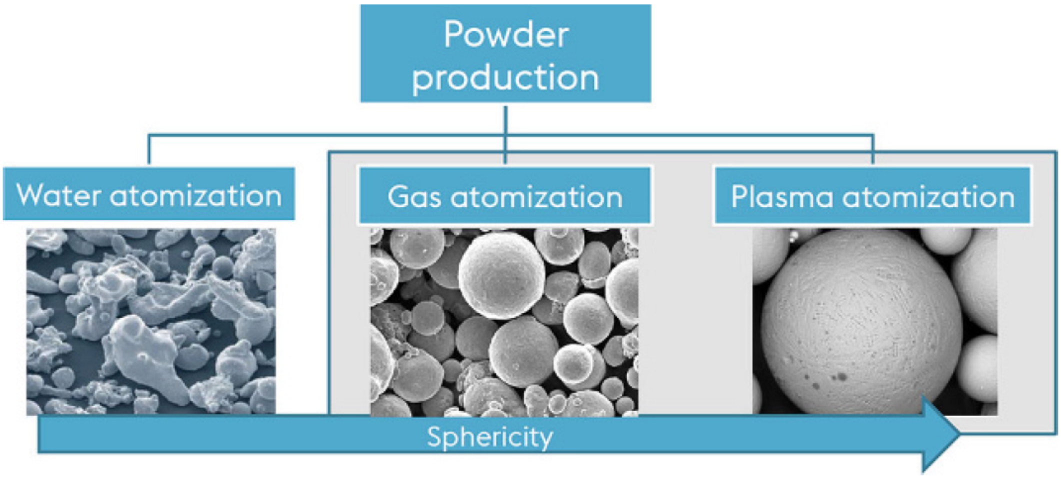

Figure 1.14 – Shape of metal powders produced by water, gas and plasma atomization [65].

Characteristics

The specific characteristics of the powders used in laser powder bed fusion have a direct impact on how the powders behave during the process. One of the key challenge of AM is to understand how powder characteristics influence the outcome of final parts properties and to propose characterization techniques allowing to identify powders matching the process requirements [66].

Benson and Snyders [67] highlighted several factors which play a key role and need to be understood, like the powder flow behavior for sufficient and consistent spreading or the powder packing for maximum layer density. A number of powder characteristics can be measured, as summarized in figure 1.15.

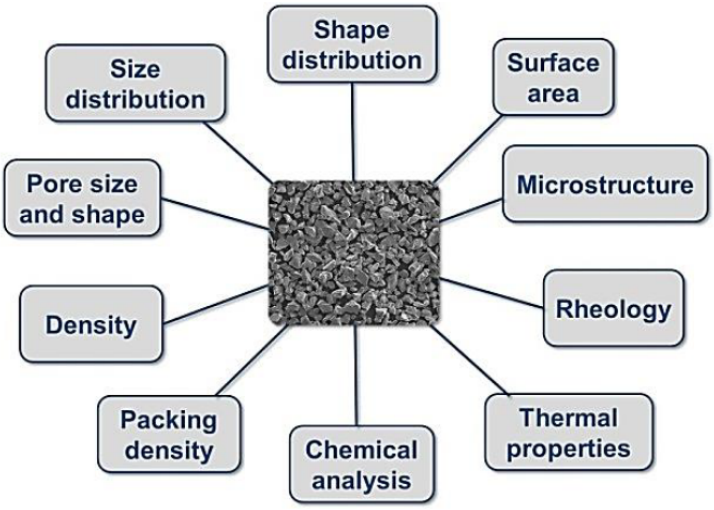

Figure 1.15 – Typical powder characterization parameters [67].

Standardization of the existing and used test methods to characterize properties of metal powders used for AM processes has developed recently, with the release of ASTM F3049 [68]. Sutton et al. [69] reviewed a number of methods commonly used to characterize AM powders. Spierings et al. [70] proposed a specific powder flowability characterization methodology, to be more in line with what powders experience in powder-based processes like L-PBF.

The correlation between these powder characteristics and their impact on the L-PBF process is complex, and some of the influences will be described in the following.

Influence

The main characteristics identified in the literature in relation to the properties of materials manufactured by L-PBF are the particle morphology, particle size distribution and chemical composition.

To study the influence of **particle morphology** on final density of parts, existing researches compare the behavior of water atomized powders and gas atomized powders. As seen previously, gas atomized powders have a more spherical morphology than water atomized ones (figure 1.14). This results in L-PBF samples with a denser structure [71] [72]. The claim of Karapatis et al. [73] or Brika et al. [74] is that particles with **spherical**

morphology lead to higher powder layer density, and can result in denser elaborated parts upon appropriate manufacturing conditions. The shape of the particles influences the packing efficiency of the powder, but also the rheological behavior.

More spherical powders have a **better flowability** due to lower surface friction and mechanical interlocking [74]. This characteristic is crucial in powder-bed systems because it has an impact on the layer spreading. Poor powder flow can lead to non-uniform spreading onto the build platform, therefore to part defects. This is even more important for new 3D printers that tend to use hopper powder delivery mechanisms instead of traditional piston-based system. These systems have the advantages of being in a close loop which reduces the operator exposure and have the potential for automated powder recycling. However, the introduction of powder into the chamber is highly dependent on gravity and powder rheological behavior [75].

Spherical shape does not guarantee high flowability properties. The flow behavior is also influenced by the **particle size distribution**. High fine-fraction is not recommended as it increases powder cohesion and inter-particle frictions. It favors agglomeration of particles, which impacts negatively the powder bed packing [76–78]. On the other hand, fine particles present also advantages for powder bed density, with the ability to fill the voids between the large particles. Karapatis et al. demonstrated that bi-modal distribution increases the packing density, and proposed a coarse to fine size ratio of 1:10 with 30 wt% of fines for optimum density [73]. The right combination of coarse and fine powder grades to achieve maximum packing density is complex, as schematized in figure 1.16. Besides, a good compromise has to be found with fine particles for both packing density and flowability qualities.

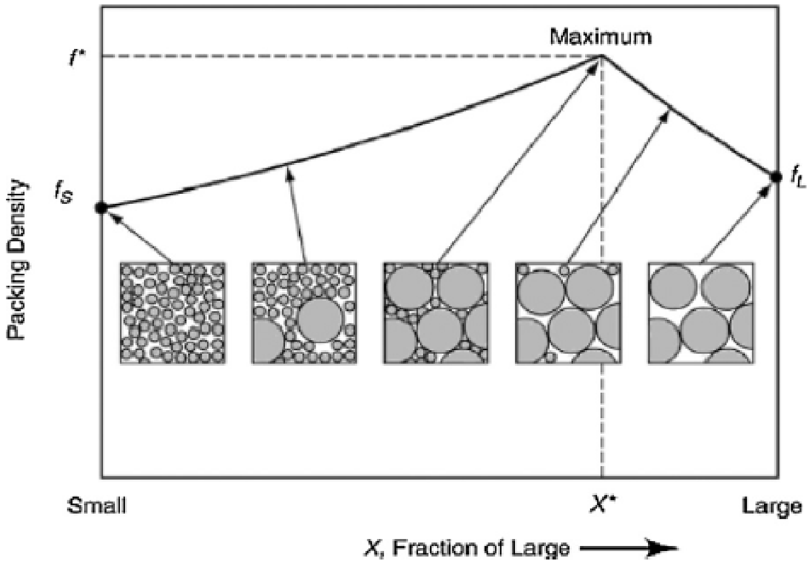

Figure 1.16 – Particle size composition vs Packing density [77].

Particle size distribution (PSD) is usually Gaussian-like with slight asymmetry. A number of studies focused on the influence of different PSD. Spierings and Levy [79] obtained better density for L-PBF samples produced with powder with asymmetric Gaussian PSD towards fine particles. They proposed the requirement that D90 (the particle size of the 90th percentile of the powder) should be about 5 times more than the particle size of the 10th percentile (D10), to have sufficient amount of fine particles. The PSD is often characterized by its D10, D50 and D90, and the width of the size distribution curve can be quantify by its span value, defined as (D90-D10)/D50. Engeli et al. [80] observed that a narrower size distribution span induced better flowability at a given median size. Liu et al. [81] reported higher powder bed density and smoother surface finish of parts from powders with larger span. It is challenging to define a standard particle size distribution which provides optimum packing density while satisfying the needs of powder rheological behavior suitable for the L-PBF process.

The nature of the material, and the **chemical composition** are also strong influential factors. The presence of impurities such as oxygen, hydrogen, nitrogen, carbon can lower the properties of the final parts [67]. As explained previously, components manufactured with water-atomized powder do not present a great density compared to parts elaborated with gas-atomized powder. This comes from the difference in powder sphericity, but also from the higher oxygen contents and the presence of surface oxides on water-atomized powders [82]. Simchi [83] studied different initial oxygen concentrations of iron powder with regards to L-PBF parts density and observed an increase in porosity with higher oxygen contents in the powder. The influence of the surface composition and surface oxides in particular needs to be further investigated, and will be explored during this thesis.

Alloying elements can have beneficial or harmful effects under different conditions and applications. Additives can be found in order to improve the laser powder bed fusion process, for example by lowering the material melting point [69]. Enhanced absorptivity, or reduction of cracking are also possible with chemical composition alterations, often applied to aluminum alloys for a better material process-ability [84].

For stainless steels, bulk composition has also an influence as mentioned subsection 1.1.3, resulting in different amounts of δ-ferrite and γ-austenite phases in the powder feedstock. However, the potential impacts of powder microstructure on printed parts have not been strongly established yet [69]. The solidification mode is also influenced by the cooling rates, which can lead to variations for recycled powders and will be discussed in subsection 1.3.1.

Even though some rules seem to emerge in terms of influence of particles sizes and shapes, it depends as well on the choice of processing parameters. Irrinki et al. [82] studied the density and mechanical properties of parts elaborated with water-atomized and gas-atomized powders and with different laser powers and scanning speeds. The powder characteristics play a key role, with higher density and mechanical properties for gas-atomized powders. Nevertheless, the size and shape differences can be compensated with high laser energy density. With appropriate processing conditions, they achieved comparable properties for parts elaborated with water-atomized powders. Heiden et al. [85] conducted an extensive process parameters investigation with two grades of SS316L with different PSD. They found that higher energy was needed to fully melt larger sized particles and obtained high parts density in both cases. Cacace et al. [72] also studied the influence of two L-PBF parameters and production processes of powders on the density of samples. They pointed out the significant interaction between powder granulometry and layer thickness. When the powder layer thickness is larger than the size of the large powder particles, all particles are spread on the build platform. On the other hand, for thinner layers, a great amount of large particles will be dragged past the platform by the recoater, which will favor the deposition of thin particles [86]. It leads to higher powder bed density [87, 88]. This phenomenon is illustrated figure 1.17.

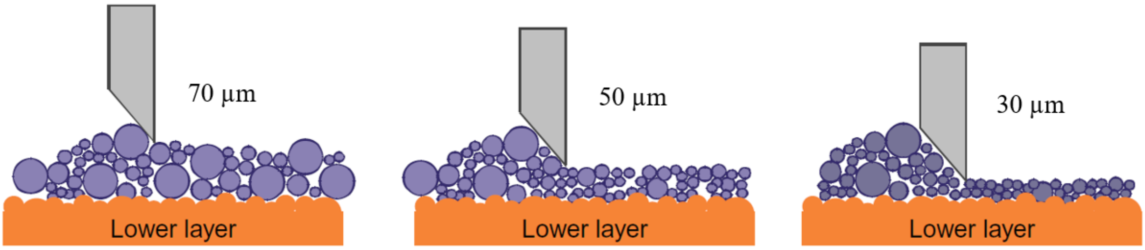

Figure 1.17 – Schematic of the influence of powder layer thickness and particle sizes on packing density [87].

Some conclusions can be made from the studies of powders attributes in the literature. Powder particles with spherical morphology present higher flowability and powder bed packing than irregular-shaped particles. They allow to fabricate parts with high density.

However, the influence of powder characteristics on L-PBF parts is strongly correlated with processing parameters. The particle size distribution of the powder entails adequate choices in terms of powder layer thickness for optimum powder layer density, and other processing parameters to completely fuse the powder.

These different laser powder bed fusion process parameters and their impacts will be presented next.

1.2.2 Process

Parameters

As seen previously and listed in figure 1.12, some influential factors are material related, and other numerous ones are processing parameters and conditions.

The parameters mostly studied in the literature because of their influence on parts quality and their ability to be simply modified are the laser power (P, in watts), scanning speed (v, in mm.s^{-1}), hatch distance (h, in mm) and layer thickness (e, in mm). Figure 1.18 provides an illustration of these parameters with a close up of the L-PBF process.

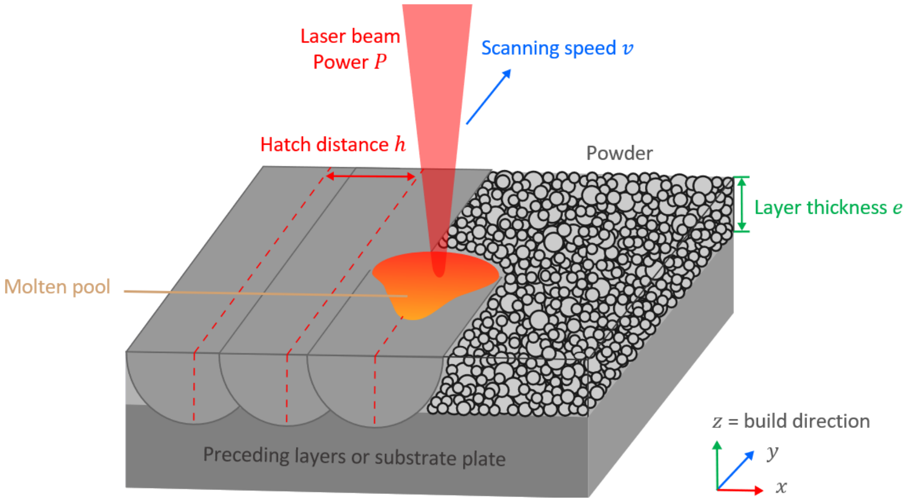

Figure 1.18 – Schematic of L-PBF process parameters.

These four parameters can also be used to express the energy density, E_{vol}, in J.mm^{-3}, an approach to characterize the laser heat input density on the powder bed (1.1) [89, 90].

$$E_{vol} = \frac{P}{v\,h\,e} \tag{1.1}$$

This value is widely used as a reference for optimal processing in the literature, but it has to be taken carefully. It does not take into account interactions effects between each factor, and does not integrate important other parameters like the laser beam diameter, the gas flow, the scanning strategy, etc. [91]

The linear energy density, E_{lin}, in J.mm^{-1}, is sometimes used (1.2), which does not consider hatching and layers, nor the spot size.

$$E_{lin} = \frac{P}{v} \tag{1.2}$$

A more local definition of the input volumetric energy density, in J.mm^{-3}, includes the laser beam diameter, is defined as follows (1.3) [92, 93]:

$$E_{vol/spot} = \frac{P}{v\,S} = \frac{4P}{v\,\pi d^2} \tag{1.3}$$

where S is the surface of the laser spot and d is the laser beam diameter. These various definitions are discussed in the paper of Sow et al. [94] who propose an interesting distinction between the physical volumetric energy density (1.3) and the energy per built volume (1.1).

In order to understand the influence of operating parameters on final parts in L-PBF, it is important to take a closer look at the interactions between laser and material and the solidification mechanism of laser powder bed fusion.

Laser-material interaction and solidification mechanism

One of the major aspect of laser-material interaction is the absorptivity of the powders to laser irradiation. The absorptance is defined as the ratio of energy flux absorbed by the material compared to energy flux incident upon it. Fiset al. [95] demonstrated that powders absorptance is significantly higher than that of dense metals. This can be explained by the multiple reflection of the laser beam in the powder bed [96]. The energy absorption by the powder bed affects the temperature profile, melt pool geometry, solidification, microstructure and properties of the part. It depends on both the heat source and material characteristics.

Sufficient laser energy absorbed by the particles lead to rapid heating and melting of the powders. With the scanning laser leaving the melt pool region, rapid solidification of the molten metal occurs. The cooling and solidification mode mainly depends on the laser energy density and the interaction time. The interface temperature gradient G and the solidification growth rate R are used to describe the solidification structure. The product GR, i.e. the cooling rate at the interface, affects the size of the structure, and the ratio G/R affects the morphology of it [33, 97]. Figure 1.19 illustrates these effects on the solidification microstructure.

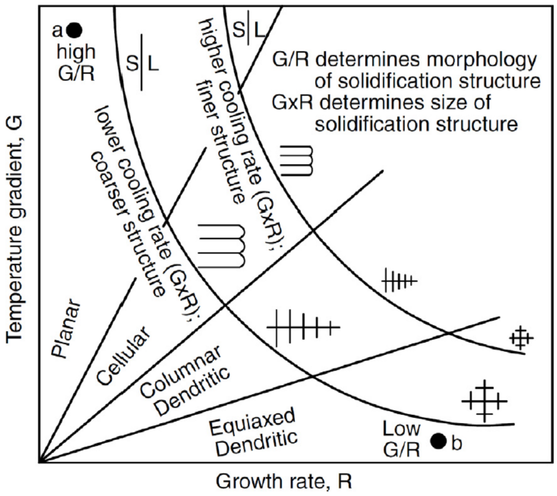

Figure 1.19 – Influence of temperature gradient G and growth rate R on the scale and type of microstructure [98].

The heat and mass transport phenomena is affected by the fluid behavior of the melt, related to the surface tension, viscosity, wetting, evaporation and oxidation [99]. The non-uniform temperature in the melt pool can induce surface tension variations and generate thermocapillary flow also known as Marangoni convection. It causes instabilities in the pool, usually driving the melt flow from high to low temperature (low to high surface tension), therefore from the laser spot to the sidewall and edge of the melt pool [99]. Melt pool instabilities, combined with unfavorable parameters can lead to different phenomena and defects typical to the L-PBF process.

L-PBF defects

One particular phenomenon in L-PBF is called **balling**. It is due to insufficient wetting of the molten metal with the underlying layer due to the various interface tensions (see figure 1.20 (a)), which leads to the liquid metal shrinkage into a spherical shape, according to the principle of minimum surface energy [100]. The size of the drops can exceed the diameter of the laser, resulting in a rough surface and can create voids. Balling usually happens in long thin melt pools, and the phenomenon can be associated to Plateau-Rayleigh instabilities [101,102]. Kruth et al. [103] proposed a criterion of non-balling defined as follow: the surface of the melt pool (approximated by a half cylinder) has to be smaller than the surface of a sphere with similar volume. This can be written as : $l < 2d$ with l the length of the melt pool and d the laser beam diameter or width of the melt pool. It is illustrated figure 1.20 (b).

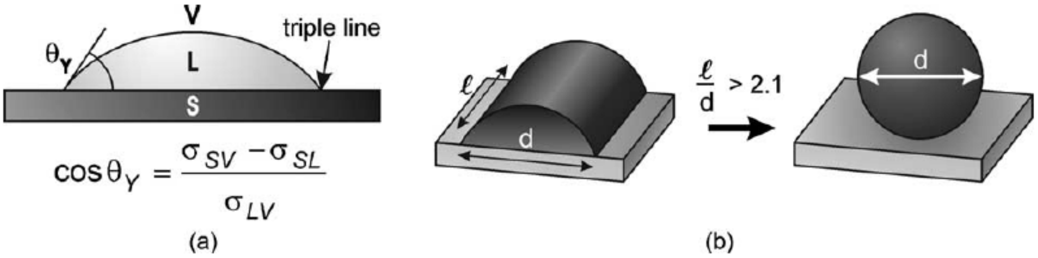

Figure 1.20 – (a) Wetting of a liquid on a solid substrate and equation of Young with σ_{SV}, σ_{SL} and σ_{LV} the surface free energies of the system, (b) Balling criterion [103].

Several authors studied the effect of process parameters such as scanning speed and laser power in order to identify zones of stability regarding balling phenomenon. They found out that low energy density promoted large size balling [104,105]. Conversely, high energy density will limit the phenomenon.

However, excessive temperature can also cause evaporation of some alloying elements of the material. It produces a vapor recoil pressure which adds extra forces to the surface of the liquid [106]. When the recoil pressure is high, it drives a strong metal liquid flow in the melt pool in addition to Marangoni effect, and molten droplets may be ejected. This is known as **spatter** formation [92]. According to the shape of the spatters observed, Lutter-Günther et al. [107] proposed formation mechanisms and distinguished two types of droplets spatters. *Spherical spatters* which are ejected from the melt pool at a high angle, leaving enough time for solidification in flight and minimization of the surface energy. *Agglomerated spatters* which are ejected at a low angle and land on the powder bed in the liquefied state. It forms large agglomerates with irregular shapes.

Wang et al. [108] classified spatters into three types according to their formation mechanism, as shown in figure 1.21 (a). Type II known as *droplet spatters* are ejections of molten metal under recoil pressure and melt pool turbulence, as mentioned above. When entering in contact with the powder bed, the droplets can be in partial state of solidification and can adhere to the surface of virgin powders, forming what is called satellites. Type I termed *metallic jet* forms when the spatter is ejected passing through the incident laser beam. When expelled and entering in contact with the atmosphere of the chamber, it cools rapidly as smooth and spherical droplets. Type III called *powder spatters* or *vapor-entrained particles* are virgin powders drawn in by continuity from fume evaporation in proximity of the melt pool, whose pass can cross the laser beam. In that case they will be molten and resolidify upon cooling (hot spatters). Conversely, if a vapor entrained particle does not cross the laser beam, it will remain solid (cold spatter), as detailed by Ly et al. [109] and illustrated in figure 1.21 (b). The authors stated that 60 % of spatters are hot entrained particles, 25 % are cold entrained particles and only 15 % are coming from the melt pool.

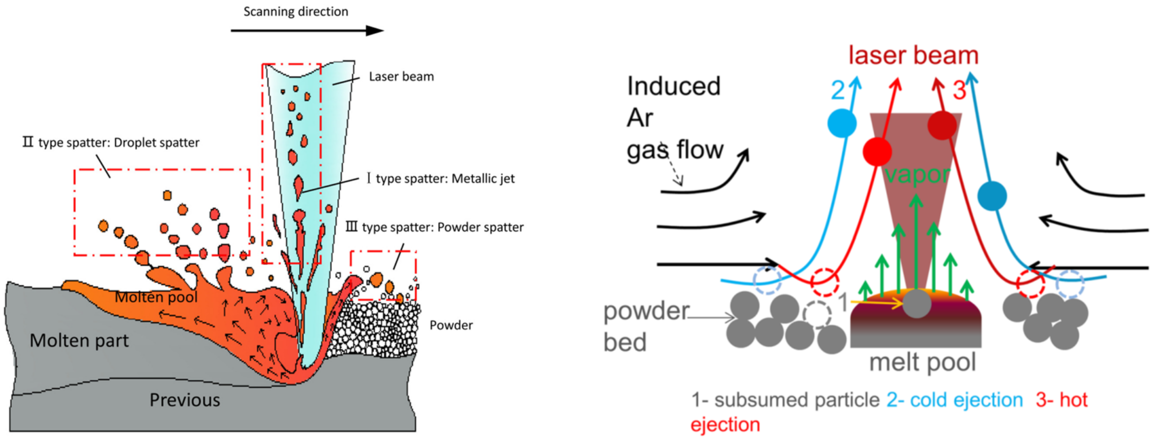

(a) (b)

Figure 1.21 – (a) Schematic of the formation of different types of spatters in L-PBF [108], (b) Schematic of powder particle entrainment due to vapor jet and gas flow [109].

Spatter particles can fall down on the unmelted powder or the solidified layer. Either way, the laser will have to melt an excess of material which can lead to an inclusion in some cases, depending on the size of the spatter, when the laser energy is insufficient. This defect formation mechanism is illustrated in figure 1.22.

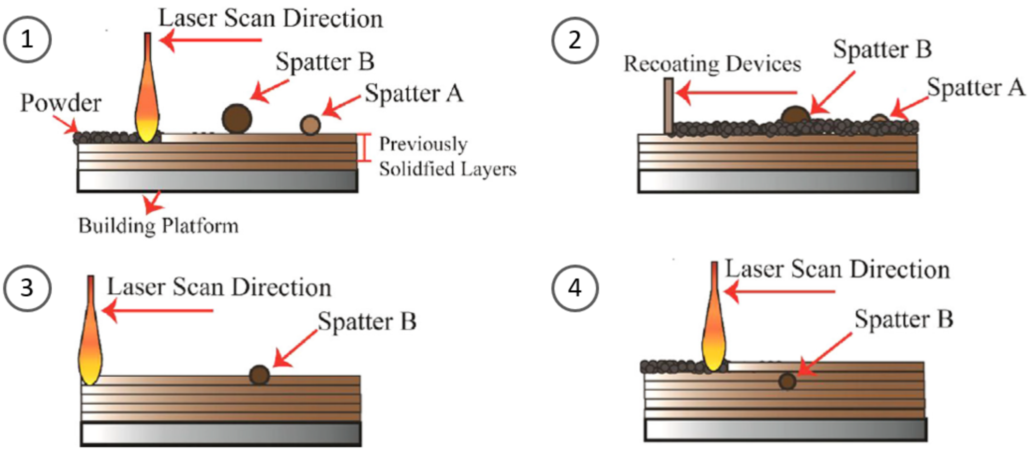

Figure 1.22 – Schematic representations of the defect formation mechanism by spatter particles [110].

Taheri et al. [110] observed that increase of the scanning speed or decrease of the laser power reduce the formation of spatters, figure 1.23, and that scanning speed has a stronger effect than power. However, minimizing the laser energy to reduce particles ejection is not sufficient as still some spatters will result. High power is needed to diminish the defect formation induced by spatters as high energy will melt the larger spatter particles.

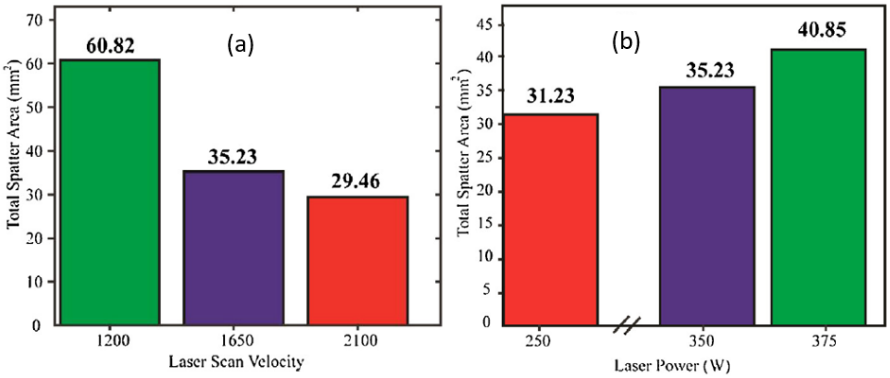

Figure 1.23 – Total spatter area in function of (a) scanning speed, (b) laser power [110].

Finally, non-optimal heat input can also lead to **porosities**. They are considered as one of the major defects in L-PBF, and can be divided in three categories, illustrated in figure 1.24, according to their production mechanism [33, 97]:

- *Gas entrapment*, which forms microscopic spherical porosities. They come from the protective atmosphere (Ar or N) or gas already present in the powder bed.
- *Lack of fusion void*, due to inadequate penetration of the molten pool of a new layer on the previously deposited one. With insufficient laser input energy, it causes incomplete remelting of the previous layer and a poor metallurgical bond. These pores are irregularly shaped and common at the interface between layers.
- *Keyhole porosity*, which comes when L-PBF is operating at very high energy density. Melting is therefore performed in "keyhole" mode instead of conduction mode, with a strong recoil pressure that significantly distorts the liquid-vapor interface. This lead to the formation of an unstable deep keyhole cavity inside the melt pool, and its collapse leaves void of entrapped vapor [111]. Those porosities are spherical and often large, the size depending on shape and size of the keyhole.

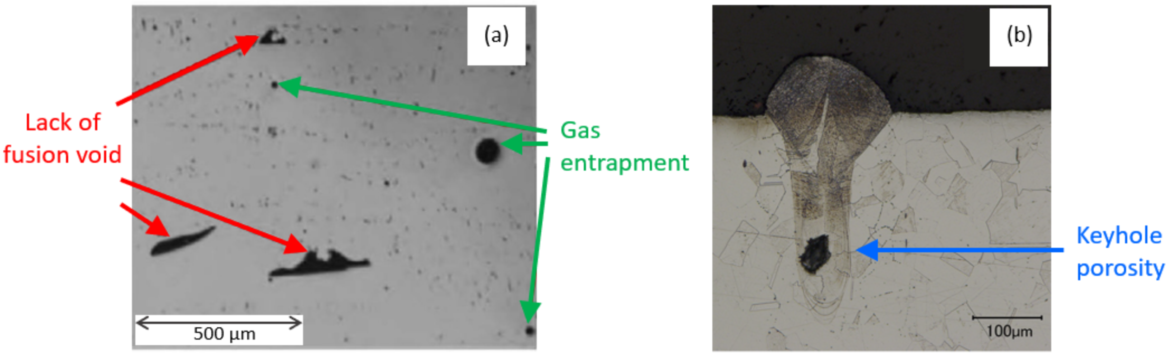

Figure 1.24 – (a) Lack of fusion pores and gas induced porosities [112], (b) Keyhole induced porosity [111].

Porosity has to be minimized in L-PBF because of its negative impact on mechanical properties. Size and shape are indicators of the material health. Lack of fusion pores are considered more harmful than microporosities. Indeed, these non-spherical voids can be the source of cracks, the sharp edges of the porosities acting as stress concentrators under applied loads. Fortunately, lack of fusion voids are parameter-based pores and can be reduced with appropriate processing parameters.

An overview of the effects of different factors in L-PBF will be presented in the following, with regard to porosity and other defects introduced previously.

Influence of process parameters

The majority of the L-PBF parameters optimization studies in the literature is based on the influence on final parts density. As stated by Kruth et al. [113], the density of the part is a key factor determining its mechanical properties which has a direct influence on the product performance. Therefore, the goal in L-PBF is to achieve 100% dense parts.

Among the four parameters of the energy density formula (eq. 1.1), the **laser power** has the strongest influence on density [114]. Jiang et al. [115] evaluated the effect of the parameters and their interactions with an analysis of variance (ANOVA). Yakout et al. [116] performed a factorial design of experiments (DOE) and proposed zones of stable melting for stainless steel 316L, figure 1.25, with an optimum value of energy density comprised between the balling zone and keyholing zone.

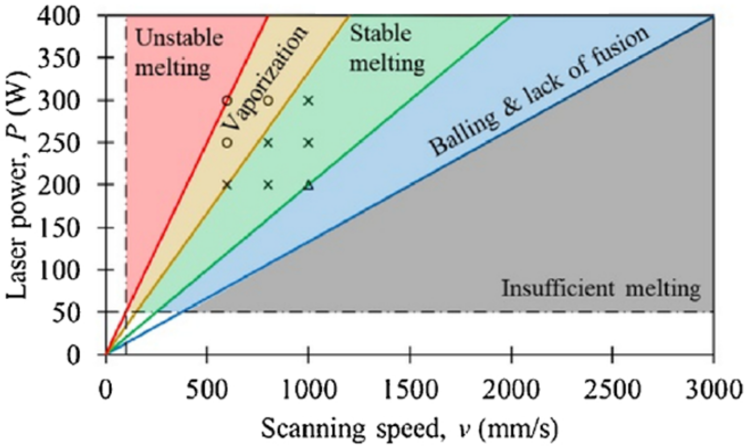

Figure 1.25 – L-PBF process map of 316L showing laser power P and scanning v stability zone (with hatch distance h = 0.08 mm and layer thickness e = 0.04 mm) [116].

The **laser power** and **scanning speed** are often combined, as their effects are closely linked. Indeed, increasing the scanning speed will not have the same effect at different power values. It was shown by Kamath et al. [117], with the representation of SS316L samples density in function of the scanning speed for different laser powers, figure 1.26. However, tendencies are equivalent : for a given power value, the increase of the speed will lead to insufficient melting and lower density, and low speed results also in density reduction as porosity will appear due to keyhole mode. Montero-Sistiaga et al. [118] used a high-power laser of 1kW to increase the scanning speed and thus the productivity rate for SS316L. They observed more elongated columnar grains growing along the building direction.

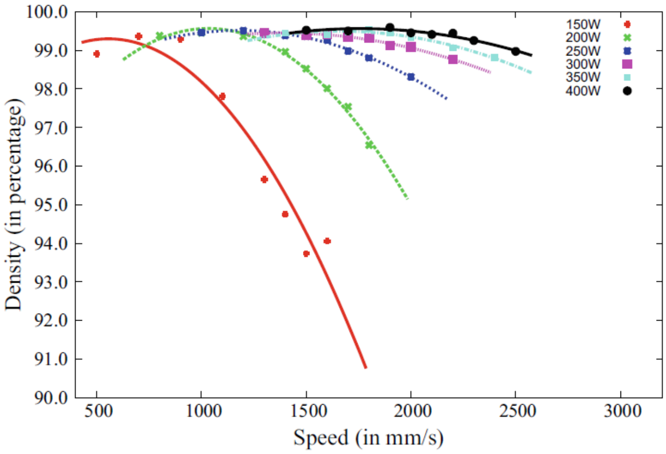

Figure 1.26 – Relative density as a function of laser power and scan speed (with hatch distance $h = 0.15$ mm and layer thickness $e = 0.03$ mm) [117].

Hatch distance or hatch spacing impacts the lateral overlap ratio between adjacent laser tracks. Similar to laser scanning speed, increasing too much the hatch distance will lead to decrease of the relative density due to lack of fusion voids [119, 120]. This is illustrated in figure 1.27. Once again, hatch distance has to be related to heat input parameters, laser power, scanning speed but also laser beam diameter, influencing the melt tracks width and penetration [97].

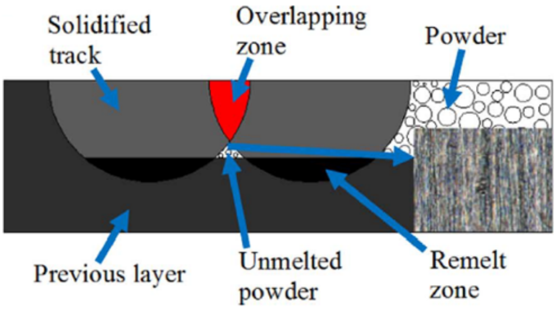

Figure 1.27 – Schematic of too large hatch distance in L-PBF [120].

Layer thickness has a strong effect on the building rate. For a given geometry, its increase induces a diminution of number of layers. Therefore, it reduces the laser scanning time but also the fixed (non parameter dependent) time of powder spreading by the recoater all along the process. However, high layer thickness tends to reduce parts density. As presented before (section 1.2.1, figure 1.17), the powder bed packing density is impacted negatively. A thick powder layer contains more voids and gas entrapment will be favored [87]. Besides, surface roughness increases as the layer thickness increases [121]. For parts with overhanging, geometrical accuracy will be reduced as the curves will be sliced into less and thicker layers. Balling tendency can be limited also by decreasing powder layer thickness [104].

The **scanning strategy** is not taken into account on the formula of energy density and most parameters optimization studies, but it has a direct effect on porosities and location of the latter. The strategies mostly used are schematized figure 1.28. Rotations between layers avoid an alignement of the porosoties and reduce the crystallographic texture of the material [122]. The rotation of 67° is more and more applied as it minimizes the laser vector coincidence with the previous layers, the scheme being repeated every 180 layers [123]. The use of islands or stripes reduces the length of the vectors and results in a higher temperature environment around the solidifying pool, and a reduction of the thermal gradient. Therefore, adjacent tracks are scanned shortly one after the other, improving the wetting conditions [103]. It reduces also significantly the residual stresses (induced by repeated thermal dilatation and contraction of the solidified layers) [113, 124].

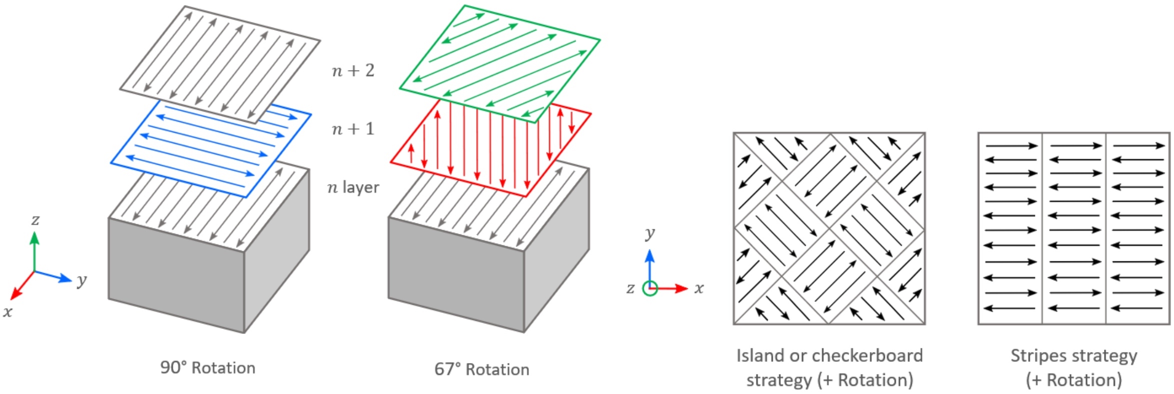

90° Rotation

67° Rotation

Island or checkerboard strategy (+ Rotation)

Stripes strategy (+ Rotation)

Figure 1.28 – Typical scanning strategies used in L-PBF.

The **chamber atmosphere** has a major impact on the quality of the parts in L-PBF, and is often underestimated. Atmosphere purity is required to protect from oxidation. Several researches have been conducted on the nature of the protective gas (Ar, N_2, He) [48, 125]. Samples elaborated under argon and nitrogen present better densities. Argon is often preferred as it is a noble gas, unlike nitrogen which can dissolve in the molten metal. Other studies focused on the influence of the chamber pressure. Masmoudi et al. [126] stated that the use of high pressure could decrease the convective movements and lower the vaporization rate. Ladewig et al. [127] studied the effect of different gas flow velocities. The shielding gas flow has to be as high as possible in order to avoid deposition of spatters in the build area. High velocity also promotes effective removal of vapor plume, which limits the resultant decrease in laser penetration and wettability [128].

Finally, **oxygen content** is also a key factor in L-PBF and for the problematic of this thesis. Due to oxygen in the build chamber, Simonelli et al. [129] observed selective oxidation on the surface of spatter particles. They assumed that the oxide formation occurred during the particle solidification, with a surface enrichment with volatile alloying elements with high affinity to oxygen (in the case of 316L, Mn and Si). Gasper et al. [130] also studied spatters and oxides formation and showed that oxidation occurs at the melt pool surface, as they found similar oxides on the spatter particles and on the surface of parts.

Surface oxidation increases the absorption of laser irradiation, therefore surface tension variations become more dominant [83]. Marangoni convection in the melt pool depends on the sign of the gradient of surface tension to temperature $d\gamma/dT$. With presence of oxygen, the sign can be reversed (from negative to positive) which reverses Marangoni flow and results in changes in the shape of the melt pool [99, 131]. Instability of the melt pool causes more liquid metal to leak out forming spatters [108].

Moreover, wetting characteristics will be worsened by the formation of an oxide film at the wetting interface. Poor wetting between the liquid metal and the underlying substrate will directly result in the balling phenomenon [31]. Thus, it is important to avoid oxidation, and use sufficient laser energy to break down oxide films with sufficient remelting of the previous layer, providing clean solid-liquid interface [103]. Oxidation content inside the build chamber needs to be as low as possible. Balling characteristics of 316L stainless steel processed under different oxygen concentrations are presented in figure 1.29.

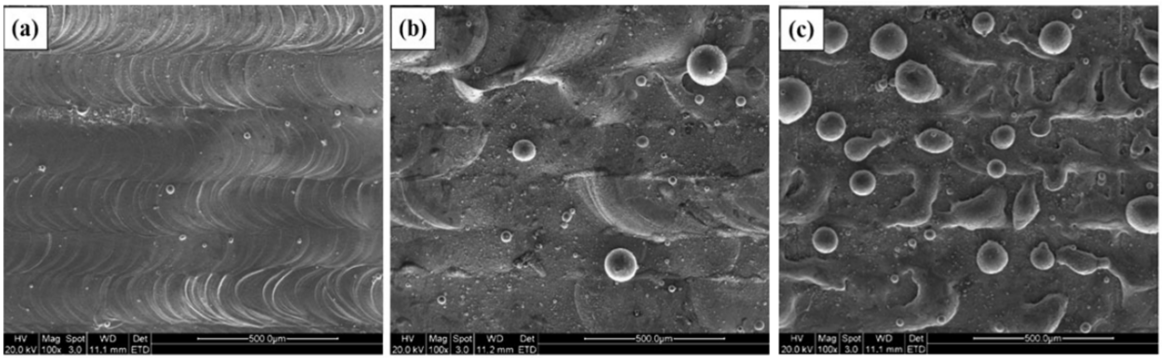

Figure 1.29 – Influence of oxygen content in atmosphere on the balling characteristics : (a) 0.1%, (b) 2%, (c) 10% [132].

A greater oxygen concentration in the build chamber during processing also leads to an increase of the printed parts oxygen content and surface roughness [133, 134], which can alter the mechanical properties. Improper storage conditions of powder feedstock can also be detrimental to the process stability with moisture and oxidation, although Hryha et al. [135] demonstrated that the increase in oxide layer thickness on titanium powders after long-term storage was not that significant.

Laser powder bed fusion is a complex process involving numerous phenomena and driven by many parameters and conditions. All of these processing parameters (laser power, scanning speed, hatch distance, layer thickness, scanning strategy, chamber atmosphere, oxygen content) greatly influence the quality of elaborated parts, their mechanical properties, surface characteristics, corrosion resistance, etc. However, these processing conditions still have to be correlated with the attributes of starting powders.

In a context of circular economy, in view of reusing the un-melted powder in the L-PBF process, an understanding of the effects of the process on the attributes of the powder feedstocks and manufactured parts needs to be developed. The detailed findings of the literature regarding these aspects will be presented in the following section.

1.3 Powder recycling

1.3.1 Influence on powders

During L-PBF process, only a small fraction of the build area (10-50%) is used by the solidified parts [4, 136, 137]. There is a significant amount of powder leftover which is not melted by the laser beam. The reuse or not of the non-melted powder highly influences the resource efficiency of L-PBF products [138]. Reuse of the powder, also referred to as recycling, would strongly benefit the economy of the L-PBF process as 5-46% of the total costs are attributed to feedstock material costs [5].

However, properties of powder that has been subjected to the L-PBF environment may deviate from the virgin material. It is therefore necessary to understand the effect of recycling on powder characteristics, to provide fabrications without deterioration of part quality.

Types of recycled powders

After the process, all the particles non incorporated into the parts are collected. Among these particles, not all of them have the same thermal history.

Pinto et al. [139] divided the unused powder into three groups, schematized in figure 1.30. Group I are *as-virgin* particles, which are far from the consolidated parts (therefore the heat source) and do not undergo any modifications. Group II are powders in the *heat affected zone (HAZ)*, in the near vicinity of the melt pool. Finally, group III consists of *spatter particles*, which can be divided itself into three types : *metallic jet*, *droplet spatters* and *powder spatter* [108], as presented in section 1.2.2.

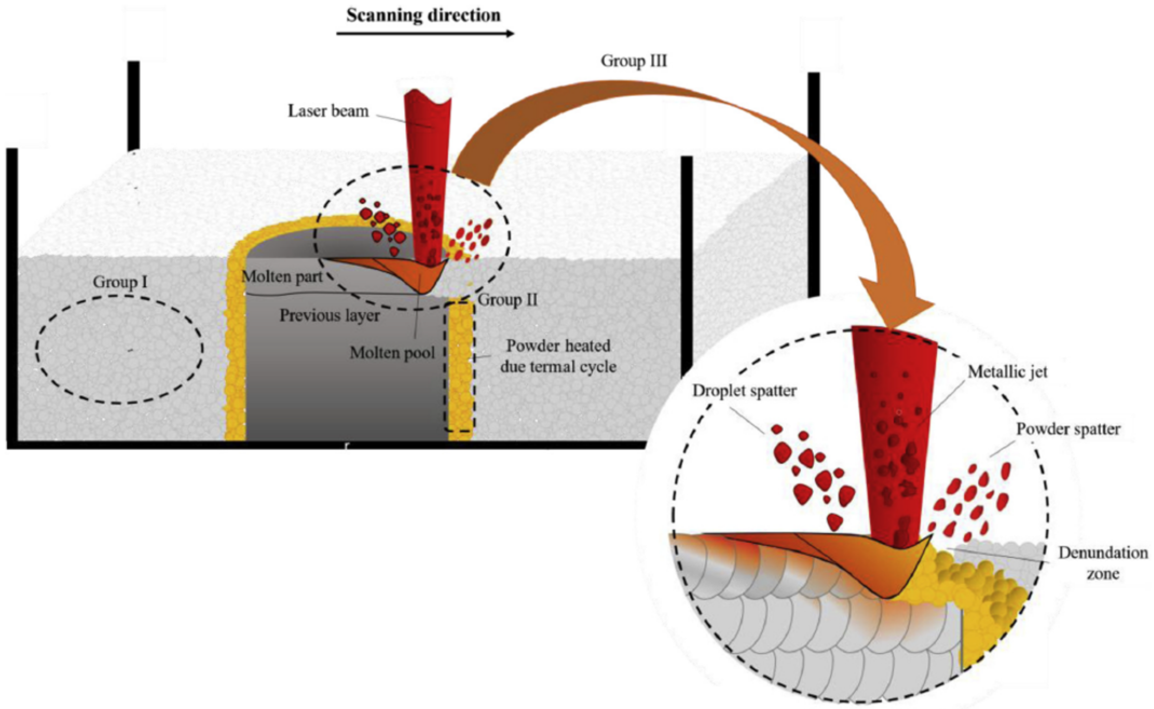

Figure 1.30 – Schematic of groups of recycled powders, including different spatters [139].

Several studies focused on understanding the impact of recycling on metal powders, for different materials, *e.g.* titanium-, nickel-, aluminum-based alloys, and steels. The authors tried to investigate how the powder is affected during the process in terms of **shape**, **size**, **chemical composition** and **microstructure**. Researches concentrate on recycled powder characteristics as a whole, to compare to virgin powder, but also focus on spatter properties to assess recycling degradation [137, 140].

Morphology

Sieving is meant to remove agglomerated or fused particles larger than the mesh size, generally around 50 - 75 µm. However, changes in particles size and shape are still reported after powder reuse. Irregular shape particles with sizes bigger than the mesh in one direction can pass through, like the particle displayed in figure 1.31 (d). All recycling studies did not show identical results but tendencies emerged. The particle size distribution tends to shift to larger mean sizes as powder is reused [141–144]. There is an increase of irregularly shaped particles and number of satellites in recycled powders. A first possibility is that this comes from the sintering of droplet spatters falling down on the powder bed. Particles in the HAZ, close to the melt pool, are also likely to partially sinter. Bonded particles and agglomerates are often reported with intensive reuse, as shown in figure 1.31, with scanning electron microscope images of 17-4 PH stainless steel powder after several recycling cycles. Fumes condensates are also observed in recycled powder, as a form of submicron powder sattelites created through vapor condensation on unused particles [137, 145].

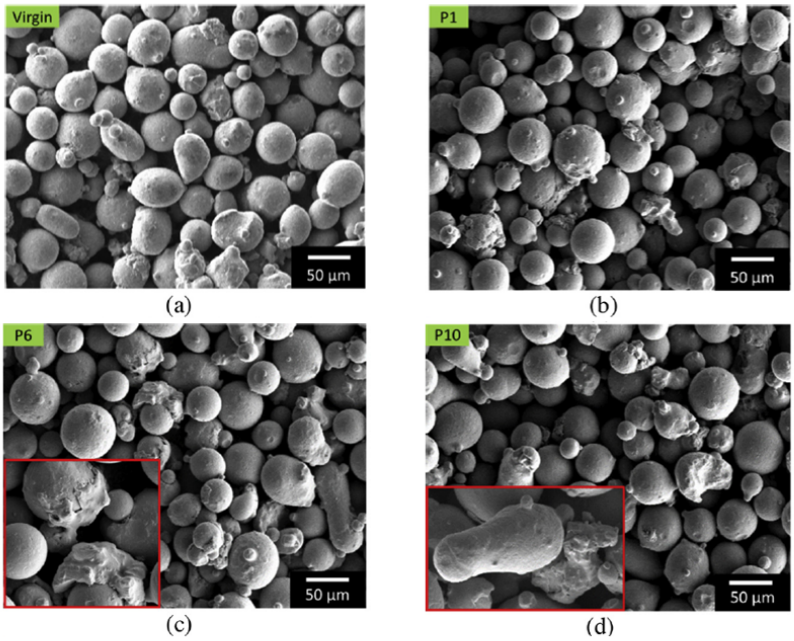

Figure 1.31 – Scanning electron microscope images of 17-4 PH stainless steel powders: (a) virgin, (b) post print 1, (c) post print 6, (d) post print 10 [146].

Several authors noted that sphericity analysis can be a good indicator to assess morphology changes. Recycled powder highlights a reduction of high sphericity particles and a greater percentage of low sphericity particles in some cases [146]. However, this can be questioned due to the fact that a number of spatters tends to be more spherical than the virgin powder and have the opposite effect.

Cumulative particle size distribution shifts towards larger values with reuse, as shown for titanium alloy Ti-6Al-4V in figure 1.32 (a). Other authors found that recycled powders present narrower PSD [147–149], figure 1.32 (b).

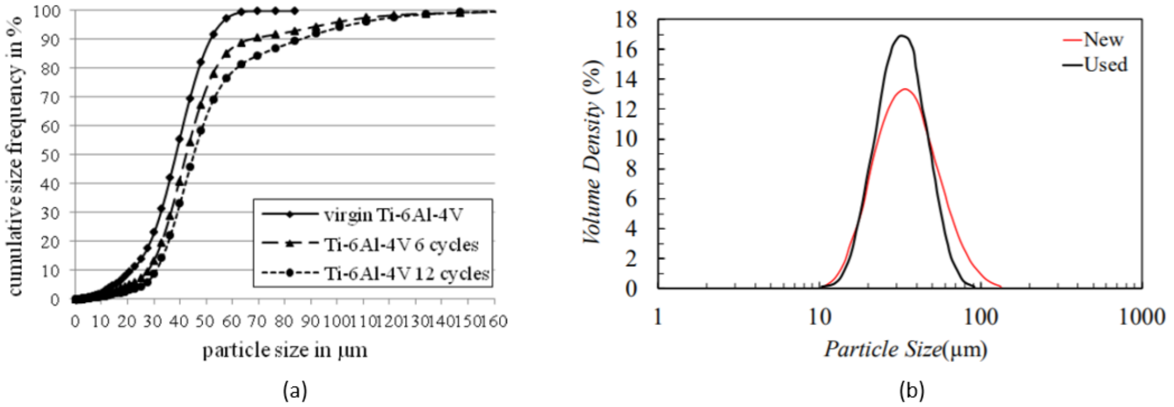

Figure 1.32 – Comparison of virgin and recycled Ti-6Al-4V powders (a) Cumulative PSD [141], (b) PSD [149].

Recycled powders also exhibit smaller amounts of fine particles [137,140,150], as it can be seen on the PSD curves. This decrease is caused by the sintering of small particles to form satellites. Another explanation is that during L-PBF process, particles larger than the powder layer thickness are preferentially carried by the recoater past the build area, while small particles will be deposited on the platform (see section 1.2.1, figure 1.17). Fine particles are therefore more likely solidified and less are collected for reuse.

Flowability of the powder increases with recycling. It is likely due to this smaller amount of fine particles, with the reduction of inter-particle adhesion and frictions, even if the particles being less spherical and the presence of satellites generally negatively affects the flow behavior [140,149,151]. Figure 1.33 presents images of virgin and recycled titanium powder heaps, and agglomerations can been in the virgin powder.

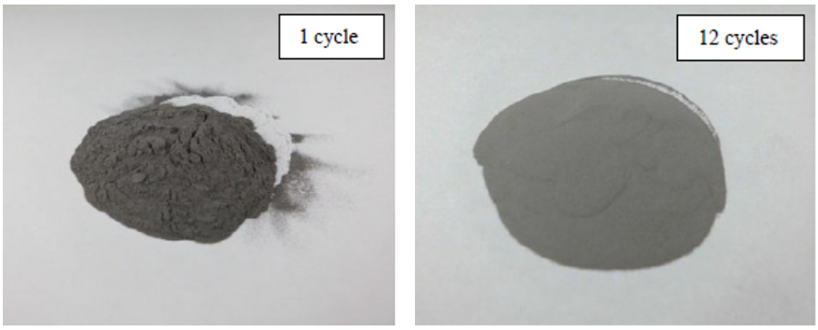

Figure 1.33 – Flowability of virgin and recycled Ti-6Al-4V powder [141].

Flowability can also be assessed using different powder metallurgy techniques [152]. One way to rudimentary predict powder flow is by calculating the Hausner ratio. This dimensionless number is defined as the tap density over the apparent density. Tap density is the powder density after repetitive vertical tapping. The apparent density of the powder is measured after freefall of the latter. Jacob et al. [153] used the powder bed density (PBD), considered close to the tap density for the ratio. PBD was measured with powder bed density capsules elaborated to capture the density directly on the build platform during the L-PBF process. Figure 1.34 represents the powder bed density, apparent density, and the ratio of those to assess flowability of stainless steel powder in function of multiple printing cycles. As the ratios slightly decreases, the powder becomes more flowable, which was in correlation with measured flow rates through calibrated funnels. A decrease in apparent density is noticeable at build 6, but it is explained as some virgin powder was re-introduced in the recycled powder, showing influence of reuse on material cohesiveness.

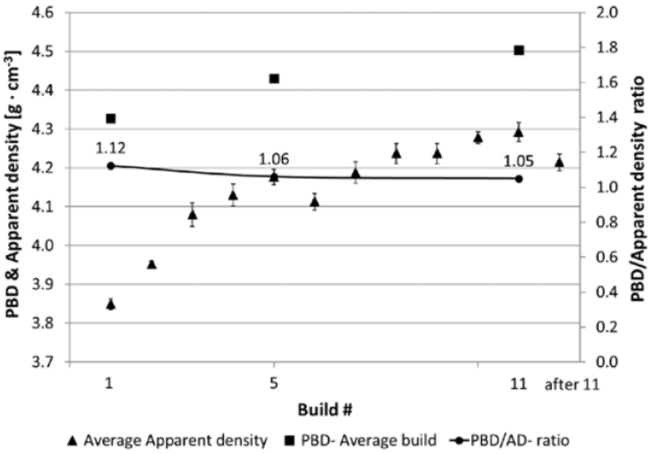

Figure 1.34 – Flowability, powder bed density and apparent density of stainless steel 17-4 PH recycled powder [153].

Increase of packing density with reuse was also reported by other authors and for different materials [140, 149]. This suggests that the virgin powder may not have the optimal PSD to pack most efficiently, even though the reduction of fine particles with reuse may also lead to lower packing density as less fines are present to fill the voids between large particles [137].

All these particles sizes, shapes and behaviors modifications with multiple reuse were reported and compared for different materials. Even if general trends can be assessed, some divergences exist between different studies. Some authors also find no significant changes in terms of PSD, sphericity, flowability or density in their conditions [154–156].

Chemical composition - Oxygen content

In addition to the morphological changes, powder chemical composition can be subjected to variations due to multiple powder reuse. An increase of oxygen content in recycled powder has been repeatedly reported [140, 144, 147, 157–159]. The oxygen pickup intensifies with the number of build cycles [140, 147]. Nonetheless, the chemical composition of recycled powders generally stays within the limits of the alloys specifications [160]. Figure 1.35 (a) and (b) represent the variation of oxygen content in powders with reuse cycles for stainless steel 304L and titanium alloy Ti-6Al-4V respectively.

Further investigations revealed that there is usually no change in bulk composition, but the increased oxygen is due to the formation of oxides on the surfaces of the particles [129,137,161]. Powder oxidation can be observed by optical microscopy, with blue and brown coloration of recycled particles [156] as shown in figure 1.36 for stainless steel 316L powder reused 30 times [137].

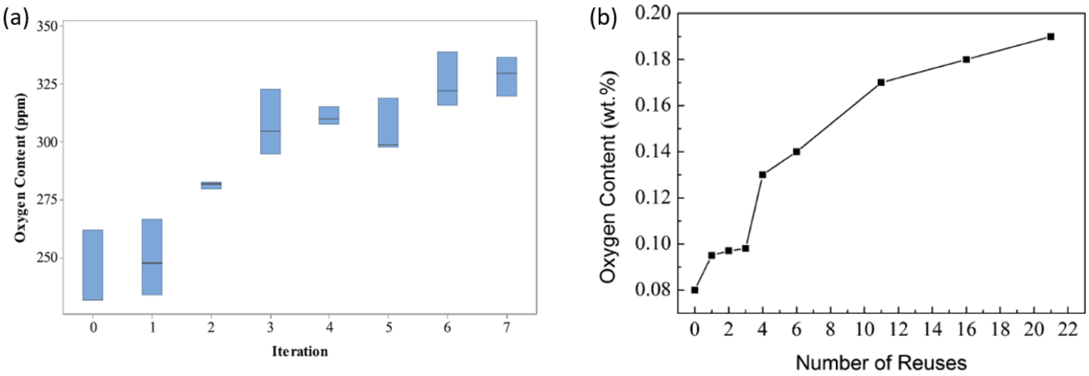

Figure 1.35 – Variation of oxygen content (wppm) in recycled powder through reuse iterations for (a) stainless steel 304 L powder [140], (b) Ti-6Al-4V powder [147].

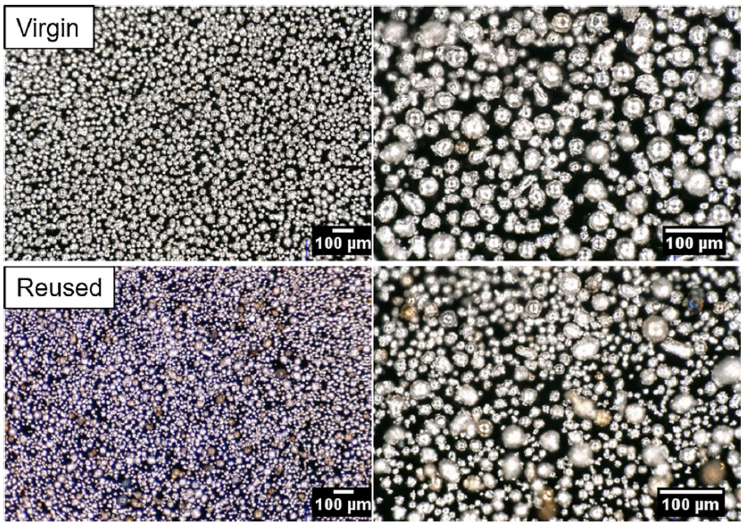

Figure 1.36 – Optical images of virgin and reused 316L powder [137].

Oxygen distribution is very heterogeneous in the recycled powder, with strong particle to particle variations [137,148]. Liquid spatter particles are likely responsible for oxygen pickups. The number of affected particles depends on the processing conditions and parts geometries. The number of spatters will increase if more area of the powder bed is used for printing [162]. Galicki et al. [163] reported that oxygen content also varies as a function of the relative position to the laser beam, with increased oxygen content measured in powder samples located near the melt zones.

Some spatters are highly spherical, and dark regions can be seen on SEM micrographs on the surface of some affected particles, which reveals a different chemistry, figure 1.37 (a). Composition analysis of the oxide layers found on the surface of spatters for stainless steels show selective oxidation of silicon and manganese elements, as presented in figure 1.37 (b) [129, 137, 145, 164–166].

Indeed, in stainless steels, Mn and Si are elements with the greatest affinity to oxygen [129]. The Ellingham diagram informs that oxides can form on steel even with relatively low oxygen concentration, and conditions inside the build chamber during the L-PBF process are sufficient (usually significantly above 100 wppm, and often of the order of 1000 wppm). Mn and Si contain the lowest equilibrium oxygen partial pressures among elements of stainless steels [145].

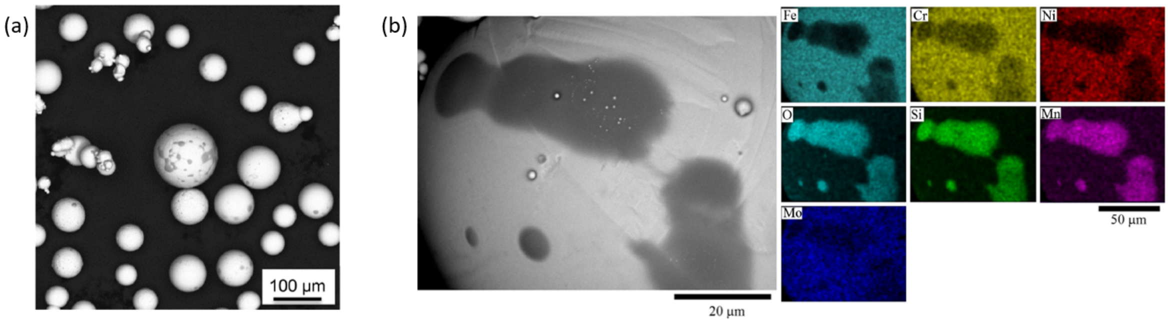

Figure 1.37 – (a) SEM image of 304L spatter [145], (b) EDS maps indicating the distribution of the alloying elements in the surface oxides of 316L spatter [129].

The presence of chromium was also reported on the surface of ejecta. Sutton et al. [145] suggested that complex oxides such as $MnSiO_3$, $NiFe_2O_4$ and $NiCr_2O_4$ are potentially present on stainless steel spatters. Heiden et al. [137] observed SiO_2 and $MnCr_2O_4$ oxides nodules on SS316L reused powders. They also reported a thin Ni-rich layer below the surface of the particles, that they attributed to a depletion zone caused by the surface segregation of Mn, Si and Cr that have high affinity to oxygen.

Mostly, oxides do not form a continuous film on the surface of reused particles and are often visible as islands and small nodules. The explanation proposed was that the high cooling rates of spatters do not give enough time to islands to coalesce and merge into a continuous film of oxide [145]. Figure 1.38 highlights the presence of oxide islands on the surface of a spatter particle, which are not observed on virgin powder of stainless steel 304L.

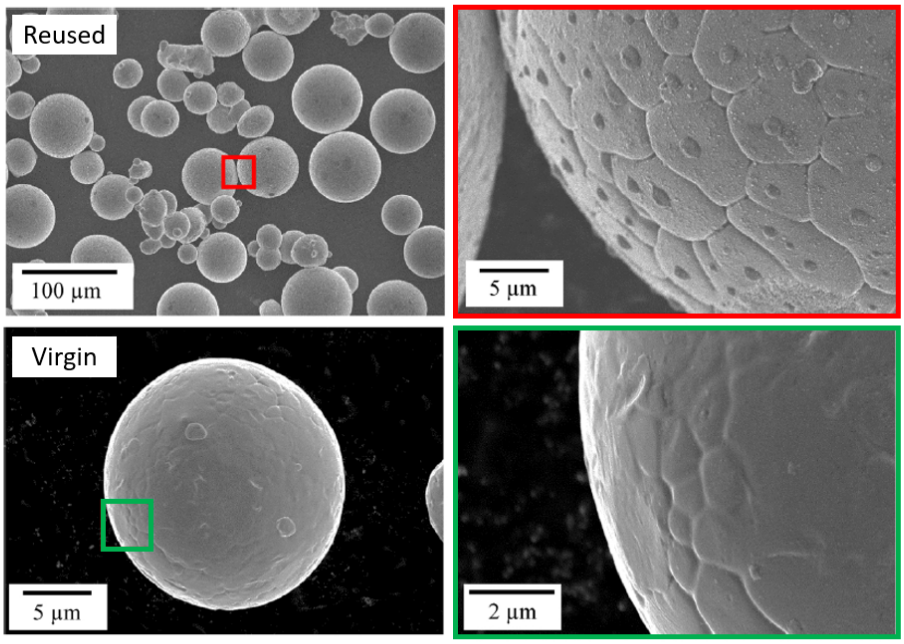

Figure 1.38 – SEM images of 304L spatter containing oxide islands compared to virgin powder of 304L [140].

Fully oxide particles were also reported by Heiden et al. [137] for SS316L powder and Gasper et al. [130] for Inconel 718. In the case of SS316L, the oxides were registered as primarily Fe_3O_4, and it was assumed that they were generated directly from the melt pool.

Providing there are no volatile elements in the starting powder composition, increase of oxygen content is generally the only modification in powder chemical composition due to its recycling. When comparing different materials, it seems that some are more prone to oxygen pickup, such as aluminum or titanium alloys. Besides, chemical composition changes depend a lot on the processing conditions and particularly the limit of oxygen content inside the build chamber during fabrication, which can vary from one L-PBF machine to another. Some studies on stainless steel did not find any change in chemical composition [153]. Oxygen content change in reused powders depends as well on the laser and scanning-related parameters as different energy density inputs result in more or less spatter ejections, and various HAZ extent. These are mostly responsible for oxygen increase and can also lead to microstructural modifications. The different methods of reuse, as well as the build characteristics (parts volume, printing time, etc.) will also impact the oxidation rates of the materials [167].

Microstructure

For stainless steels, as mentioned earlier (section 1.1.3) the microstructure of virgin powders is either composed exclusively of fcc γ-austenite phase, or combined with a small fraction of bcc δ-ferrite phase. Whether with 17-4 PH [142, 153], 304L [140] or 316L [137, 139, 159], an increase of the volume fraction of the ferrite phase is observed with powder recycling, along with a corresponding decrease in the austenite phase. For example, in these studies, the volume fraction of δ-ferrite is about 6-8 % in the reused powders while being 0-0.5 % in the virgin powders.

Heiden et al. [137] discovered that the increase of bcc phase in the reused powder comes from highly spherical fully ferritic particles. Figure 1.39 represents EBSD phase maps and inverse pole figures for fcc γ-austenite (blue) and bcc δ-ferrite (red) regions in virgin and reused 316L powders. Through correlation to laser welding experiments, they suggested that these bcc single crystal particles are spatters ejected from the melt pool or particles that passed through the laser plume due to entertainment by gas flow.

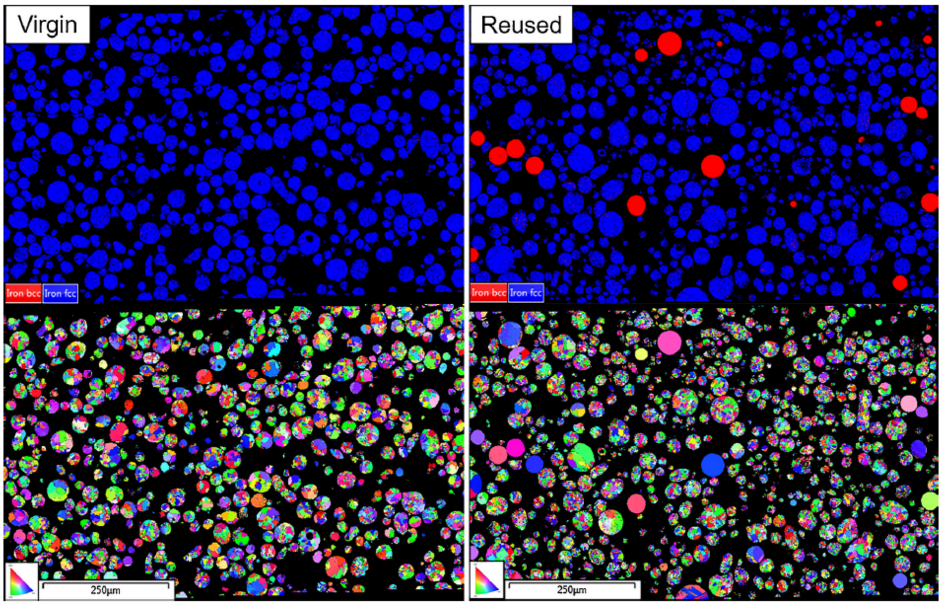

Figure 1.39 – EBSD phase maps and inverse pole figures for austenite (blue) and ferrite (red) regions in virgin and reused SS316L powders [137].

As introduced in section 1.2.1, the microstructure of 316L is affected by the chemical composition, with the $\mathrm{Cr}_{\mathrm{eq}}/\mathrm{Ni}_{\mathrm{eq}}$ ratio, but also by the cooling rate. According to the composition ratio, 316L solidifies as primary ferrite then austenite. However, for metallic droplets, high cooling rates hinder diffusion and therefore the solid state transformation of ferrite to austenite ($\delta \rightarrow \gamma$). This allows the retention of the δ-ferrite phase.

However, at very high cooling rates (on the order of 10^5 - 10^6 K/s), nucleation of δ phase can be bypassed resulting in the solidification of primary austenite [4]. This effect should be more important at small particle sizes, as the cooling rate of smaller particles is faster, due to less thermal mass. Sutton et al. [145] analyzed the amount of each phase present in the recycled powder separated into different size fractions. They observed an increase of δ-ferrite when the particle size increases. Slotwinski et al. also highlighted a huge variation in the sieve residue, the powder collected that did not pass trough a sieve of 80 µm, with a volume fraction of ferrite around 45 % [142]. Cooling rates of large spatters are not high enough for undercooling and solidification by primary austenite, but sufficient to retain δ-ferrite. Smaller particles, and virgin powder have extremely high cooling rates achieved due to their size, which allow a supercooled liquid to be present below the stable solidus leading to austenite solidification.

These theories can however be questioned and other explanations and observations have been reported. Pinto et al. [139] found that the mean size of the ferritic particles is smaller than the virgin ones, with a lot of very fine particles (< 10 µm). Nevertheless, they also attributed the presence of ferrite to the high cooling rates inhibiting the solid sate transformation of ferrite into austenite. Heiden et al. [137] claimed that 316L powder should follow a primary austenitic solidification sequence. In that case, δ-ferrite particles are formed due to undercooling.

Kriewll et al. [4] studied the effect of the amount and volume of parts present in the build on powder degradation for 304L. They showed that the amount of δ-ferrite in the powder increases with the area fraction builds and with each iteration. Part spacing and number of parts also have an influence: for a same area fraction (50%), powders collected from builds with 11x11 cubes had more δ-ferrite than powders retrieved from builds containing 5x5 cubes. It can be explained as smaller and more numerous parts increase the probability that spatters fall down on sections of the powder bed not scanned by the laser.

Increase of ferrite content in the powder leads to a higher magnetic susceptibility and magnetic moment, the ferritic particles being ferromagnetic. This favors particles clustering due to ferromagnetic interactions and can have detrimental effects on the powder bed packing and layer uniformity during L-PBF process. Pinto et al. [139] proposed to use magnetic separation after sieving to remove δ-ferrite particles.

Heiden et al. [137] assembled a map of particle-laser interactions compiling the changes observed during their study on stainless steel 316L powder recycled 30 times, figure 1.40.

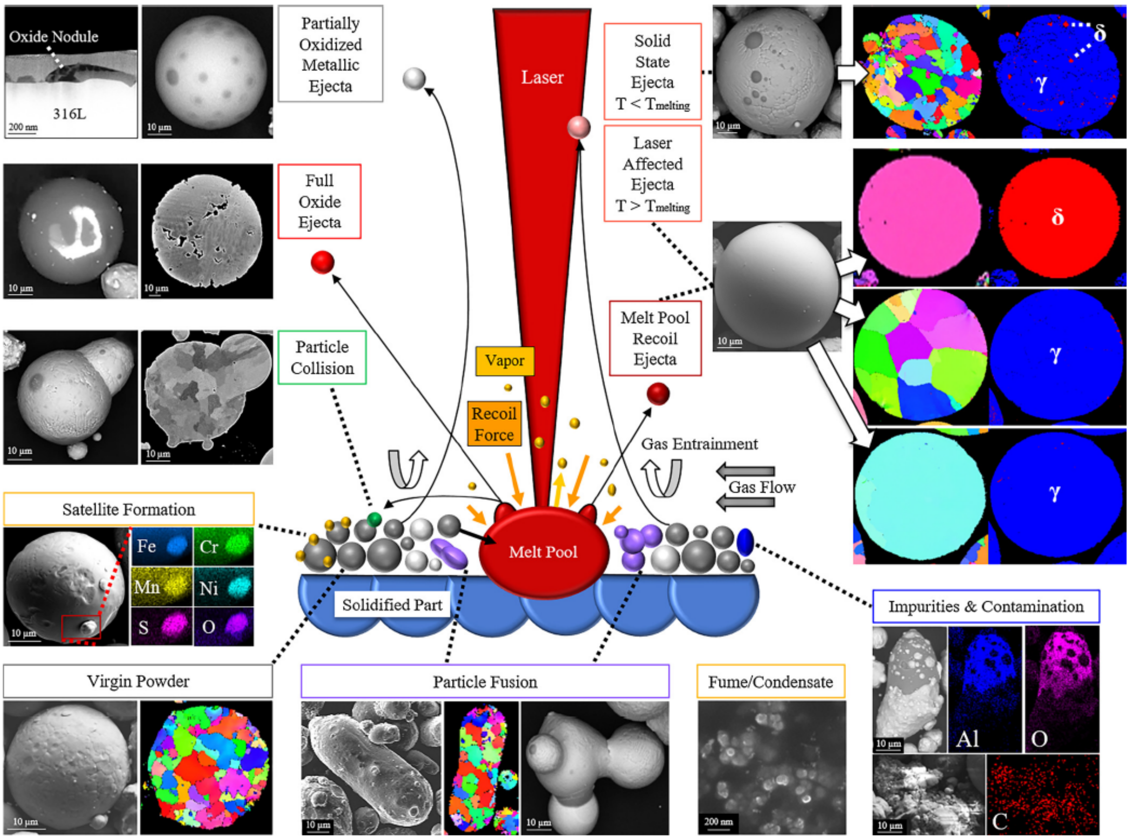

Figure 1.40 – Particle-laser interactions found in the L-PBF process for SS316L [137].

Recycling of powder in L-PBF causes deterioration of powder attributes. Particles are more irregularly shaped, with increases of satellites, bonded particles and agglomerates. Oxygen pickup in reused powder also occurs with selective oxidation on the surface of spatter particles. Finally, microstructural changes are observed, with increase of δ-ferrite phase in the case of SS316L powder. Fortunately, a large proportion of powder altered by the process is removed by the sieving process.

However, some damaged particles will still be present on the powder feedstock for future printing as some spatters are highly spherical and with similar size as virgin powder. The number of spatters, which are responsible for the most part of powder degradation, depends on the laser input and processing conditions. Therefore, it is difficult to determine a common rule about the number of recycling cycles guaranteeing suitable powder properties for L-PBF process. There is consequently a need to characterize the powder in-situ, in order to control the proper functioning of powder recycling and L-PBF processing, and eventually implement corrective actions.

1.3.2 Influence on printed parts

In addition, it is important to understand the effect of recycling on printed parts. The effects of using recycled powder on the density, microstructure, surface roughness or mechanical properties of printed parts have been investigated in the literature, but studies are not that numerous.

Density

It was found that the part density can decrease slightly with intensive reuse [137, 146, 150]. Heiden et al. [137] suggested that this density alteration could be partially influenced by the amount of oxygen present in highly reused powders. Other studies did not show any consistent trend or clear correlation between parts density and recycling of the powder [153,155,164,168]. Sartin et al. [164] observed consistent weld penetration depths and melt pool shapes for SS316L parts elaborated with virgin and 12 times recycled powders. Figure 1.41 presents metallographic images of samples etched for these two cases, where melt pool tracks and boundaries are clearly visible.

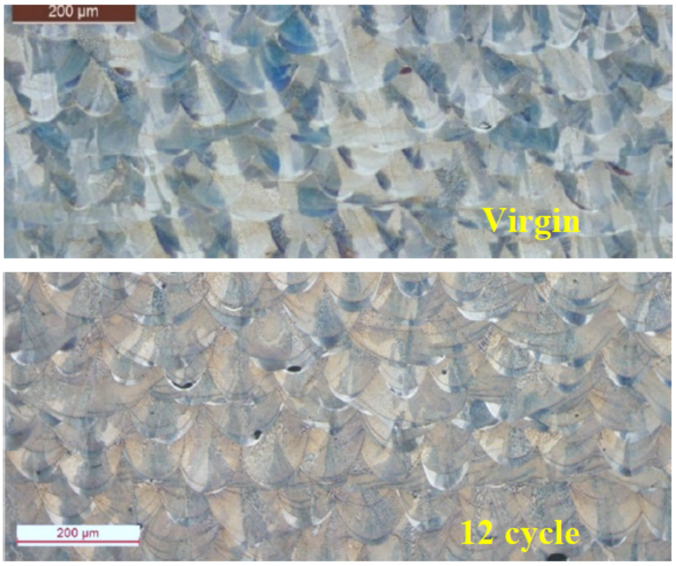

Figure 1.41 – Metallographic images of SS316L samples elaborated with virgin and 12 times recycled powders [164].

Once again, parts density is strongly correlated to the L-PBF processing conditions, and possible changes in powder attributes can lead to various results on the final parts depending on the manufacturing conditions. Seyda et al. [141] found that the porosity of L-PBF test specimens decreased with subsequent recycling builds. In their case, they explained this improved density because of the better flowability and packing density of the recycled powder on the build platform.

Microstructure, **crystallographic phases** do not seem to show any significant difference between parts printed from new and recycled powder [146, 169]. As observed on powder particles, the **oxygen content** of the elaborated specimens can also increase with powder reuse [168,170]. In addition, powder oxidation induces poor wetting during the L-PBF process, which can lead to the balling phenomenon or increase amount of spattering, as mentioned in section 1.2.2. This results in the presence of inclusions and an increased porosity.

Roughness

Increased surface roughness has been observed as the powder was recycled multiple times [141, 146]. Figure 1.42 shows the surface roughness measurements on the side, front and top surfaces of 17-4 PH stainless steel cubic samples printed with different powder reuse cycles.

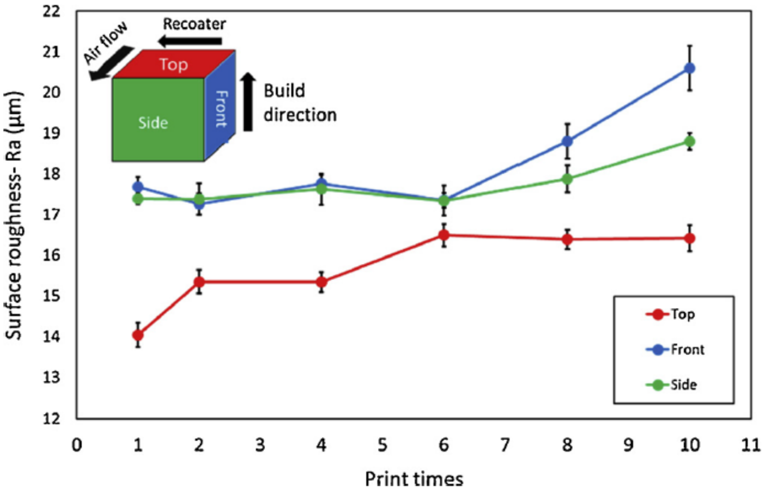

Figure 1.42 – Surface roughness evolution of the side, front and top surfaces of 17-4 PH printed parts through recycling [146].

This deterioration of surface finish is also due to the particle size distribution of the recycled powder, and the higher proportion of large particles and agglomerates. These large spatter particles can fall back and adhere to the surface of printed parts, which consequently gets rougher. Heiden et al. [85] showed that the lowest roughness values for different powders when testing a very large number of processing parameters is generally approaching the D10 value of the powder used. Whenever present, balling can also adversely influence the surface roughness of the printed parts.

Mechanical properties

Powder degradation due to its recycling, including the oxygen pickup can affect the mechanical properties of printed parts as well.

Hardness of parts made out of virgin and recycled powder is generally comparable [153,164]. Some studies found a slight increase in the hardness measurements, especially with titanium powder. It was assumed that powder oxidation and oxygen atoms trapped in the melt leading to oxides precipitates once solidified are responsible for the material hardening [141]. Phase transformation can also be a cause of enhanced properties [171]. Giganto et al. [172] measured a decrease in hardness for stainless steeel 17-4 PH, attributed to a slight increase in the γ-phase.

Regarding tensile testing, the majority of studies, on all materials exploited by L-PBF highlighted very minor changes in terms of **ultimate tensile strength** (UTS) and **yield strength** (YS). On the other hand, **elongation** at break is susceptible to decrease with recycled powder [146, 149, 150, 169, 172, 173]. Figure 1.43 illustrates this tendency with the tensile stress-strain curves of stainless steel 15-5 PH samples produced with virgin and reused powder.

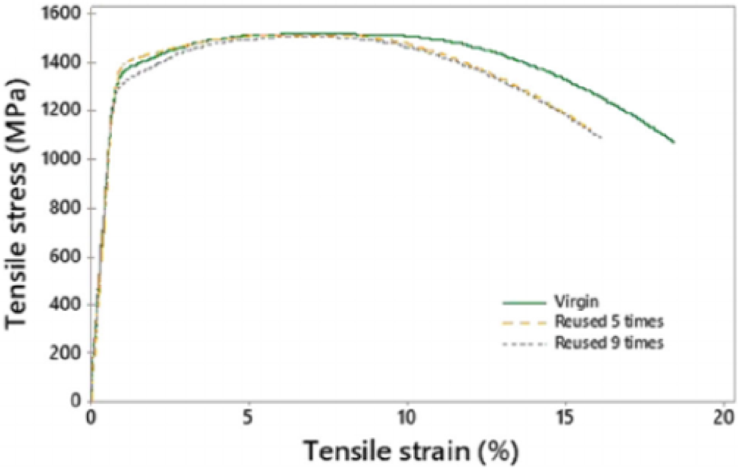

Figure 1.43 – Stress-strain curves of 15-5 PH samples produced with virgin and reused powder [173].

Strondl et al. [150] observed that a degradation of ductility was present in material exhibiting the higher oxygen content. Ahmed et al. [146] noticed an important and increased number of pores near the fracture surface of tensile test pieces with recycling. Sutton et al. [170] also found a steady decrease in part impact toughness with reuse of SS304L.

The same trend is observed in the **fatigue behavior**, with samples made of reused powder presenting shorter lifetime in terms of number of cycles to breakage [169, 174]. Fractographic examination after fatigue tests and tensile tests performed by Popov et al. [169] showed pores but also partially melted particles and lack of fusion. They revealed different fracture mechanisms in samples made of new and recycled powder. The fracture of samples with virgin powder began in the sample's center, while with recycled powder, the fracture started from the surface defects. Indeed, fatigue failure is often influenced by surface roughness, which allows cracks to initiate from the micro-notches on the surface rather than from internal defects [149]. Sometimes the specimens are machined and polished, consequently internal defects play a major role in crack initiation. Figure 1.44 shows the fracture surface of Ti-6Al-4V specimens fabricated with recycled powder in the as-build condition and in the machined surface condition. At least five crack initiation sites indicated by the red arrows are visible, all originated from micro-notches on the rough surface of the part. When machined, the enhanced view shows crack initiation from an internal defect.

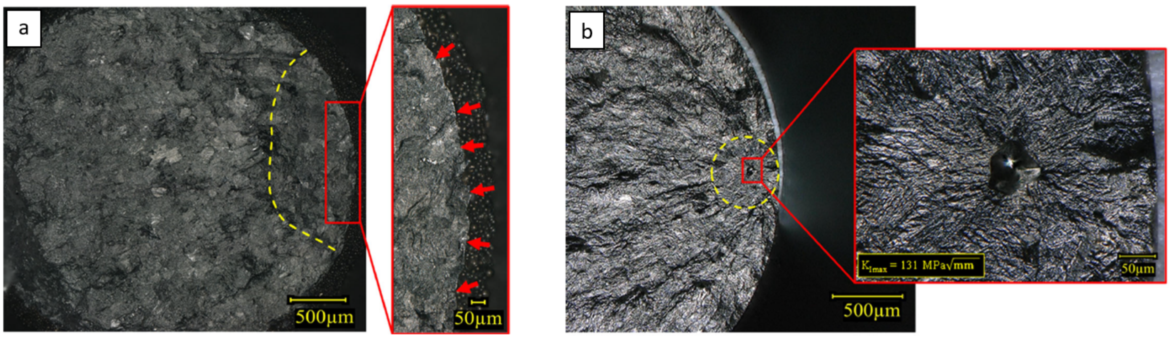

Figure 1.44 – Fracture surfaces of specimens fabricated with Ti-6Al-4V recycled powder (a) in the as-build condition, (b) in the machined surface condition [149].

Even if mechanical properties of parts elaborated with recycled powder are generally in conformity with the existing relevant standards, some properties are negatively affected. Moreover, a significant dispersion can be observed between samples. Unpredictability of defect occurrence for example is a cause of the non-repeatability of mechanical properties.

Manufacturing of parts with L-PBF using recycled powder has an influence on the quality of the printed products. The part density is susceptible to decrease. It is also the case for the part ductility or the fatigue limit, while the material surface might get rougher. Other parts properties do not show significant change or trend when fabricated with reused powder, such as the chemical composition (except for oxygen content), microstructure, ultimate tensile strength, yield strength and hardness. Even the altered properties generally stay within the existing norms, but an important dispersion is present among results of mechanical tests.

This repeatability issue comes from the degradation of the recycled powder which occurs unevenly between the particles. Besides, the part properties deterioration are also dependent on the process parameters used for manufacturing, and have to be correlated to the powder attributes. In order to perform the L-PBF process using recycled powder, particles degradation due to printing has to be understood, as well as the interaction between powder characteristics and processing conditions. Furthermore, in situ monitoring or preliminary control of the powders attributes has to be implemented to be able to carry out the correlations regarding the process parameters.

The following section will shortly describe in-situ monitoring and characterization of the L-PBF process implemented in the literature.

1.4 Process monitoring

The aim of monitoring is the improvement of the reliability of the process within a single manufacturing and between several productions. Due to the multitude of factors in L-PBF, and the high complexity of phenomena taking place during part production, the lack of process robustness and repeatability have been pointed out by many as a major barrier for the industrial breakthrough of metal AM [6, 29].

In-process monitoring allows to check the quality of the process in the earliest possible stage, during the layer-wise growth of the parts. Moreover, it could enable to adapt the process parameters based on the in-situ measurements, with closed loop control algorithms to manage machine operation [175].

This review of laser powder bed fusion monitoring will be divided according to different process signatures: the melt pool, the slice and the powder bed. The term ”slice” refers to the slice of the part scanned by the laser at each layer, and ”powder bed” refers to the layer of powder spread by the recoater onto the build platform, before laser scanning of the current layer [176]. The last two categories are used by some authors as layerwise monitoring.

1.4.1 Melt pool monitoring

In L-PBF, the most commonly monitored target is the melt pool. Research efforts concentrated on this area for a better understanding of the process, gathering of information regarding the related phenomena. Most studies demonstrate the capability of measuring relevant quantities and signatures and to study the influence of parameters on these features. Few authors proposed monitoring for quality control, automatic default detection with corrective actions when possible [176].

Melt pool size, shape and temperature (intensity and profile) can be monitored, but this is a challenging task due to both small length scales and short time scales. Therefore, in-situ sensing systems have to present sufficient spatial resolution and very high sampling rates. Sensors setups for in-situ data collection can be classified into two mounting strategies: *co-axial* and *off-axial*. Co-axial sensing technologies use the optical path of the L-PBF system to monitor the melt pool, while off-axial techniques use sensors placed outside the optical path [177]. Existing monitoring systems generally employ one or a combination of different sensors : in visible light, with regular or high speed cameras; in the infrared (IR) range based on the acquisition of a radiation, with photodiodes, pyrometers, thermal cameras. The cameras usually present various technologies of transfer of information, with CCD (charge-coupled device) or CMOS (complementary metal-oxide semiconductor) sensors [178].

Kruth et al. [179] designed a co-axial system with feedback control to adjust the laser power based on the temperature distribution on the melt pool. They used a CMOS camera to monitor geometry and temperature distribution and a photodiode to measure the intensity. Craeghs et al. [180, 181] from same research group in Leuven used the same setup with a feedback control. The latter allowed to improve the geometrical accuracy of overhang structures (i.e. downfacing surfaces) and test the parts quality of other special geometries such as acute corners. Then, Clijsters et al. [182] integrated real time data capturing and processing algorithm to create melt pool maps. In the case of overheating of the liquid, reconstructed 3D build defects from the mapping were comparable to ex-situ X-ray computed tomography (XCT) measurements. Similar optical hardware have been developed by Lott et al. [183]. They expanded the setup with an illumination laser beam to enhance the visualization of the melt pool dynamics.

Another co-axial monitoring system was presented by Doubenskaia et al. [184, 185] with the use of a two wavelength pyrometer and a CCD camera to measure temperatures from the melt pool. Bayle and Doubenskaia [186] also proposed an off-axial setup. They employed an IR thermal camera coupled with a pyrometer to monitor temperature evolution.

Different techniques are used to characterize the melt pool size and shape and dynamics for a better understanding of the related phenomena. In-situ x-ray imaging have been widely used by several authors for direct observation beneath the surface [187–192]. For example, Guo et al. [189] related x-ray images showing melt pool variations with different combinations of laser power and scanning speed, figure 1.45. In this study, IED, the input energy density was defined as $P/(vd)$ with a unit of J/cm^2. Simonds et al. [190, 193] combined high-speed x-ray imaging and absorption measurement to understand the melt pool fluctuations and pore formation in keyhole mode with periodic energy absorption variations. Other studies focused on the spatter generation in L-PBF with off-axial high speed camera imaging [93, 109, 194].

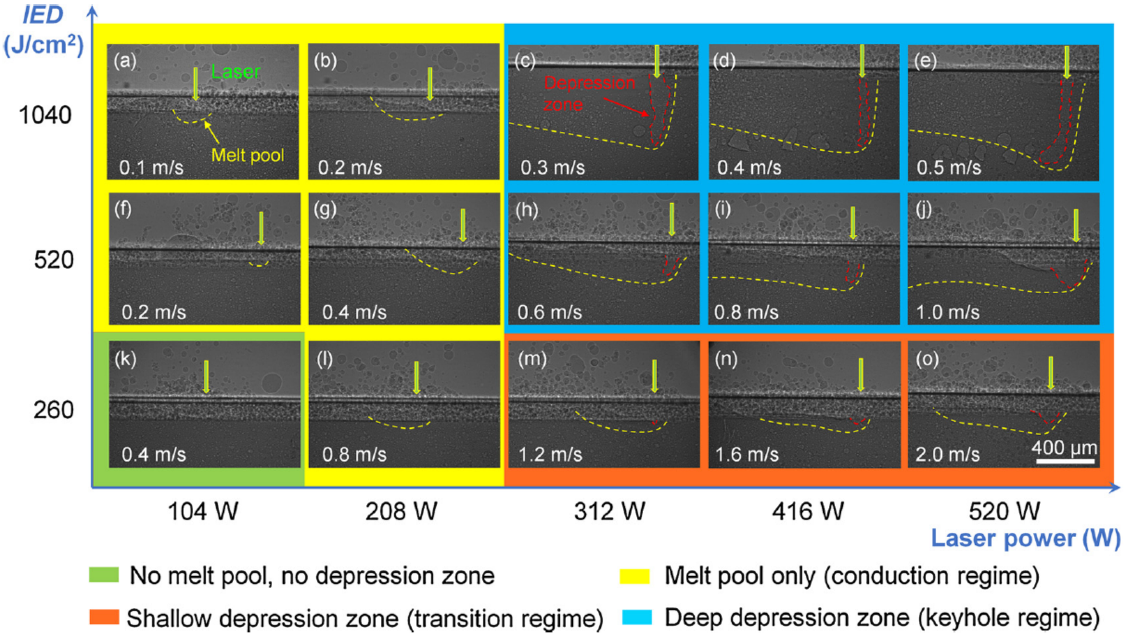

Figure 1.45 – X-ray images showing melt pool variation under different combinations of processing parameters P and v [189].

The impact of parameters variations can be seen in the melt pool behavior, however in order to achieve robust technologies for online control of the L-PBF process, it is not sufficient to only monitor the melt pool.

1.4.2 Slice monitoring

Image processing techniques can also be used to detect material discontinuities and errors on a layerwise level. After exposure of the laser beam and solidification, it is possible to gather in-situ information. The main purposes of slice monitoring are to characterize the surface patterns to detect defects, to rebuild the slice geometry for all layers and to quantify the geometrical accuracy compared to the nominal dimensions [195, 196].

High speed cameras in the visible range are mostly used for slice monitoring. Kleszczynski et al. [197, 198] mounted a CCD camera outside the chamber combined with an illumination system with reflectors blades inside the building area to monitor the surface pattern of the slices. With the same setup, zur Jacobsmühlen et al. [199, 200] were able to identify super-elevated area compared to the CAD geometry of the part and create mappings of these deviations, shown in figure 1.46. Detecting out-of-plane deviation from regular surface was also developed using cameras and a fringe projector by Zhang et al. [201, 202]. They presented topography maps and measured the height profile of each layer. Guerra et al. [203] employed off-axis high resolution optical tomography to detect geometric distortion on overhanging structures, this solution offering the advantage of requiring limited image processing steps.

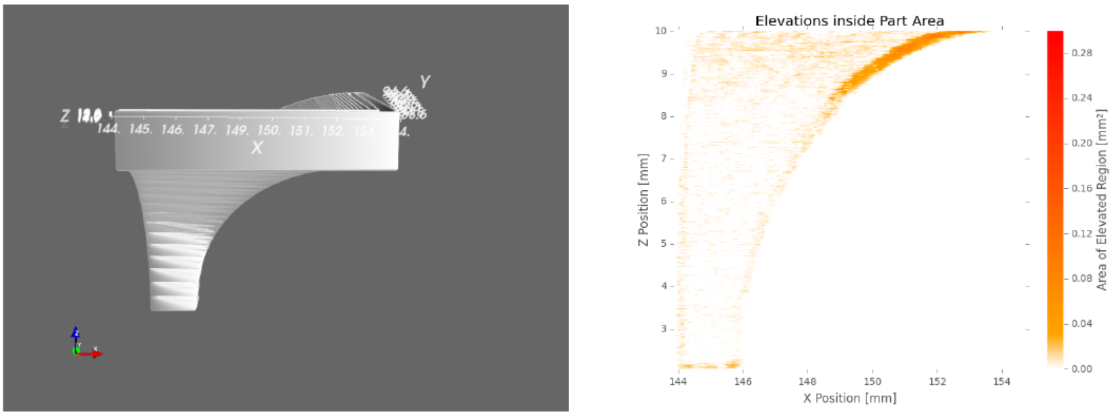

(a) (b)

Figure 1.46 – (a) CAD Geometry of the monitored part with decreasing overhang angle for increasing z, (b) x/z plot of elevated area locations and severity [200].

Segmenting layerwise images allowed Foster et al. [204] to present 3D reconstructions of the part geometry. Other studies used slice images to autonomously detect surface anomalies with contour segmentation [205, 206]. Gobert et al. [207] used layerwise images of the slices and different pixel intensities to detect local pores in printed parts, and performed comparison between their 3D reconstruction of the part and XCT results. IR thermography was also used to detect in-situ defects based on slices surface temperature measurements by Bartlett et al. [208]. Spurek et al. [209] performed as well a layerwise measurement of part density, using an Eddy current testing system mounted on the recoater of the L-PBF machine.

Most of these studies collected images or data at each layer after selective melting of the powder bed, but also after powder deposition. Characterization of the powder bed area before scanning of the laser beam is the earliest possible in-situ control.

1.4.3 Powder bed monitoring

In the case of powder bed monitoring, the data acquisition can be performed after or during the deposition of the thin powder layer. Powder spreading can result in heterogeneities of the bed density due to a poor control of the feeding system, defects in the recoater, inadequate powder attributes, but also due to previous laser-induced defects such as spatters. For instance, spatters falling down on the powder portion of the build area can be dragged by the linear motion of the recoater. One major goal of powder bed moniroting is to detect local inhomogeneities that could have a detrimental effect on the quality of the part.

Foster et al. [204] used image processing for detection of powder bed defects in addition to the above mentioned study of part geometry. On their 3D reconstruction from layer-by-layer images, irregularities in layer thickness caused by recoater damage and spatter particles dragged by the latter were observed. Craeghs et al. [180] also detected stripes in the powder bed images parallel to the movement of the recoater. They proposed an image processing algorithm to detect wear or damage of the latter. Bartlett et al. [208] captured images of recurrent powder spreading errors and observed defects at the same (x,y) position at multiple layers through the fabrication.

Scime et al. [210–212] developed an algorithm to achieve autonomous powder bed anomaly detection and classification with machine learning techniques. Images were captured with a relatively low resolution camera provided by the L-PBF machine manufacturer. They illustrated the capability of their system with a case study where multiple powder bed anomalies arose and were detected and classified automatically, as shown in figure 1.47.

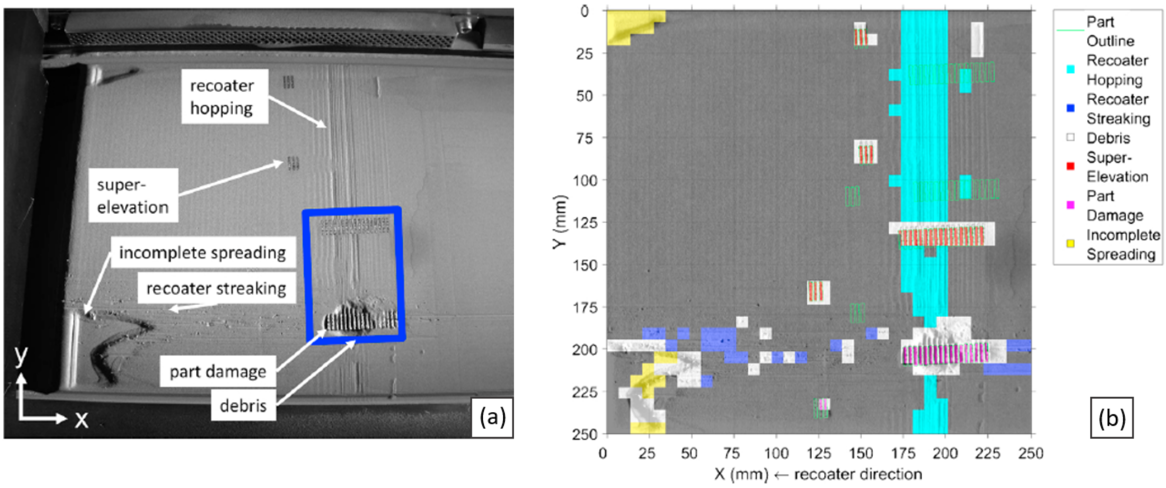

Figure 1.47 – (a) Raw powder bed at layer z with selected instances of anomalies manually annoted (b) Corresponding layer z with the powder bed anomalies classified by the algorithm [211].

Image acquisition task is limited by the compromise between spatial resolution and field of view. All these techniques and methodologies are performed with relatively low spatial resolution, in order to cover the entire powder bed area [195]. Therefore, only large powder bed defects can be detected in this manner.

But in reality, defects can be as small as the powder particle size and can occur anywhere across the build area. Pedersen et al. [213] proposed to use contact image sensors to scan the surface of the powder bed during the recoating procedure. These sensors are commonly used in flatbed document scanners and offer single digit micron resolution. This technology has the potential to image the entire powder bed with individual powder particles resolution. Besides, image acquisition occurs normal to the powder bed surface. Thus, unlike with off-axis digital cameras, there is no need to correct image distortions and perspective errors, which are known to reduce accuracy in detecting powder bed defects [197]. Another advantage is that this setup is composed of its own illumination system and avoid any heterogeneous illumination conditions across the build area [196]. A similar system was also patented in 2016 by EOS GmbH [214], describing a scanning device (typically line sensors) mounted on the recoater and a method of process control with the capture of the build area by means of the scanning device allowing the control of potential defects and unevenness on the applied powder layer.

Le and Seita [215] developed a similar setup, with a powder bed system integrating a contact image sensor unit to the powder recoater module. The recoating motion was synchronized with the image acquisition rate using a microcontroler. They exploited out of focal plane zones of their mappings to detect non-uniformity in the powder layer thickness, as illustrated in figure 1.48. These thin variations were detected owed to the narrow depth-of-field of contact image sensors, generally used to scan very flat objects, and the authors were able to assess the height and depth of the defects with numerical image analysis techniques. Surface roughness and surface particles density were also evaluated with this method to study the influence of different recoating strategies and powder batches [216].

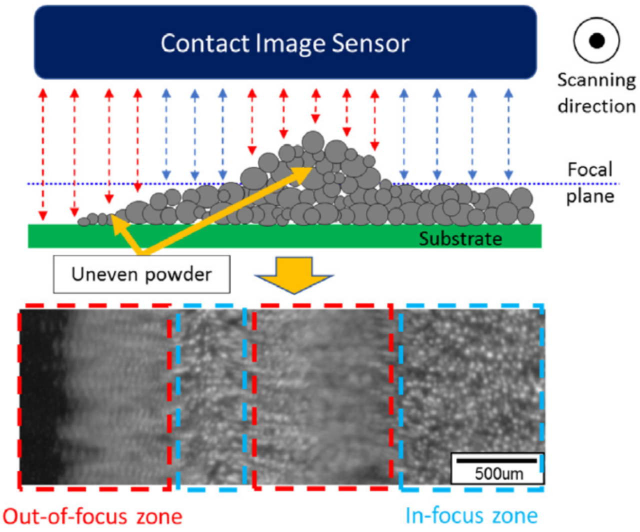

Figure 1.48 – Schematic of a defective powder bed layer and its corresponding top-view scan [215].

Recoater-based monitoring was also employed for other applications and with different sensors, taking advantage of the access to the entire powder bed area before and after laser scanning. Barrett et al. [217] installed a laser scanning profilometry allowing to draw height maps of each layer. Fisher et al. [218] used a similar recoater-based architecture with high-resolution line camera to obtain a better vertical resolution than with contact image sensors. However, this setup can be challenging to integrate in L-PBF machines due to space limitations in the build chamber. Bugatti and Colosimo [219] presented a first implementation in an industrial L-PBF machine of an in-line scanner as described above, to demonstrate the setup performances regarding in-situ monitoring and detection of both large-scale and small-scale defects on the entire powder bed area.

This new method for in-situ monitoring of the powder bed in L-PBF offers new possibilities, with this ability to detect individual powder particles across the entire powder bed. This technology will be used in this PhD thesis, with the aim of performing in-line control of powder degradation. A better monitoring of the powder quality during the process would allow to conduct more reliable powder recycling strategies, and potentially take subsequent actions regarding the processing parameters, with a controlled reintroduction of virgin powder, etc. The apparatus and methodology will be further described resppectively in chapter 2 and 4.

Development of in-situ monitoring of the L-PBF process concentrates on the use of imaging systems and non-contact temperature measurements. First efforts were focused on monitoring the melt pool, for instance to develop a better understanding of the complex phenomena occurring during laser-powder interactions. Layerwise monitoring can be a great value to provide real-time part qualification with slice geometry control, and offers the earliest in-situ information with powder bed monitoring. Improvement of the latter to detect small-scale defects and powder attributes could ensure a better correlation between powder properties and processing conditions, therefore increase the robustness of the L-PBF process.

1.5 Summary

Laser powder bed fusion is one of the most promising technology of additive manufacturing. It allows the production of high performance components, with complex geometries and very high precision. However, this process is intricate and impacted by many parameters that will affect the quality of the printed parts and the repeatability of the process. Among the many factors, the impact of the quality and the attributes of the powder material is so far insufficiently explored and taken into account.

In a context of circular economy and the objective of fulfilling one of the main purpose of AM that differentiates it from subtractive processes by using the right amount of material to manufacture the parts, powder recycling is essential in L-PBF. Laser-material interactions, high temperatures and imperfectly controlled environments during processing inevitably result in some degree of alteration of particles attributes, including high temperature oxidation.

Studies in the literature have shown that successive powder reuse affect the powder, with unavoidable degradation regarding the particles size, oxygen content or sometimes microstructure. Powder recycling and these changes of particles characteristics can lead to an alteration of the elaborated parts properties. The effects can vary from material to material and especially from one machine to another, and according to the manufacturing conditions. The processing conditions greatly influence the quality of the solidified specimens, and must be correlated with the powders attributes.

For a better correlation between the processing parameters and powder properties, there is a need of preliminary or in-situ characterization of the powder particles in L-PBF, for further adjustment regarding the observed features. Monitoring of L-PBF is developing in line with this real need to strengthen the robustness of the process. Some interesting technologies have been implemented to control the parts during or after melting/solidification at each layer, but also to characterize the powder after its spreading on the powder bed area. In-situ powder monitoring would enable more robust powder recycling procedures, with the detection of powder characteristics that are not homogeneous but particle-dependent, and not necessarily representative when performed ex-situ. A better knowledge of the influence of the feedstock properties on the performance of the final product, correlated to controlled/adequate operating parameters thanks to powder bed monitoring would bring L-PBF sustainability and repeatability to another level.

These problematics of analysis of the influence of powder recycling, development of a methodology to monitor powder degradation, but also of understanding the effects of the parameters and conditions of fabrication on this degradation in order to minimize it will be explored during this PhD thesis.

Chapter 2

Materials and Methods

This chapter presents the materials and methods used during this thesis. Characteristics and operating conditions of the L-PBF printer are detailed in the first part. Techniques for microstructural characterization of materials, employed for both powder particles and printed parts are described in the second section. The third and fourth sections deal with the additional characterization techniques used specifically for the powder material and the solid samples respectively. Finally, the last part presents the set-up used for the monitoring of powder bed.

2.1 L-PBF processing

2.1.1 Trumpf machine

A TRUMPF TruPrint series 1000 L-PBF machine (figure 2.1 (a)) was used for this work. This printer is equipped with a 200 W continuous Yb-fiber laser (1070 nm wavelength) and a spot size of 55 µm. The manufacturing system is not in closed loop for the powder feedstock, *i.e.* the enclosure comprises a powder supply cylinder, a build cylinder with a volume of ⌀100 mm × H 100 mm, and a powder recovery tank, allowing full control over the powder material and its reuse (figure 2.1 (b)).

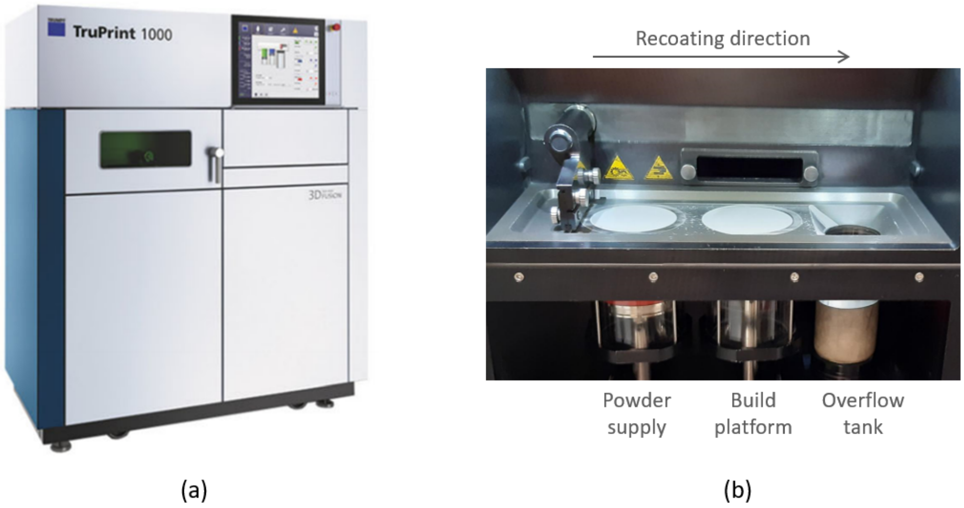

Figure 2.1 – (a) Trumpf TruPrint 1000 L-PBF machine, (b) Build chamber of the printer.

The process takes place in the build chamber under controlled atmosphere. All builds were conducted in an argon environment, using ultra high-quality Argon 5.7, with a laminar flow over the build platform seeking to carry away as much of the spatter particles as possible out of the powder bed. A maximum oxygen content requirement has been set to 0.03 wt.% for most of the fabrications, except in chapter 5 where the influence of oxygen atmosphere was investigated, with some of the prints being carried out with an oxygen target of 0.1 wt.% maximum.

Powder layer thickness was set to 30 µm. The powder recoater of the machine is a soft *V-type* rubber blade. Powder feedstocks were sieved using a 50-µm mesh size prior to being inserted into the powder supply cylinder. Laser scanning strategy followed a 10 mm wide stripes scanning, and a 67° rotation between layers (figure 2.2).

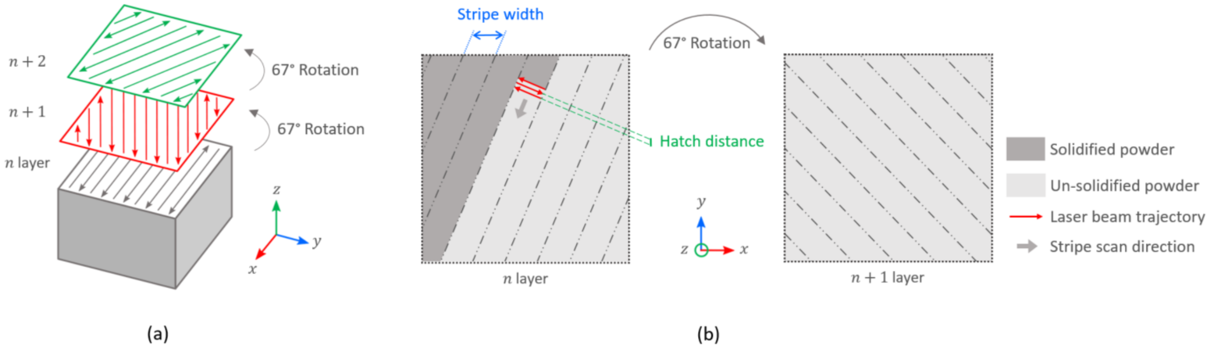

Figure 2.2 – Laser scanning strategy used in this work - (a) Overall representation of the rotation between layers and (b) Close-up of the laser scanning path.

Laser parameters were optimized regarding the density of SS316L elaborated parts (detailed briefly in appendix). The selected process parameters used to investigate powder recycling and powder degradation in L-PBF are reported in table 2.1.

Table 2.1 – Selected L-PBF processing parameters

Laser power	Scanning speed	Hatch distance	Layer thickness
165 W	950 mm/s	0.05 mm	0.03 mm

2.1.2 Samples elaboration

Parts and build preparation in L-PBF is achieved using the Materialise Magics software. The latter allows to create simple 3D parts (*e.g.* cubic specimens, cylinders, tensile testing specimens) and import more complex ones previously designed using a CAD software, and converted to the STL format. Build preparation then includes various operations to make the parts printable, such as positioning the parts on the build plate, labeling the parts, choosing the build orientation, generating support structures, or even repairing the meshing of damaged CAD files. The software enables the visualization of the parts in the build volume, but also to preview the slices that will be laser melted during the process. A build processor manager specific to the L-PBF printer to be used further on in the fabrication is included in Magics Materialise, and allows to define all the processing parameters, and also to create different sets of parameters. After the assignment of the parameter sets to the different parts composing the fabrication platform, the components are sliced into cross-sectional layers of a previously defined thickness. This creates a build job file, comprising the laser beam movements of each layer, that is ultimately sent to the L-PBF machine to proceed with manufacturing. Figure 2.3 schematizes this L-PBF build preparation workflow, going from a 3D part file to a job file ready to be printed.

After the digital preparation with the creation of the build job file, a few steps of manual preparation are required before the automatic layer by layer manufacturing (schematized in figure 2.4). The sieved powder is inserted in the powder supply cylinder. The powder volume (*i.e.* the height of the supply cylinder) is determined by the machine according to the height of future print and the parameter set for powder spreading dosage. During the printing process,

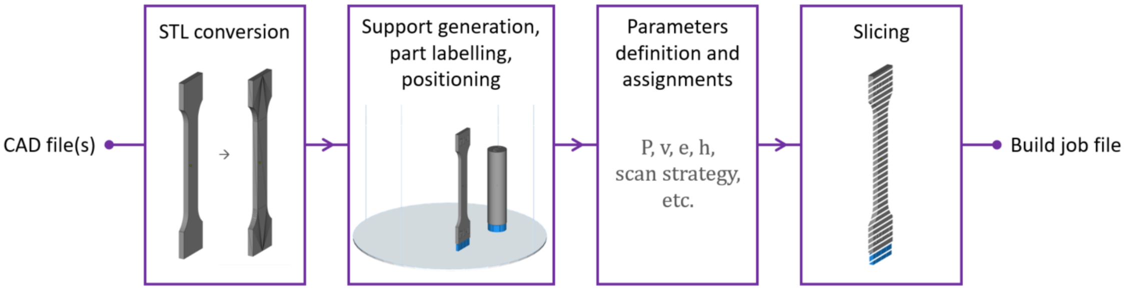

Figure 2.3 – L-PBF build preparation workflow - Digital preparation.

in order to guarantee a good coverage of the entire build area, a larger dose of powder than needed is spread by the recoater and the excess powder is deposited in the recovery tank. A SS316L build plate with a diameter of 100 µm has to be installed on the build cylinder. This substrate must be sandblasted beforehand in order to increase its surface roughness and to ensure a good adhesion of the parts and supports. Indeed the build plates, in their raw condition coming from the machinist, have a very smooth surface which inhibits an evenly powder spreading during the first layer. The last component to be installed in the build chamber is the recoater. After fitting the rubber blade to the recoater, the assembly is fixed to the motorized arm, with a height adjustment relative to the chamber frame. Finally, the first layer of powder is deposited "manually" using the recoater, and the height of the build plate is adjusted to ensure a thin first layer before starting the consolidation process. At the start of the process, after inerting with argon, this first layer is scanned twice by the laser beam to guarantee the bonding of the solidified material to the substrate.

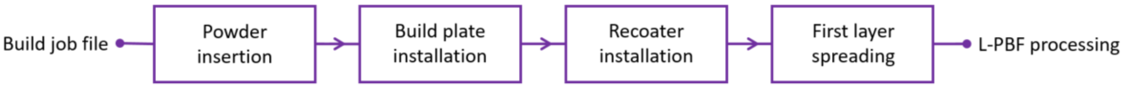

Figure 2.4 – L-PBF build preparation workflow - Manual preparation.

After the process, the un-melted powder is brushed out into the overflow tank. The remainder of the cleaning is completed with a vacuum cleaner. The recovered powder is then sieved in a Retsch AS 300 vibratory sieving station using a 50 µm screen. The printed parts are separated from the substrate using a band saw. The specimens thus obtained are sandblasted and cleaned with ethanol in an ultrasonic tank to eliminate the powder deposited on the surface and still contained in the supports. Finally, the support structures are removed manually by polishing. The final parts are then analyzed mostly as-build for various characterization, or can be machined to perform tensile testing. Figure 2.5 summarizes the last steps carried out for the elaboration of the samples, with the post-processing steps.

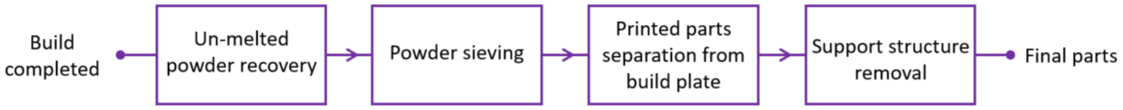

Figure 2.5 – L-PBF workflow - Post-processing.

2.2 Microstructural characterization techniques

During this PhD thesis, metal powders and parts elaborated by L-PBF were characterized regarding numerous aspects. Among them, the microstructural characterization was common to these two types of materials. This section presents the tools and techniques used for these analyses.

2.2.1 Sample preparation

Sample cutting

For the metallographic observations of the printed parts, cubic specimens ($10 \times 10 \times 10$ mm^3) were manufactured and cut in order to analyze different orientations and to be certain that the cross sections are located in the core of the material. The samples were cut with a precision cut-off machine (Accutom-5, Stuers) equipped with a diamond blade. The orientations of the cross sections are schematized in figure 2.6. Obviously, metallic powder did not undergo such step, and their sample preparation started directly with the embedding in epoxy.

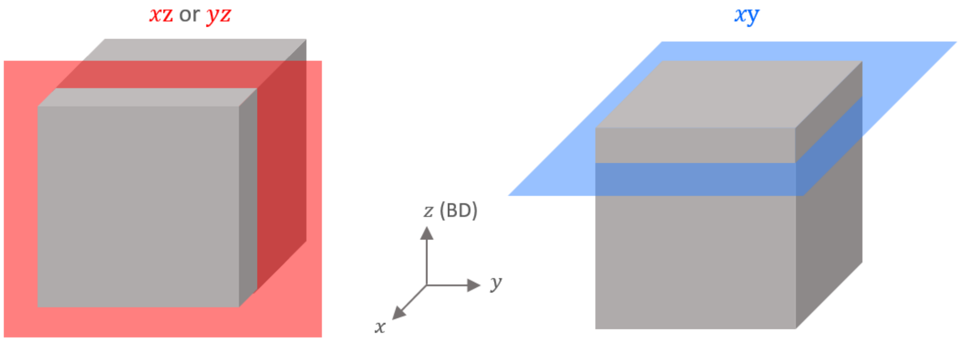

Figure 2.6 – Cross sections of the cubic samples for microstructural characterization.

Embedding and Polishing

The samples were embedded in epoxy before polishing, with a CitoPress-15 mounting press from Stuers and hot mounting Polyfast resin.

Mechanical grinding and polishing was performed with a Tegramin-20 semi-automatic polishing equipment from Struers. All cubic specimens were ground with SiC abrasive papers from 500 to 2000 grit, followed by polishing with 3 µm and then 1 µm diamond suspension. Finally, the samples were polished for 10 minutes with a 0.04 µm colloidal silica suspension (O-PS). Some specimens were also polished manually without being mounted in conductive resin. The preparation of the powder samples followed the same pattern but was more diverse depending on the results, with shorter polishing times and lower applied forces (10-15 N compared to 20 N for printed parts). Indeed, the small diameters of the particles make it rather difficult to polish the material without some particles being expelled by the loss of matter. All samples were cleaned with water and ethanol in an ultrasonic tank.

Electrolytic polishing and etching

The last step of metallographic preparation performed on the samples was the electrolytic polishing and etching. This was conducted with LectroPol-5 Struers instrument. The as-build L-PBF samples that were not polished manually were removed from their mounting prior to the electrolytic polishing. Although the resin is conductive, it does not allow to perform these operations that require higher intensities than those encountered in a SEM. Electrolytic polishing in a 10% oxalic aqueous solution was applied for 30 s at 15 V, which implies an intensity between 0.7 and 0.9 A. This step allowed to reveal the microstructure of the printed parts, with the melt pool boundaries, grain boundaries and cellular substructures.

Concerning the powder, the latter cannot be removed from its resin. Therefore, the powder samples were manually etched with Adler's reagent solution (hydrochloric acid, ammonium copper chloride, ferric chloride and water) for 5 s.

Optical microscopy (OM) was used to control the quality of polishing and etching. The ZEISS Axio Imager 2 microscope was also used for powder morphological observations and elaborated parts density analysis. The instrument and methodology will be detailed in section 2.4.1. Figure 2.7 shows a 3D reconstruction of the microstructure of a cubic specimen captured by OM after metallographic preparation of the cross sections, which highlights melt pool tracks and and grains at this magnification.

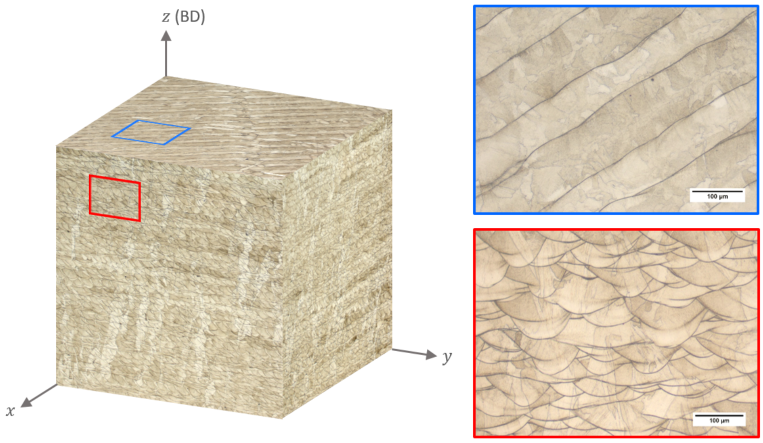

Figure 2.7 – Optical micrographs of printed parts cross sections with 3D representation of the microstructure after electrolytic polishing.

2.2.2 Scanning Electron Microscopy (SEM)

Scanning electron microscopy (SEM) allows to acquire images with high magnifications, great spatial resolutions, combined with a large depth of field. An electron beam is focused on the sample surface and penetrates to a depth of about 1 µm. The interaction between the beam and the material produces different types of radiations which allow to obtain different information about the material:

- Secondary Electrons (SE) are low energy electrons produced by inelastic interactions. They have limited escape depth, so only the secondary electrons generated close to the surface (< 10 nm) are detectable. SE mode is used to get the topographical information of the analyzed sample.

- Backscattered Electrons (BSE) are produced by elastic interactions of beam electrons with nuclei of atoms in the sample. They have a high energy and therefore a large escape depth. BSE analysis is primarily used to determine the chemical contrast: the heavier the atoms (with a large atomic number), the more primary electrons are scattered back out of the sample and detected, resulting in brighter images or zones. This mode is also sensitive (to a lesser extent) to phases and crystallographic orientations, allowing the detection of grain boundaries.

- X-rays can also be emitted due to the primary electron beam in a SEM. With the ejection of electrons, atoms can be in an excited sate, and the return to their ground state emits X-rays of different energies depending on the elements and the electron shells. An energy dispersive X-ray spectrometer (EDS) is used to detect and measure the energy of the X-rays emitted by the sample. EDS analyses allow to observe the chemical composition of the sample on the entire scanned surface (EDS mapping), or to measure the elements on profiles or single points.

In this work, metallographic observations were performed using a JEOL JSM-7000F SEM equipped with a field-emission gun. Micrographs were acquired with an acceleration voltage of 15 kV and an intensity of 2 nA. The SEM is also equipped with a Bruker XFlash 5010 detector for EDS analysis.

2.2.3 Electron Backscattered Diffraction (EBSD)

Electron backscattered diffraction (EBSD) is a SEM based technique that allows to correlate the crystallography with the microstructure of the analyzed sample. The latter is placed on the SEM with a 70° tilt with regard to the electron beam. The technique is based on the principle that some of the backscattered electrons diffract with the crystallographic planes under Bragg conditions, and form diffraction cones. An EBSD detector is present in the chamber in front of the tilted sample. The detector is composed of a fluorescent screen on which the diffraction cones are projected, and a low light level camera that acquires the image of the diagrams. On the screen, the segments of truncated cones appear as lines, called Kikuchi lines. Each analyzed point on the sample (corresponding to each pixel) consists of a diffraction pattern, and its analysis, also called indexing, allows to identify the crystalline orientation and the phase. Subsequently, various information can be retrieved on the overall surface sample such as the grain reconstruction, the crystallographic texture or the mapping of phases or grain boundaries. The indexation of Kikuchi lines is an automated process in EBSD systems but is one of the main challenges of this technique, and requires a thorough sample surface preparation.

The JEOL SEM used in this thesis is equipped with a Bruker Nano Quantax EBSD detector. The samples were fixed to the SEM stage with aluminum tape and silver paint supplied by Oxford Instruments, which also ensure conductivity between the sample holder and the sample. EBSD mappings were acquired with an acceleration voltage of 15 kV, a current intensity between 7 and 10 nA, and a working distance (WD) around 15-17 mm. The mapping resolution was fixed to 1024 × 768 pixels. The exposure time varied depending on the diffraction pattern quality, with longer times for powder samples for instance. The post processing of the EBSD data was carried out using Esprit 2.0 software. It allowed to determine grain size distribution weighted by surface, grain aspect ratio distribution, and their spatial orientations on the mapping. EBSD analyses were performed in this work to investigate the printed parts grain characteristics, and the powder particles phases.

2.2.4 X-Ray Diffraction (XRD)

X-ray diffraction (XRD) is another technique of investigation allowing to identify the crystallographic phases present in the material. An X-ray beam is directed towards the sample and will diffract with the various lattice planes under certain conditions, and the diffracted radiation is collected by a detector. The conditions are determined by Bragg's law (Eq. 2.1), where the waves add constructively for specific angles which are characteristics of the organization of atoms in the crystal lattice.

$$n\lambda = 2d\, sin\, \theta \tag{2.1}$$

with d the spacing between lattice planes, θ the incident angle, λ the X-ray beam wavelength and n an integer. By varying the orientation of the sample with respect to the incident X-ray beam, several Bragg orientaion peaks can be detected. The detected signal is transformed into a diffractogram, representing the intensity of the diffracted radiation in function of the diffraction angle. The position of the peaks and their relative intensity allows to identify the phases.

A Bruker D8 Advance diffractometer equipped with a copper anticathode with an emission wavelength Cu-K_α of 0.154 nm was used for the XRD analyses (figure 2.8 (a)). The Bragg-Brentano (θ-2θ) geometry has been employed, where the sample is fixed and both the X-ray source and the detector are rotating simultaneously (schematized in figure 2.8 (b)). XRD data were collected after scans acquisition under 40 kV voltage, 40 mA current, over an angular range of 20-120° with a step size of 0.02° and a time per step of 2 s. Indexing of the peaks position was conducted on EVA Bruker software with the database provided by the Joint Comitee on Powder Diffraction Standards (JCPDS). Both powder samples and printed parts were analyzed for phase identification. Rietveld refinement was performed using MAUD software [220] to quantify the fraction of the crystalline phases. This method consists in simulating a theoretical diffractogram from a crystallographic model of the sample, using least squares approach to refine it and make it match the measured profile. It allows to determine different information, including the phases fractions.

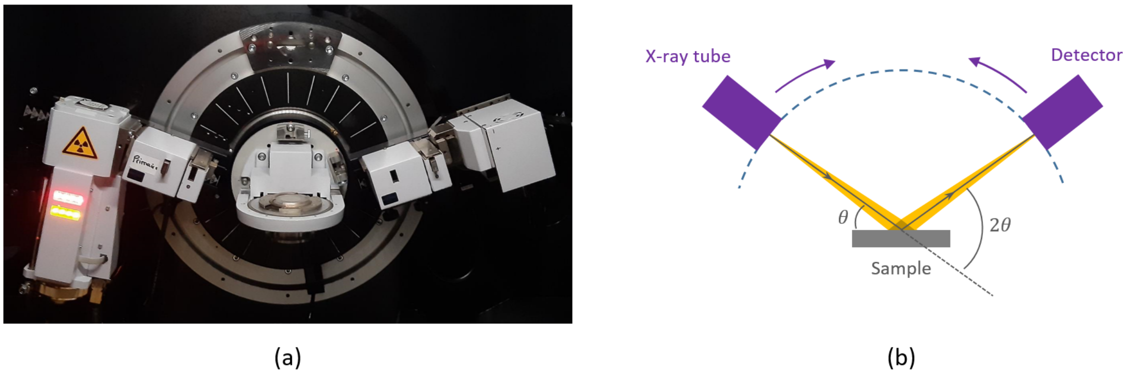

Figure 2.8 – (a) Bruker D8 Advance X-ray diffractometer, (b) Schematization of the Bragg-Brentano geometry.

2.3 Powder characterization techniques

This section focuses on the description of the characterization tools used specifically for the metallic powder, in addition to the microstructural characterization techniques described previously in section 2.2.

2.3.1 Morphology

Laser granulometry

Powder morphology relates to the particles size and shape. Particle size distributions (PSD) were measured by laser granulometry, with the Horiba Partica LA-950 analyzer. Dry measurements were conducted on the samples, with particles being scattered by compressed air stream and exposed to a laser beam (figure 2.9 (a)). The analysis of the particles size is performed by laser diffraction on the dispersed particles (figure 2.9 (b)). The values are determined in function of the diffraction angles measured and intensities, based on the Franhaufer approximation. The analysis is based on the assumption that the powder particles are all spherical, which can alter the results when the particles shapes are highly irregular. Despite this rather strong limitation, this method has become a standard in the powder metallurgy community, as it allows to measure a large number of particles in a short amount of time.

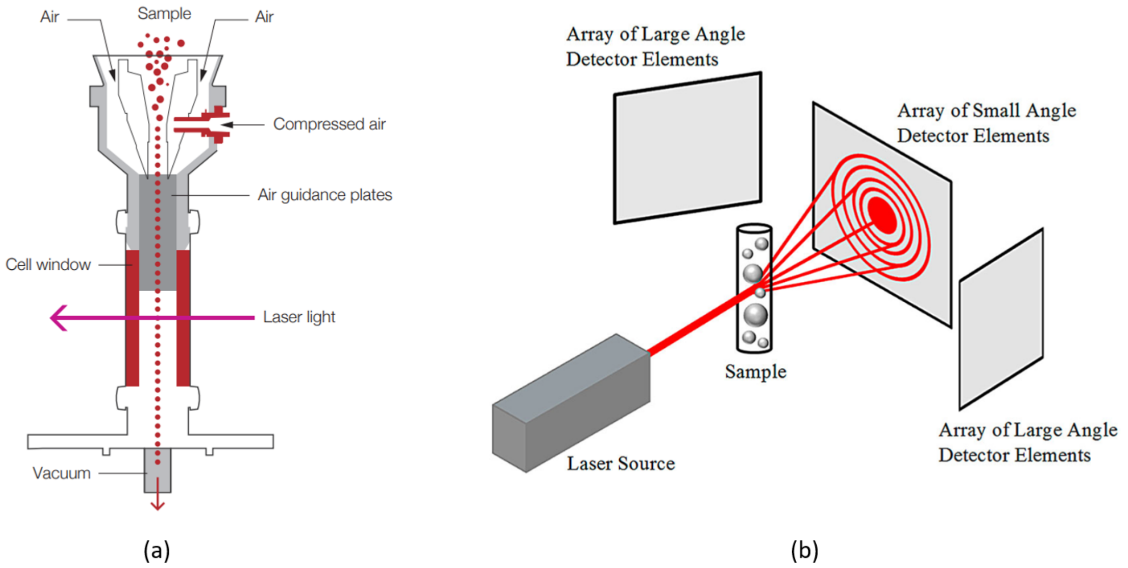

Figure 2.9 – (a) Overall schematization of the dry measurement system of the Horiba Partica LA-950 analyzer [221], (b) Simplified illustration of the laser diffraction principle [69].

In this work, three to five measurements of at least 5000 particles were analyzed per sample. At the end of the measurement, the PSD is defined by the volume frequency or cumulative frequency in function of the diameter, and also by the values of D_{10}, D_{50} and D_{90}, corresponding to the size of the 10th percentile, the median and the 90th percentile respectively.

Microscopy

Optical light microscopy (OM) was used to control visually the morphology of the particles. The ZEISS Axio Imager 2 microscope allowed to autonomously acquire z-stack images, which is necessary for non-planar samples and therefore the observation of powders. OM made it possible to observe the color changes in particles degraded by the L-PBF process, and in particular for the analysis of powder oxidation in furnace which will be detailed in chapter 4.

SEM was also employed to observe the particles morphology, with much higher resolutions than the OM. This enabled the identification of specific particles, and correlations between the two microscopy techniques were carried out to combine the different information.

2.3.2 Flowability

Flowability of a powder refers to its ability to flow freely. This rheology behavior is highly dependent on the particles properties such as the morphology and the surface chemistry. It is difficult to fully understand and predict flowability with one single test, and numerous approaches can be conducted to assess powder flowability. During this PhD thesis, only one standard method, based on the Hall funnel, was employed, for comparison purposes between different states.

To perform flow rate measurements on the powder samples, the following methodology was implemented: 50 g of powder are poured in the Hall funnel, and their descent time is clocked, a lower flow time being an indicator of a better flowability. Tests were conducted according to the ASTM B213-20 norm [222]. Three to five repeatability measurements were carried out on each powder batch. Figure 2.10 illustrates the Hall flowability measurement principle.

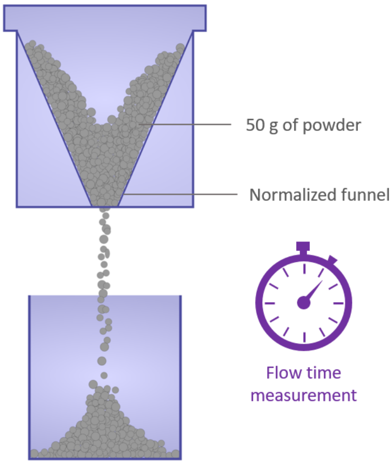

Figure 2.10 – Illustration of the flowability measurement with the Hall flowmeter funnel.

2.3.3 Chemical composition

Spectrometry analysis

Powder chemical composition was analyzed for comparison with the manufacturer data sheet, and to follow the possible changes with intensive powder reuse. This was performed externally by inductively coupled plasma atomic emission spectrometry (ICP-AES) for major elements and by glow discharge mass spectrometry (GD-MS) for traces, with Thermo Fisher Scientific instruments.

Inert gas fusion

Oxygen content and nitrogen content were measured by inert gas fusion, with the Horiba EMGA 820 AC analyzer (figure 2.11 (a)). The powder sample, in an amount of 0.25 g, is placed in a tin capsule, which is itself inserted in a graphite crucible (figure 2.11 (b)). The sample is heated up quickly by a pulse furnace, which applies an electric current to the graphite crucible. The oxygen in the sample reacts with the graphite in the crucible and is released in the form of carbon monoxide or carbon dioxide. These compounds are quantified by a non-dispersive infrared detector (NDIR). Nitrogen is detected by a thermal conductivity detector (TCD). The detected gas are converted into signals allowing to determine the oxygen concentration and nitrogen concentration extracted from the powder particles.

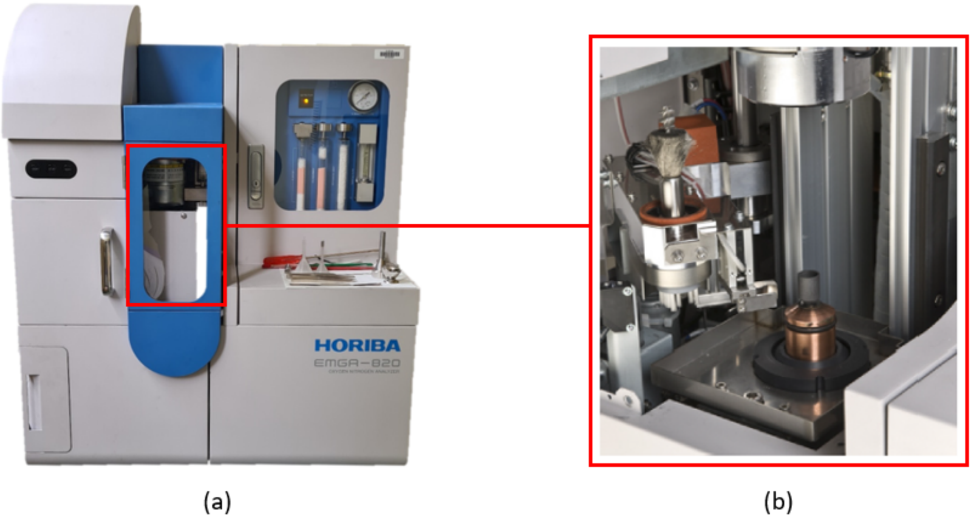

(a) (b)

Figure 2.11 – (a) Horiba EMGA 820 AC analyzer, (b) Chamber of the inert gas fusion analyzer where the sample is placed in the graphite crucible.

This analysis has been extensively employed throughout this PhD thesis, to follow changes in powder oxygen content after multiple L-PBF printing cycles (chapter 3), to implement a powder bed monitoring methodology based on particles color to oxygen content correlations (chapter 4), and to investigate the influence of L-PBF processing parameters on powder degradation (chapter 5). For each condition, three to five repeatability measurements were conducted.

EDX

X-ray energy spectra using energy dispersive spectroscopy (EDS), presented in section 2.2.2, was also used to assess the chemical composition of powder particles. EDS mappings and point analyses allowed to identify selective segregation of elements on the surface of some specific particles.

2.4 Parts characterization techniques

The characterization techniques used specificaly for the elaborated part, in addition to the previously described microstructural characterization techniques (section 2.2), are presented in this part. Some of the following methods require prior metallographic preparation of the samples as detailed in subsection 2.2.1.

2.4.1 Density analysis

Archimedes method

The density measurements of the as-build samples were first carried out with the Archimedes method. This method is based on hydrostatic weighing, with the measurement of the sample mass in the air and then in a fluid. The figure 2.12 illustrate the process of Archimedes double weighing. The density of the sample ρ_{sample} can be calculated according to the Eq 2.2 [223]:

$$\rho_{sample} = \frac{m_{air}}{m_{air} - m_{fluid}} \rho_{fluid} \tag{2.2}$$

where ρ_{fluid} is the density of the fluid, which depends on the temperature, m_{air} is the mass of the sample in air and m_{fluid} is the mass of the sample in the fluid.

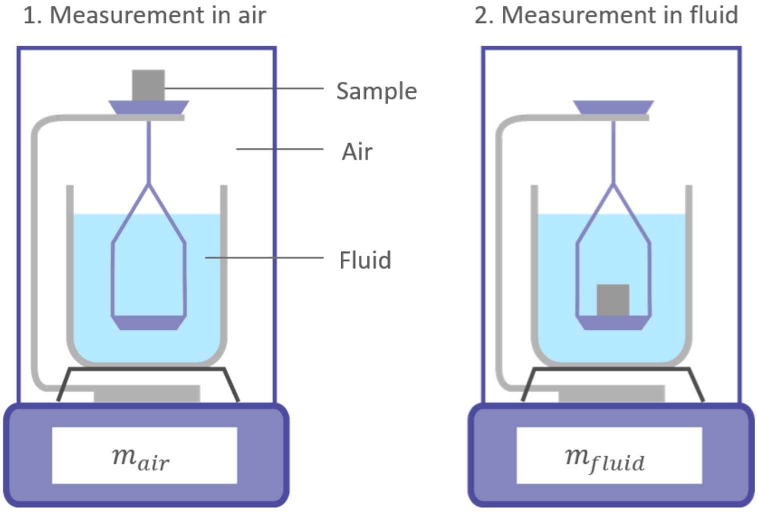

Figure 2.12 – Illustration of Archimedes method density measurement.

Archimedes method is not necessarily the most accurate, with density variations that can be significant for small mass variations especially on small size samples, however it stands out for its simplicity and the advantage of analyzing the entire sample, which has made it become one of the standards for density measurement.

Cubic specimens were manufactured for the density analyses. Each sample was measured independently three times in air and water, using of an electronic balance with an accuracy of 0.1 mg. The density values (in g.cm^{-3}) were compared to the theoretical value of 7.99 g.cm^{-3} for SS316L to obtain a relative density (in %) and be able to compare the results to those obtained by other methods that will be presented next.

Metallographic observation

Metallographic observation was also conducted to evaluate the printed parts density. After sample cutting and preparation according to the methodology described in section 2.2.1, micrographs of cross sections were acquired. For each cross section, an assembly of images with a magnification of 50× was obtained by OM, allowing to capture the entire sample surface (100 mm^2) with a high enough resolution to detect small porosities (pixel size of 1.094 µm). The images were analyzed and binarized using ImageJ software to determine the porosity rate.

First, the image is transformed to gray scale with a conversion into an 8-bit image. Then, a tresholding operation is applied to binarize the picture into black and white, in order to identify the pores (black pixels) and the dense material (white pixels). Similar light acquisition conditions on the optical microscope and tresholding value were applied to all the samples. Potential scratches or stains that can appear during the sample polishing can be deleted with the tresholding due to contrast differences, or are removed manually using the brush tool. Figure 2.13 shows an example of image binarization using ImageJ.

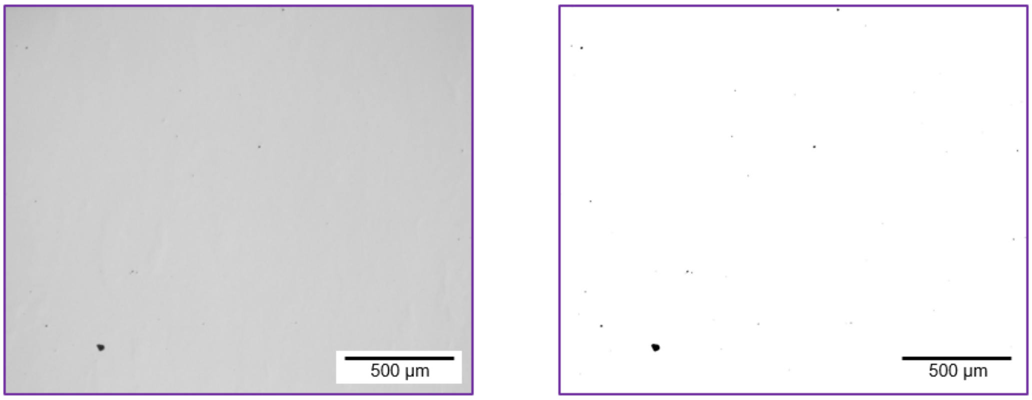

Figure 2.13 – Optical micrograph and its corresponding binarized image for density analysis.

The porosity rate is calculated as the ratio between the number of black pixels and the total number of pixels. This method also allows to get additional information such as the number of pores, the characteristics of each pore, their size, their circularity, which is interesting to identify the kind of pores present in the material (lack of fusion, entrapped gas or keyhole pores). On the other hand, metallographic observation only assess 2D slices and therefore does not take into account the entire sample volume.

X-ray computed tomography

A third method was used to detect part porosity. X-ray Computed Tomography (CT) is a non-destructive measuring technique for the detection of internal porosity within the entire part volume. A CT scan consists of the acquisition of multiple 2D X-ray projections at various angles. The 3D sample is reconstructed in voxels (volumetric pixels) with the assembly of these projections.

The X-ray CT was performed externally, using the GERIM2 scan platform of the CEA-List, leading to data with a voxel size of 16 × 16 × 16 µm^3. Analysis of the porosity was conducted on the Volume Graphics VGStudioMax 3.2 software. The analysis of the SS316L cubic specimens (1 cm^3) was difficult because of the material's density which attenuates the x-rays, leading to a non optimal contrast. To overcome this, the samples were also cut in 4 pieces which consequently reduces the thickness of the samples.

2.4.2 Mechanical properties

Microhardness

Microhardness measurements were implemented on the polished cross sections of cubic parts using the Vickers hardness (HV) test. In this technique, a diamond square base pyramid indenter with a 136° angle between opposite faces is applied with a defined load on the sample surface. This will result in an indentation of a surface area which depends on the material's resistance to local plastic deformation. A measure of the diagonals of the mark left on the sample allows to calculate the corresponding harness HV according to the following equation (2.3):

$$HV = \frac{2\,F\,sin(136/2)}{d^2} \tag{2.3}$$

with F the applied force and d the average length of the two diagonals of the mark left by the indenter.

Figure 2.14 represents the Vickers hardness test principle, with the determination of the two diagonals after indentation. In this work, the values were acquired autonomously with a Struers DuraScan 70 system. For each sample, 15 measurements were taken at various location along a diagonal of the cross section, under a load of 1 kg.

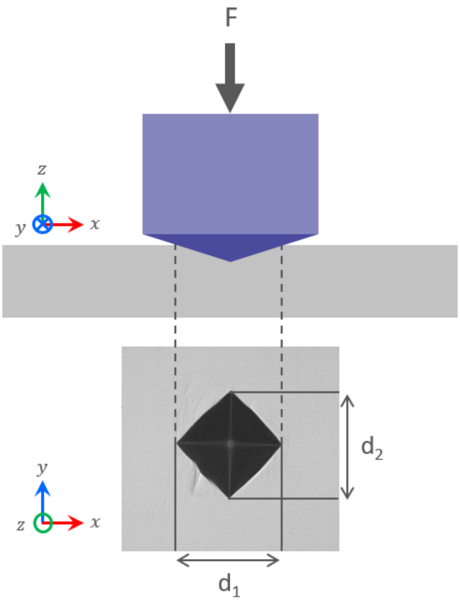

Figure 2.14 – Vickers Hardness test principle.

Tensile testing

Tensile testing is a simple and effective way to evaluate the static mechanical properties of the parts elaborated by L-PBF. Horizontal cylindrical samples (⌀10 mm × 40 mm) were printed and machined into cylindrical tensile specimens. The specimen dimensions are presented in figure 2.15 (a) and were determined according to the ISO 6892-1 standards [224].

Three uniaxial tensile tests per condition were conducted with a MTS Criterion 43 electromechanical system (figure 2.15 (b)). Tests were performed at room temperature, at a displacement-controlled loading rate of 1 mm/min. Due to the small size of the specimens, the use of an extensometer was not possible, and the stress-strain plots took into account the displacement of the crossbeam. The values obtained are those commonly determined by this method, *i.e.* the yield strength (YS), the ultimate tensile strength (UTS) and the elongation at break.

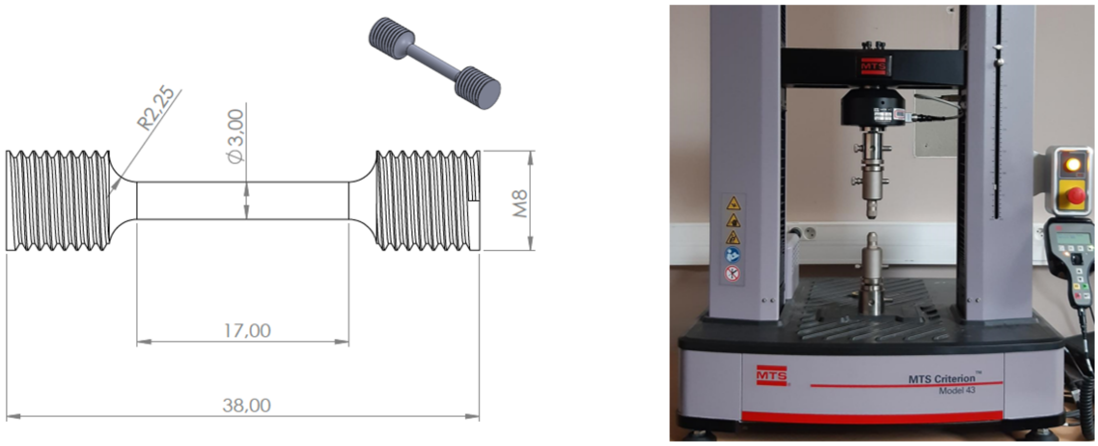

(a) (b)

Figure 2.15 – (a) Schematic of tensile specimens dimensions (in mm), (b) MTS Criterion 43 test system.

2.4.3 Surface characterization

Surface roughness

3D optical profilometry was implemented to assess the surface roughness and topography of printed specimens. This measurement technique is fast and contactless with the acquisition of an image and analysis of the entire observed surface. In this work, a Bruker ContourGT-K optical profiler was used (figure 2.16), combined with Vision64 software.

Figure 2.16 – Bruker ContourGT optical profiler.

Coherence scanning interferometry technique is employed in this system, using white light to achieve interference fringe localization. Interference between the measurement beam reflected off the sample surface and a reference beam which is reflected off an extremely flat reference mirror inside the objective allows the calculation of surface height.

Measurements of areal average surface roughness Sa (in µm) were carried out on the side surfaces of printed parts (xz or yz plane, see figure 2.6), on three different regions with the dimensions of 1255 µm × 941 µm. This system allows to draw height maps of the analyzed surfaces to illustrate the results.

2.5 Powder bed monitoring setup

This section presents the powder bed scanning set-up used to monitor powder beds. The development of the monitoring methodology, based on the oxidation of the powder particles will be detailed in chapter 4.

2.5.1 Scanner setup

A customizable L-PBF test bench from the Processes and Engineering in Mechanics and Materials laboratory (PIMM-ENSAM) was used to implement a powder bed scanning system. The latter is based on the work of Pedersen et al. [213] and Le and Seita [215], with the integration of a scanner into the spreading unit of the machine. The schematic of the powder bed scanning setup is illustrated in figure 2.17. A 210 mm wide contact image sensor taken from a Canon Cano LiDE 220 flatbed scanner was mounted on two micrometric positioning tables that allow height adjustement and a slight correction of the inclination. The whole was assembled on the recoater arm of the L-PBF machine, which is controlled by an Aerotech servomotor. Figure 2.18 (a) and (b) shows pictures of the experimental setup, taken from the back and front of the machine respectively. The large blue arm is the recoater unit, and the scanner is mounted on the white 3D printed plastic support, itself fixed on the recoater arm.

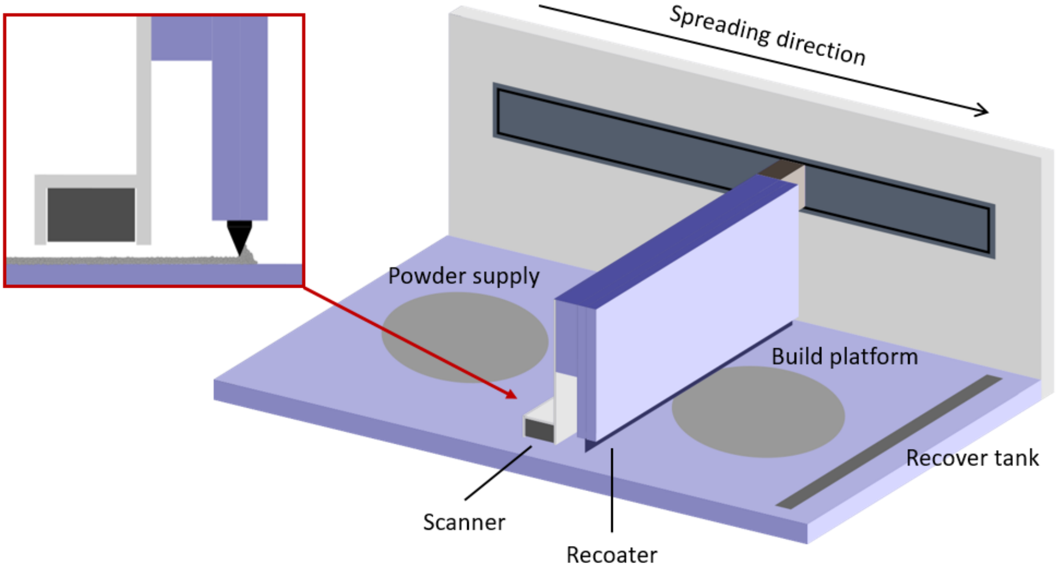

Figure 2.17 – Schematic of the powder bed scanning setup.

This system allowed to acquire colored scans of the entire powder bed area (⌀150 mm) with a resolution up to 4800 dpi (dots per inch). The commercial software of the flatbed scanner, Canon ScanGear, was used to control the scan acquisition and compilation of the raw images. A sensor was installed in the build chamber to enable the scanner positioning detection during the recoater advance and therefore initiate the scan acquisition.

Speed calibration was performed to avoid any image distortion, by matching the recoater arm speed to the image acquisition rate of the scanner. This calibration was conducted by iteration, with the scanning of the build plate, which is circular, the analysis of the image, and the adjustment of the motion speed of the arm comprising the recoater and the scanner. The circularity of the substrate on the acquired scans was analyzed using ImageJ software and the speed was increased or decreased based on weather the plate appeared elongated or flattened.

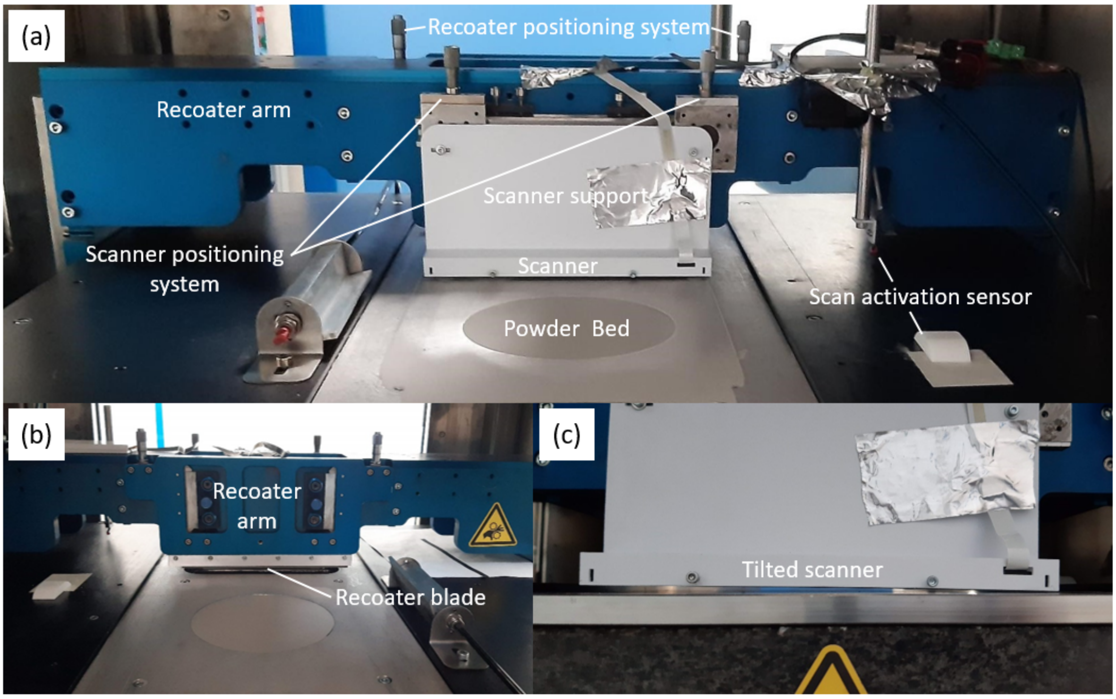

Figure 2.18 – Experimental setup: (a) Back view, (b) Front view, and (c) Focus calibration of the scanner.

Focus calibration was also carried out, with adjustments of the scanner inclination. Using the micrometer positioning stages, defined tilts were imposed to the contact image sensor unit with regard to machine frame, as showed in figure 2.18 (c), in order to find the focal height.

2.5.2 Powder bed scans acquisition

Different resolutions can be chosen for the scan acquisition, which consequently impacts the time of acquisition and required motion speed of the scanner, as well as the size of the acquired image. Speed calibrations were performed for all resolutions of colored scans. Table 2.2 summarizes the spatial resolutions, scanning speed and time, and image size for the different acquisition settings.

The colored scans at 4800 dpi allow for an individual powder particles resolution, with a pixel size of 5.3 µm × 5.3 µm. However, this results in an extremely slow scanning speed that is not representative of spreading speeds used in L-PBF processing. Therefore, powder layers were spread at a more common velocity of 50 mm/s, and the powder bed scans were captured at 0.16 mm/s on the way back.

Table 2.2 – Resolutions, scanning speed and time, and image size for different colored image acquisition settings.

Resolution (dpi)	Spatial resolution (µm)	Scanned area (mm)	Scanning speed (mm/s)	Scanning time (s)	Image size (MB)
600	42.3 × 42.3	210 × 165	10	17	58
1200	21.2 × 21.2	210 × 165	2.52	65	233
2400	10.6 × 10.6	210 × 165	0.64	258	932
4800	5.3 × 5.3	210 × 165	0.16	1031	3729

Figure 2.19 shows an example of a powder bed scan displaying the entire build platform. Digital zooms of the raw image, acquired at 4800 dpi, highlight the high spatial resolution of this configuration. Variations in particles color can be observed, with the presence of oxidized particles in orange-brown and blue. Raw data automatically pre-processed by the Canon ScanGeer software (contrast, brightness) did not undergo any post processing and were used as such for the image exploitation and development of powder bed monitoring. Image analysis based on color analysis was carried out using ImageJ software and Python programming, and will be detailed in chapter 4.

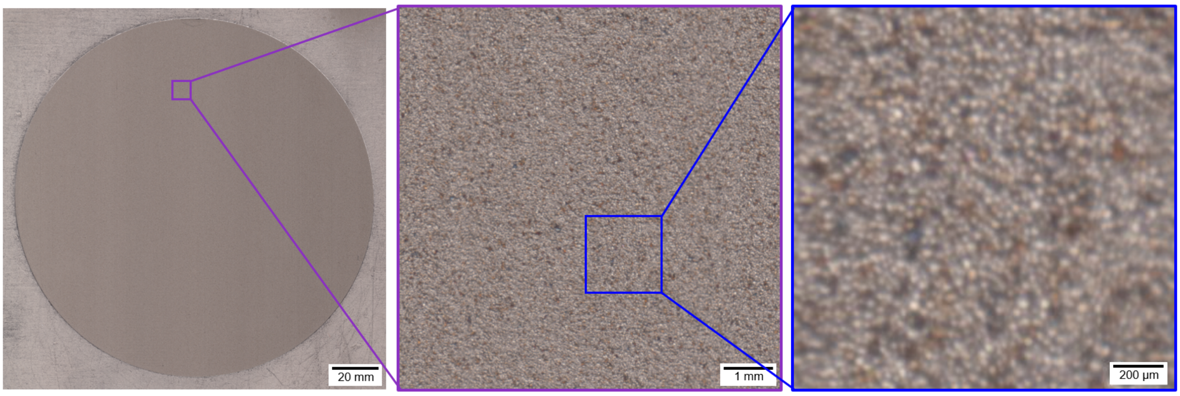

Figure 2.19 – Powder bed scan of recycled powder at 4800 dpi with digital zooms of the raw image.

Chapter 3

Investigation of powder recycling in L-PBF

Published paper associated to this chapter:

T. Delacroix, F. Lomello, F. Schuster, H. Maskrot, and J.-P. Garandet, "Influence of powder recycling on 316L stainless steel feedstocks and printed parts in laser powder bed fusion," *Additive Manufacturing*, vol. 50, p. 102553, Feb. 2022.

3.1 Introduction

The state of the art helped to identify the challenges of the L-PBF process. This complex technology involves many factors influencing the quality of the manufactured parts. Many efforts have been focused on the optimization of the process parameters, such as the laser power, scanning speed, hatch distance, layer thickness or scanning strategy, which directly affect the printed material properties. The effect of the raw material characteristics, *i.e.* the metallic powders, is also an important consideration in order to produce reliable parts and improve the process repeatability. In addition, one of the main advantages of L-PBF and AM in general compared to the conventional processes is the strict addition of material needed to manufactured the parts, which consequently reduces waste. During the L-PBF process, only a small fraction of the powder bed is solidified as part, and cost and material yield strongly depend on the ability to reuse powder efficiently. Powder leftover properties may deviate from those of the virgin material after being exposed to the L-PBF environment. The reuse of the powder can also lead to a deterioration of the final components properties.

Understanding the impact of powder recycling on both powders and printed parts is essential. Among the recycling studies found in the literature, some trends emerge but not all of them reach the same conclusions, especially concerning the influence on the final parts properties. Moreover, a number of studies only focused on the comparison between the virgin condition and a recycled state. The purpose of this chapter is to assess both the powder feedstock degradation and the effect on printed specimens throughout multiple powder reuse. One batch of SS316L powder was used, recovered and reused to produce 15 successive L-PBF prints without addition of virgin powder. Recycled powders were characterized throughout each iteration to investigate changes in particles morphology, rheology, crystal structure and chemical composition. Solidified specimens features such as density, oxygen content, microstructure, and mechanical properties were also examined.

3.2 Powder recycling study methodology

3.2.1 Feedstock material

Gas-atomized AISI 316L powder manufactured by Oerlikon Metco Europe GmbH was used for this work. The powder is mostly spherical, with a particle size distribution of 20 - 45 µm. Figure 3.1 shows two SEM images of the powder, in SE and BSE mode, both at a magnification of 300×. The chemical composition of the powder is reported in table 3.1. The observed composition fits within the range of the ASTM F3184 norm [43] for stainless steel 316L presented in table 1.1 in chapter 1.

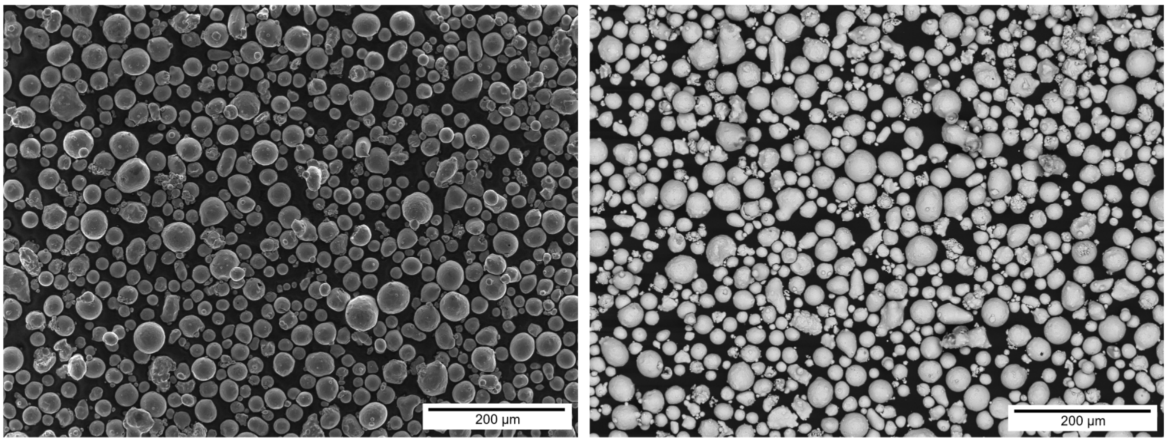

Figure 3.1 – SEM images of the SS316L powder at 300× magnification.

Table 3.1 – Chemical composition of the SS316L powder (wt%).

Element	Fe	Cr	Ni	Mn	Mo	Si	N	C	P	S	O
wt.%.	Bal.	17.5	12.6	1.5	2.4	0.04	0.1	0.02	0.002	0.001	0.048

Further methods of characterization were implemented on the virgin powder and will be presented in section 3.3 as part of the comparison between the different recycling states.

3.2.2 Powder recycling methodology

Figure 3.2 illustrates the approach used to study the influence of powder recycling on the feedstock and elaborated parts. Starting with a virgin powder batch called R0, an L-PBF print is conducted on the Trumpf TruPrint 1000 machine. At the end of the process, on the one hand the printed parts (named R0) are cut and collected from the substrate plate for characterization regarding numerous aspects. On the other hand, the un-melted powder is recovered from the build plate and the overflow tank, sieved using a 50 µm screen, and is now called R_1 (or R_{n+1} at later stages). A small sample is collected for ex-situ characterization, and all the remaining powder is then re-introduced in the Trumpf machine for a new fabrication. 15 printing cycles followed this loop, without addition of any virgin powder during the successive productions.

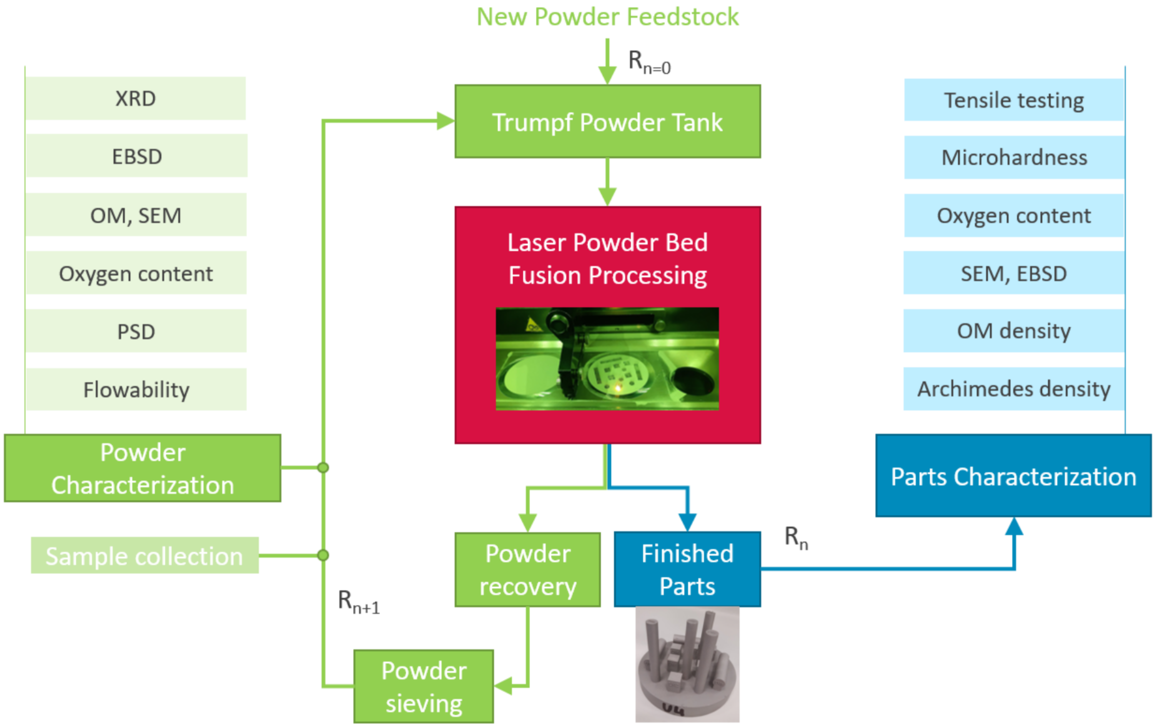

Figure 3.2 – Chart of the powder recycling methodology.

Each of the fabrications was composed of fixed parts of interest for the several characterizations, *i.e.* 6 cubic samples (10 × 10 × 10 mm^3) for density analysis, microstructure investigation and microhardness testing, and 3 horizontally build cylindrical specimens (⌀10 mm × 40 mm) for tensile testing. In addition, 4 vertically built cylinders were printed per iteration, whose height was dependent on the amount of remaining powder. These cylinders were used to fill the powder tank to the maximum at the beginning of the study and to ensure that the whole powder set was subjected to L-PBF processing at each iteration. They controlled the height of the fabrications, which was consequently decreased after each powder recycling as less powder was available after parts solidification, powder sieving and powder sample collection. As a result, the fraction of melted volume in the build area increased gradually with powder reuse, going from 6% to 22%.

Figure 3.3 shows a few examples of build plates with the R0, R4, R9 and R14 prints, corresponding to the 1st, 5th, 10th and 15th manufacturing respectively.

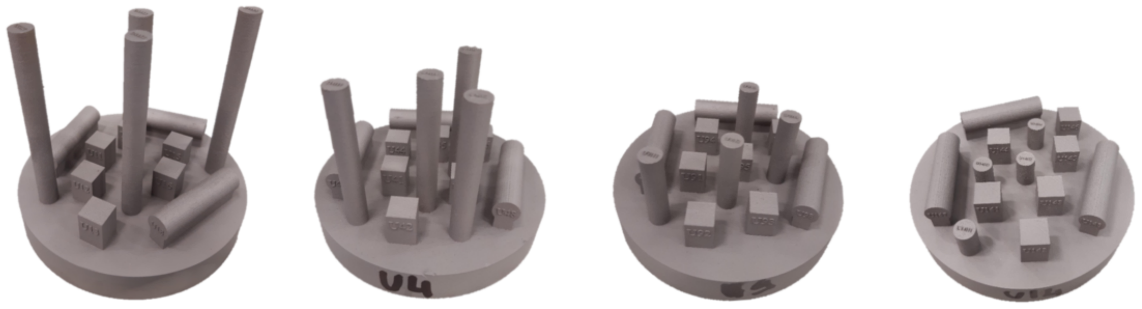
R0 (print 1)   R4 (print 5)   R9 (print 10)   R14 (print 15)

Figure 3.3 – Build plates of R0, R4, R9 and R14 prints.

The decrease of fabrication height can be observed on the reduced vertically printed cylinders. Figure 3.4 provides a graphical representation of this fabrication height as a function of the printing cycles.

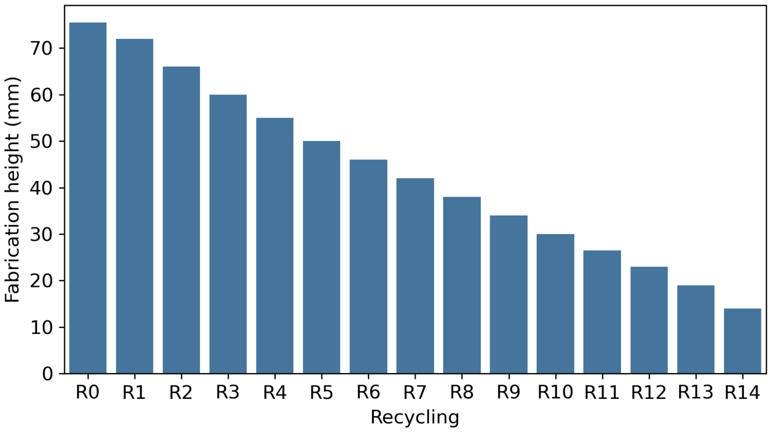

Figure 3.4 – Evolution of fabrication height as a function of recycling.

Powder samples and parts collected after each L-PBF cycle were characterized, and the influence of this successive powder reuse is presented in the following.

3.3 Influence of powder recycling on the feedstock attributes

A total of 16 powder samples were characterized to investigate the influence of powder recycling on the feedstock attributes, starting with virgin powder (R0, inserted in the machine for the first print) and ending at R15, *i.e.* the powder collected and sieved after the R14 print (15th print). In addition, sieved residues were also analyzed to assess the attributes of particles discarded by this step, and will be presented in subsection 3.3.6.

3.3.1 Morphology

Particles size distribution

Particle size distributions (PSD) were analyzed by laser granulometry. Figure 3.5 (a) presents the cumulative PSD (in volume) of powders collected after each L-PBF processing and sieved through a 50 µm mesh. It can be observed that particles tend to become larger with recycling, despite the fact that the sieving step should have removed the really large particles. It is nonetheless possible that some large and irregular shaped particles, with a high aspect ratio, can pass through the mesh in one direction. It can be noted that the powder used in this work does not really contain fine particles, with diameters smaller than 10 µm. Therefore, the significant decrease of fine particles that has been reported by other authors [137,140,150] is not as pronounced in this case.

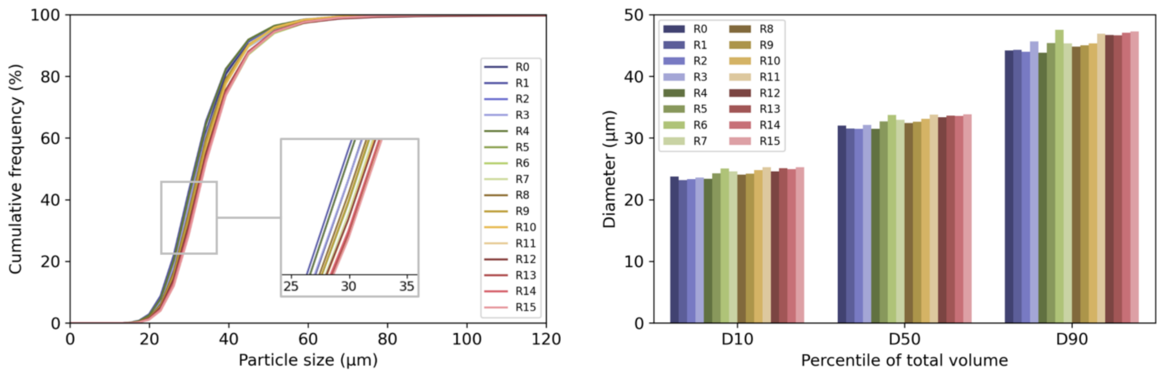

(a) (b)

Figure 3.5 – (a) Cumulative particle size distributions of powders at each recycling state, (b) D_{10}, D_{50} and D_{90} of the powders.

Figure 3.5 (b) shows the D_{10}, D_{50} and D_{90} of the SS316L powders of all recycling states. These characteristic values are nevertheless slightly increasing with multiple powder reuse. Different reasons can be considered to explain this increase in particles size. First, the complex laser-material interactions of this manufacturing process lead to the ejection of molten metal as spatter, and the latter can fall back in the powder bed in a semi-liquid state. This can lead to the sintering of small powder particles to the large ejecta, and these agglomerates are then discarded by the sieving process, thereby reducing the number of small particles. Figure 3.6 is an SEM image of an agglomerate removed by sieving, composed of a large spatter and numerous as-virgin small particles attached as satellites.

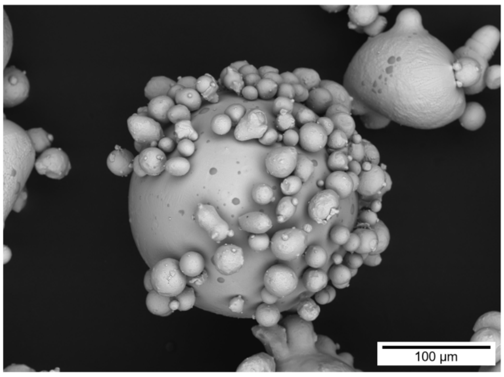

Figure 3.6 – SEM image of an agglomerate composed of a large spatter with numerous small particles sintered as satellites.

Another explanation for the increased size could be mechanical, due to the fact that the powder layer thickness was set to 30 µm. Smaller particles are preferentially deposited on the build platform and solidified as parts. On the other hand, particles larger than the layer thickness might be dragged past the platform and directly end up in the powder recovery tank [87, 88]. After several powder reuse, the feedstock becomes mainly composed of the largest particles.

In order to ensure a total coverage of the powder bed during L-PBF, a powder dosage of mbox200 % is fixed on the Trumpf TruPrint 1000 machine. This means that for each slice, when the build plate is lowered by one layer, the powder supply cylinder is raised by 2, to be certain to have a sufficient amount of powder spread, especially on the edges of the platform. This configuration can accentuate the phenomenon described above, with significant quantities of powders going directly into the overflow bin.

Particles shape

Powder shape is also affected by the repeated L-PBF processing. Backscattered electron micrographs of the virgin powder (R0) and most recycled state (R15) are displayed in figure 3.7. Light optical images of the virgin powder and the sieved powder after 5, 10 and 15 prints are shown in figure 3.8.

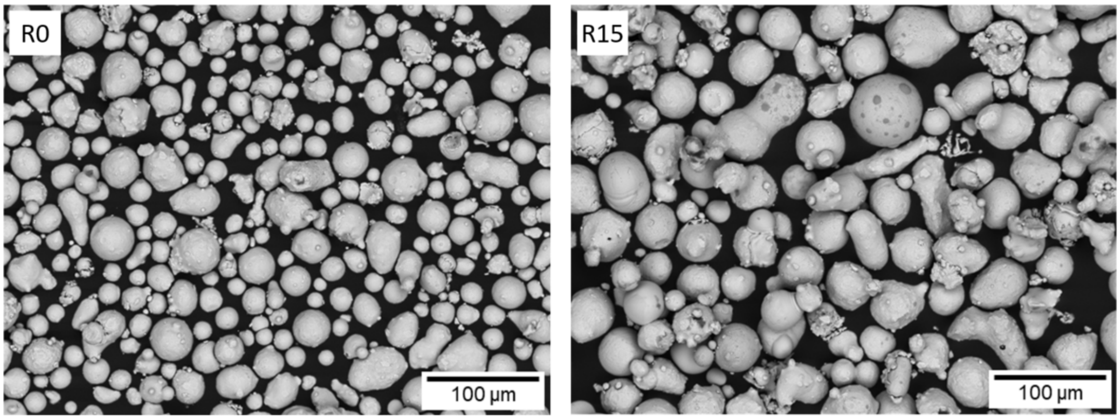

Figure 3.7 – SEM micrographs of R0 and R15 powders at 500× magnification.

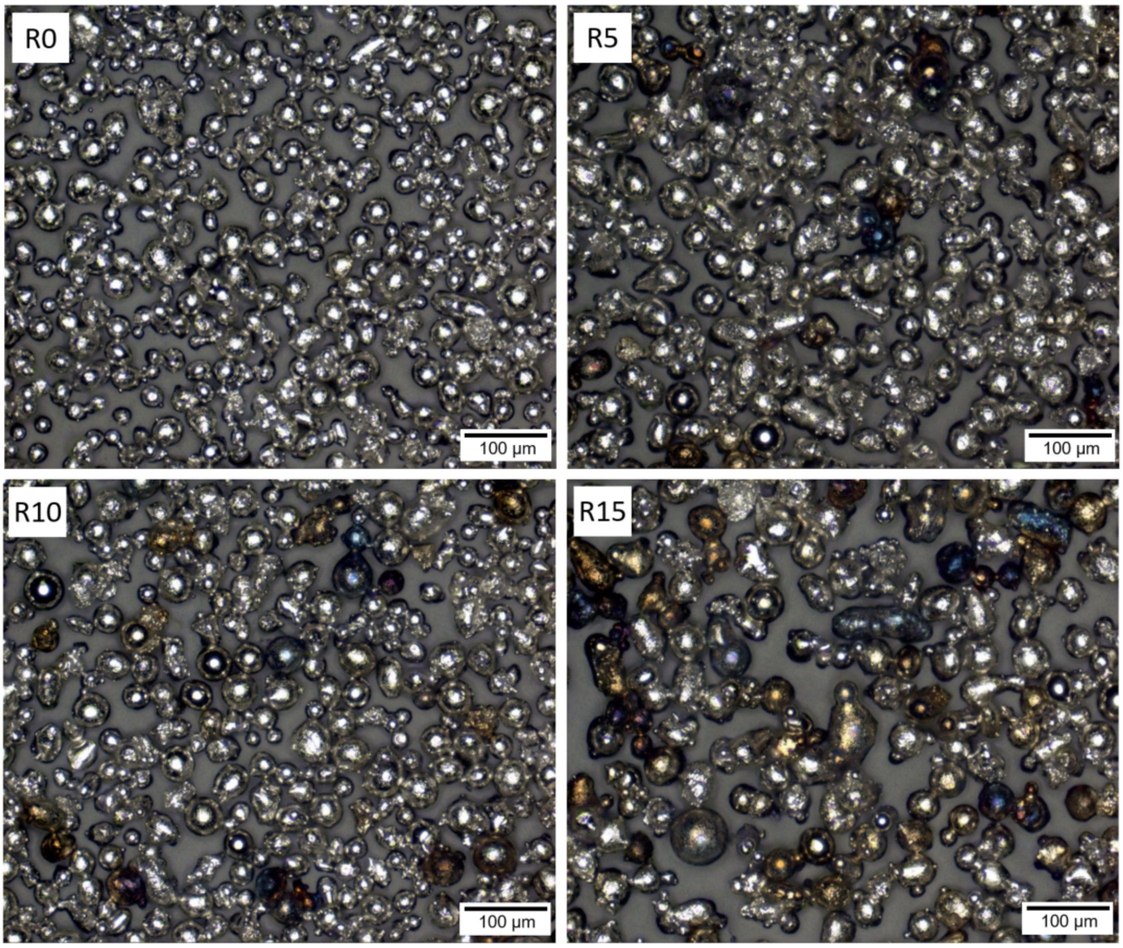

Figure 3.8 – Optical images of R0, R5, R10 and R15 powders at 200× magnification.

Particles tend to be less spherical with powder reuse. A number agglomerates, elongated and irregularly shaped particles are visible both by OM and SEM. A few really smooth and spherical particles are still noticeable. It can be observed as well that colored particles are visible in the recycled samples. These particles do not seem to have a particular morphology related to this color change, with both irregular shaped and spherical particles presenting yellow-brown, violet or blue colors.

3.3.2 Flowability

Particles size and shape are well known to influence the powder rheology behavior [74]. Flowability tests were conducted using the Hall flowmeter funnel. Flow times for 50 g of powder through the Hall funnel of each sample collected and sieved after each printing cycle are shown in figure 3.9. The flow times are decreasing, which means that the flowability of the feedstock is increasing with successive recycling.

This improved flowability is in accordance with the decrease of the number of smaller particles, as it was found by other authors on various materials [140, 149, 151]. Smaller amounts of fine particles result in reduction in inter-particles interactions and frictions.

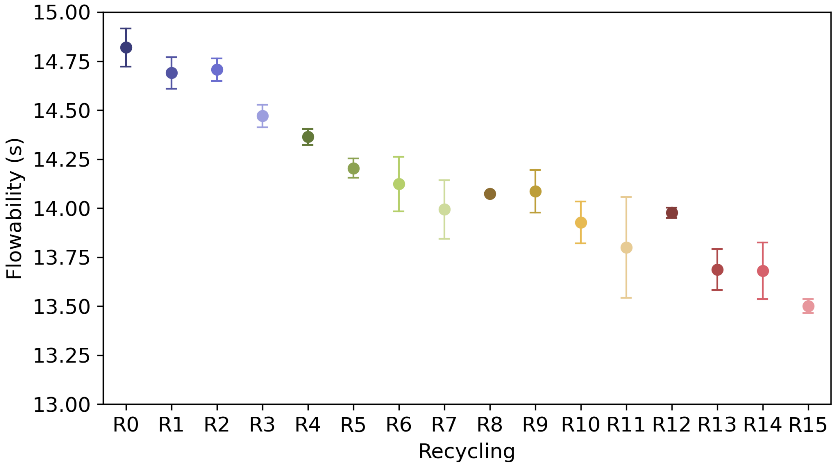

Figure 3.9 – Powders flow time through Hall flowmeter funnel in function of recycling.

In addition to the shift of PSD toward larger values, another reason for the shorter flow times of reused powders could be the presence of oxides on the surface of some particles, as observed in figure 3.8. Following the statement of Sutton et al. [140], oxides on metals can reduce adhesion and increase powder flowability, with less friction and surface energy at the contact between particles.

In this study, the dominant mechanism responsible for the increased powder flowability could be the accumulation of colored oxidized particles. Indeed, although the average diameter of the particles is increasing with recycling, as do the D_{10}, D_{50} and D_{90} values, the size of the 10th percentile of the virgin powder is already quite high (> 20 µm). As mentioned earlier, the decrease of really fine particles is therefore not as pronounced.

In any case, these two effects combined seem to have a significant influence on the powder flow behavior, being able to counteract the damaging effect of irregularly shaped particles, known to degrade the flowability [74].

3.3.3 Chemical composition - Oxygen content

The chemical composition of the virgin powder (R0) and the highly recycled state (R15) was assessed by ICP-AES, GD-MS and inert gas fusion. No significant difference was found as th variations remained within the measurements uncertainties, expect for the oxygen concentration. In any case, the observed chemical compositions remain well within the alloy-specific composition [43], as shown in table 3.2.

Table 3.2 – Chemical composition of the virgin (R0) and highly recycled powder (R15), compared to the ASTM F3184 requirements for 316L stainless steel in AM (in wt.%).

Element	Fe	Cr	Ni	Mn	Mo	Si	C	P	S
R0 powder	Bal.	17.5	12.6	1.5	2.4	0.04	0.02	0.002	0.001
R15 powder	Bal.	18	12.7	1.5	2.2	0.044	0.02	0.002	0.001
ASTM F3184	Bal.	16-18	10-14	< 2	2-3	< 1	< 0.03	< 0.045	< 0.03

Figure 3.10 presents the variation of oxygen content in the powder with successive L-PBF powder recycling. There is a gradual increase of oxygen content throughout the 15 cycles, going from 454 wppm for the virgin state to 665 wppm at the end of the study. The concentrations remain within acceptable range, but could still have a detrimental effect on the elaborated parts.

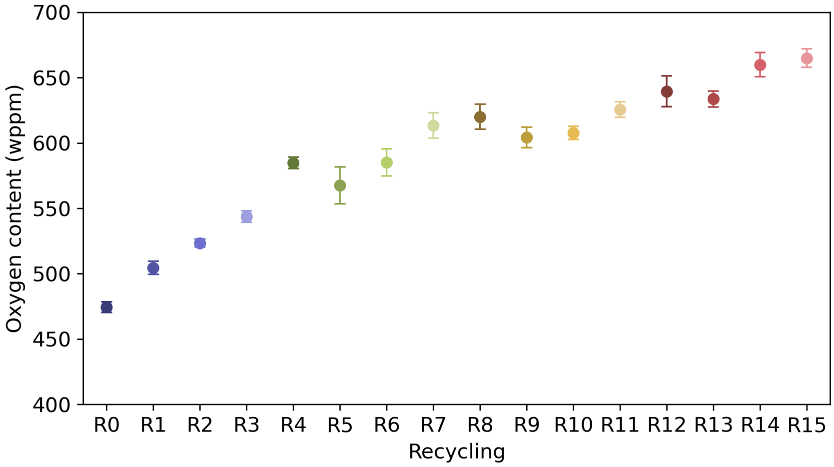

Figure 3.10 – Oxygen content of the powder with recycling.

3.3.4 Altered particles

Colored particles

Our opinion is that the measured oxygen pickup can be related to the colored particles present in the recycled feedstocks (figure 3.11). Different colors can be observed on oxidized particles due to different oxide film thicknesses (and therefore oxygen content). The oxide films display interference colors with exposition to white light. No size effect was observed regarding the coloration of these particles.

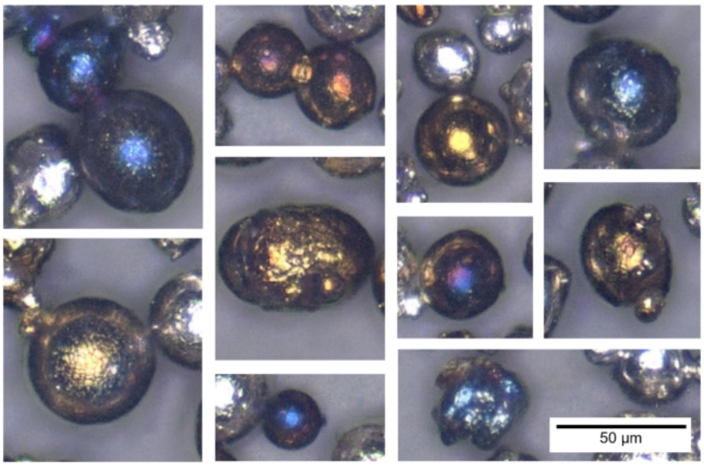

Figure 3.11 – Examples of different colored particles found in the recycled powder samples captured by OM.

It can be assumed this *coloration* oxidation happens for particles laying in the near vicinity of laser tracks and solidified parts, where heat transfer induces a significant temperature increase and possibly for a long period of time. Indeed, the overall temperature of the printed parts is gradually increasing with periodic heating by the laser melting of the top layer [225] and powder particles in the HAZ near the consolidated material can be affected, as schematized in figure 3.12.

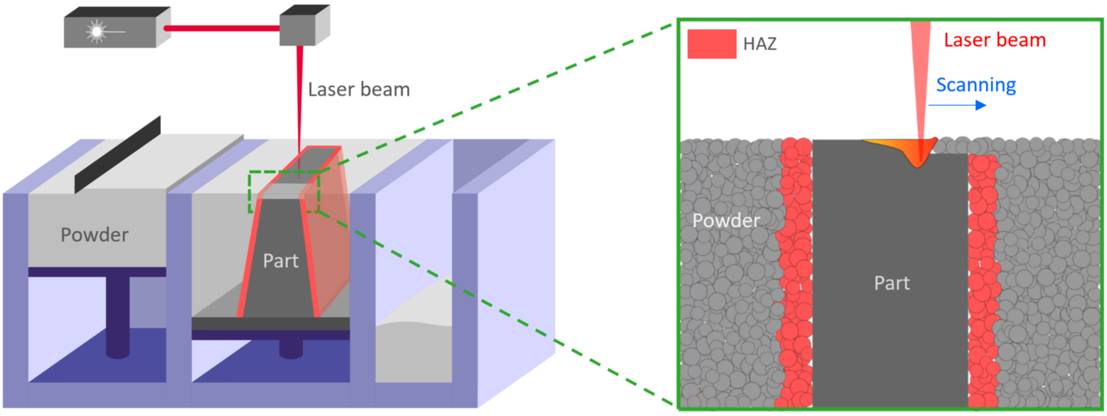

Figure 3.12 – Schematic diagram of the heat affected powder near the vicinity of the solidified parts during the L-PBF process.

Partially oxidized particles

Other kind of oxygen-affected particles were identified by SEM in the recycled powder samples. These particles, such as the one highlighted in figure 3.13, present oxide nodules on their surface.

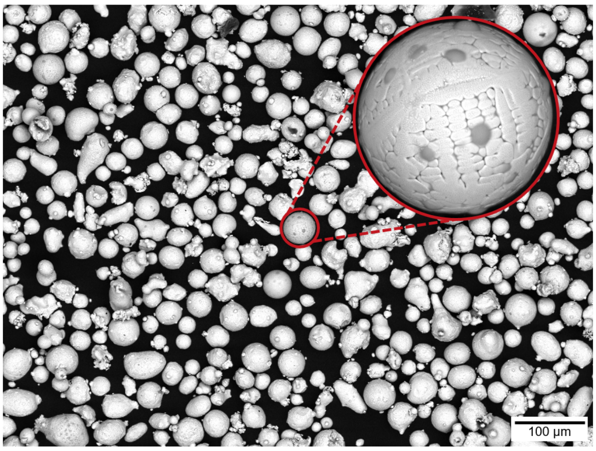

Figure 3.13 – SEM image of R10 powder highlighting the presence of a partially oxidized particle.

EDS mappings were performed and show that the nodules are Mn and Si rich oxides, as presented in figure 3.14. Similar selective oxidation was found in the sieved residues on large ejecta, and by different authors who studied stainless steels spatter [129,137,145,164,165]. The selective oxidation can be attributed to the limited O_2 in the build chamber being captured by the stronger reductants such as Si or Mn with high affinity to oxygen [226]. Such elements also have a greater volatility compared to Fe and Cr, which can result in an increased diffusion toward the particle surface [129].

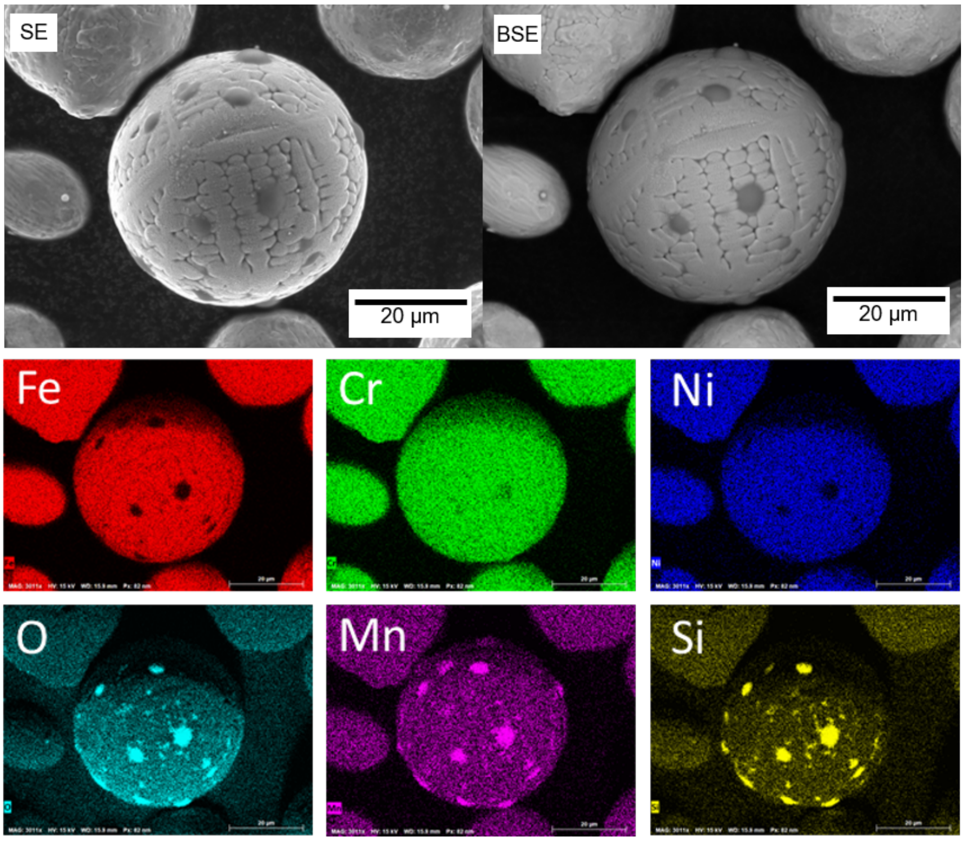

Figure 3.14 – Secondary Electrons and Backscattered Electrons images and EDS maps of a partially oxidized particle in the recycled powder.

Selective oxidation was found in abundance in the sieved residues on large particles (> 100 µm). However, the present study shows that some of the partially oxidized particles are small enough to pass through the sieving mesh of 50 µm, with sizes comparable to the virgin powder. They were observed in all the collected and sieved recycled powder samples, even after only one L-PBF print.

It can be assumed that these small partially oxidized particles could be vapor-entrained powder, *i.e.* virgin particles from the surrounding of the melt pool that are entrained with sufficient momentum by the vaporization flux to pass through the laser beam, melt partially or fully, but in all case are exposed to sufficiently high temperature to oxidize in flight [109]. Oxides are in a form of nodules or islands and do not form a continuous film on the particles surface. This can be explained by the high cooling rates of such particles, with limited time at high temperature during their flight from the surroundings of the melt pool. This does not give enough time to nodules to coalesce and form a continuous film [145, 227]. Figure 3.15 shows a particle with oxide nodules of one or a few microns and sub-micron islands showing the initial nucleation stage of oxidation. It can be presumed that with longer time before solidification and/or with more abundant oxygen concentration in the chamber, those nano-islands would have coalesced into larger nodules to finally merge into a continuous oxide film.

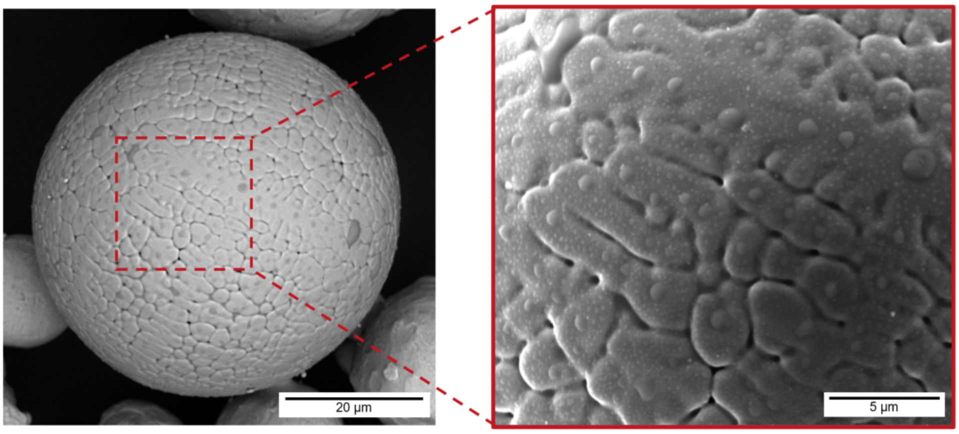

Figure 3.15 – SEM image of a partially oxidized particle displaying micrometric oxide nodules, with a close-up view highlighting these nodules surrounded by nanometric island oxides.

Correlations between SEM and OM were conducted to observe the visual colors of the particles identified with oxide nodules. Some of the latter also present a coloration oxidation in addition to the oxide nodules. In fact, most of the ejecta identified in the samples collected after numerous printing cycles (10 - 15) and observed by OM are colored. On the other hand, partially oxidized particles found in the R1 powder seem to only or almost only present the classical gray color, typical of the virgin SS316L powder. This could mean that the particles may have partially oxidized in flight during one L-PBF processing, and then with multiple reuse, were heated and colored-oxidized while being in the HAZ (figure 3.12) during following fabrications. Different partially oxidized particles, captured by both OM and SEM are shown in figure 3.16. The three particles present a selective oxidation of Mn and Si, with oxide nodules identified by EDS, but have different surface coloration. It is important to note that most of the colored particles observed in the recycled feedstocks do not present oxide nodules.

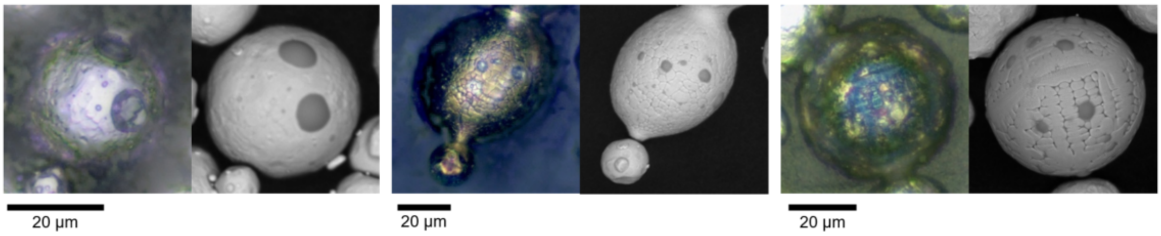

Figure 3.16 – OM - SEM images correlations of partially oxidized particles found in the recycled powder.

Magnetic particles

Another kind of altered particles has been identified, firstly by OM. Extremely bright, smooth and spherical particles are noticeable in the reused powder samples (figure 3.17; the very bright circular area on the zoom view of the particle is the reflection of the incident light from the OM). These particles were found to be magnetic, therefore it was possible to extract them with a standard magnet for specific analysis.

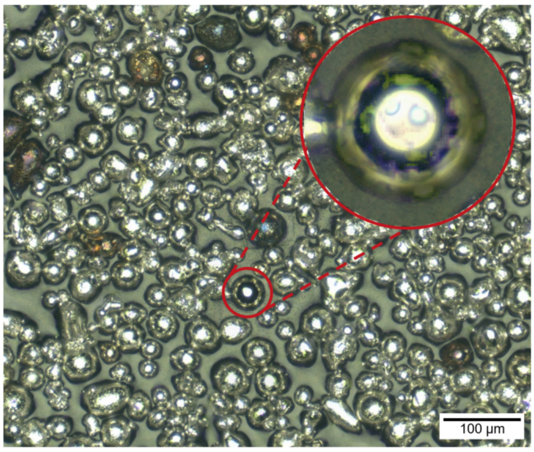

Figure 3.17 – OM image of R10 powder highlighting the presence of a bright magnetic particle.

Back scattered electron observations revealed the presence of darker regions on the surface of the magnetic particles, which indicates a difference in chemical composition. EDS mapping in figure 3.18 shows that these spots are also rich in O, Mn and Si, as were the oxide nodules of the partially oxidized particles.

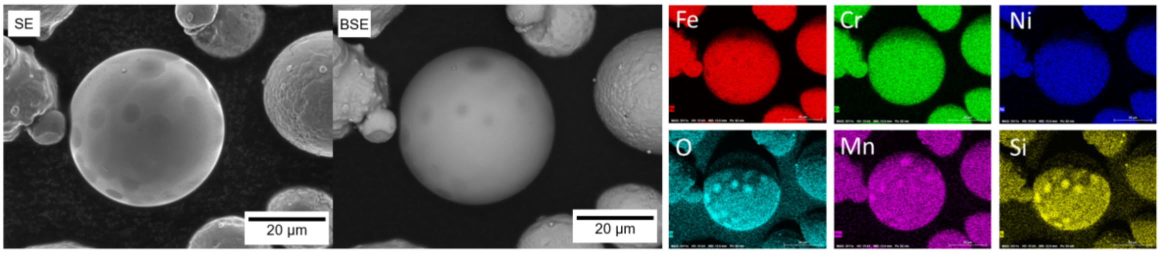

Figure 3.18 – Secondary Electrons and Backscattered Electrons images and EDS maps of a magnetic particle in the recycled powder.

EDS point analysis was carried out to compare the oxides of the two kinds of particles (magnetic and partially oxidized) on a semi-quantitative basis. As it appeared visually on the BSE images, with less pronounced contrast variation for the oxides of the magnetic particles, EDS confirmed that the element concentrations (in wt.%) of the latter are less important than those of the non-magnetic particles: O $\sim$ 17 %, Mn $\sim$ 10 % and Si $\sim$ 7 % compared to O $\sim$ 35 %, Mn $\sim$ 25 % and Si $\sim$ 15 %. This may imply that this type of particles did not have as much time at high temperature and had a faster cooling than the particles analyzed before.

3.3.5 Crystallographic phases

Magnetic particles

EBSD analysis was performed to investigate the crystal structure of the magnetic particles. This shows that such particles are fully ferritic and single crystals. All other particles, including the ones with oxide nodules on their surface are austenitic and polycrystalline. Figure 3.19 (a) presents an optical microscopy of magnetic particles (really bright and spherical) next to a few as-virgin particles that were attracted with them, on the bottom right of the image. In figure 3.19 (b), EBSD images of such powders (taken on a different set of particles) are displayed. The three ferritic particles (BCC) analyzed are single crystals of different orientations, while the austenitic one is polycrystalline.

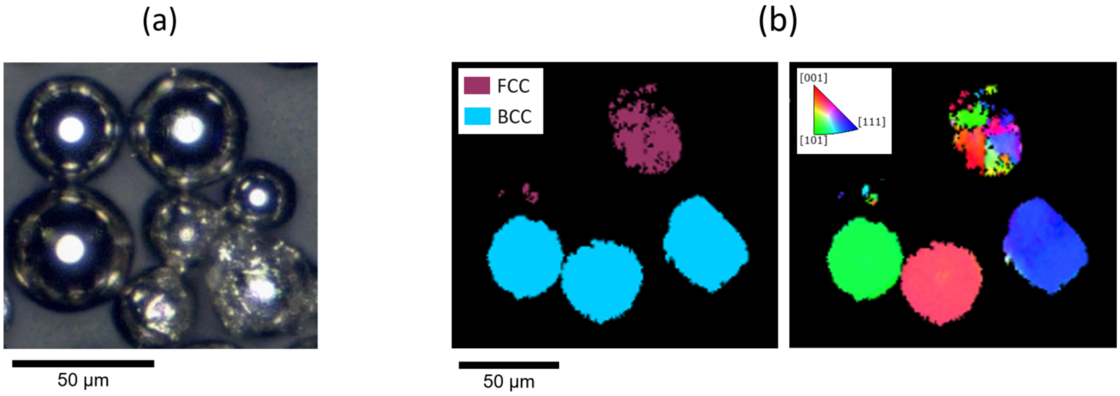

Figure 3.19 – (a) OM observation of magnetic (bright-spherical) and as-virgin particles, (b) EBSD phase map and inverse pole figure of magnetic and as-virgin particles.

As previously introduced (section 1.1.3), the solidification mode of austenitic stainless steels can be tentatively predicted by the ratio of chromium equivalence (Cr_{eq}) and nickel equivalence (Ni_{eq}), according to Korinko and Malene [44]. Several formulas are proposed by different researchers for the calculation of this ratio, and are shown in table 3.3.

Table 3.3 – Different equations for calculation of Cr_{eq} and Ni_{eq} [44].

Authors	Cr_{eq}, wt.%	Ni_{eq}, wt.%
Schaeffler	Cr + Mo + 1.5Si + 0.5Nb	Ni + 0.5Mn + 30C
WRC-1992	Cr + Mo + 0.7Nb	Ni + 35C + 20N + 0.25Cu
Hammar and Svenson	Cr + 1.37Mo + 1.5Si + 2Nb + 3Ti	Ni + 0.31Mn + 22C + 14.2N + Cu

According to the chemical compositions of the initial SS316L powder and 15-times recycled powder (table 3.2), the respective chromium and nickel equivalencies and their ratios were calculated and are reported in table 3.4. Using the WRC-1992 equivalence equations and the WRC-1992 diagram proposed by Siewert and Kotecki [228], the ratio is 1.29 and 1.31 for the virgin powder and highly recycled powder respectively. Such compositions should both follow an AF solidification mode, as shown in the WRC-1992 constitution diagram with the values of this study reported in green and red for R0 and R15 powders compositions (figure

3.20). In process conditions typical of welding, the AF solidification sequence, with primary austenite (γ) then ferrite (δ), and finally back to austenite is the following: $\mathrm{L} \rightarrow \mathrm{L} + \gamma \rightarrow \mathrm{L} + \gamma + \delta \rightarrow \gamma + \delta \rightarrow \gamma$.

Table 3.4 – Calculation of Cr_{eq}, Ni_{eq} (in wt.%) and the ratio for the virgin (R0) and highly recycled powder (R15), according to different equivalence equations.

Authors	Cr_{eq}	Ni_{eq}	$\mathrm{Cr}_{eq}/\mathrm{Ni}_{eq}$	Cr_{eq}	Ni_{eq}	$\mathrm{Cr}_{eq}/\mathrm{Ni}_{eq}$
	Virgin powder (R0)			Recycled powder (R15)		
Schaeffler	20.49	13.95	1.47	20.87	14.05	1.49
WRC-1992	19.90	15.40	1.29	20.22	15.46	1.31
Hammar and Svenson	21.38	15.02	1.42	21.73	15.09	1.44

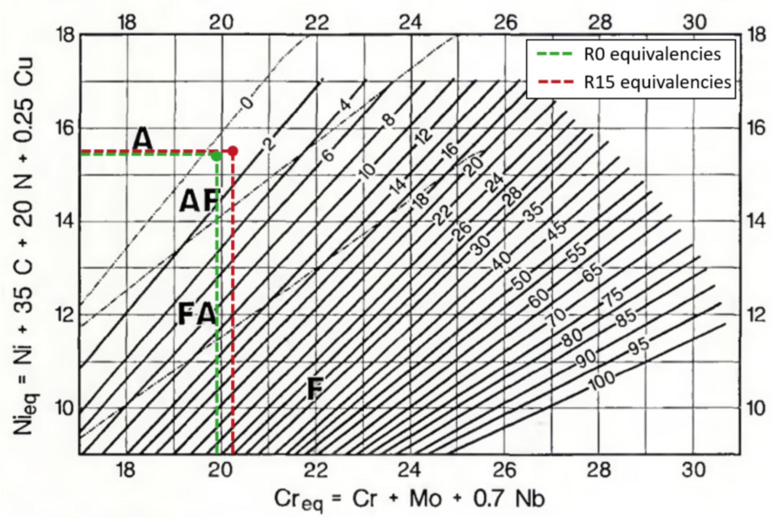

Figure 3.20 – WRC-1992 constitution diagram with the Cr and Ni equivalencies reported for the virgin (R0) and recycled (R15) powders [228].

However, the alloy composition criterion is not adequate to support the formation of fully ferritic particles that were observed in the reused feedstocks. Cooling rates can also be expected to have an influence, and it can be assumed that they are fast enough to cause sufficient amount of undercooling to bypass the nucleation of austenite and form metastable δ-ferrite. At a given cooling flux, smaller particles have a higher cooling rate, and conversely, at a given particle diameter, a higher heat exchange coefficient will result in a higher cooling rate. Therefore, it can be suggested that the magnetic particles retrieved after L-PBF processing are particles entrained through the laser beam or melt pool spatter ejected at high velocity, as suggested by Heiden et al. [137]. Young et al. [229] studied and distinguished different types of spatter in the L-PBF process, by in-situ high speed high energy x-ray imaging. They found that among them, droplets exhibiting the smallest sizes also presented the highest velocities.

Powder crystallographic structure

XRD was conducted to investigate the crystal structure of the powders. Figure 3.21 shows the comparison of the XRD patterns of the virgin powder and the highly recycled powder (R15). Commonly found austenitic peaks are present in both patterns. The indexing of a peak at an angle of 44.6° in the R15 powder is characteristic of the δ-ferrite phase. This confirmed the observations made by OM and SEM, with the presence of bright magnetic particles in the recycled samples. Quantification of the phases fraction in the two diffraction patterns was performed by Rietveld refinement. It showed an increased fraction of δ-ferrite phase, going from 0-1 wt.% for the virgin material to 4 wt.% after 15 L-PBF prints.

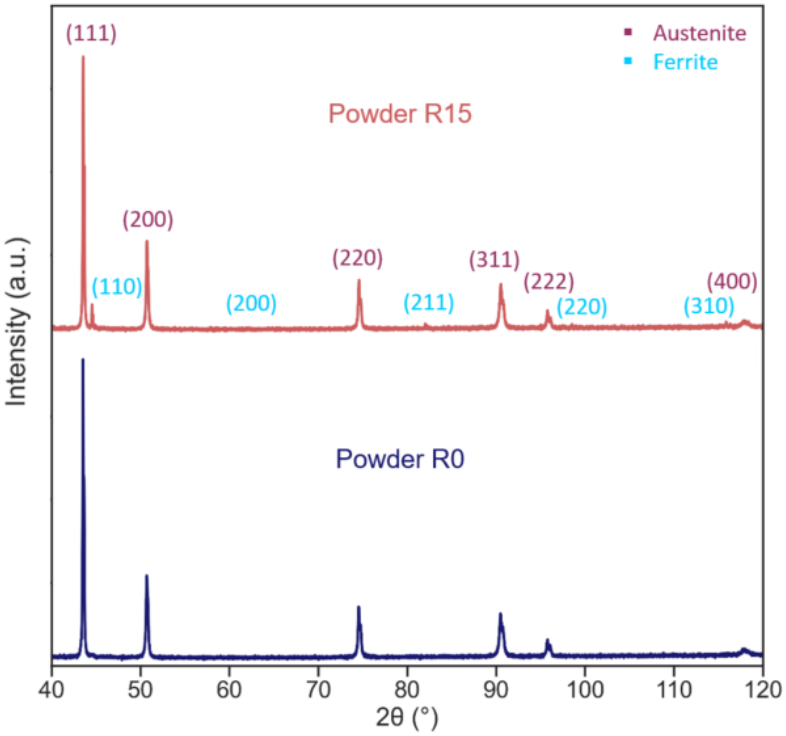

Figure 3.21 – XRD diffractograms of the virgin (R0) and 15-times recycled (R15) powders.

This increase of ferrite fraction in the recycled stainless steel powder was also observed by other authors [137, 139, 140, 159]. This results in an increase of the magnetization intensity and magnetic field strength [230], which can negatively affect future L-PBF fabrication with particles clustering that alters the powder bed uniformity and create defects [139].

EBSD analyses were also carried out on powder samples collected after various fabrication cycles. However, it was difficult to obtain images displaying numerous particles and therefore estimate the proportion of austenitic and ferritic particles on these EBSD analyzed samples. The small diameters of the sieved powders make it quite difficult to prepare samples with many uniformly distributed particles, with some of the particles embedded in epoxy being expelled during the polishing step. In this respect, EBSD performed on sieved resides were easier to implement due to their larger size, and will be presented and compared in the next subsection.

3.3.6 Sieved residues (SR)

Sieved residues (SR) are composed of particles and agglomerates larger than 50 µm that did not pass through the sieving mesh. They were collected after each powder recovery and analyzed to complete this comprehensive study of powder recycling, and evaluate the importance of this screening step.

More powder in fraction was sieved off after each build, related to the total amount of powder recovered at the end of the fabrications. It increased from 1.4 % for the first print to 4 % for the final job. This is associated with the fact that the fraction of melted volume in the build area is gradually increasing, as presented in section 3.2.2. Indeed, when comparing the mass of SR collected after each fabrication to the melted volume of the corresponding print, the ratio remained stable over the 15 runs (average ratio of 2.1 ± 0.2).

The sieving process is clearly effective regarding the particles size. Table 3.5 shows the comparison of particle size distributions for sieved powders and sieved residues, with the values of average diameter, D_{10}, D_{50} and D_{90} for different cycles.

Table 3.5 – Average particle size distributions of recycled powders and corresponding sieved residues. Numbers in parentheses are standard deviation.

Powder (Stdev)	Average diameter (µm)	D_{10} (µm)	D_{50} (µm)	D_{90} (µm)
Recycled powder after sieving				
R1	32.7 (0.5)	23.2 (0.1)	31.5 (0.3)	44.3 (0.8)
R5	34.2 (0.7)	24.3 (0.1)	32.7 (0.4)	45.4 (1.8)
R11	35.3 (1.1)	25.3 (0.5)	33.8 (0.7)	46.8 (2.5)
R15	35.4 (0.2)	25.2 (0.3)	33.8 (0.3)	47.3 (0.4)
Sieved residues (SR)				
R1 SR	85.5 (2.1)	58.5 (1.4)	80.1 (1.9)	117.8 (4.2)
R5 SR	85.6 (3.4)	58.0 (2.0)	80.3 (3.0)	118.7 (6.4)
R11 SR	91.7 (2.4)	59.7 (0.5)	84.7 (0.7)	132.2 (7.7)
R15 SR	91.5 (2.9)	58.4 (1.3)	83.2 (1.6)	135.6 (6.6)

Figure 3.22 is composed of an OM image and a SEM image of powder recovered after one print, before sieving. This illustrates the difference in particles sizes, as well as the particle shape, as shown earlier in figure 3.6 with the satellites on the large spatters.

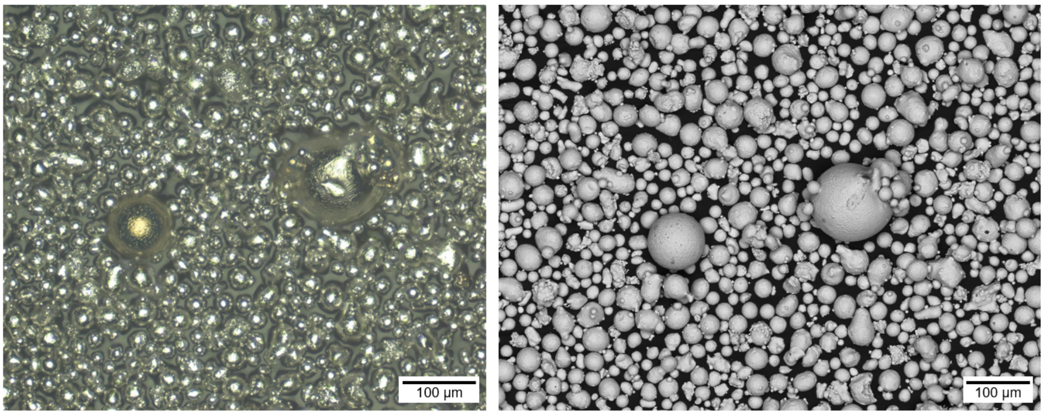

Figure 3.22 – OM and SEM images of R1 powder prior to the sieving step.

The morphology of SR is even clearer in figure 3.23, with OM and SEM observations of only SR particles, discarded by the sieving of R15. On top of being extremely irregular in shape, the particles/agglomerates present an important coloration oxidation and selective oxidation, with larger oxide nodules due to the larger size and longer cooling time of these particles.

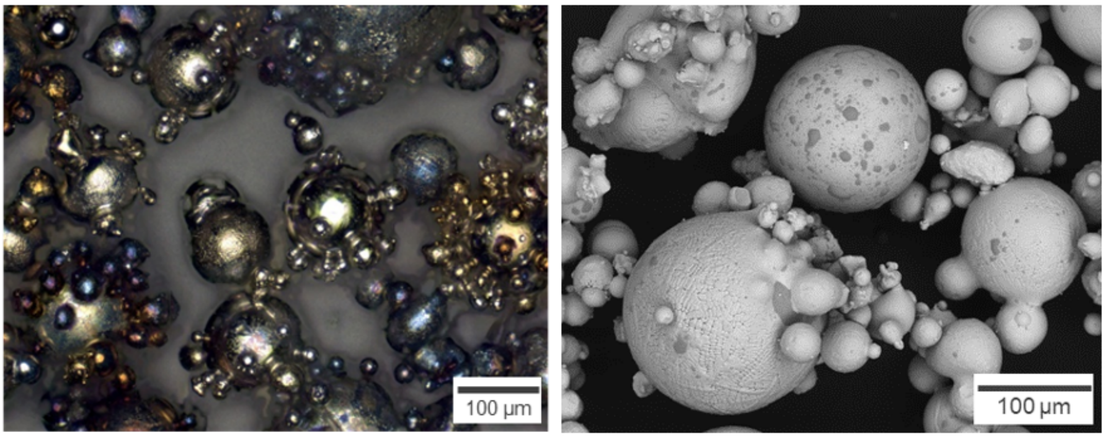

Figure 3.23 – OM and SEM observations of sieved residues.

Inert gas fusion was conducted to evaluate the oxygen content of the SR. The latter was three times higher than those of the sieved powders, with an average content of 1600 wppm. It is clear that the presence of such particles in the powder bed during L-PBF is detrimental for the process.

In addition, ferritic particles were observed in abundance in the SR. Figure 3.24 shows EBSD phase maps and inverse pole figures of sieved R15 powder and the SR collected after the vibrating sieving.

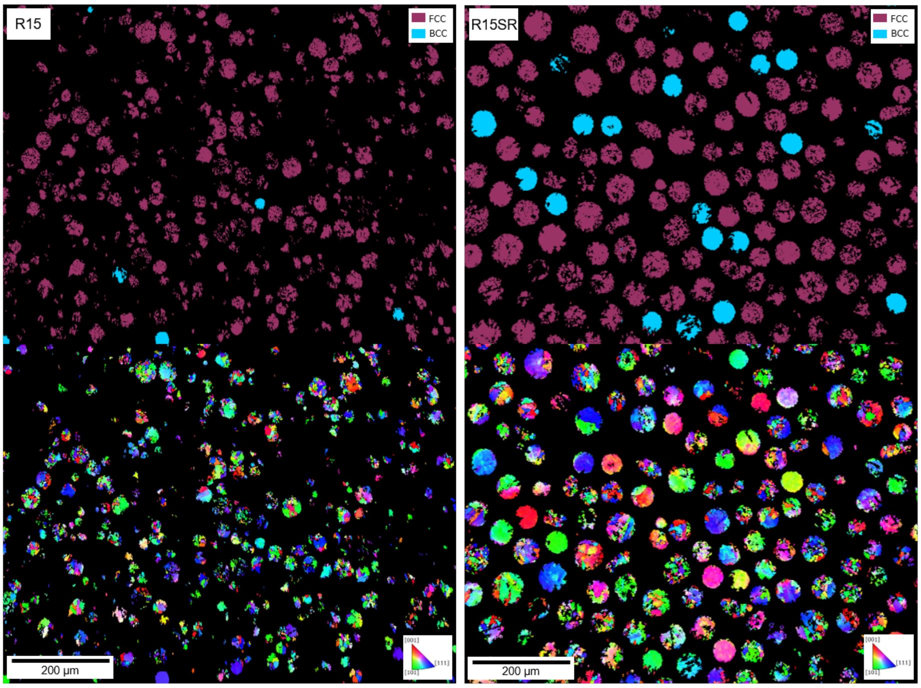

Figure 3.24 – EBSD phase map and inverse pole figure map of sieved recycled powder (R15) and sieved residues (R15SR).

Magnetic separation in the SR samples were conducted and showed that the bright magnetic particles, even if coming from the SR, are relatively small. Figure 3.25 presents an OM image of particles extracted from SR with a standard magnet. The diameter of the bright and smooth particles does not exceed 70-80 µm, and a majority is even smaller than 50 µm. This size would have theoretically allow them to pass through the mesh, but it can be assumed that their magnetic attraction favored particles clustering and their collection after sieving.

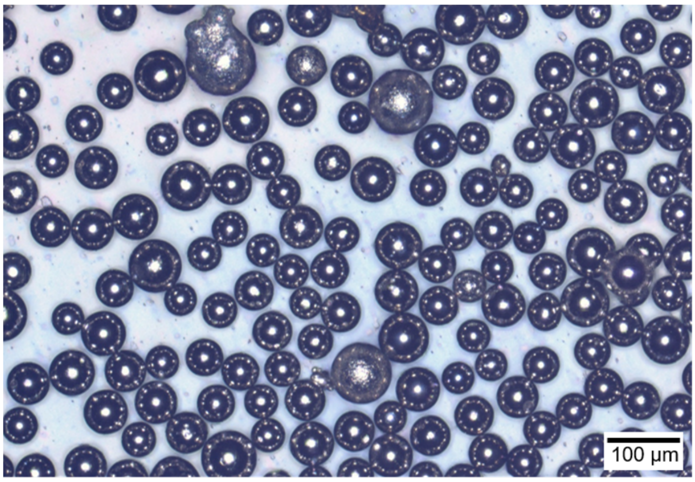

Figure 3.25 – OM observation of magnetic particles extracted from SR with a standard magnet.

This observation is in accordance with the assumption that fast cooling provoke the solidification of BCC particles, with particles of smaller diameters solidifying at higher cooling rates [139]. In addition, the fact that the selective surface oxidation of magnetic particles present lower concentrations in Mn, Si and O elements than the austenitic ones, as presented in section 3.3.4, also supports this idea.

This analysis of the particles discarded by the sieving step highlights all the non-beneficial attributes of the residues for the L-PBF process. The particles size is way larger than the required powder layer thickness, along with really irregular shapes due to numerous satellites. The oxygen content is increased by 300 % compared to virgin particles, and the SR are also composed of numerous magnetic particles. All these characteristics show the importance of sieving, which is crucial to limit powder degradation and process alteration during powder reuse in L-PBF. Sieving even limits the increase of δ-ferrite phase by discarding magnetic particles even smaller than the sieve mesh. However, it still does not remove all altered particles, as presented above, which could alter future fabrications.

3.3.7 Particles overview

The different kinds of particles encountered in the SS316L recycled powder are summarized in figure 3.26. This includes as-virgin particles, elongated particles and agglomerates, colored particles, partially oxidized particles, magnetic particles and sieved residues.

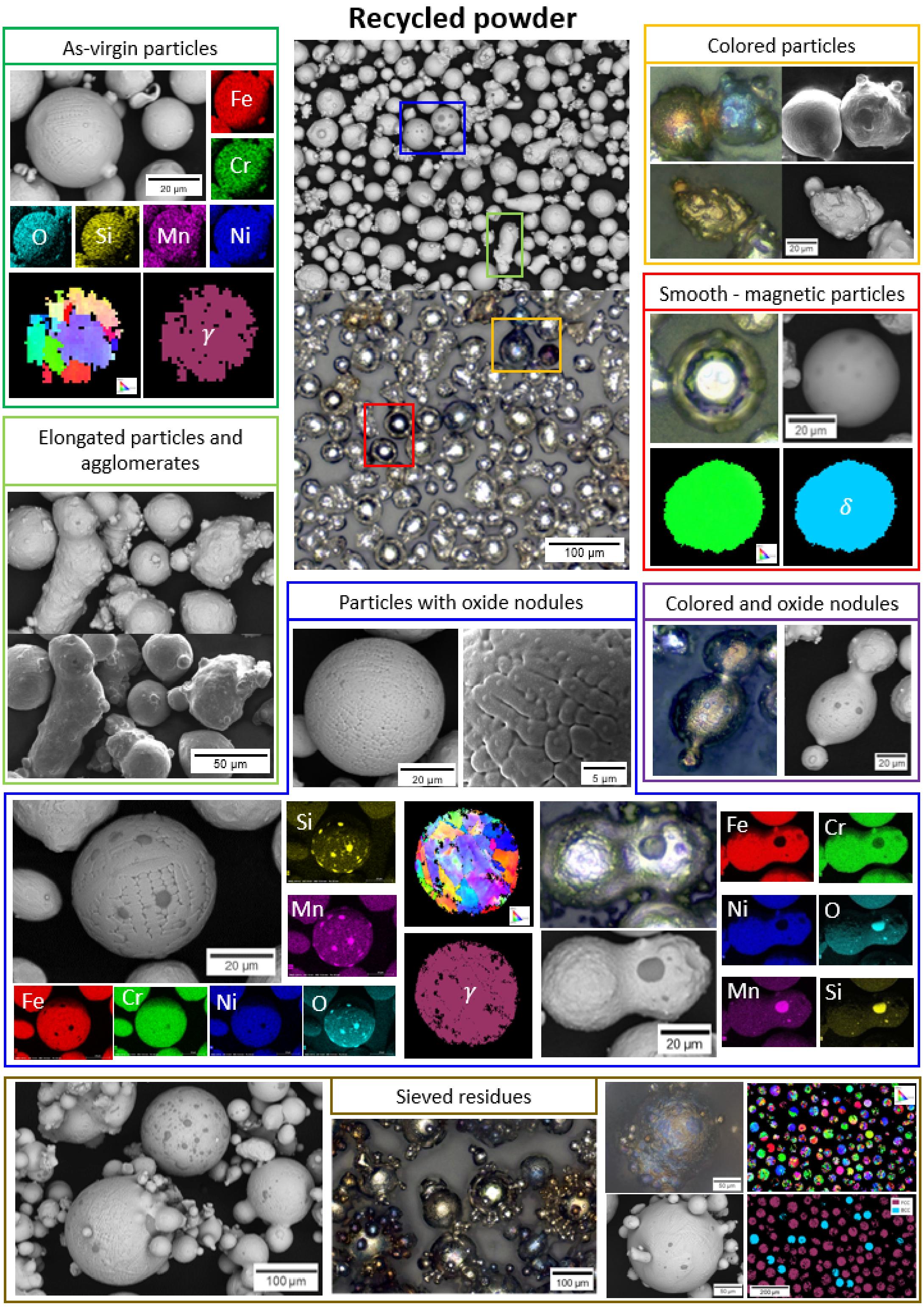

Figure 3.26 – Summary of particles identified in the recycled powder.

3.4 Influence of powder recycling on the printed parts properties

In parallel with the characterization of the powders, parts elaborated during this recycling study were analyzed, throughout the 15 prints with powder reuse. This section details the characterization conducted to follow potential changes regarding parts metallurgical attributes, chemical composition and mechanical properties.

3.4.1 Density

Printed parts density was assessed by different methods. Figure 3.27 shows the evolution of the cubic specimens density measured by Archimedes method and metallographic observation. Archimedes density is rather stable for 5-6 cycles, around 99.6 % of relative density, then decreases progressively as powder recycling is pursued, with final densities slightly over 98 %. On the other hand, the second approach estimates greater densities and small variations over the 15 fabrications. The image analysis of the samples cross sections showed very few porosities, and remained stable over 99.9 % density.

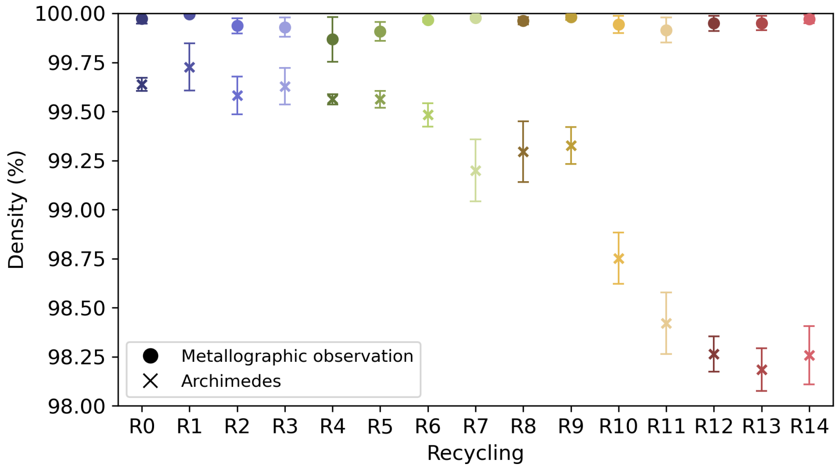

Figure 3.27 – Printed parts density measured by Archimedes method and metallographic observation in function of recycling.

The metallographic observation method only evaluates the components density on 2D slices with surface observation. This might not be representative of the entire part, and differences are not necessarily captured, especially for really high densities and minor variations. As noted and illustrated by de Terris et al. [231] porosities morphology can be irregular in L-PBF, and depending on the depth of the cross section analyzed, the corresponding porosity can be very different (figure 3.28).

A first explanation to account for the decrease in parts density measured by Archimedes method is that surface oxidation observed on the recycled powder (section 3.3.4) can increase the absorption of laser irradiation, which results in increased recoil pressure and surface tension variations [83]. These phenomena can lead to more liquid metal leaking out as spatters, which can create defects such as inclusions and pores when ejectas are falling back on powder bed areas scanned by the laser beam in the following slices.

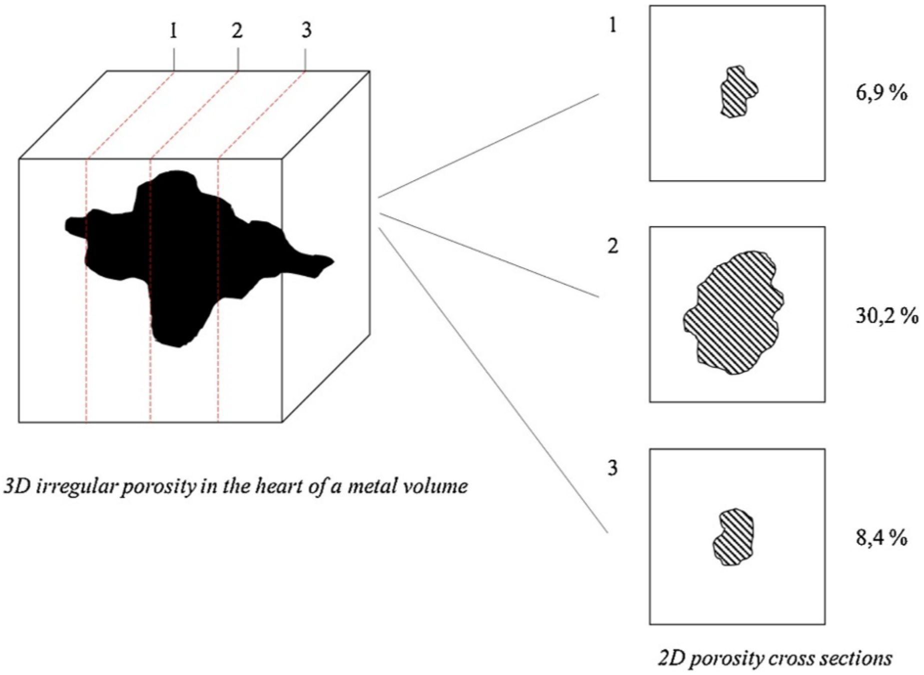

Figure 3.28 – Schematic illustration of porosity cross sections in function of the depth of the micrograph section [231].

Another assumption for the observed decrease of density can be related to the PSD increase with powder reuse. Indeed, as had been invoked in the literature [146], larger particles need more input energy to be melted, and since the L-PBF processing parameters were kept constant, this may lead to voids such as lack of fusion pores. However, as seen in part 3.3.1 with figure 3.5, the particles size increases are not that extreme, and this explanation might not be the most suitable one in the present case.

X-ray computed tomography (CT) was also employed as a third way to assess elaborated parts density. This was conducted only on a few samples (two cubes of R0, R8 and R14 each), and the results did not show a great consistency and reproducibility. Too much variation in calculated porosity rates were possible only by applying different image processing and filters. The contrast of the images was not optimal due to the SS316L specimens density which attenuates the X-rays, and the system allowed a minimum voxel size of 16 µm. Samples were cut in 4 pieces to reduce de samples thickness but it did not yield to better results. Porosity varied between 0.06 % and 0.36 % with no tendencies between the recycling states, and large deviations between the pairs of samples for each state.

More efforts should still be made to go further in this of the study, with more tests and correlations, because this tool has nevertheless allowed to observe irregular porosities in the samples. Figure 3.29 shows an example of a cubic specimen analyzed by X-ray CT with image processing highlighting the pores in the cross sections acquired in 3 directions.

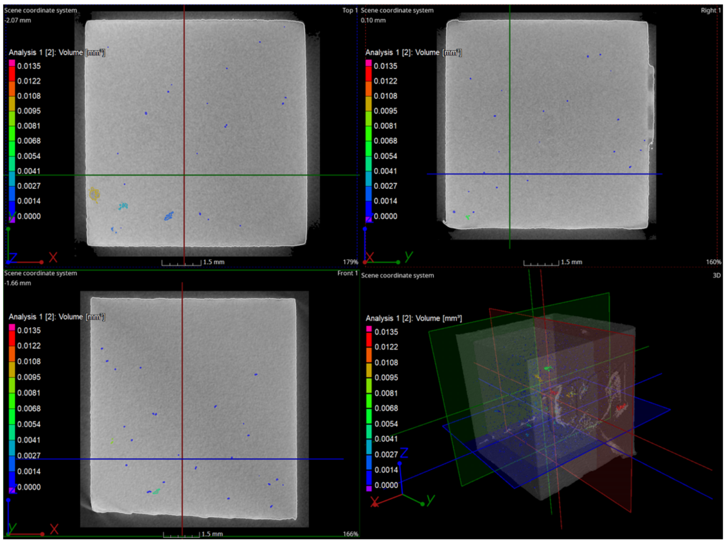

Figure 3.29 – Example of cubic specimen analyzed by X-ray computed tomography.

3.4.2 Microstructure

Cubic specimens cross sections (xz plane) were prepared for metallographic observation by OM and SEM. Typical L-PBF microstructure was found, with large columnar grains, melt pool boundaries and cellular network structures [52]. Figure 3.30 shows SEM micrographs displaying these features, on a sample etched with oxalic acid.

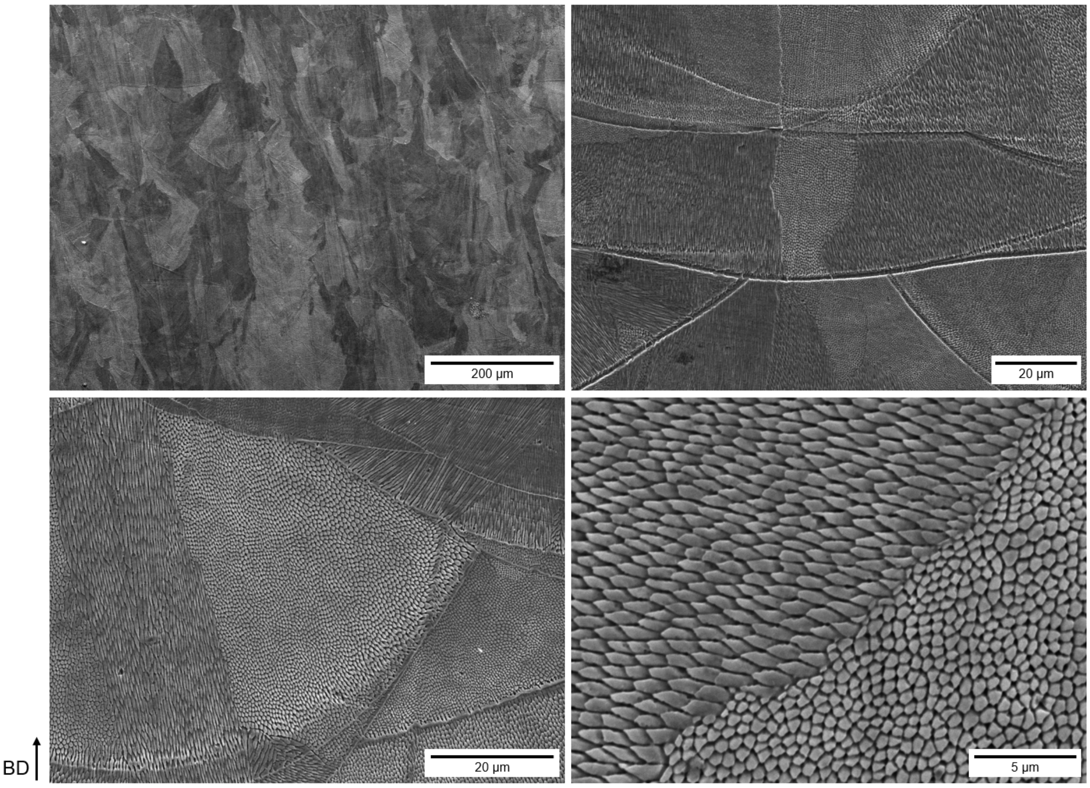

Figure 3.30 – SEM micrographs of SS316L part printed by L-PBF, showing melt pool tracks, elongated grains crossing several melt pools and fine cellular structures inside the grains.

Grains are elongated and aligned with the building direction (BD, parallel to z axis) and extending across multiple melt pools. EBSD inverse pole figures (ipf-x) and grain maps of parts elaborated with virgin powder (R0), 7-times reused (R7) and 14-times reused (R14) powders are shown in figure 3.31. Grains boundaries were determined using a criterion of boundary misorientation angle of 5°.

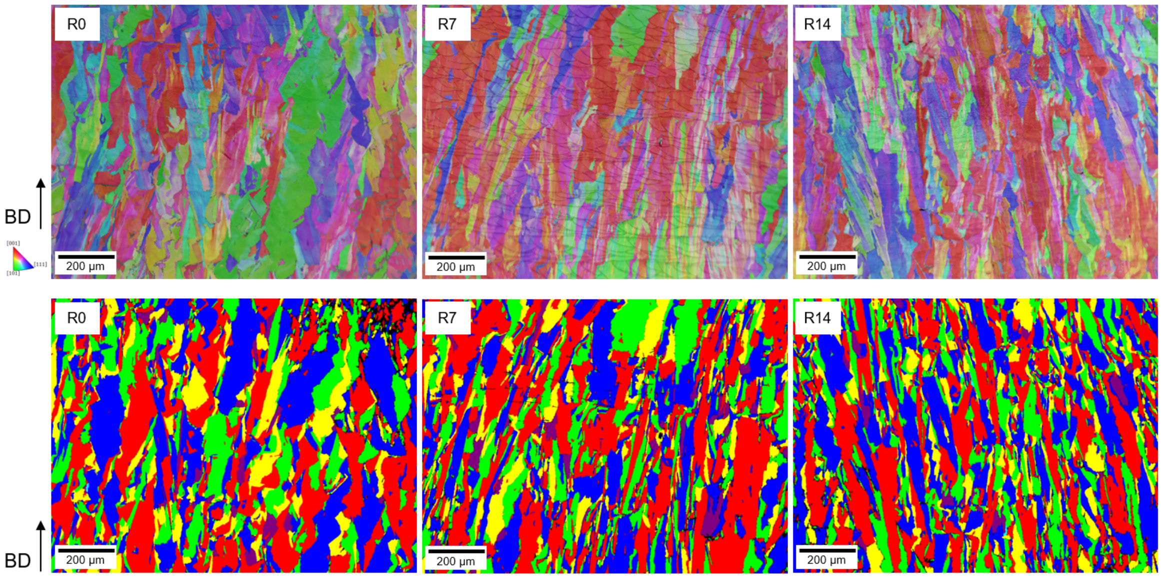

Figure 3.31 – EBSD inverse pole figures and grain maps of cross sections in building direction (BD) of R0, R7 and R14 cubic samples.

It is noticeable that the grains become finer and more numerous for parts elaborated with recycled powders. Grain size and shape analysis was performed to confirm this visual impression. Table 3.6 presents the values of grains number, median size and average size (calculated reported to the surface) of the three EBSD grain maps.

Table 3.6 – Grains number, median and average sizes in EBSD maps of R0, R7 and R14 specimens.

Recycling	Grains number	Median size (µm)	Average size (µm)	Standard deviation (µm)
R0	1157	97.9	108.5	65.6
R7	1369	85.4	99.5	66.9
R14	1680	72.5	80.5	49.4

Grain analysis conducted with boundary misorientation angles criteria of 10 or 15° followed the same trend. Between R0 and R14, the number of grains increased by 40-45 %, while the average size decreased by 20-25 %. No significant changes were observed in terms of grains aspect ratio or grain inclination angle.

These changes in grains size and number could be explained by the increase in oxygen content observed in the recycled powders (section 3.3.3). Fairly uniform distribution of nano-oxides are commonly found and expected in parts elaborated by L-PBF [53]. In the case of austenitic stainless steels, the oxide inclusions were found to be rich in Si, Cr, Mn and Mo [53,59,232,233].

These inclusions may influence the microstructure of the solidified parts with two possible mechanisms. The oxides may act as nucleating sites for grain germination and therefore promotes grain refinement [234]. Otherwise or additionally, they could contribute to pinning of grain boundaries, which inhibits grain growth [51].

Identical processing parameters were used for all fabrications, therefore the slight refinement cannot be attributed to a change in cooling rate. EBSD mappings presented only the austenite phase, which was also confirmed by XRD on the printed parts. Nucleant particles such as ferrite could be expected to impact the grain size of the solidified samples, but none was ever observed.

3.4.3 Oxygen content

Oxygen content measurements were also carried out on the printed parts, by inert gas fusion. Figure 3.32 shows the evolution of oxygen concentrations in wppm of specimens elaborated from the 15 L-PBF builds.

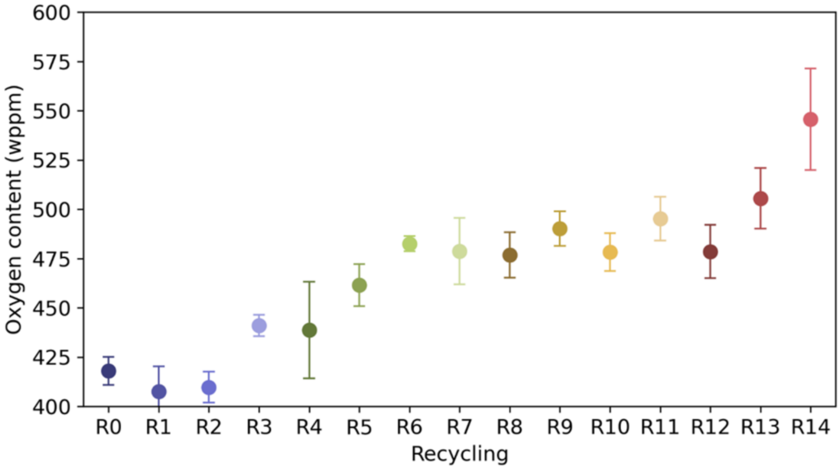

Figure 3.32 – Oxygen content in the printed parts with recycling.

A gradual increase of oxygen within the part is present, with a difference of almost 150 wppm between R0 and R15. This can be related to the increased oxygen content in the powder feedstocks with successive reuse (figure 3.10). It is also noteworthy that although the content of the parts increases, the latter always exhibits lower values than the powders. This was also observed by Tang et al. [147] or Pauzon et al. [48]. This could be due to the low oxygen content level imposed in the build chamber with continuous Ar gas flow during fabrication. Oxygen gas can be produced by the dissociation of oxides on the surface of powder particles when irradiated by the laser beam, and then be removed by the laminar gas flow. Secondly, the loss of oxygen can also be balanced by the huge oxygen pickup of large spatters ejected from the melt pool and observed in the sieved residues (section 3.3.6).

There is no specifications regarding the oxygen concentration in SS316L components, as it can be the case for titanium alloys. Nevertheless, an increase of oxygen in the printed parts could cause detrimental effects on the mechanical properties such as the impact toughness [170,235]. Such tests were not implemented in this study.

3.4.4 Mechanical properties

An in depth characterization of the mechanical properties of the fabricated parts was beyond the scope of the present work, but it appeared nevertheless interesting to perform preliminary investigations all along the 15 recycling cycles.

Microhardness

Figure 3.33 presents the microhardness tests results conducted on the cubic samples under load of 1 kg. The standard deviation is representative of 15 measurements performed on 6 parts per condition.

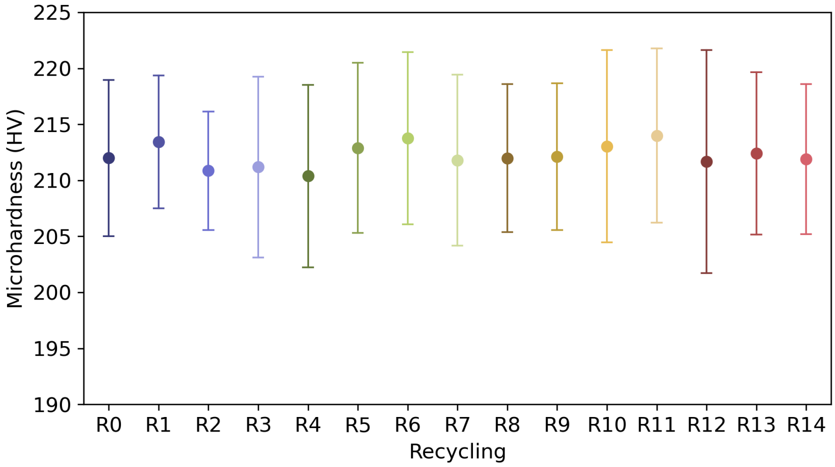

Figure 3.33 – Vickers microhardness of printed parts with recycling.

No significant difference was found between the different powder recycling conditions. The values are steady, with an average hardness of 212 HV, and a standard deviation of 8 HV. This value compares positively to hardness measurements reported in other researches on SS316L manufactured by L-PBF [85, 119, 236].

Tensile testing

Uniaxial tensile texts were conducted at room temperature on machined cylindrical samples. Figure 3.34 (a) shows the conventional stress-strain curves of all tested conditions. Figure 3.34 (b) presents the average ultimate tensile strength and yield strength values in function of the recycling state, and figure 3.34 (c) displays the average elongation at break of the specimens with recycling.

As for the microhardness, YS, UTS and elongation at break remain stable with the successive powder reuse. The tensile tests led to satisfactory values of 580 MPa for YS, 670 MPa for UTS and 40 % of ductility, with standard deviations of 8 MPa, 9 MPa and 5 % respectively. These values are well above the requirements of minimum YS, UTS and elongation of 205 MPa, 515 MPa, and 30 % respectively specified in the ASTM F3184 norm [43]. They also compare favorably to mechanical properties of SS316L L-PBF parts reported in the literature [237,238].

No significant difference was therefore found in terms of mechanical strength, ductility or hardness despite the small grain refinement observed previously (section 3.4.2). It can be assumed that the large and elongated grains are not the main contributor to the tensile properties of parts elaborated by L-PBF, as suggested by Leicht et al. [239] and Wang et al. [59]. The variations of mechanical strength are mainly caused by the fine cellular structure inside the grains or even more by the nano-precipitate structure. It is indeed known that changes of laser input energy affect the cell size and part properties. The cellular networks of the cubic specimens produced with virgin and reused powders were inspected by SEM. However, large deviations of cell size within a single cross section were observed and did not enable to determine an average cell size or any trend regarding the different printing cycles.

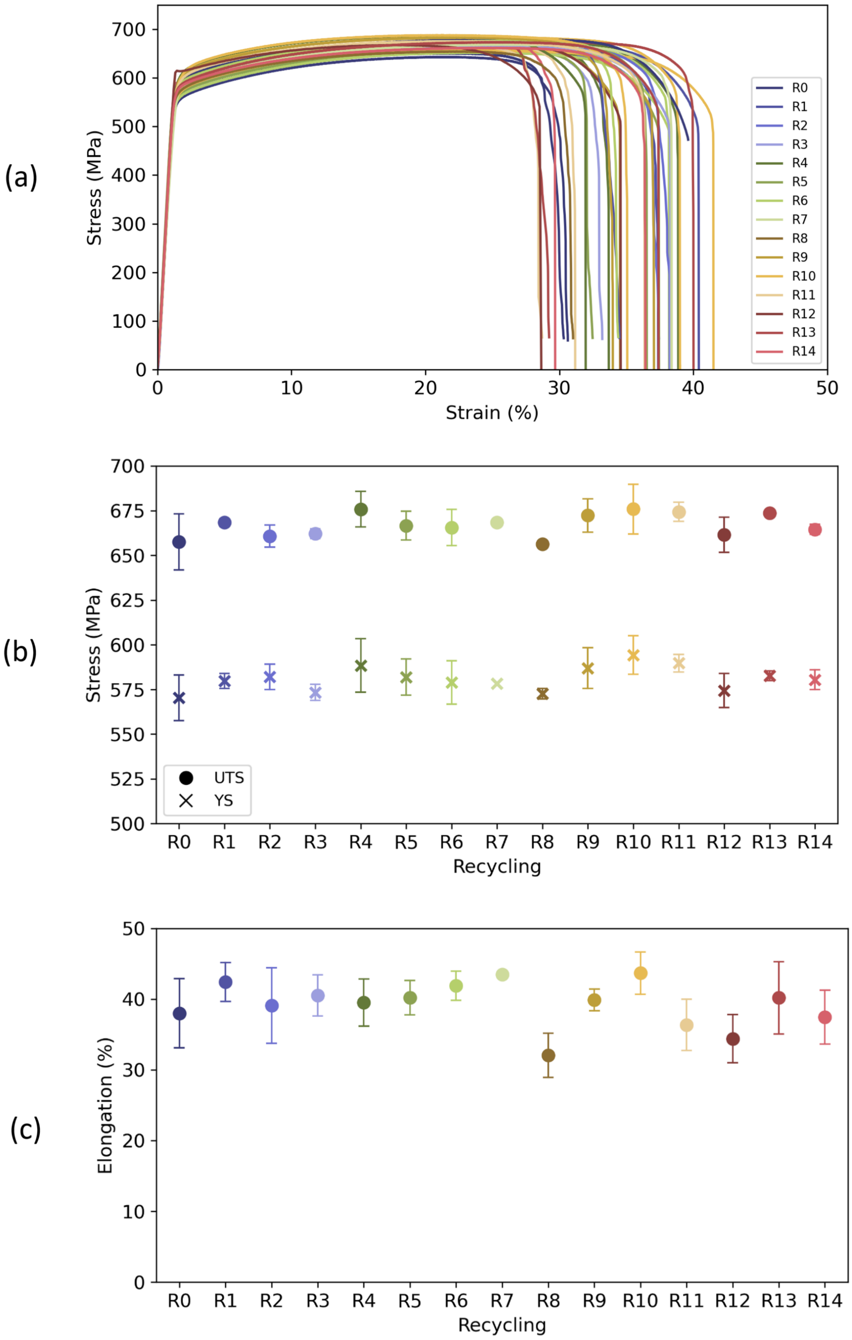

Figure 3.34 – (a) Stress-strain curves of parts elaborated at each printing cycle, (b) Ultimate tensile strength, yield strength, and (c) Elongation at break of printed parts with recycling.

3.5 Summary

This chapter focused on a study of powder recycling in L-PBF technology. Focusing on 316L stainless steel, gas atomized powder was used, recovered, sieved and reused to produce 15 successive prints without adding fresh material. A thorough investigation of powder attributes and parts properties was carried out after each L-PBF cycle, to investigate the influence of powder reuse on both the raw material and the elaborated specimens. Identical L-PBF processing conditions were applied to all fabrications.

Particle size distribution shows a shift towards larger values with successive powder reuse. All characteristic values such as the average diameter, D_{10}, D_{50}, or D_{90} slightly but gradually increase from R0 to R15. The presence of elongated and irregularly shaped particles is also reported in the recycled feedstocks, even after a sieving step using a 50 µm mesh. Due to the size increase, recycled powders exhibit an improved flowability which is beneficial for the process.

Another reason for the reduced adhesion and inter-particles frictions is the presence of oxides on the surface of some particles. OM observations indeed shows an increase of colored oxidized powder with recycling, with the presence of yellow-brown and blue particles. This phenomenon is related to a measured oxygen content pickup in the powder samples, going from 474 to 675 wppm between R0 and R15. No other significant changes are found in the chemical composition of the highly recycled powder.

Different kinds of altered particles are identified in the recycled samples and can be responsible for the rise of oxygen concentration. Partially oxidized particles, commonly found in the sieved residues are also observed in the reused powder after sieving. These particles present selective oxidation on the surface with Mn and Si rich oxide nodules. The latter could be vapor-entrained particles that oxidized in flight after being exposed to the laser beam. The short amount of time at extremely high temperature and fast cooling do not give enough time for the oxides to coalesce.

The partially oxidized particles can also present a coloration oxidation after multiple reuse, in addition to the oxide islands. The proposed mechanism for this coloration is a longer exposition time at relatively high temperature with their presence in heat-affected zones near the vicinity of melt pool tracks and solidified parts during fabrication, giving time to a more homogeneous oxidation.

Really smooth, bright and spherical particles are also noticed in the recycled powder samples and correspond to magnetic particles (δ-ferrite BCC), which can also present selective oxidation of Mn and Si in less pronounced concentrations. A significant amount of this phase is found in the 15-times recycled powder after sieving (4 wt.%), compared to virgin powder which is fully austenitic. The magnetic particles are present in even greater amount in the sieved residues due to their magnetic attraction and clustering. However, their size do not exceed 70-80 µm, and they solidify in single crystal ferrite. This leads to the assumption that these particles are melt pool spatter or vapor-entrained powder expelled at really high velocity, resulting in a solidification under supercooling conditions.

The characteristics of the sieved residues demonstrate that the sieving process is crucial to limit powder degradation and L-PBF process alteration with powder reuse. The particles discarded by the 50 µm screen can be extremely large and irregular with numerous satellites and agglomerates. Their oxygen concentration is more than three times higher than the one of the virgin powder. Moreover, the sieved residues are also composed of numerous magnetic particles. However, this step does not remove all altered particles from the powder as explained above, which can alter future manufacturing.

Elaborated parts density remain rather stable for 5-6 fabrications, around 99.6 % measured by Archimedes method, then decreases progressively for a final relative density slightly over 98 %. Parts microstructure highlights a small grain refinement over the 15 L-PBF runs, with more numerous and finer grains potentially coming from the increased oxygen content in the powder leading to more oxide inclusions acting as nucleation sites or contributing to the pinning of the grain boundaries. Oxygen content in the manufactured samples is also increasing gradually with powder reuse, going from 405 to 545 wppm.

Despite these changes, no significant difference in printed samples microhardness and tensile properties is found with recycling. The specimens show consistent and satisfactory properties with a hardness of 212 HV, YS of 580 MPa, UTS of 670 MPa and elongation at break of 40 %. In the conditions of the present study, SS316L powder can thus be used up to 15 times with the L-PBF technology without compromising mechanical properties of elaborated parts.

Chapter 4

Determination of powder bed oxygen content by in-line monotoring

Submitted paper associated to this chapter:

T. Delacroix, F. Lomello, F. Schuster, H. Maskrot, V. Jacquier, P. Lapouge, F. Coste and J.-P. Garandet, "Measurement of powder bed oxygen content by image analysis in laser powder bed fusion," submitted to *Materials & Design*, 2022.

4.1 Introduction

Additionally to the technical challenge of qualification and certification of AM and L-PBF parts, resulting in a need to better understand the process and influential factors such as the powder material and its reuse, in-situ process monitoring is another key element for the development of the reliability of AM technologies.

In the perspective of waste minimization through the reuse of the powder raw material in the L-PBF process, it has been observed in the precedent chapter that intensive powder recycling leads to a degradation of the particles attributes, especially with regard to the oxygen content. This alteration can also impact the properties of the final components. Evolution of feedstocks characteristics is not necessarily linear with successive recycling and the degradation is heterogeneous, with the presence of altered particles dispersed in the recovered powder.

Powder characterization is generally performed ex-situ, requires various instruments, and is time-consuming. Besides, only small quantities of particles are usually analyzed compared to the amounts used for printing, and examination can be destructive. The purpose of this chapter is to develop a new monitoring methodology allowing to directly control in-line the quality of the powder, on fully representative batches, to assess powder degradation in L-PBF. As seen in chapter 1, most of the research efforts have been implemented on in-situ sensing of the melt pool, or the detection of structural defects on a layerwise level. Among studies focusing on the in-situ control of the powder material, the majority is performed at relatively low spatial resolution to monitor the entire powder bed, therefore only detecting large anomalies such as recoating errors. In this respect, the use of sensors mounted on the recoater unit allows to capture the entire powder bed area without any distortion and at really high spatial resolutions. This kind of setup offers the opportunity to perform in situ powder bed quality assessment regarding numerous features. To the best of our knowledge, no powder bed monotoring studies in the literature exploited the advantage of acquiring high resolution scans in color, in order to investigate particles oxidation.

The color of the particles can be a good indicator of the powder feedstocks oxygen content. In chapter 3, the presence of colored particles was reported in the recycled samples, with different shades of colors, and a gradual increase of the number of colored particles, along with increased overall oxygen contents. As different colors can be observed on oxidized powders due to different oxide thicknesses, the present study aims at correlating the particles color to the oxygen concentration. To this end, several samples of virgin SS316L powder were submitted to controlled furnace oxidation and characterized. An instrumented L-PBF platform with a customized recoater module including a flatbed scanner was used to acquire colored scans of powder bed layers with individual particle resolution. The development of the methodology, with the correlation between the particles color and the oxygen concentration is detailed in the following. Validation results obtained in actual L-PBF process conditions are also presented with the in-line scanning and analysis of several grades of altered powders, such as the powders degraded by successive reuse in the L-PBF process of chapter 3.

4.2 Particles color to oxygen content correlation

4.2.1 Powder bed monitoring methodology

The purpose of this work is to assess the quality of powders by in-situ monitoring of the powder bed in L-PBF. The method takes advantage of the relation between stainless steel particles coloration and their oxidation level in order to determine the powder layers oxygen concentration. The methodology is based on a preliminary calibration allowing to derive a functional correlation between the colors of the particles and their oxygen content, with the ultimate objective of performing measurements of powders oxygen concentration by in-line scanning of powder bed layers.

This calibration was carried out according to the following main steps:

(i) Oxidation of powder samples in furnace under different combinations of time and temperature;

(ii) Measurement of oxygen content in these oxidized powders by chemical analysis;

(iii) Scan acquisition of powder bed layers of these oxidized samples, with the determination of their RGB color values;

(iv) Determination of a functional correlation between oxygen content and RGB color values.

The development and results of this calibration leading to a coupling between the color of a particle acquired by a scanning system and the corresponding oxygen content will be detailed in the following, section 4.2.2 for steps (i) and (ii), and section 4.2.3 for steps (iii) and (iv).

All the furnace powder oxidation calibrations were conducted using identical virgin gas-atomized SS316L powder as the one presented in section 5.5 and employed for the recycling study.

Validation results were obtained with the scanning of various powder beds composed of altered particles, and the determination of the corresponding average oxygen content in the powder layers. Data were obtained from several samples including recycled powders collected from the previous recycling study. Other artificially degraded powder samples were also investigated with the present powder bed scanning technique, with mixes of virgin and furnace-oxidized particles at different fractions and oxygen contents. In all cases, the in-line measurements of oxygen concentration were compared to results obtained by conventional ex-situ characterization using inert gas fusion.

4.2.2 Powder oxidation in furnace

As mentioned earlier, several samples of virgin SS316L powder were oxidized in a Nabertherm B180 furnace to be used afterwards for the color-oxygen correlation on the powder bed scanning setup. The samples were disposed in alumina crucibles and heated in air at different combinations of temperature and duration. The table 4.1 lists the oxidation conditions, corresponding to three heating temperatures and 5 durations per temperature. Cooling also took place in air at ambient temperature. Figure 4.1 shows the powder in crucibles at the end of the furnace oxidation, with samples heated for different duration at 400 °C on the left and 500 °C on the right.

Table 4.1 – Conditions of heating time and temperature for powder oxidation.

Temperature (°C)	Duration (min)
[300 ; 400 ; 500]	[10 ; 30 ; 60 ; 90 ; 120]

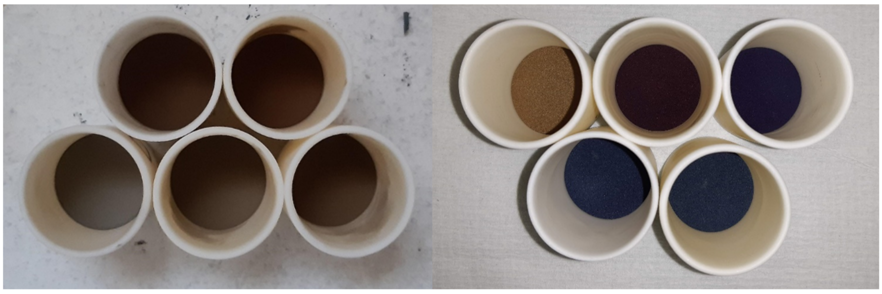

Figure 4.1 – Images of powder samples in crucible after furnace oxidation.

The results of oxygen content measurements performed by inert gas fusion on the samples collected after furnace oxidation are presented in figure 4.2, showing the evolution of oxygen content in the powder as a function of heating time and temperature.

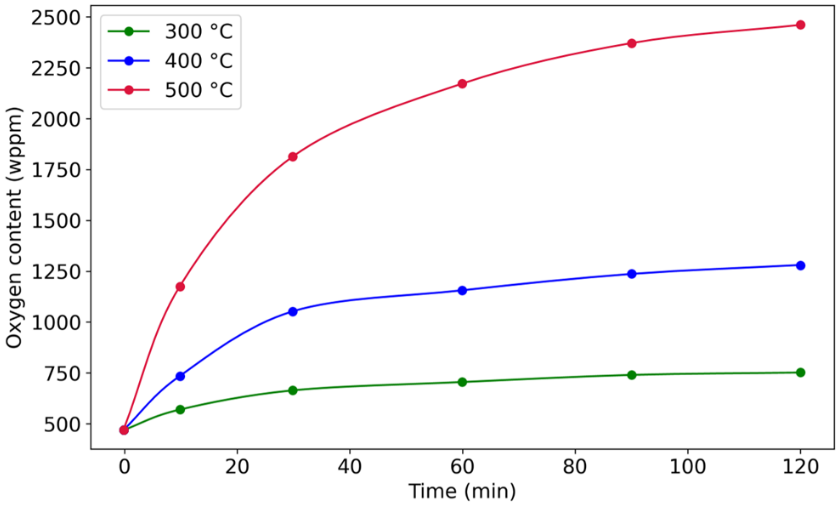

Figure 4.2 – Oxygen content of furnace-oxidized powders in function of heating time and temperature.

The three temperatures curves seem to follow parabolic oxidation kinetics. The latter is known for high temperatures of alloys with an oxide film growth controlled by diffusional phenomena [240, 241]. In the case of stainless steel materials, Cr_2O_3 oxide (chromia) can be expected to grow, following the parabolic rate law reported in equation 4.1 [242–244].

$$\left(\frac{\Delta m}{A}\right)^2 = k_p\, t + C \tag{4.1}$$

with k_p the parabolic oxidation rate constant (in $g^2.cm^{-4}.s^{-1}$), $\Delta m/A$ the mass gain par unit area (in $g.cm^{-2}$), t the duration of isothermal holding at the oxidation temperature (s) and C another fit parameter.

The parabolic oxidation rate constant k_p was determined for each temperature, resulting in k_p equal to 1.9×10^{-16}, 1.6×10^{-15}, and 9.6×10^{-15} $g^2.cm^{-4}.s^{-1}$ at 300, 400 and 500 °C respectively. The fitted curves obtained to determine these values featured coefficients of determination R^2 ranging between 0.95 and 0.98. This slight deviation can be attributed to uncertainties in the temperature uniformity in the furnace used, temperature variations due to sample removal and uncertainties in the oxygen content measurements. In any case, this does not affect the rest of the calibration, which does not depend on the heating conditions but solely on the measured values of oxygen content and the colors of the powders.

Figure 4.3 is an Arrhenius plot displaying the evolution of the parabolic oxidation constants in function of the inverse temperature. The linear nature of this graphs, with an R^2 of 0.998 points towards a temperature activated diffusional mechanism.

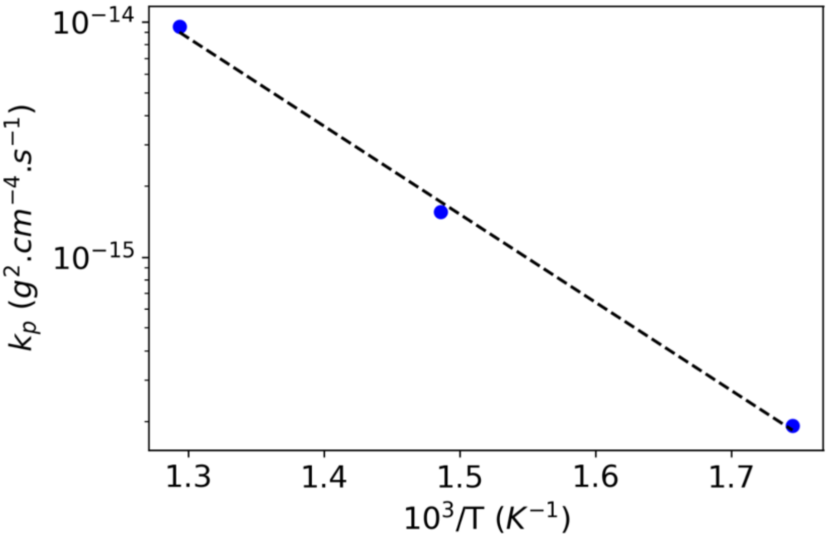

Figure 4.3 – Arrhenius diagram of the parabolic oxidation constants of SS316L powder.

The k_p values are in accordance with the literature for the growth of a protective film of chromia. They follow the trend of oxidation rates determined at higher temperatures, such as by Mortimer and Post [245], Felten [246] or Hindam and Whittle [240], with k_p constants ranging between 5×10^{-14} and 1.3×10^{-13} $g^2.cm^{-4}.s^{-1}$ at 650 °C, or between 3×10^{-13} and 5×10^{-12} $g^2.cm^{-4}.s^{-1}$ at 800 °C.

Oxide scale thickness can be estimated on a semi-quantitative basis considering a hypothetical purely spherical SS316L particle. The calculation uses the powder oxygen content measured by inert gas fusion, the average particle radius of the powder determined by laser granulometry (r = 16.0 µm) and assumes that the oxide film is uniform and consists of chromia. The approximation also includes the assumption that all oxygen (initial and picked up) is present in the external oxide layer, and does not exist as solid solution in the material. The calculation of oxide thicknesses was addressed using equation 4.2 [163]:

$$t_{oxide} = \sqrt[3]{\frac{3\, m_o\, M(Cr_2O_3)}{4\,\pi\, \rho_{Cr_2O_3}\, S_o\, M(O)} + r^3} - r \tag{4.2}$$

with t_{oxide} the oxide scale thickness, m_o the mass of oxygen contained in the oxide film, $M(O)$ and $M(Cr_2O_3)$ the molar masses of oxygen and chromia respectively, $\rho_{Cr_2O_3}$ the density of the oxide, S_o the stoichiometry of oxygen in the oxide, and r the radius of the particle.

The estimations yielded oxide thicknesses between 12 nm and 63 nm for particles presenting oxygen contents between 500 and 2500 wppm. These values are the result of many assumptions that might probably overestimate the thickness, but the orders of magnitudes are in agreement with surface oxide thicknesses measured on stainless steel particles, powder used in L-PBF or on oxidized powder samples [163, 226, 247, 248]. These estimations can also be conducted using other natures of oxides such as Fe_2O_3 as it was observed experimentally on the surface of gas-atomized SS316L powders [226].

Powder oxidized in furnace were observed by OM. Figure 4.4 shows images of these samples classified by temperature and heating time.

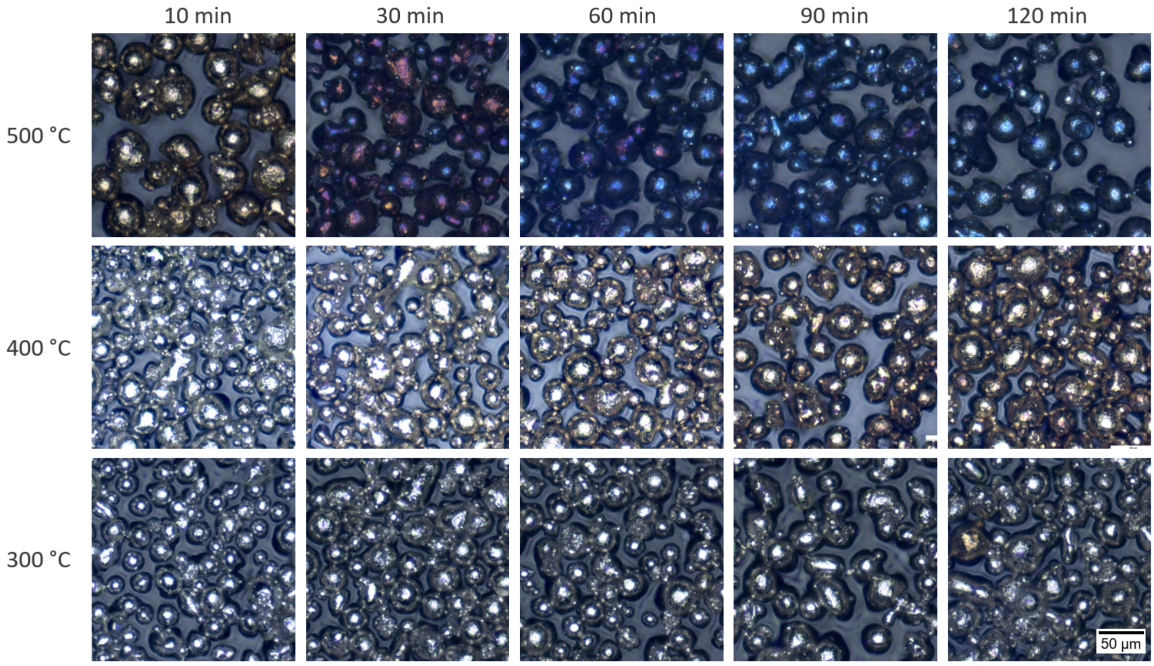

Figure 4.4 – OM images of furnace-oxidized powders in function of heating time and temperature.

The optical observations showed that similar coloring can be visible on oxidized powder particles obtained at various calibration conditions. This is consistent with the fact that different combinations of temperature and heating time can lead to a similar oxygen concentration, as shown in figure 4.2. The oxygen content can be related to the oxide thickness, and results in a specific color when exposed to white light. Due to interferences between the light reflecting off the film/steel interface and the light reflecting off the top of the oxide surface (air/film interface), different colors can be obtained with different oxide layer thicknesses.

It was possible to sort the powders by increasing oxygen content, as presented in figure 4.5 on a limited set of oxidized samples. In some oxygen ranges, a sudden color change was observed with relatively small oxygen differences. Additional oxidation conditions were tested and analyzed, such as a heating temperature of 500 °C and duration times of 15 and 20 minutes, to add data points and observe smoother color transitions.

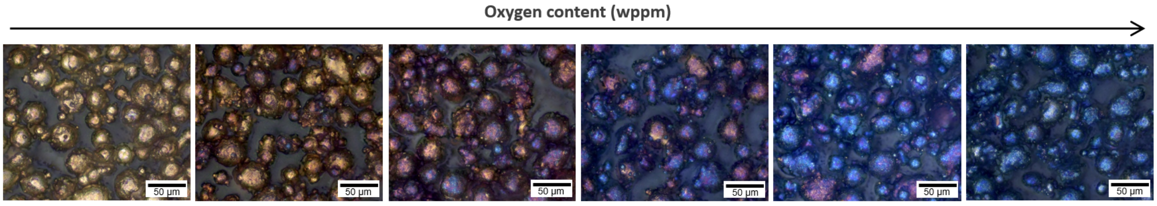

Figure 4.5 – OM images of furnace-oxidized powders sorted by increasing oxygen content.

Correlations were conducted between OM and SEM observations to assess semi-quantitatively by EDS the chemical composition of individual particles with known color thanks to the OM images. EDS point analysis showed that local oxygen concentrations confirmed the overall tendency noticed with larger powder samples and global oxygen concentration data. Figure 4.6 (a) presents a set of furnace-oxidized particles displaying different colors, observed by both SEM and OM. Figure 4.6 (b) shows colored particles on which multiple EDS point analyses were carried out, allowing to sort the particles by increasing measured oxygen content. The classification of these individual particles is consistent with the one obtained globally by inert gas fusion (figure 4.5).

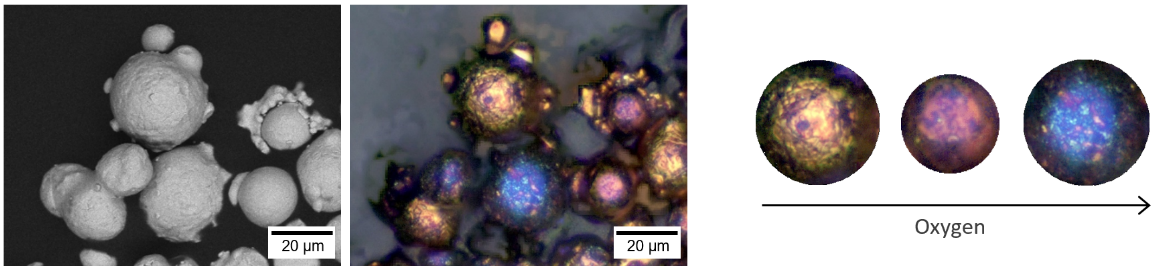

(a) (b)

Figure 4.6 – (a) SEM - OM correlation of oxidized powder, (b) Colored particles sorted by increasing oxygen content evaluated by EDS point analysis.

4.2.3 Correlation of scans color with oxygen content

All powder samples oxidized in furnace were scanned using the powder bed scanning system presented in section 2.5. The system allows to acquire high resolution images of the entire powder by scanning the powder bed area thanks to the motion of the recoater arm on which the flatbed scanner is installed. Images were acquired in color, with the highest spatial resolution (4800 dpi). Raw images were then processed with a cropping of the area of interest (the build plate), and the average RGB color values (Red, Green, Blue) of each scan were calculated. Each pixel of the image is coded on 3 bytes, one per color channel, amounting to intensity values between 0 and 255. The combination of these three primary colors produce the color of the pixel.

Figure 4.7 shows examples of powder bed scans of different oxidized samples and their corresponding average color, with the average (R, G, B) values.

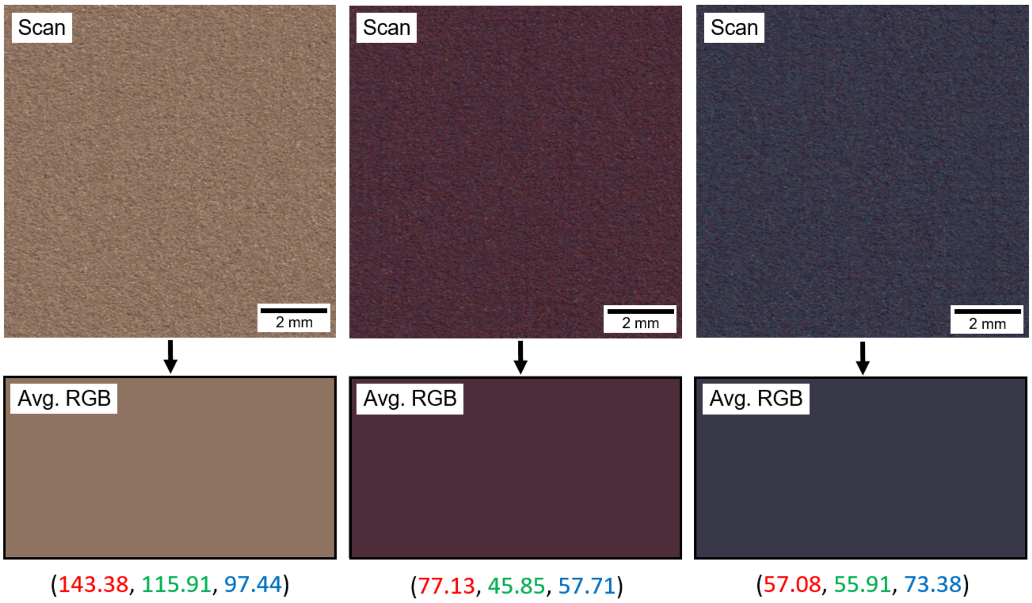

Figure 4.7 – Powder bed scans of oxidized powders and their corresponding average color, determined by average RGB channels values in parenthesis.

The average RGB values of all the scans acquired with powder bed layers of the furnace-oxidized samples can be linked to the corresponding oxygen content of the powders, previously measured by chemical analysis. Figure 4.8 shows the average color of the powders scanned by the in-line setup sorted by increased oxygen content. Particles color starts with the classical grey color of virgin particles, then turns to orange, purple and blue with oxygen pickup.

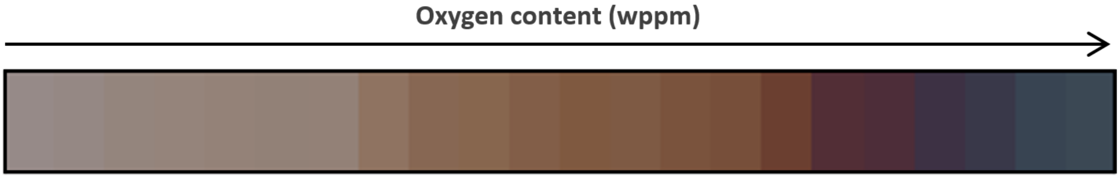

Figure 4.8 – Average color of powder bed scans of oxidized powders ranked by increased oxygen content.

These color changes with increased oxygen can also be represented on a chromaticity diagram, using CIExy 1931 color space derived from the RGB values [249]. The chromaticity diagram is often used in colorimetry to illustrate color variations. Figure 4.9 shows this color space diagram with a few points numbered from 1 to 7 corresponding to SS316L powders color with increased oxygen. The RGB triangle represents the colors that can be reconstructed by the RGB system of a computer screen. The position of the 7 points associated to 7 furnace-oxidized samples with oxygen contents listed in table 4.2 highlights the bijective relationship between color and oxygen concentration in the range of interest, with a given color being related to a unique oxygen content.

Table 4.2 – Oxygen content of oxidized powder samples points indicated in the chromaticity diagram.

Sample	1	2	3	4	5	6	7
Oxygen content (wppm)	474	1055	1347	1579	1707	1946	2458

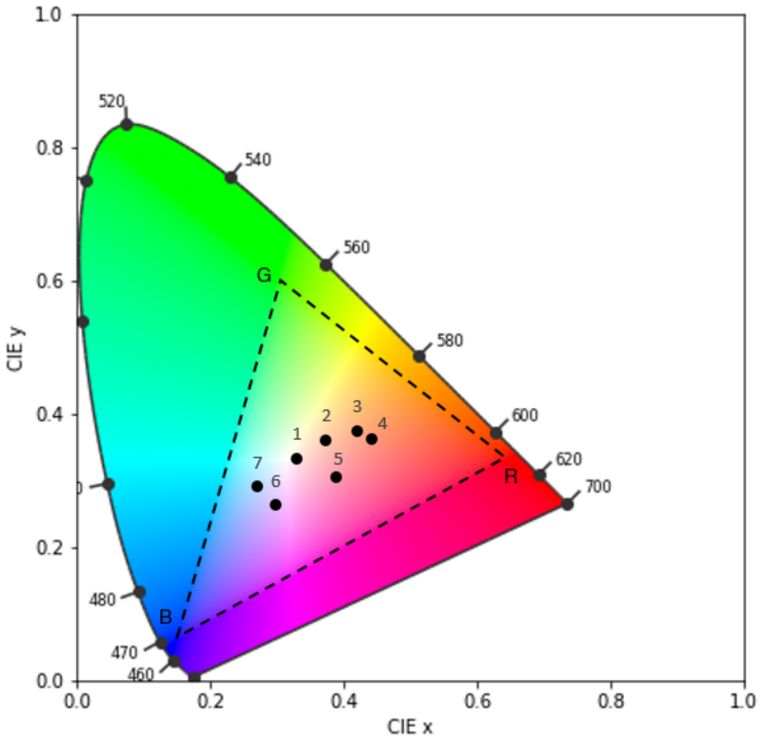

Figure 4.9 – CIE 1931 chromaticity diagram including the RGB color space and 7 experimental points of oxidized powders with increasing oxygen content.

This classification is nevertheless only used to illustrate the variation of particles color in our case, and it is the RGB coding, directly obtained for each pixel by the scanner that is of interest and that will be exploited. Figure 4.10 illustrates the evolution of RGB channels intensity in function of the oxygen content in the powders. The three curves present a similar shape qualitatively, which is not unexpected since the measurement is essentially the result of interference phenomena associated with reflections from an incident white light.

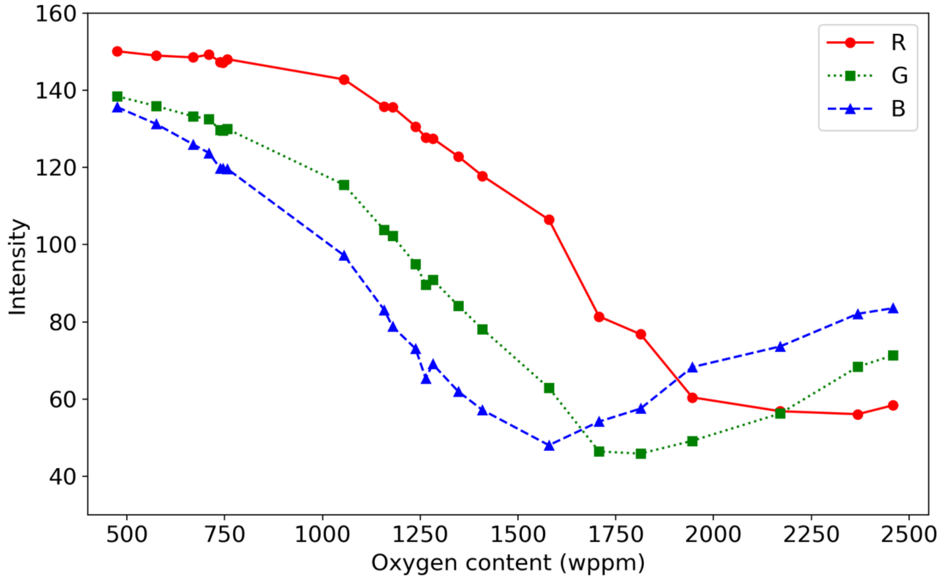

Figure 4.10 – Average values of Red (R), Green (G) and Blue (B) channels in powder bed scans of oxidized powders as a function of their oxygen content.

These calibration data allow to model the oxygen content as a function of the particles colors, represented by the three variables (R, G, B). A second-degree polynomial model of the form $(1, x, y, z, xy, xz, yz, x^2, y^2, z^2)$ was used, with the optimization of the coefficients to minimize the error. The calibration function O = f(R,G,B) is presented in equation 4.3. The latter fits the experimental values with a calculated correlation coefficient R^2 of 0.99824.

$$\begin{aligned} O = 4036 - 18.26 * B - 0.4010 * B^2 + 45.54 * G + 0.363 * B * G + 0.054 * G^2 \\ -49.05 * R + 0.3103 * B * R - 0.59 * G * R + 0.2411 * R^2 \end{aligned} \tag{4.3}$$

Other polynomial models such as $(1, x, y, z, x^2, y^2, z^2)$ or $(1, x, y, z, xy, xz, yz)$ have also been tested, leading to slightly degraded determination coefficients R^2 of 0.99676 and 0.99642 respectively after regression analysis.

This oxygen prediction function allows to correlate the color of a given SS316L powder batch to the corresponding oxygen concentration and to evaluate a potential degradation of powder bed layers quality by in-line scanning and image analysis in the L-PBF process. A summary of the calibration methodology developed in this work is illustrated in figure 4.11.

It can be envisaged that this methodology could be applied to other metallic materials in L-PBF such as titanium or nickel alloys which are also known to display different colorations with oxidation. This would require the determination of new correlation functions specific to each material. For this, the same approach can be followed, by preparing a plurality of powder samples with a known and distinct oxygen concentration for each sample. Then, an image of each sample could be made, and the associated average color is determined, coded by an (R, G, B) triplet. Finally, the calibration function would be calculated from the calibration data by regression.

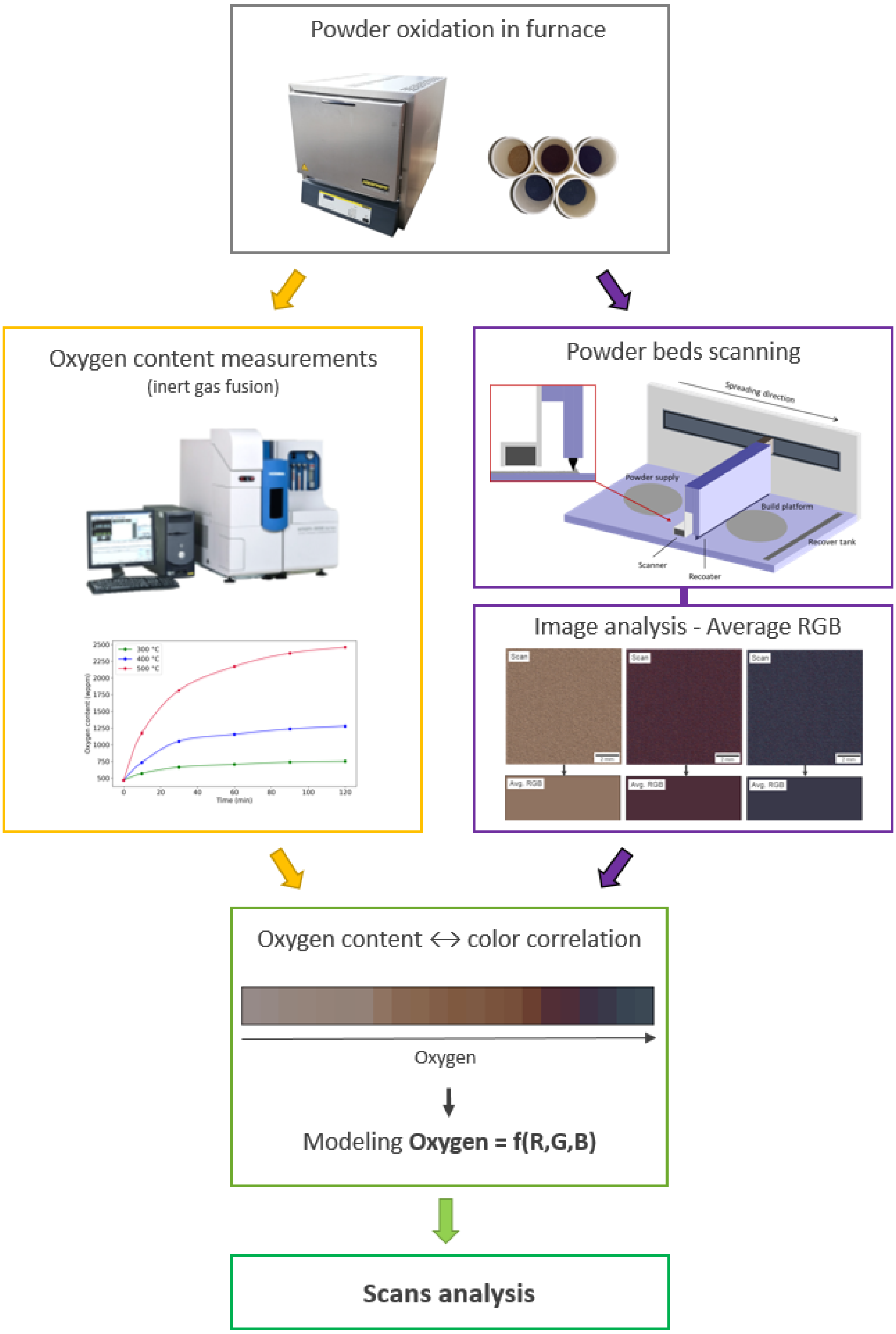

Figure 4.11 – Summary of the methodology developed for the correlation between powder color and powder oxygen content.

4.3 Determination of powder beds oxygen content

With the correlation function determined for SS316L powder, scan analyses can be carried out to perform in-line measurements of powder bed oxygen content to test the potential of the technique in actual L-PBF conditions. This section presents the results of scan analyses performed on different grades of degraded powders. Repeatability analyses and axes of improvement are also provided and discussed.

4.3.1 Scan analysis methodology

The methodology of in-line monitoring of the powder bed by scan analysis is relying on the correlation function between particle color and oxygen content that has been defined. Scan analysis consists in the following steps:

(i) Spreading of a powder layer on a substrate plate or an already existing powder bed;

(ii) Scan acquisition of the powder bed area at high spatial resolution to resolve single powder particles in color;

(iii) Image analysis and determination of oxygen content in the powder bed using the correlation function.

In order to study various spatial scales at which the oxygen function prediction should be carried out, and to propose image analysis of different execution times, two approaches corresponding to item (iii) of the methodology were developed. These two methods are schematized in figure 4.12. The first method consists in applying the prediction function to obtain the oxygen concentration of each pixel, then the average oxygen content of the powder bed is calculated by summation over all individual pixels. In the second method, the average RGB values are calculated first, then the prediction function is applied with these three channel values as arguments to get the average powder bed oxygen content. Method 2 is obviously much faster, but could lead to different results, due to the non linear form of the polynomial function O = f(R,G,B), and the heterogeneous distribution of colored particles in powder beds.

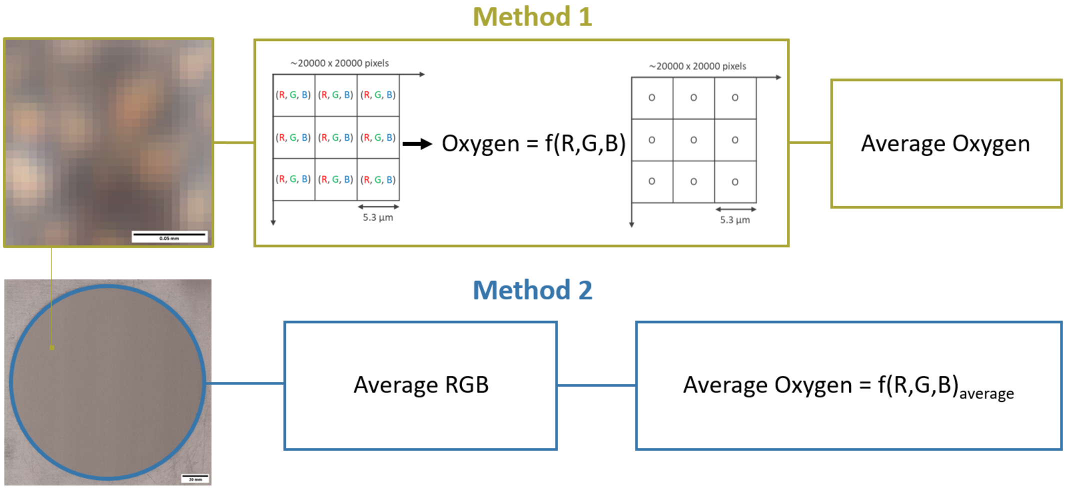

Figure 4.12 – Scan analysis methods for oxygen content measurement in powder bed scans.

4.3.2 Scan analyses of recycled powders

Scan analyses were conducted on several powder samples collected during the recycling study presented in chapter 3 [250]. As a reminder, the SS316L powder was used, recovered, sieved and reused to produce 15 successive L-PBF fabrication on the Trumpf machine, without adding any virgin material. Powder bed scans were acquired with the virgin powder (R0), 1-time recycled (R1), 5-times recycled (R5), 10-times recycled (R10) and 15-times recycled (R15) powders.

Figure 4.13 shows powder bed scans acquired at 4800 dpi with digital zooms of the virgin powder (R0) and the highly recycled powder (R15). It can be observed that on the global views, the hue of the two scans observed globally are slightly different. The R15 powder bed appears somewhat darker than the virgin one, with a brown shade compared to a rather grey powder bed for R0. Close-up views on the scans highlight the diversity of colors and the dispersion of colored particles in the powder bed for recycled powder. Spatial resolution allows to notice particle to particle changes, which would seem a priori necessary in view of the non-uniformity of the powder bed with regard to this color feature.

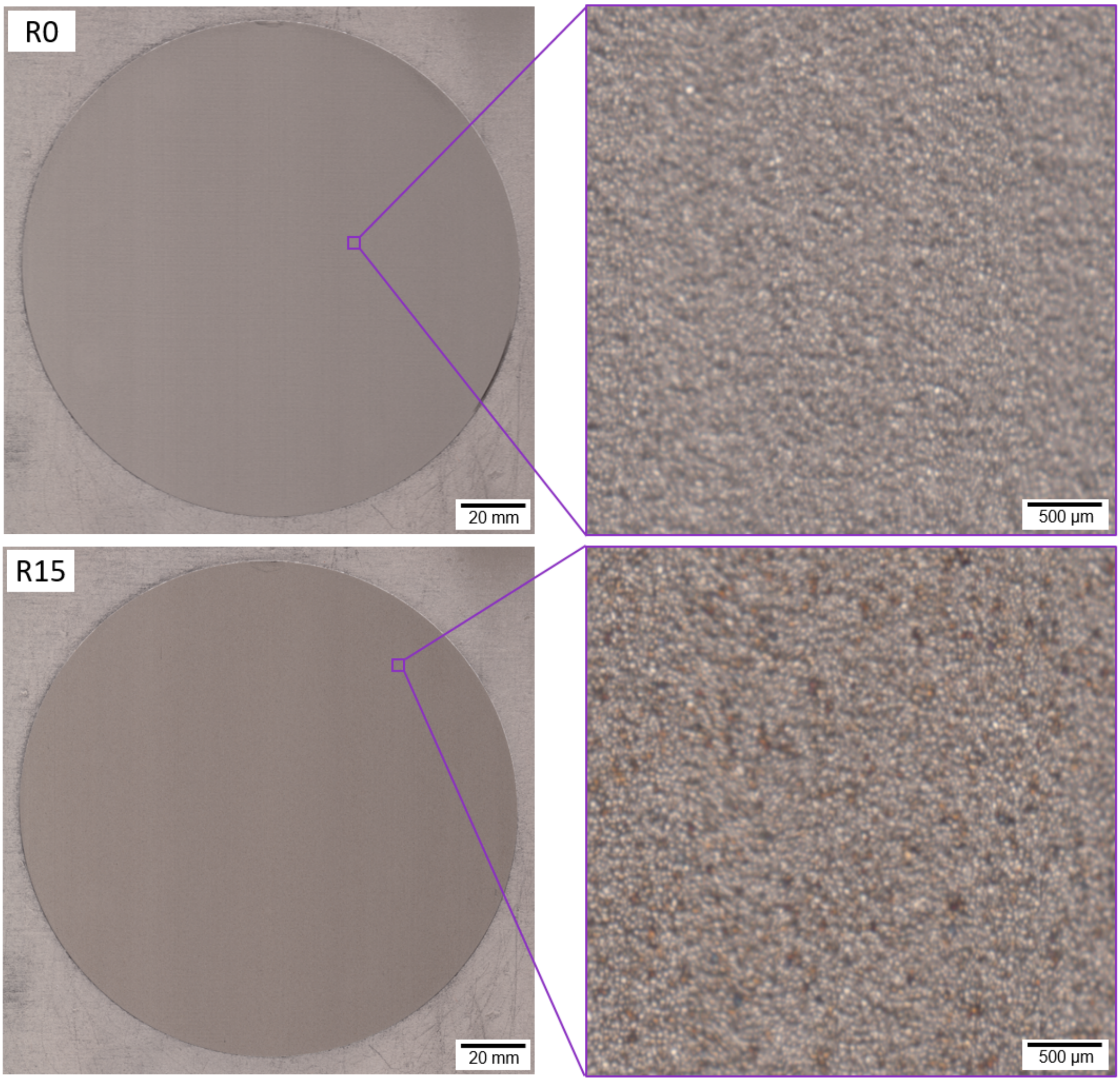

Figure 4.13 – Powder bed scans of virgin (R0) and 15-times recycled (R15) powders.

All the scans of virgin and recycled powders were analyzed using the two methods presented in figure 4.12, and compared to ex-situ measurements of oxygen contents by inert gas fusion. Figure 4.14 presents the measured oxygen concentrations in wppm obtained with the two scan analysis methods and the ex-situ conventional method, in function of powder recycling state.

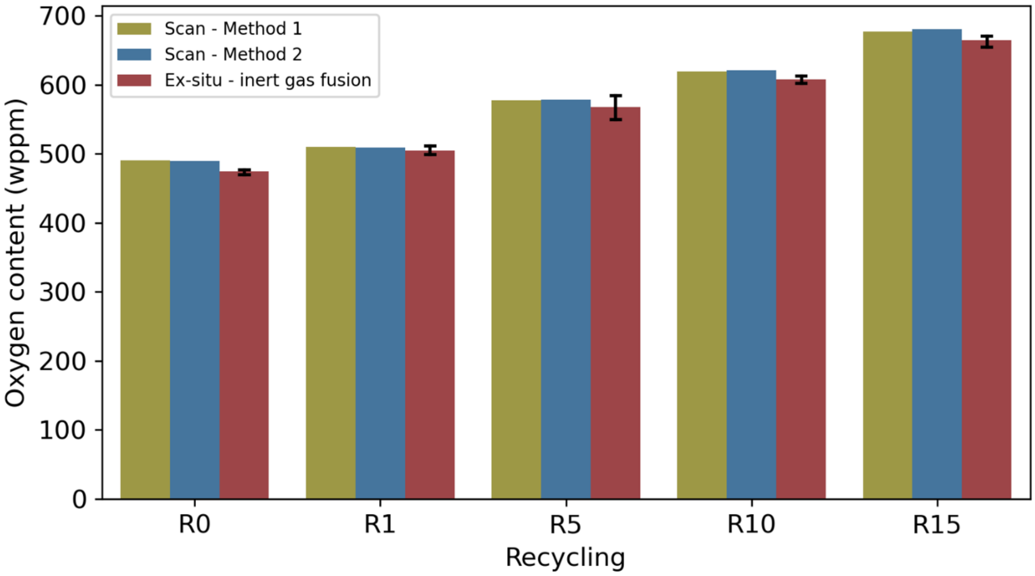

Figure 4.14 – Oxygen content of powder measured by scan analysis and inert gas fusion in function of recycling.

The first positive result is that the scans results successfully follow the trend of increased oxygen content as the powder is successively recycled in the L-PBF process, with an oxygen rise up to nearly 200 wppm between R0 and R15. Even for small variations, such as between the virgin powder and the one recovered and sieved after one print (R1), the accuracy of the in-line monitoring measurement is sufficient to account for an oxygen increase of only 20 wppm. The results are slightly higher with the scanning methods 1 and 2 compared to ex-situ measurement, up to 10-15 wppm, but still remain most of the time within the standard deviation of the inert gas fusion values.

Another positive result is that the two scan analysis methods yielded to extremely close results, and especially that the results of method 2 are very similar to those of the first method (less than 5 wppm of difference). The first method should be theoretically more robust because it applies the calibration to each pixel, and the average of the calculated oxygen values can thus be assumed to represent the physical amount of oxygen present in the surface of the powder bed. The second method is faster because the image processing of determining RGB average values on a set of pixels is very simple, and the calibration function is applied only once. It was a priori far from being obvious that the two methods would present close results in view of the diversity of colored particles present on powder beds of degraded materials. Moreover, as mentioned above, significant differences could have been expected from a mathematical point of view due to the non-linear model employed for the regression leading to the calibration function (equation 4.3).

Given the similarity of the scan results, only the second method could be applied for future analysis to obtain an almost instantaneous oxygen content value of a powder bed layer (code execution of 70 ms for a 100 mm^2 area / 7 s for a 10 cm^2 area). Method 1 is nevertheless more rigorous, and opens a number of possibilities to evaluate oxygen content of a given powder bed at various spatial scales, if the relevant integration is carried out a posteriori.

4.3.3 Repeatability analyses

Several repeatability analyses were conducted to evaluate the robustness of the methodology and monitoring setup developed within this work. First, the potential dispersion that could occur between scans of multiple layers of an a priori identical powder batch was studied (figure 4.15).

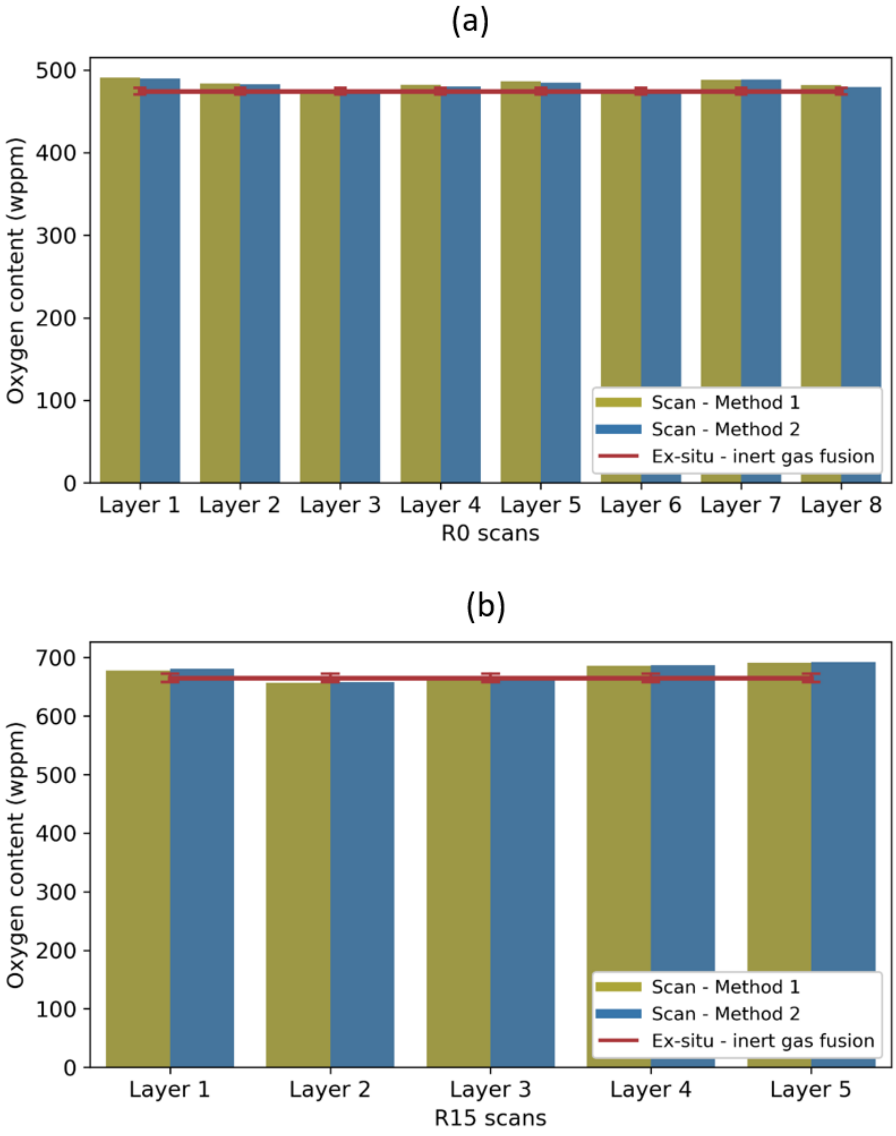

Figure 4.15 – Scan analyses repeatability with oxygen concentration measurements of different layers of (a) virgin powder R0 and (b) R15 powder, compared to the corresponding content measured ex-situ.

Figure 4.15 (a) presents in-line measurements of oxygen content for different powder bed layers of virgin powder (R0), and figure 4.15 (b) shows the same type of data for different layers of R15 powder. For each layer, both scan analysis methods were performed, and the fixed value of ex-situ measurement of the powder oxygen concentration is also displayed in the graphs. The oxygen contents measured by image analysis are consistent, and therefore in close agreement with the value measured ex-situ, as it was the case in figure 4.14. The recycled powder R15 presents larger variations between different layers than the virgin powder, that transletes in a standard deviation of 15 wppm between the investigated 5 scanned layers of R15, as compared to 6 wppm between the 8 layers of R0. The differences observed with the highly recycled powder can be explained by the fact that this batch contains a randomly distributed fraction of oxidized particles, and several powder spreadings can lead to physically and chemically different powder beds. On the other hand, virgin powder is not expected to feature fluctuations and should theoretically be free of contamination, which was mostly confirmed with this repeatability analysis showing a much more uniform oxygen concentration in different powder bed layers.

Other explanations, of technological nature, can also be the cause of fluctuations in the results of in situ analysis. Since the technique developed in the present work relies on the evaluation of the color of the powder in an image, optical artifacts can therefore alter the determined values. Any types of defects in the powder bed will distort the color results. For instance, defects on the recoater or large particles being dragged by the latter can create lines parallel to the linear motion of the recoater. Additionally, variations of the recoating velocity or super elevated parts can induce linear defects perpendicular to the direction of spreading. These linear irregularities usually appear darker than the rest of the powder layer in the acquired images, as shown in figure 4.16 (a). Consequently, this leads to an overestimation of the calculated oxygen concentration in the powder bed scan.

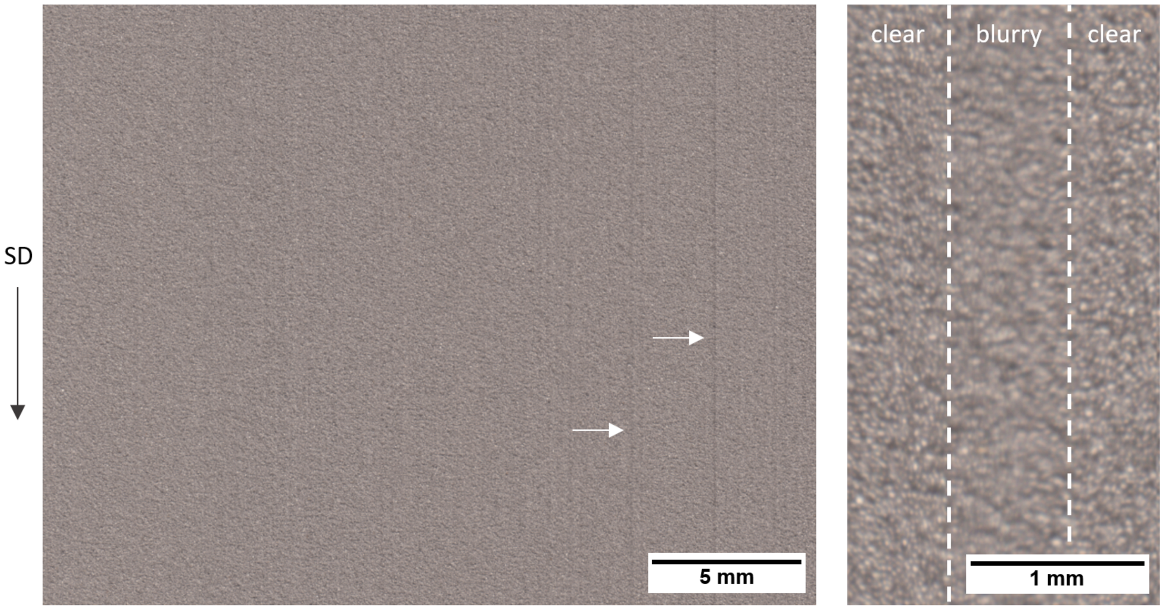

Figure 4.16 – Examples of defects in powder beds scans: (a) recoater lines (indicated by white arrows) parallel to the spreading direction (SD), (b) Focus fluctuation at high magnification due to powder layer height variations.

Besides, the scanner used in the powder bed scanning setup, based on contact image sensors presents a really narrow depth-of-field, as its original purpose is to acquire images of flat planes. In L-PBF, a powder bed layer is never fully flat with the presence of particles of different sizes, and certain zones can appear blurry due to layer height variations (figure 4.16 (b)). This is actually what Le and Seita [215] exploited on a similar monitoring setup, using out of focal plane blurriness level to determine variations in powder layer thickness. In the present study, this feature can be a reason for alteration of the results in terms of oxygen content.

Other types of image analysis could be considered to limit fluctuations and improve the monitoring process reliability. For example, particle detection could be implemented in order to remove the edges and keep only central pixels of each particle. Any change of image analysis methodology needs to be also carried out during the calibration leading to the correlation function. On the other hand, the present method also stands out because of the simplicity and quickness of the analysis employed.

Another kind of repeatability analysis was implemented, to investigate the consistency of the results spatially, on the surface of the powder beds. To this end, after scan acquisition, a large square of 106.8 cm^2 inside the build platform was sliced into a 10×10 square grid and analyzed zone by zone using the two scan analysis methods. This procedure allowed to draw oxygen content maps with the image analysis measurements in each of the 100 zones. This spatial repeatability analysis was conducted on several samples of different grades of powders. As expected, there were again no significant differences regarding the two scan analysis methods, with results varying by less than 5 wppm. However, differences on the surface were observed, with similar trends for all powder bed layers analyzed. Figure 4.17 shows the data acquisition procedure with the division of the powder bed image into a grid, along with the oxygen content maps obtained for R0 and R15 powder bed layers. The measurements presented here were obtained on each zone with the second image analysis method.

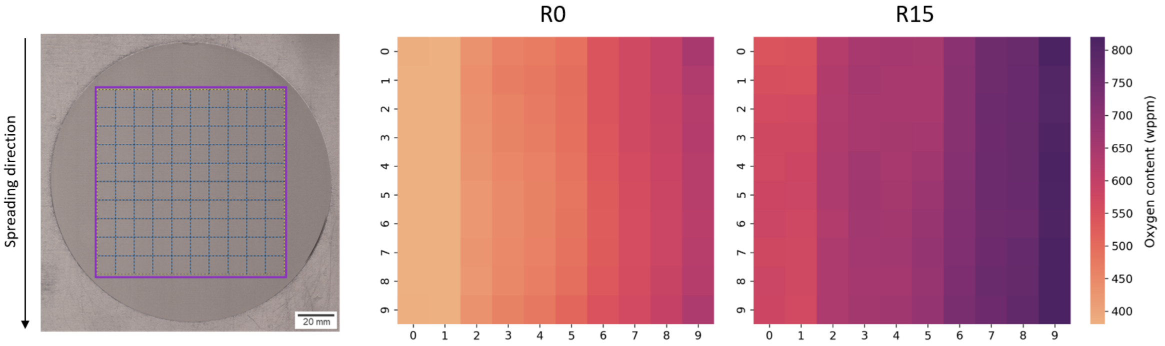

Figure 4.17 – Oxygen content maps measured by scan analysis for virgin (R0) and R15 powder beds.

The oxygen maps created show the presence of columns of different colors representing different average oxygen concentrations calculated by scan analysis. There is thus a good uniformity of the results obtained along the direction of the powder spreading (from the top to the bottom of the images). However, significant variations are noticeable between the left and the right of the scans, *i.e.* transverse to the motion of the recoater arm. The bias is progressive over the width of the scan, with systematically smaller values measured on the left and larger ones on the right.

Different explanations can be proposed to explain these variations across the width of the powder bed, that are associated to the experimental setup. A first probable cause is related to a flatness defect of the build platform or build plate. The scans were acquired on powder beds and not single layers, after the spreading of several layers in order to replicate conditions that would occur during L-PBF processing, or at the end of a printing. However, due to the small amounts of powder in hand, such as the samples recovered after successive recycling, the overall thickness of the powder beds still remained quite low. A planarity issue had indeed been identified during the spreading of a single layer, with thinner thickness on the left hand side of the build plate. Therefore, it can be suggested that the powder bed thicknesses employed did not compensate this flatness defect. Thinner layers usually appear brighter, which can explain the smaller oxygen contents calculated on the left hand side.

Flatness deficiency on the experimental setup can also be caused by the recoater arm. The recoater height, and subsequently the force applied by the rubber blade on the frame and build platform during its motion is set with micrometric positioning stages. This manual adjustment may lead to flatness defect in the powder bed.

Another potential explanation for the observed spatial distortion could be a potential tilt of the scanner. As explained and showed in section 2.5, figure 2.18, the scanner is mounted on the recoater arm and adjusted manually with two micrometric positioning tables. This manual adjustment could have altered the planearity of the sensors, affecting the acquired images. However, analyses carried out on images acquired with a desired inclination of the scanner also revealed the same distortion from left to right, although the tilt led to really large areas being blurry. Therefore, the hypothesis of the flatness defect, caused by either the plate or the recoater, remains the most plausible and leaves room for further improvement.

Nevertheless, it should be mentioned that this spatial bias did not lead to distorted results thanks to its identification. All the experiments, including the calibration with the scans of oxidized powders, the modeling of the oxygen prediction function, and the results of scan analyses presented above, were replicated and all carried out on a central area of the powder bed images. Moreover, a positive byproduct of the methodology developed in the frame of the present study, even though not directly related to the oxygen concentration, is that the monitoring process could assess other defects and issues associated with the spreading of a powder bed in L-PBF.

4.3.4 Scan analyses of other degraded powders

In addition to the scan analyses carried out on recycled powder samples (presented in section 4.3.2), other types of degraded powders were scanned and analyzed to enlarge the collected database and to further validate the concept implemented in this work.

'Artificially' degraded powder samples, consisting in mixes of virgin powder and furnace-oxidized powders were also analyzed. Four mixes were prepared then scanned after spreading of a powder layer on the powder bed area. Two mixes were composed of 5 and 10 wt.% respectively of furnace-oxidized powder with an oxygen concentration L1 (1000 wppm), the remaining 95 and 90 % being fresh powder, and two others contained the same fractions of oxidized powders (5 and 10 wt.%) with an oxygen level L2 of 2370 wppm. The results of determined oxygen content by image analysis of the powder bed for these four artificially degraded samples, as well as the theoretical values and ex-situ measurements are reported in figure 4.18. The theoretical values represent the expected oxygen content of the powder mixes based on the oxygen concentrations and mass fractions of the two constituents (virgin powder and furnace-oxidized powder).

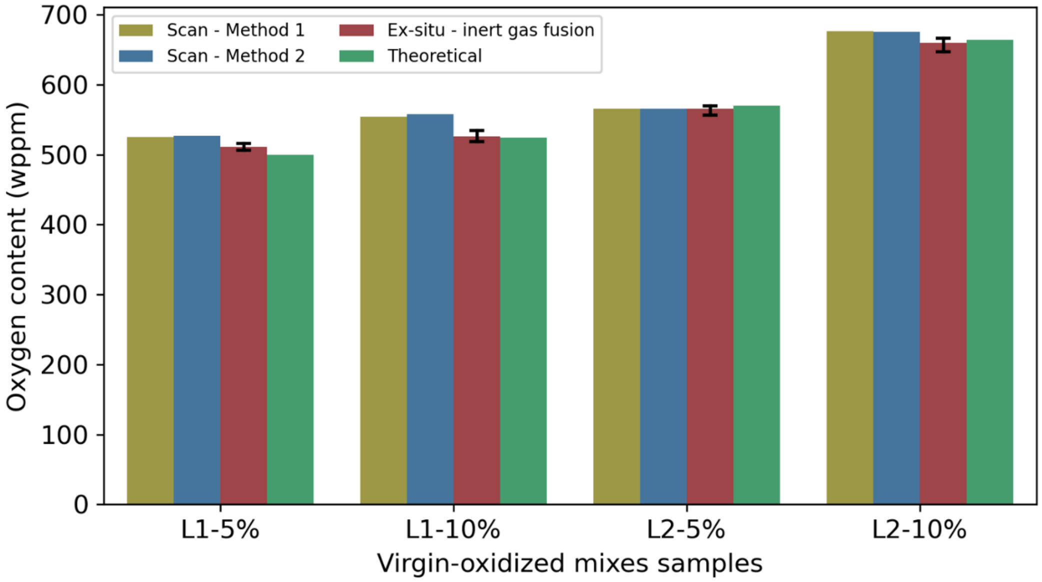

Figure 4.18 – Oxygen content of mixes of virgin and furnace-oxidized powders measured by scan anlysis and inert gas fusion in function of recycling.

Inert gas fusion measurements are almost in perfect agreement with the theoretical values, for all four conditions. Regarding the results with the in-line scan analysis procedure, both methods are again in very close agreement. Even though the trends are respected, a slight overestimation of the values compared to those measured ex-situ is nevertheless observed.

It can be noted that for a given fraction of oxidized particles in the mixes, the overestimation is more important for the L1 samples. The oxidized particles blended in these L1 samples are light orange particles, while the L2 samples are composed of blue oxidized particles, as shown in figure 4.19. An interesting feature to be observed is that in both L1 ans L2 samples the edge of colored particles are darker, certainly because of the particles sphericity and the resulting angle with respect to the light source during image acquisition. This phenomenon can potentially lead to an overestimation of the oxygen level and could explain the difference between L1 and L2 batches. Indeed, L2 oxidized particles are blue and already quite dark, therefore the edge effect is not as pronounced, with less color variations. On the other hand, these variations are more present with the lighter colors of oxidized particles in L1 samples, which could explain the larger differences observed compared to the L2 mixes. Moreover, for a given batch L1 or L2, the oxygen concentration overestimation is more important for the samples containing 10 % of colored particles. The increase in the number of colored particles amplifies the edge effect, and consequently leads to larger divergences.

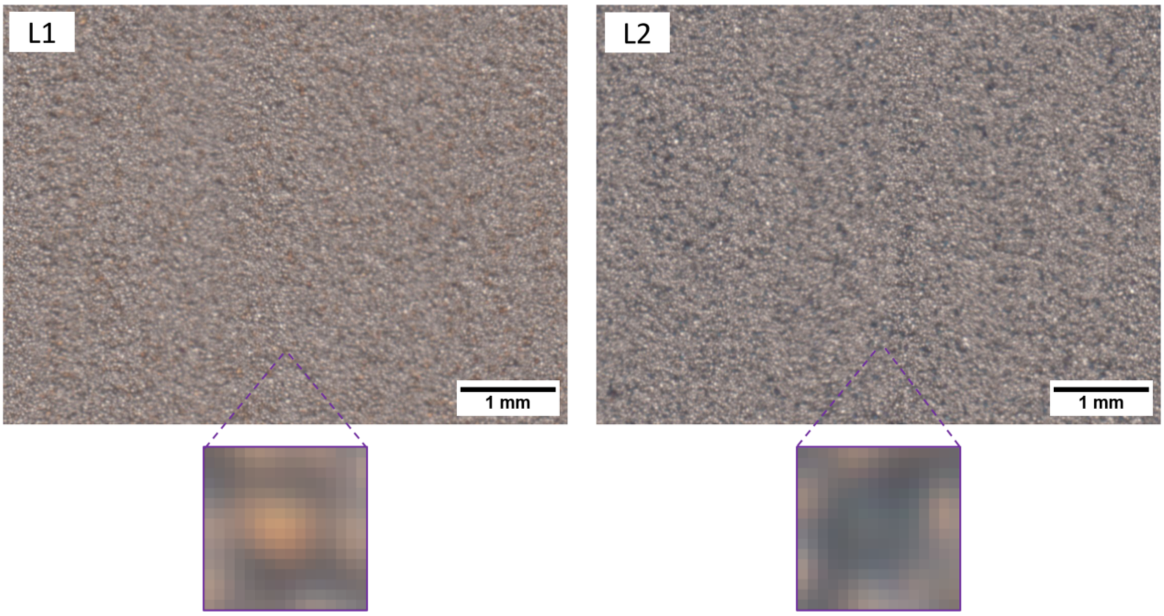

Figure 4.19 – Powder bed scans of L1 and L2 samples with 10 % of oxidized particles, and close-up view on a single oxidized particle of each batch highlighting the edge effect.

Some other samples of degraded powders recovered after L-PBF processing were also investigated. Another R1 powder (called P1), collected after one fabrication in the Trumpf TruPrint 1000 machine has been evaluated. Up to now, all recycled powders presented in section 4.3.2 had been analyzed after being subjected to a sieving step to remove large particles. Here, a batch of un-sieved powder was also analyzed (P1-u), in addition to the P1 sample collected after the screening procedure through the 50-µm sieve. Figure 4.20 is a scan image of the powder bed with un-sieved powder recovered after one print (P1-u). Extremely large spatter particles, ejected from the melt pool during laser scanning are visible, and are correlated with a very high oxygen pickup as seen in chapter 3. The sieving procedure allows to limit powder degradation and oxygen increase, as confirmed by ex-situ measurements of oxygen concentration by inert gas fusion: P1-u presents an oxygen content of 535 ± 11 wppm, versus 519 ± 12 wppm for P1.

The oxygen concentrations were reliably predicted using the in-situ scan analysis approach, with values of 540 wppm and 516 wppm for P1-u and P1 respectively, using the second scan analysis method presented in figure 4.12. It was not yet obvious that the method would work for such samples, where the oxygen pick-up is mainly due to the presence of large, highly oxidized particles, which are not necessarily colored. Moreover, some artifacts such as lines on the powder bed surface are present (as presented in figure 4.16 (a)) due to these large particles being dragged by the recoater, which could theoretically also falsify the calculation.

Figure 4.20 – Powder bed scan of un-sieved powder after one printing cycle (P1-u) displaying large spatters on the surface.

Finally, powder beds made entirely of sieved residues collected from various L-PBF prints and sieving stages were also tested (figure 4.21). The scanning method calculated an average oxygen concentration around 1400 wppm, compared to 1600 wppm estimated by the chemical analysis. Even though the difference in the results of oxygen concentration between in-situ and ex-situ measurements is much larger compared to the previously tested conditions, the in-line approach is still once again quite consistent, even with this very unconventional powder bed. Indeed, the latter is composed solely of particles and agglomerates larger than 50 µm, with severe oxidation and oxygen contents coming from extreme conditions undergone during the L-PBF process.

Figure 4.21 – Powder bed scan of sieved residues.

Two factors can be responsible for the observed underestimation, and are related to the unconventional characteristics of the sieved residues. First, these particles are clearly not optimal for powder spreading as shown above and in section 3.3.6, figure 3.23. The sieved residues have large sizes and low sphericity with the presence of satellites and agglomerates. This results in a poor spreading as for the P1-u sample, with dragged particles leaving areas without powder. The overall powder bed shade is darker than that of virgin or recycled powders. In this case, lack of powder and holes can appear lighter, or even grey in some cases due to the small amount of sieved residues available, the trails revealing areas of the build platform underneath. This effect can minimize the calculated oxygen concentration.

Secondly, sieved residues contain melt pool spatters, which are known in the literature and were found in chapter 3 to present a selective oxidation of Si and Mn on the surface for stainless steel powders [129, 137, 145]. EDS point analysis revealed that the oxides nodules present really high contents of oxygen (O $\sim$ 35 %). This selective oxidation is not taken into account by the image analysis method, with the nodules and spatter particles being not necessarily colored. An additional point to be mentioned is that the oxygen concentration of some sieved residue particles might be above the highest tested range during the calibration and determination of the correlation function.

Nevertheless, with all these limitations in mind, it is remarkable that the scanning procedure was able to provide a decent estimate of the oxygen concentrations for powder beds completely different from the usual standards of the L-PBF process. Besides, the scanning method remained really accurate for commonly recovered un-sieved powders having typical fractions of spatter blended with the other particles.

4.4 Summary

In this chapter, a new monitoring technology was developed to measure the oxygen content of powder beds by in-line scanning of spread powder layers. Owing to the layer-by-layer fabrication of specimens typical of AM and L-PBF, it is possible to control material quality at a layer-wise level. An L-PBF system was customized to integrate a flatbed scanner into the spreading unit of the machine, allowing to acquire in-line colored scans capturing the entire powder bed area at really high spatial resolution (4800 dpi, 5.3 µm × 5.3 µm/pixel).

The recycling study implemented in chapter 3 allowed to investigate the degradation of powder attributes with successive reuse, and identify a gradual increase of oxygen concentration with recycling coupled with an observed increase of colored particles in the feedstocks. The monitoring methodology developed in this work takes advantage of this coloration of stainless steel particles, related to their oxygen content, as an indicator of the material quality.

The approach detailed in this chapter is based on a preliminary calibration, to perform a correlation between the particles color and their oxygen content. The methodology includes the oxidation in a furnace in air of several powder batches at 300 °C, 400 °C and 500 °C, from 10 to 120 minutes, followed by the measurement of the corresponding oxygen contents by the conventional inert gas fusion technique. Then, powder bed scanning of those furnace-oxidized powders was used to determine the average RGB values of each acquired scans and to model the oxygen content as a function of the three color channels intensity (R, G, B).

The in-line monitoring technique allows to accurately predict the oxygen content in a powder bed layer, after powder bed scanning and a fast image analysis consisting only of calculating the average RGB colors and applying the oxygen prediction function. Numerous case studies were implemented to validate the concept. Recycled powder samples recovered from the recycling study of chapter 3 at different degradation states were evaluated using the scan analysis method. The determined powder beds oxygen contents proved to be in very good agreement with ex-situ measurements obtained by inert gas fusion. Other degraded powder samples were also assessed, with mixes of virgin powder and furnace-oxidized powders at different oxygen levels and fractions of altered particles, recycled powders before the sieving procedure, or even samples containing only sieved residues. Again, the comparison between oxygen concentrations calculated by the scan analysis and the ones measured by conventional chemical analysis is found to be relevant.

An advantage of the solution of in-line measurement is that this offers the opportunity to follow the quality of the powder bed regarding the oxygen concentration on really large quantities that are directly representative of the L-PBF material. With more and more L-PBF machines working in closed powder circuit loops, in-line monitoring appears to be the most viable solution to track the attributes of the particles. Moreover, the methods stands out by its simplicity, with straightforward and fast image analysis consisting only in the use of the raw image and its colors. However, a limiting factor remains the long acquisition time of the scans to provide such high spatial resolution. Solutions and perspectives will be discussed at the end of the manuscript in the conclusions and perspectives section) to circumvent this issue, as well as the limitations of the technique presented in this chapter.

Chapter 5

Influence of build characteristics and chamber oxygen concentration on powder degradation

Submitted paper associated to this chapter:

T. Delacroix, F. Lomello, F. Schuster, H. Maskrot, C. Baslari, U. Gaumet, Y. Flici and J.-P. Garandet, "Influence of build characteristics and chamber oxygen concentration on powder degradation in laser powder bed fusion," submitted to *Powder Technology*, 2022.

5.1 Introduction

The two previous chapters allowed to analyze the effects of powder recycling and develop a system to monitor the feedstock quality with regards to its oxygen content. The last part of this PhD thesis focuses on the effect of build topology and chamber oxygen content on powder degradation in L-PBF. As stated a number of times, material reuse is essential for cost savings, but the recycling study conducted in chapter 3 showed that powder alteration due to the complex laser-matter interactions in L-PBF is inevitable. One of the main changes observed in this work and a recurring finding in the literature for many materials is the increase in the oxygen content of the powder. This phenomenon, as well as other types of modifications are directly influenced by the operating parameters of the process, together with the characteristics of the build.

Numerous factors influence the alteration of particles observed in L-PBF, such as the most studied parameters for process optimization, *e.g.* laser power and scanning speed, which can affect the number of spatter particles. Other less studied parameters, referenced in the following as build characteristics, can also make a difference in the reusability of the powder [251]. The melted volume for example is related to the amount of material exposed to the laser beam and thus to the associated by-products and heat affected zones. Fabrication height, *i.e.* the duration of the process, and parts spacing can also impact powder degradation. In addition, the atmosphere in the build chamber, and more precisely the concentration of residual oxygen in the chamber could be another factor of interest, in order to limit the degradation of the powder and more precisely its oxidation.

Numerous fabrications were conducted on the Trumpf machine with parts of different volumes, spacings and heights. In addition, all fabrications were reproduced with a rather high oxygen concentration limit in the build chamber. Powder recovered after the prints in zones of interests were characterized to investigate the changes in particles attributes.

5.2 Powder degradation study methodology

The different aspects investigated for the study of powder degradation are schematized in figure 5.1. Four melted volume fractions were studied, with the elaboration of cubic specimens inside square walls, accounting for a volume (and surface) fraction of 10 %, 25 %, 50 % and 75 %. The square walls were printed to facilitate volume calculations and especially the recovery of the powder in the area at the end of the fabrication.

Influence of parts spacing and height was explored with the manufacturing of walls of fixed width (10 mm) separated by grooves of different spacing: S0.5, S1, S2, S3, S15 and S30, the values being expressed in mm. In addition, three different heights: 10 mm, 25 mm and 50 mm (H10, H25 and H50) were elaborated for each spacing. The powder was collected inside each groove separately for local characterization.

Finally, two different oxygen concentrations inside the build chamber were tested for each condition previously described. The prints were carried out first with a maximum requirement for residual oxygen content of 300 ppm, and replicated with an O_2 target of 1000 ppm, all oxygen content values being expressed in weight.

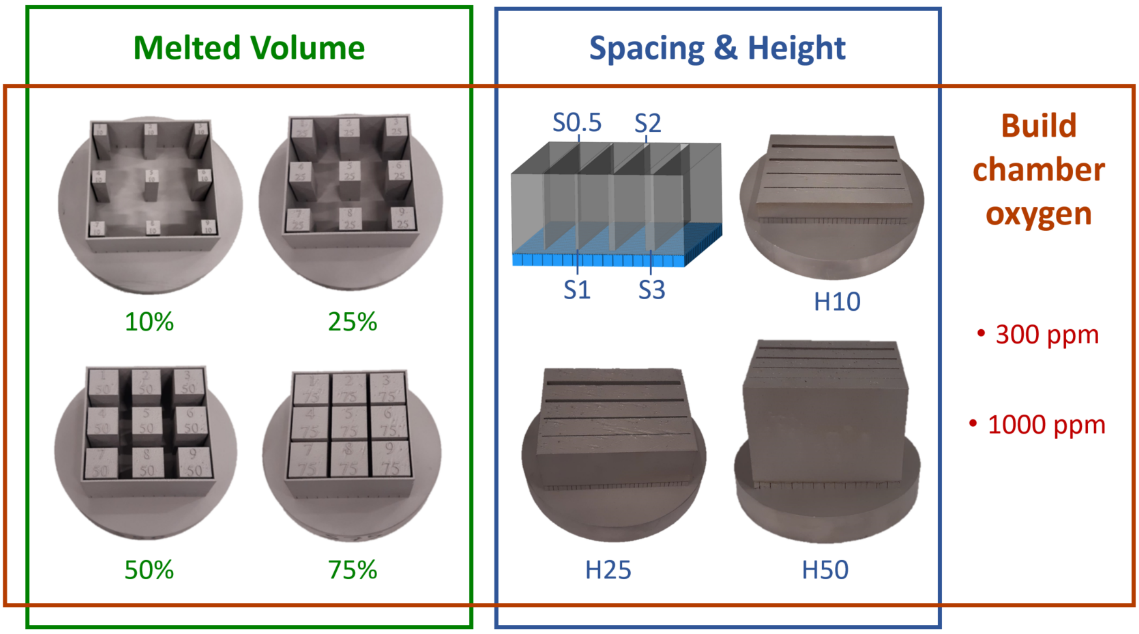

Figure 5.1 – Chart of the powder degradation study methodology.

The shielding gas used is an ultra high-quality argon (Argon 5.7) with controlled flow rate resulting in a typical laminar gas velocity flow of 3 m/s over the build platform, as represented in figure 5.2 (a). Oxygen sensors in the process chamber monitor the protective gas circulation system. The L-PBF process only starts when the oxygen content in the build chamber has reached the programmed value (0.1 wt.% O_2 or 0.03 wt.% O_2), after injection of shielding gas also called inerting. Gas recirculation takes place throughout the entire printing with the laminar flow coming from the front to the back of the build area. The gas is transported from the chamber to a filter, and the filtered gas is then reintroduced in the chamber. Supply of new inert gas is provided when the oxygen concentration exceeds the target value.

The objective of the gas flow is to carry the evaporation fumes (formed during the melting of the powder by the laser beam) away from the build area, as well as driving away the ejecta and thus limit the redeposition of these byproducts on the powder bed and solidified material. This works for a share of ejecta as it can be seen in figure 5.2 (a) with a heap of large oxidized spatters close to the gas outlet. However, the gas flow does not prevent the contamination of the powder bed for those spatters falling back on the powder bed area, as discussed in detail in chapter 3.

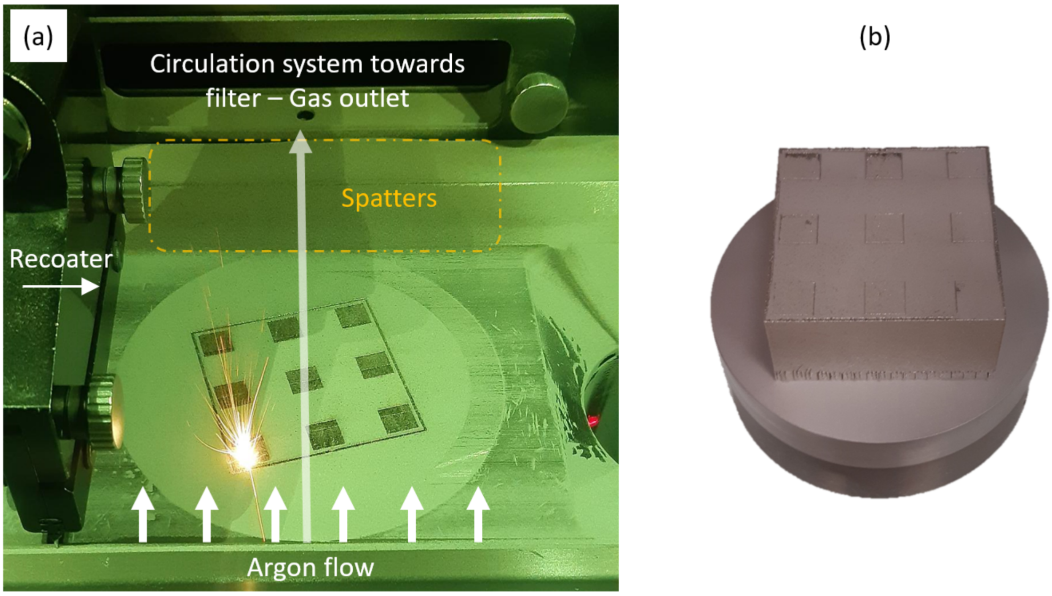

Figure 5.2 – (a) Photograph of the build chamber during the L-PBF process with 25 % of melted volume inside the square, showing the laminar gas flow and redesposited byproducts (b) Image of the completed job with 25 % of melted volume at the exit of the machine with powder kept inside the walls before its recovery and characterization.

Figure 5.2 (b) shows a completed fabrication with 25 % of melted volume inside the square walls, with powder kept inside before its recovery and characterization. As done in the recycling study in chapter 3, the powder samples recovered for each condition (inside the walls for the melted volume study, inside each groove for the spacing and height study) were sieved with a 50 µm mesh, and characterized using OM, SEM, EBSD, XRD, laser granulometry and inert gas fusion. A few parts were cut and analyzed to evaluate the impact on surface roughness, by optical profilometry.

All other processing parameters (laser power, scanning speed, etc.) were fixed in the Trumpf TruPrint 1000 printer, as detailed in chapter 2 section 2.1.1.

5.3 Influence of parts volume fraction and chamber oxygen concentration

5.3.1 Oxygen content

The oxygen content of the powder samples recovered from the build platform inside the square walls at the end of the fabrications and sieved with a 50 µm screen was measured by inert gas fusion. Figure 5.3 displays the powder oxygen content (in wppm) in function of the melted volume fraction in the print (in %), for the two conditions of chamber oxygen concentration during L-PBF processing (300 ppm in blue and 1000 ppm in red). The dotted lines represent the linear trendlines of the two series.

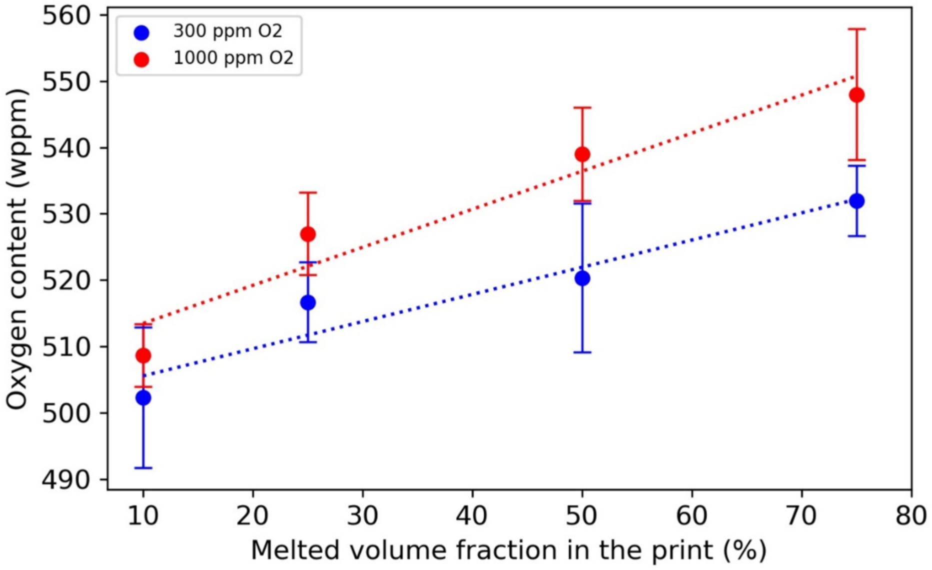

Figure 5.3 – Oxygen content of the recovered powder as a function of the melted volume fraction in the print and chamber oxygen concentration.

The results show that regardless of the oxygen concentration in the build chamber, the oxygen content of the recovered powders at the end of the L-PBF process is higher when a larger volume has been solidified as parts. The increase is even gradual and proportional to the fraction of melted volume in the print.

The second important observation is that for all conditions of melted volume fraction (10 %, 25 %, 50 % and 75 %), the oxygen content of the recycled powder is always higher for fabrications carried out with a residual oxygen concentration of 0.1 % in the build chamber, compared to those conducted with a maximum limit of 0.03 %.

As a reminder, the oxygen content of the virgin powder is 474 wppm. The values of this study are consistent with the recycling study which showed a one time recycled powder R1 with an oxygen content of 505 wppm after the first print. The manufacturing was conducted with 300 ppm of O_2 in the chamber and the melted volume fraction was slightly under 10 %, which fits with the values of the blue series, close to V10 (10 % of melted volume) at 300 ppm O_2.

5.3.2 Observations

The powder samples were characterized by OM and SEM. Figure 5.4 shows optical images of the powder recovered from the builds with 10 %, 25 %, 50 % and 75 % of melted volume (named respectively V10, V25, V50 and V75), boxed in red corresponding to the prints carried out with 1000 ppm of oxygen in the processing chamber. The observations will now be analyzed along the lines discussed in chapter 3 for the recycling study.

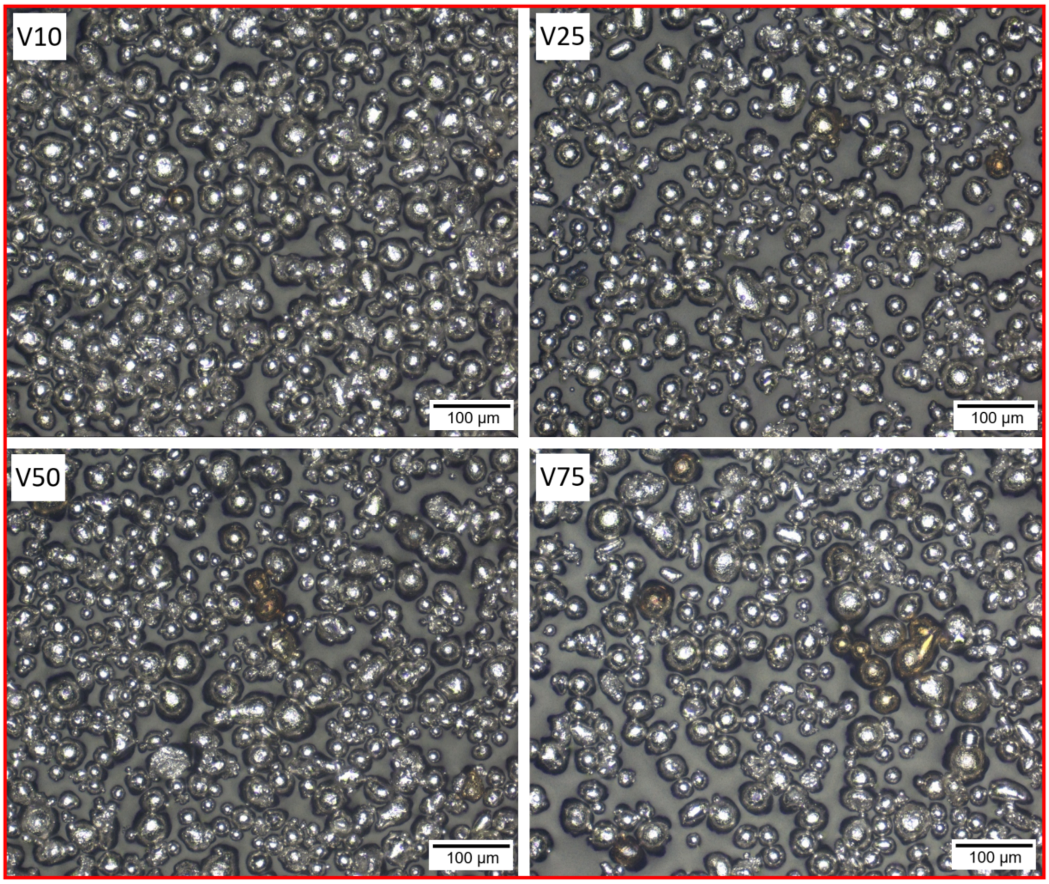

Figure 5.4 – Optical images of V10, V25, V50 and V75 powders from the fabrications conducted with a chamber oxygen concentration of 1000 ppm.

A slight increase of colored particles is noticeable with increased melted volume fraction. These observations were similar for the samples collected after manufacturing with 300 ppm of oxygen. As for the colored particles observed after numerous reuse cycles (section 3.3.4, figure 3.11 and figure 3.12), it can be assumed that the coloration oxidation occurs to particles close to the melt pool tracks and solidified parts that remain at relatively high temperature for a potentially significant amount of time, allowing the growth of a thin oxide film. In this work, the increase of parts volume (and surface per layer) leads to a longer length of lasing vectors and consequently a larger amount of powder in the vicinity of the parts edges. This results in a larger number of colored particles.

SEM micrographs of V10 and V75 powders from the two conditions of chamber oxygen concentration (300 ppm in blue and 1000 ppm in red) are presented in figure 5.5. The main difference between the samples coming from the two extremes of melted volume fraction is the number of particles with selective surface oxidation (particles with darker spots highlighted with white circles).

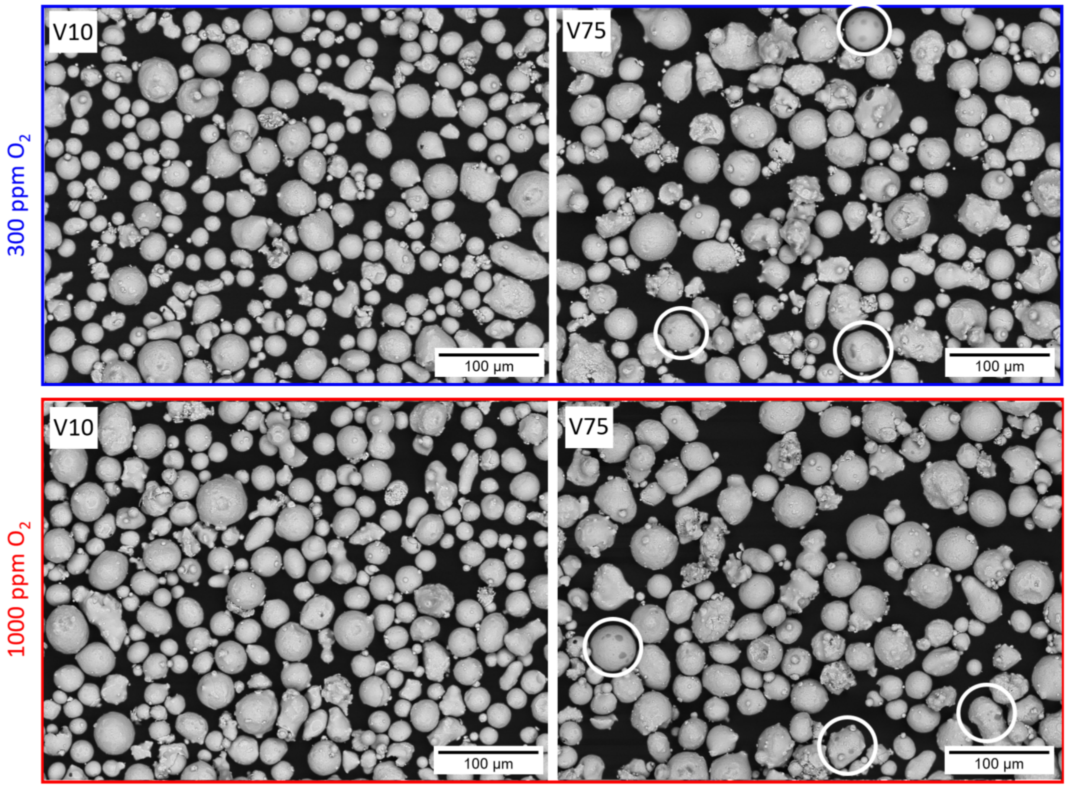

Figure 5.5 – BSE micrographs of V10 and V75 powders from the fabrications conducted with a chamber oxygen concentration of 300 ppm (in blue) and 1000 ppm (in red). White circles highlight particles with oxide nodules on their surface.

These partially oxidized particles are more abundant in V75 powders, for both chamber oxygen concentrations of 300 and 1000 ppm. EDS mapping and point analyses confirm the observations described in section 3.3.4 figure 3.14 and the literature, with again these dark nodules corresponding to a selective oxidation of Si and Mn. These particles, assumed to be melt pool spatters or vapor-entrained particles from the surrounding of the melt pool area are expected to be seen in larger amounts with larger volume of powder bed being scanned by the laser beam. The increase of melted volume fraction in the print lead to longer melt pool tracks and subsequent instabilities and spattering. However, this effect will not necessarily be translated in the same proportions to an increase of ejecta with oxide nodules in the recovered powder. Indeed, with larger volume being melted and solidified, the spatter particles have a greater probability to fall back on the parts area than the powder area, and might alter the properties of the part causing potential inclusions and lack of fusion pores in the following layers, instead of merely polluting the powder bed.

The two types of observed oxidized particles (colored and with nodules) can be held responsible for the increase of oxygen content in the recovered powder from fabrications with increased melted volume fraction. No noticeable differences in the OM and SEM observations were found between the samples from the prints with 300 ppm and 1000 ppm of residual oxygen, which does not enable to explain the measured difference in oxygen content in the powder in function of the chamber oxygen concentration during the print. Analysis of the sieved residues (particles and agglomerates larger than 50 µm, collected after the sieving of the powder) was conducted to help understanding this variation.

5.3.3 Sieved residues

Sieved residues (SR) were collected for each of the 8 conditions of recovered powder and analyzed. Figure 5.6 shows the fraction of powder sieved off from the powder samples collected in the build platform, in function of the melted volume fraction in the print and the condition of chamber oxygen concentration during the process. The blue and red dotted lines shows the linear regressions of the series of 300 ppm and 1000 ppm of oxygen in the build chamber atmosphere respectively.

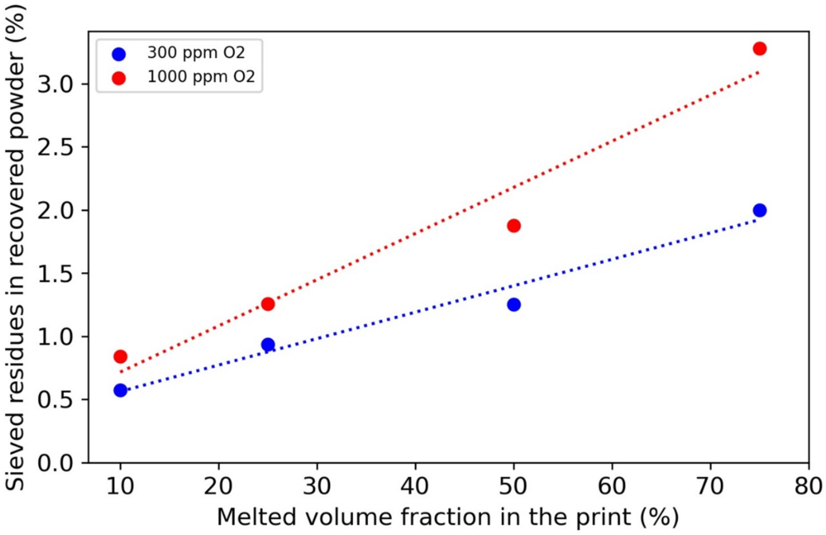

Figure 5.6 – Fraction of sieved residues in the recovered powder in function of the melted volume fraction in the print and chamber oxygen concentration.

It appears that the greater the volume of material melted in the L-PBF process, the greater the proportion of material recovered after sieving in relation to the total amount of powder collected on the build platform at the end of the process. To the first order, this increase can be taken as almost linear, for the two conditions of build chamber oxygen concentration.

In addition, all fractions of SR in the recovered powders are more important in the case of the prints carried out with a build chamber oxygen concentration of 1000 ppm. This means that for any print job in L-PBF, more agglomerates and larger particles are produced if the target of residual oxygen in the build chamber atmosphere is higher. Oxygen is known to influence the process, the morphology of the tracks, the surface tension of the molten pool and the spattering effect [99,108,131]. Other studies observed the same phenomena for titanium [252] and nickel alloys [130]. Interestingly, Chebil et al. [253] found that for aluminum alloys, a variation of chamber oxygen content from 100 to 2000 ppm showed an increase in the number of spatters ejected by less than 10 %. However, their study focused on really large spatters considered more harmful for the process, and their system might not have been able to detect smaller spatters, close to the particle size, which were found to be in the largest proportion by Ly et al. [109]. Li et al. [132] showed that an increase of oxygen content in build atmosphere leads to the increase of the balling phenomenon due to poor wetting conditions, as well as an increase of oxygen content in the printed parts. Leung et al. [131] studied the effect of powder oxidation on the melt pool dynamics by means of in-situ synchrotron X-ray imaging and quantified spatters. They revealed that the presence of oxygen, as oxides in the powder or in the atmosphere [254] could reverse the surface tension coefficient and Marangoni convection, generating inward centripetal flow. More spatters and agglomerates are reported [131].

As more large spatters are recovered after sieving for the prints conducted with high oxygen content, it can be assumed that this also applies to smaller ejecta that can pass through the mesh of the sieve, which could explain the difference measured in recovered powders oxygen content.

Morphology and surface characteristics of the SR were examined by SEM. Figure 5.7 shows BSE images of the SR of V10 powders from L-PBF processing at 300 ppm (in blue) and 1000 ppm of oxygen (in red). It is immediately clear that the SR of the powder sample recovered from the fabrication conducted with the higher oxygen level present a more severe oxidation. Oxide nodules are more numerous and especially larger at 1000 ppm. Oxygen content measurements on these two samples of sieved residues showed a significant difference as well, with 1072 wppm and 1325 wppm of oxygen for the chamber atmosphere conditions of 300 ppm and 1000 ppm residual oxygen.

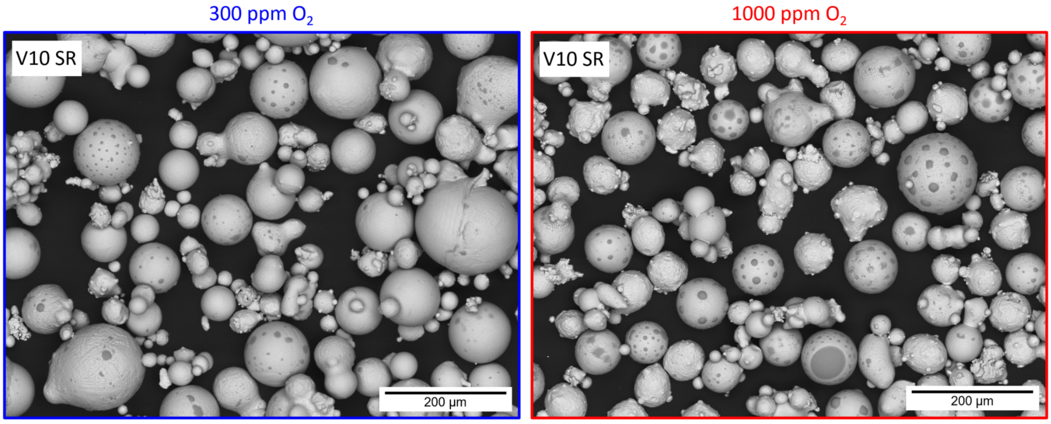

Figure 5.7 – BSE micrographs of sieved residues of V10 powders (V10SR) from the fabrications conducted with a chamber oxygen concentration of 300 ppm (in blue) and 1000 ppm (in red).

Using Inconel 718, Raza et al. [255] also studied spatters collected from various L-PBF fabrications, conducted under oxygen levels between 20 ppm and 1000 ppm in the build chamber. They showed a significant increase in spatter oxygen content with increased residual oxygen in the atmosphere. They also noticed a larger coverage of the powder surface by oxides with greater oxygen levels. In their study, the spatters analyzed are not sieved residues but are collected from the gas inlet in the build chamber and are likely to be vapor entrained particles due to their morphology. They do not exhibit the extremely large oxides nodules as presented in figure 5.7, but the authors highlighted differences in oxide thicknesses in function of the oxygen partial pressure during the process, with larger values for the highest oxygen level (above 50 nm for spatters generated under 1000 ppm O_2) [255].

This difference in surface oxides thickness could also be the case in the present study in sieved powders which can contain vapor entrained powders that could be more oxidized after processing with a build chamber oxygen level of 1000 ppm (figure 5.3). Particles smaller than the sieve size that are partially oxidized can also be expected to have more coalesced nodules as seen in figure 5.7, and this, combined with a greater number of ejecta generated under a higher partial pressure of oxygen in the L-PBF system, helps to explain the differences in recovered powder oxygen content measured by inert gas fusion.

5.3.4 Granulometry

The observations of the samples by SEM gave information about the presence of partially oxidized particles, but also on the particles size (figure 5.5). In these images, it seems that the particles are smaller and more numerous for both conditions of V10 powders, compared to the V75 samples. No great difference is visually noticeable between the two conditions of oxygen level in the processing chamber.

Laser granulometry was performed on all 8 sieved samples of this melted volume fraction study in order to assess the potential size changes in the powders recovered from the build platforms. Figure 5.8 shows the characteristics values of D_{10}, D_{50}, and D_{90} of all conditions, after sieving.

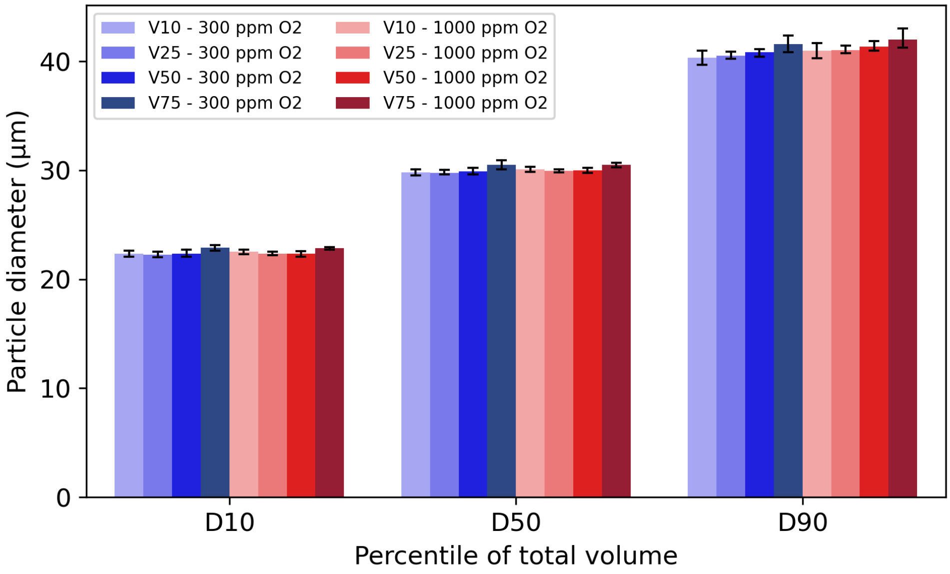

Figure 5.8 – Particle size distributions D_{10}, D_{50}, and D_{90} of the recovered powders collected from L-PBF prints of different melted volume fraction and carried out with 300 ppm and 1000 ppm of oxygen in the build chamber.

Fist of all, it can be stated that the size variations between all conditions remain very limited, with differences of less than 2 µm. However, some trends can be observed, with a slight increase of the characteristic size values when the melted volume in the build is more important. This is noticeable for the two sets of volumes with different oxygen concentration in the chamber. The values of the 1000 ppm oxygen series are marginally higher than those of the 300 ppm series. In any case, the major differences concern the D90 values, which increase more significantly with increasing part volume.

This slight increase in particle size is not unexpected given the previous results. More sieved residues and spatter were observed for larger fractions of consolidated material. Even though the large ejecta are discarded by the sieving, some can be smaller than the mesh but still larger than the virgin material, or can be larger but elongated allowing them to pass through in one direction. Vapor-entrained particles can also be exposed to the laser beam partially and merge with each other, or small particles can attach to spatters as satellites, which increase the particle size. Another factor could be the really large spatters that fall down on the powder bed in semi-liquid state creating large agglomerates with the sintering of small particles, which are then removed by the sieve.

The variations reported in this analysis are still very minor, but it is likely that the observed trends would be accentuated by successive reuses of the powder in L-PBF.

5.3.5 Crystallographic phases

X-ray diffraction was performed on all the samples of the two series (300 ppm O_2 and 1000 ppm O_2. No difference was found in the diffractograms neither regarding the different part volume nor the chamber oxygen concentration. Only austenitic peaks are present, with no discernible δ-ferrite peak allowing a Rietveld refinement for phases proportions calculation, as illustrated by the diffractogram of V75 powder from 300 ppm O_2 in figure 5.9, which is similar to all other samples. Kriewall et al. [4] also studied the effect of area fraction on 304L powders and found an increase of ferrite particles with larger melted volume and throughout three iterations of recycling. However, in their study, XRD analysis was performed before powder sieving. This can explain the difference compared to the present results, with only one iteration of powder recycling and the sieving step being carried out before characterization. Let us recall from chapter 3 that in the recycling study, ferritic particles were found but in small quantities (4 wt. %) after 15 printing cycles, and were in abundance in the sieved residues.

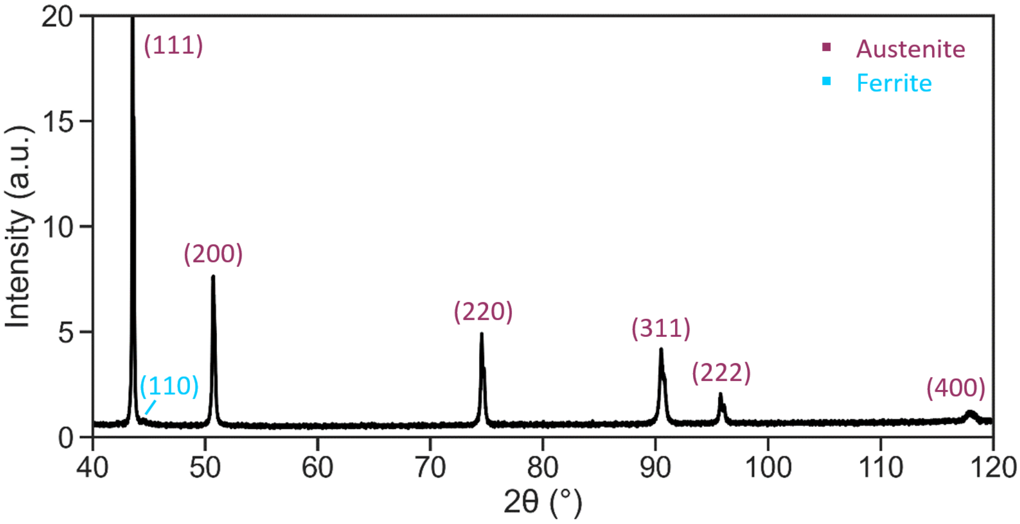

Figure 5.9 – X-ray diffractogram of V75 powder recovered after processing with 300 ppm of residual oxygen, representative of all powder samples of the volume study.

A few bright and smooth particles, identified as magnetic particles in chapter 3 (see section 3.3.4, figure 3.17) were again found in the powder samples after sieving and in the sieved residues. Figure 5.10 (a) shows an optical image of V50 powder with a circled magnetic particle in the center, and figure 5.10 (b) presents an EBSD phase map of the sieved residues, displaying austenitic and ferritic particles. Extraction of magnetic particles with a standard magnet was possible but did not allow to conclude on proportions and potential effects of the melted volume fraction or the chamber oxygen concentration on the crystallographic phases of the recovered powder.

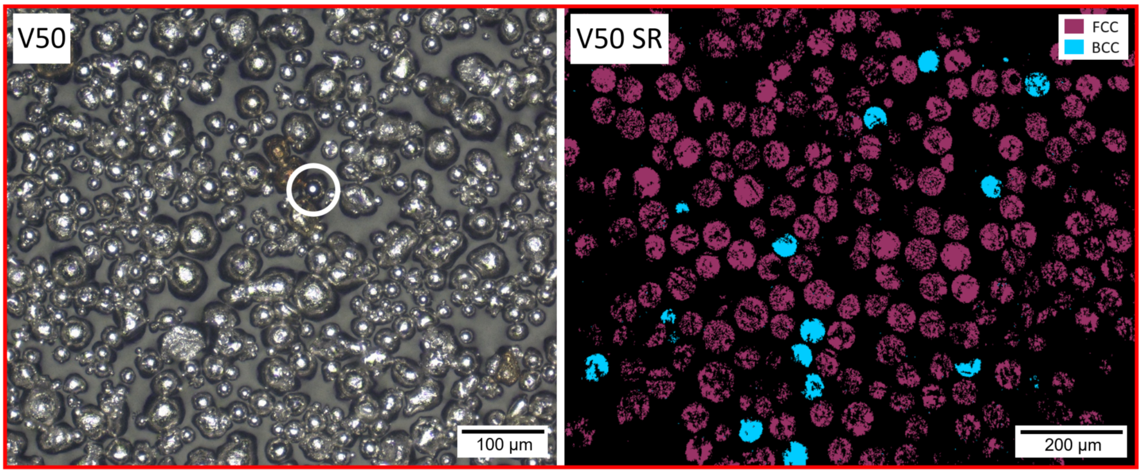

Figure 5.10 – (a) Optical image of V50 powder with magnetic particles highlighted with white circle, (b) EBSD phase map of V50 sieved residues.

5.4 Influence of parts spacing, height and chamber oxygen concentration

In this section, 36 powder samples coming from different conditions in L-PBF were collected and analyzed. Six different parts spacings, three parts/fabrications heights and two build chamber oxygen concentrations were implemented to evaluate the characteristics of powder recovered in local zones of interests on the build platform.

5.4.1 Oxygen content

Powders were collected inside each groove of different spacing between consolidated material and sieved using a 50 µm mesh. The results of oxygen content measurement by chemical analysis for each condition are presented in figure 5.11 as a function of the six different spacings between consolidated parts. The blue curves correspond to powders recovered from L-PBF prints carried out with 300 ppm of residual oxygen in the build chamber, and the curves of red shades represents powders recovered after processes performed with 1000 ppm of O_2. Three shades per color, also marked by squares, circles and triangles, indicate the three fabrication height conditions tested (H10, H25 and H50 respectively).

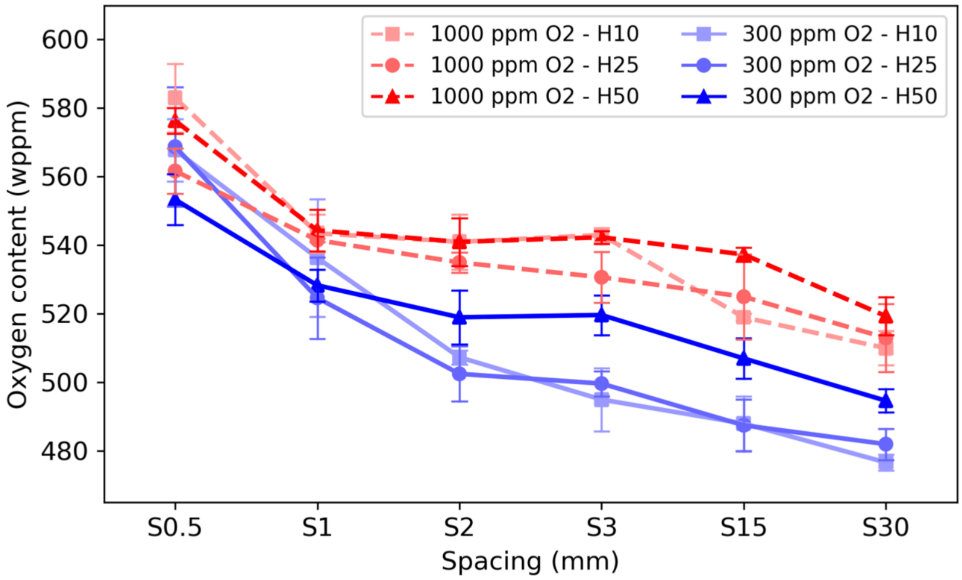

Figure 5.11 – Oxygen content of the recovered powder in function of the parts spacing, fabrication height and chamber oxygen concentration.

The oxygen content of the powder is increasing when the parts spacing is reduced. It must be noted that the x-axis shows the different spacings as categories and not in a linear format. The increase of oxygen is actually very progressive until a spacing of 1 mm, then quite strong with a spacing reduction to 500 µm. The pickup is about the same amount between 1 mm and 0.5 mm of part spacing than between 30 mm and 1 mm (around 30 wppm). To be more specific, the increase is slow from 30 to 3 mm, then almost all values are stable between 3 and 2 mm or even between 3 and 1 mm for some conditions.

This shows that powder oxidation is strongly related to the particles oxidized in the HAZ close to the printed parts (see figure 3.12), and not only by spatter particles. The spacing of 500 µm should not allow the recovery of many ejecta in such narrow groove, yet the powder in this area is the most severely oxidized. Another important observation is that a 30 mm spacing between printed parts greatly limits powder degradation, with oxygen content values relatively close to the one of the virgin powder (474 wppm), when the oxygen concentration in the chamber during manufacturing is 0.03 %.

The oxygen level of powders recovered from productions under 1000 ppm O_2 (red curves) is systematically higher than that of powders from prints with 300 ppm of residual oxygen inside the build chamber (blue curves). As for the volume study in the previous section, a higher oxygen partial pressure during the L-PBF process might promote the oxidation of powders at high temperatures, with thicker oxide layers or larger oxide nodules, resulting in higher oxygen contents.

Regarding the influence of parts height on recovered powder oxygen content, it can be observed that for large spacings (S15 and S30), higher parts lead to higher oxygen contents. This effect is still relatively present for distances of 3 mm and 2 mm between consolidated parts. For even smaller spacings, parts height no longer has any impact, with the oxygen content being governed by the spacing alone and reaching a plateau.

Parts height is directly related to build time. As an indication, fabrications with parts height of 10 mm, 25 mm and 50 mm (supports not included) lasted 10 h, 23 h and 43 h respectively (supports included). A longer printing time results in a longer exposition of certain particles to high temperatures. It has been shown by Yavari et al. [225] that the surface temperature of the parts gradually increase through the superposition of scanned layers in the L-PBF process. This heat accumulation can sometimes be observed on printed parts when the printing is conducted with a rather high oxygen concentration in the build chamber combined with small area fractions of melted material (resulting in a very short time per layer), with the parts surface presenting a gradual oxidation along the build height [225]. In the present study, no major oxidation was present on the parts surface based on the height thanks to an important time per layer due to large melted volumes, allowing longer cooling times. However, the temperature of the printed parts still must have remained high during the entire process due to thermal cycles with repeated laser scanning and heat conduction in the solidified material. The longer times at high temperature for powders close to the elaborated parts must have led to thicker oxide layer growths and thus a higher overall measured oxygen content.

Observations of the powder samples, by different means were performed to supplement these oxygen content results.

5.4.2 Observations

Optical microscopy

Optical microscopy was carried out on all powder samples to analyze the colors of the particles. Images of some samples are shown in figure 5.12. The influence of part spacing is highlighted in this figure, with three different spacings S0.5, S1 and S3. Observations of powders from fabrications with both oxygen levels in the build chamber are displayed (0.03 % and 0.1 %). The fabrication height is fixed for these 6 conditions, at 10 mm high (H10).

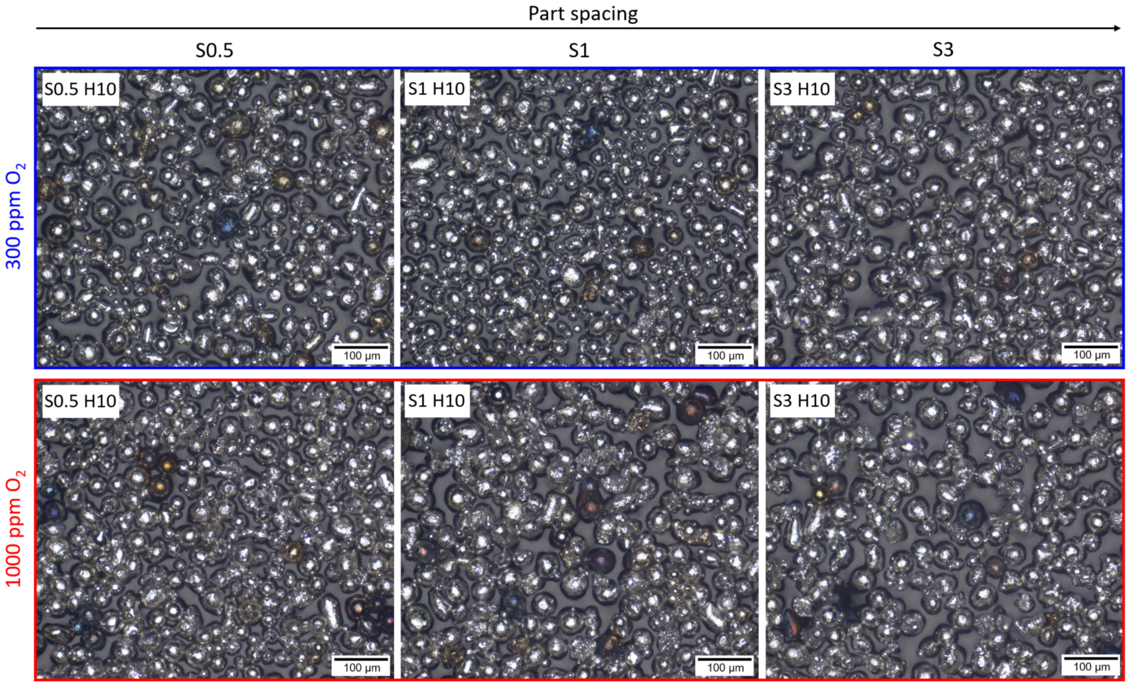

Figure 5.12 – Optical images of recovered powders from S0.5, S1 and S3 spacings, from fabrications of 10 mm high (H10), conducted with a chamber oxygen concentration of 300 ppm (in blue) and 1000 ppm (in red).

Numerous colored particles are noticeable for the smaller space distance between parts, with blue, purple and orange particles. With a spacing of 3 mm, the density of colored particles in the recovered feedstocks is smaller compared to 500 µm and 1 mm. The colors seem slightly more pronounced for the 1000 ppm O_2 series, but blue particles are nonetheless present in the 300 ppm O_2 series. As seen in the previous chapter with the powder oxidation study and oxygen-color correlation (see figure 4.5), increased oxidation with a continuous oxide film on the surface of the particles results in visually yellow, orange, purple then blue particles. In any case, the samples did not show only one type of color in addition to the grey as-virgin particles, but almost all oxidation states for these conditions.

Figure 5.13 presents the largest spacing of 30 mm, for different build heights (H10, H25 and H50). Once again, the optical images for the two conditions of chamber oxygen concentration are shown. Increasing the part spacing even way further, to 30 mm, shows a definite decrease in the number of colored particles. Higher parts, *i.e.* longer fabrication time slightly and progressively increase the oxidation of powder, which is in accordance with the measurements of oxygen content by inert gas fusion (figure 5.11). As for the smaller spacings, it seems that the oxidation is somewhat less pronounced, with lighter colors in the powder beds at the end of prints under 300 ppm of O_2, compared to 1000 ppm. The differences are however not extremely significant visually.

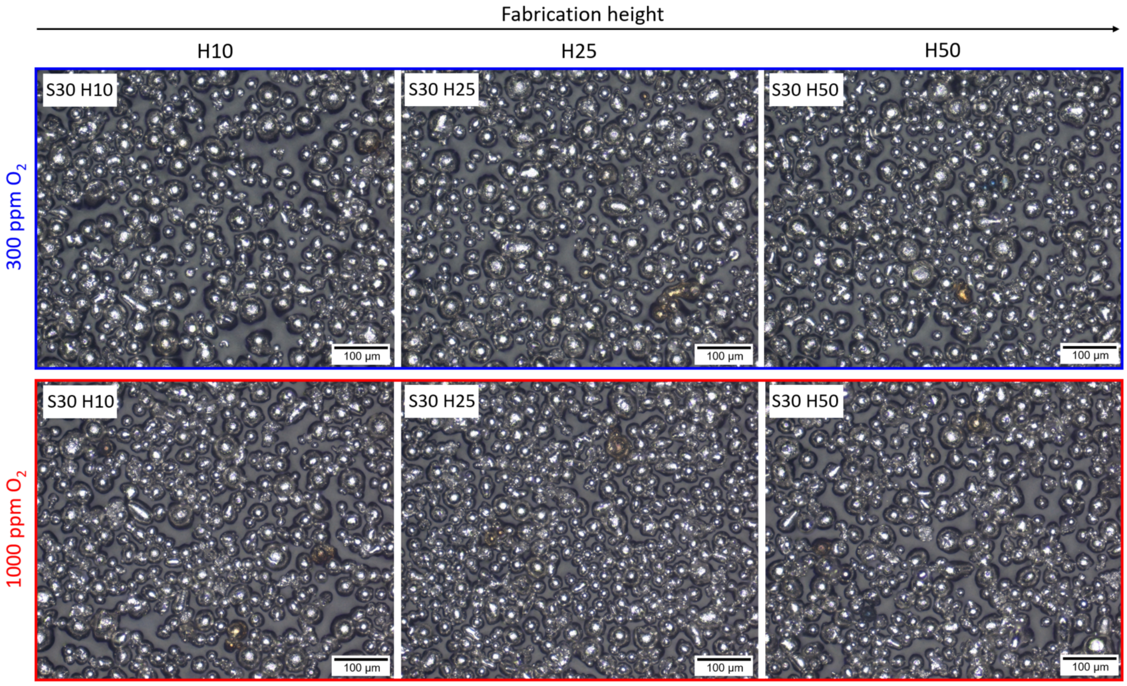

Figure 5.13 – Optical images of recovered powders from S30 spacing, from fabrications of 10 mm, 25 mm and 50 mm high (H10, H25 and H50), conducted with a chamber oxygen concentration of 300 ppm (in blue) and 1000 ppm (in red).

Scanning electron microscopy

SEM observations were carried out as well on the powder samples. Surprisingly regarding the low probabilities of spatter fallout in the very small spacing grooves, the latter present a large number of ejecta compared to powders recovered in larger spacings, as shown in figure 5.14 (a). These BSE images highlight the presence of partially oxidized particles in the recovered powder as a function of part spacing. The fabrication height and build chamber oxygen concentration are fixed in these 4 conditions, with 10 mm high and 1000 ppm O_2. Numerous spatters, small enough to pass through the sieve mesh, are found in the 500 µm and 1 mm spacings (not shown here). These are still quite present with a 2 or 3 mm spacing, but no longer in abundance in grooves of 15 and 30 mm. This trend was also observed for powder samples coming from fabrications with a residual oxygen concentration of 300 ppm in the build chamber, although in slightly lower quantity. As seen and explained previously (see section 5.3.3, figure 5.6), more spatters were found for L-PBF processing with a greater oxygen level, which was also the case in this spacing study. No influence was detected on the SEM images regarding the parts height (H10, H25 and H50), with similar trends depending on the parts spacing.

Figure 5.14 (b) presents an EDS mapping conducted on spatter particles found in the S0.5 spacing (indicated by dotted lines in figure 5.14 (a)). As before, typical partially oxidized particle (on the right hand side) present a selective oxidation of Mn and Si, characteristics of stainless steels spatters, with these oxide nodules on the surface. The particle on the left hand side is more peculiar and has not been observed so far. EDS maps show that this particle is covered with really large oxides patches of the same nature of oxide nodules on *standard* partially oxidized particles (O, Mn, Si), but in addition, the patches are covered partially with some kind of dendrite-shape structure, rich in Fe, Cr and Ni.

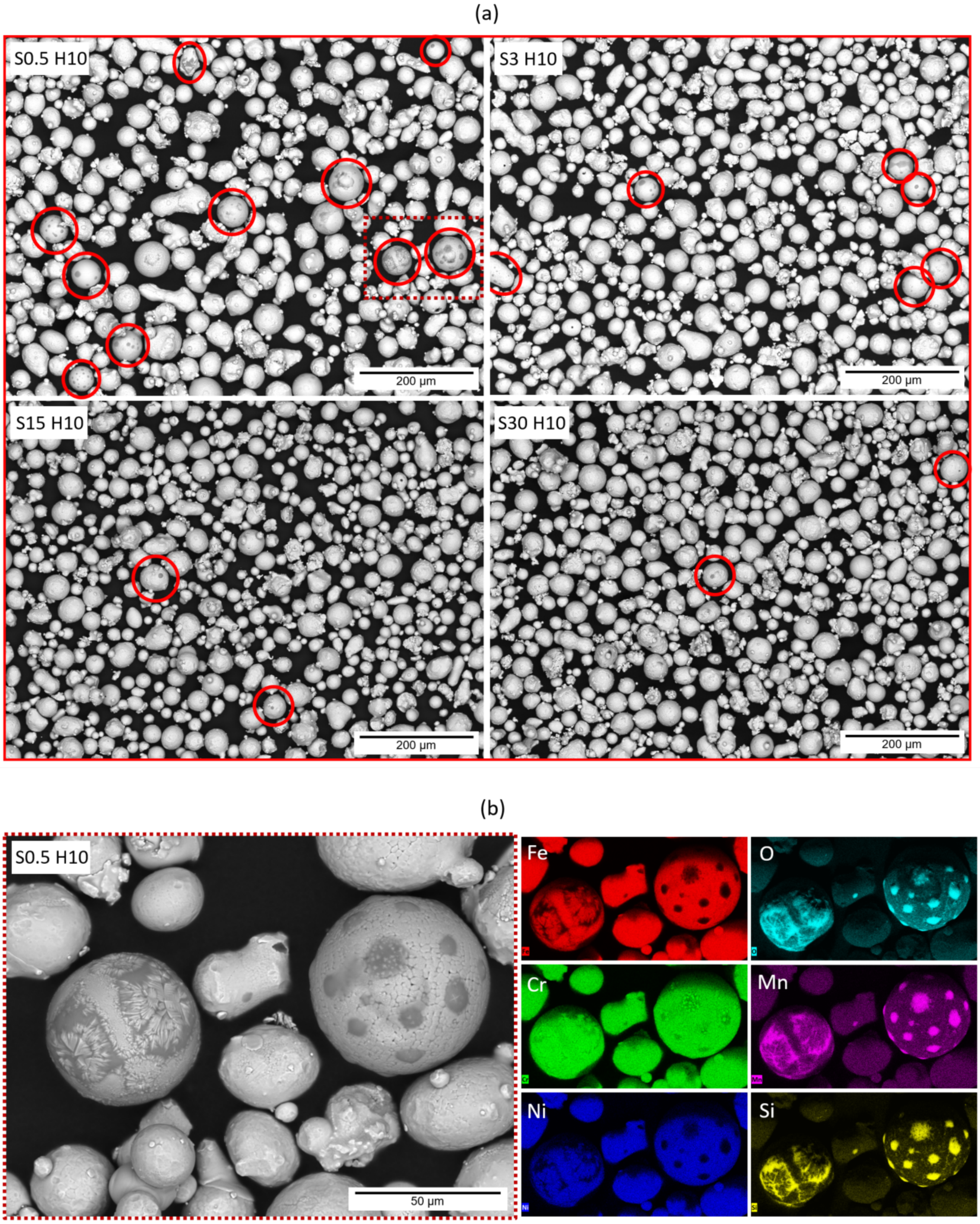

Figure 5.14 – (a) SEM micrographs of recovered powders from S0.5, S3, S15 and S30 spacings from the fabrications of 10 mm high (H10) conducted with a chamber oxygen concentration of 1000 ppm (partially oxidized particles are circled in red), (b) Close-up view on spatters of S0.5 powder with corresponding EDS maps.

Other particles of this nature were found in the powders recovered after manufacturing under 1000 ppm of residual oxygen in the build chamber, both after sieving and in sieved residues. Due to the extremely small amounts of total material recovered from the grooves, and resulting sieved residues, the latter were not counted and only a few were analyzed. However, particles with these crystal-type coating on oxide patches were also found in the sieved residues from the part volume study. Again, these kinds of particles were only observed after L-PBF processing with the relatively high oxygen level (0.1 %). Figure 5.15 displays multiple particles presenting the features described above.

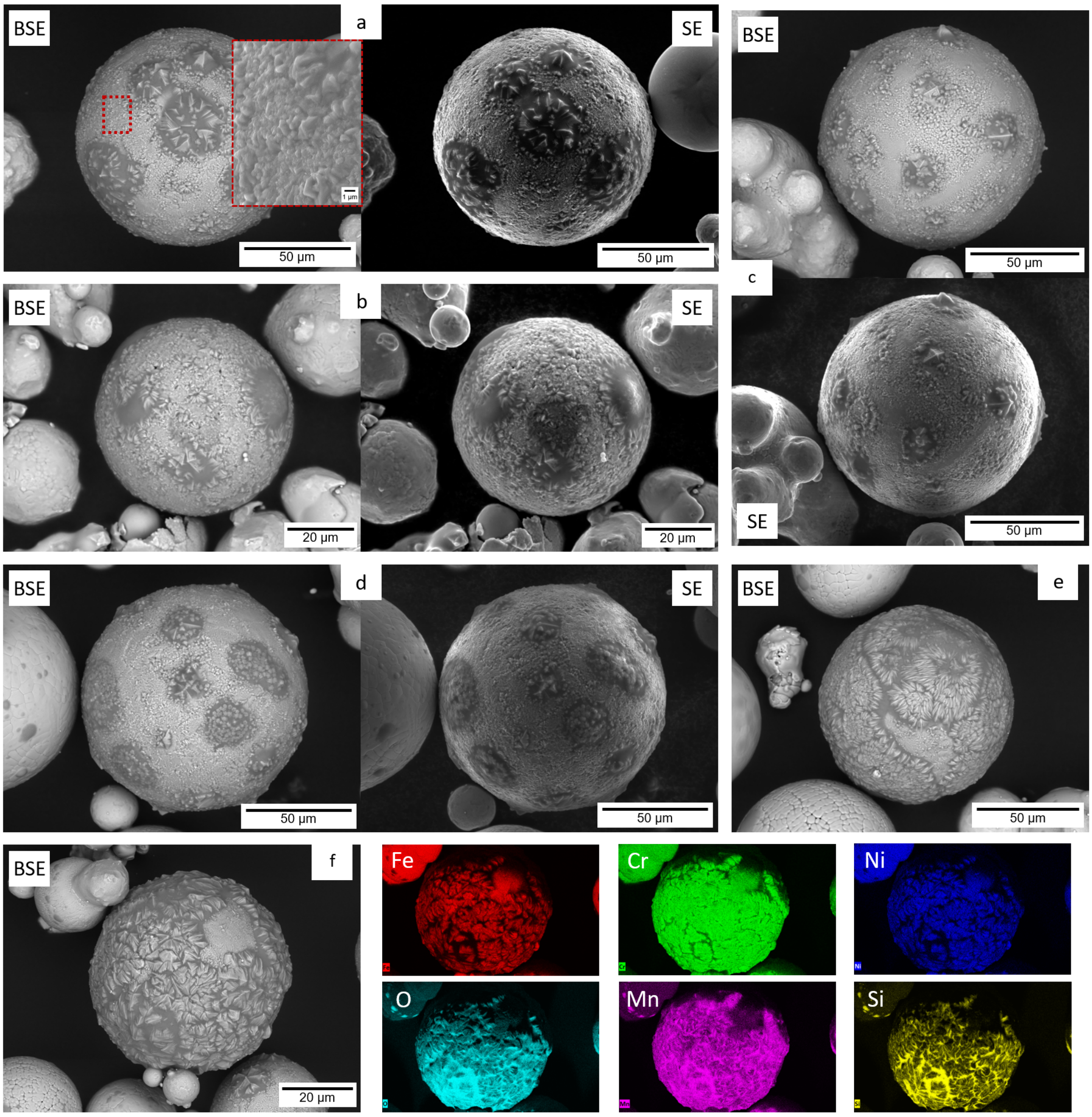

Figure 5.15 – BSE and SE micrographs of spatter particles presenting dendrite-shape structure and EDS mapping.

Different degrees of severity are noticeable, both in terms of the size of Mn and Si rich oxide patches, and in terms of coverage of the structure rich in classical elements of SS316L. Only a few dendrites or even the beginnings of dendritic structure on the oxide spots are present for particles (a - d), compared to particles (e - f) which are almost entirely covered with oxide, itself covered with this second structure. EDS maps performed on particle (f) confirms the presence of Fe, Cr and Ni in the upper structure, while the portions covered only by the oxide layer show a huge iron depletion. The newly observed structure is strongly in relief, as shown in particle (c), forming some sort of mountain-shaped peaks.

Another noteworthy observation is that the surface morphology of the area without oxides spots is also different from the usual powders (visible, for example, with the adjacent particles in figure 5.15 (b) and (d)). The surface is quite rough, and can remind of the surface of AlSi10Mg spatter particles analyzed by Raza et al. [227]. These authors found a high surface roughness with really fine dendritic structure, which consisted in a rough oxide layer formed by randomly oriented nodules. However, the roughness magnitude differs greatly, with peaks of nanometric order, compared to micrometric scales observed in the present study, as shown in the zoom of particle (a). Moreover, these sizes are not comparable to the very large ferrite-rich peaks/dendrites found on Mn-Si oxides. Nevertheless, this led to the conduct of EDS point analyses to complete the precedent mappings, with semi-quantitative measurement of surface chemical composition in the different zones. It was found that lighter areas (*i.e.* such as in the zoom of particle (a)), without Mn-Si oxide patch, showed as well an important oxygen concentration, which may suggest that these rough zones are also oxide layers. The oxygen contents (in wt. %) are slightly less important than the ones in oxide patches, but still significant ($\sim$ 6 - 10 % vs. 25 - 35 %). As a comparison, oxygen content measured on virgin particles by EDS point analysis is about 0.1 %, while the values for colored particles (orange to blue) are between 2 and 5 wt.% .

A correlation between SEM and OM was conducted to observe these particles with super dendritic structure with white light. This revealed that the latter have a dark shade, almost black, indicating a severe oxidation. Considering that these particles were mostly found in the 500 µm groove, they have experienced high temperatures with potential repeated exposure with laser scanning close to them. The presence of typical oxide nodules/patches indicates that they are spatter that oxidized selectively in flight, and must have fall back on powder bed portion close to a part. Next, they might have undergone a second oxidation, either with vapor entrainment due to recoil pressure leading to another partial exposition to the laser beam in flight, or because of their presence in the vicinity of a part that will be scanned by the laser, resulting in the growth of the rough iron/chromium-rich oxide layer. It could be assumed that the rough surface on the particle and on the oxides patches are of the same nature, but growing at different rates or from different nucleation points on the metal or on the oxides. These remain hypotheses that need to be further evaluated with more precise analyses. In any case, complex phenomena and different thermal history experienced by particles during laser-matter interactions are responsible for different oxidation structures. These particles are far from being the most represented in the recovered powder, but their presence and singularity is noteworthy.

Powder bed observation

To illustrate the observations made by SEM and OM, with the spatter particles and heat affected zones described above, images of the powder bed during L-PBF processing were acquired, using the same experimental setup that the one used in chapter 4 (see section 2.5). Powder bed scanning was conducted during printing of small cubic specimens, after laser scanning and before powder spreading. Figure 5.16 (a) and (b) show a powder bed scan with two different zooms, focusing on a cubic specimen, with part spacing distances investigated in this work being indicated on the images by dotted squares. The conditions of manufacturing are slightly different in this experimental setup, with a laminar flow of protective gas (Ar) from the right to the left on the images, and a residual oxygen concentration in the build chamber set to 0.3 %, which explains the orange-oxidized hue of the consolidated surfaces.

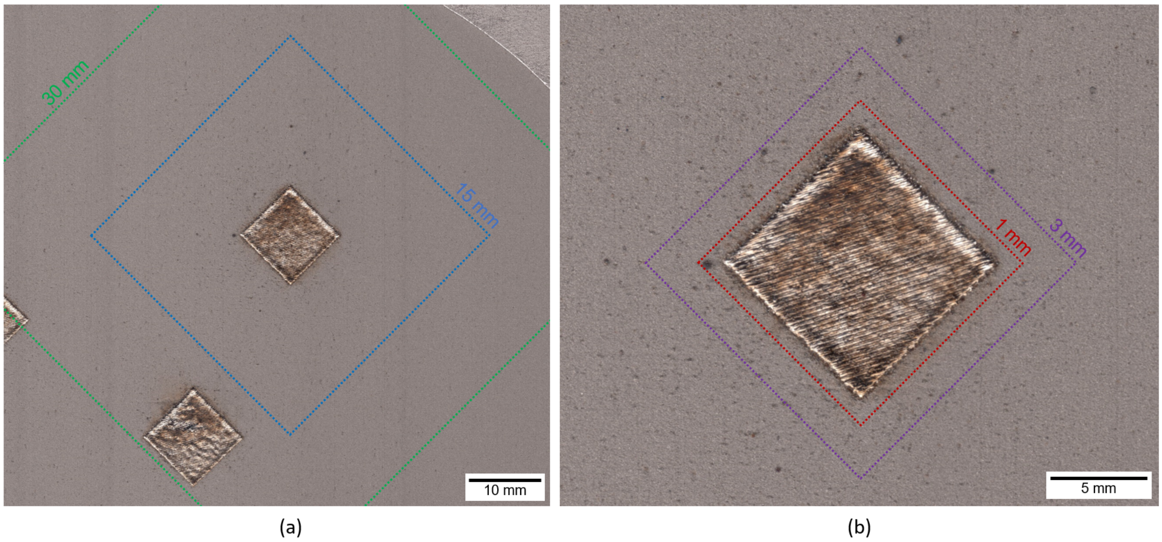

Figure 5.16 – Powder bed images after laser scanning of cubic specimens, with part spacing distances indicated by dotted squares.

Large spatters are visible and can fall back far from the melt pool tracks, as shown in figure 5.16 (a). Other ones are present on the surface of the solidified layer, and quite a lot are also close to the part (figure 5.16 (b)), as found in abundance in this spacing study in grooves of 0.5 mm and 1 mm. Spattering is known to happen towards the rear of the melt pool, but not exclusively. It has been shown by several authors using different monitoring techniques (high-speed camera imaging, in-situ x-ray synchrotron imaging) that droplets can also be ejected towards the front of the melt pool, and ultimately in just about every direction [109, 256, 257]. In addition, the different directions followed by the laser, with zigzag scanning, and rotations between layers can lead to spatter redeposit everywhere. The gas flow also influence spatters redeposition, combined with the scan strategy, as showed by Schwerz [258] which observed more spatter redeposit and impacted parts close the gas outlet, compared to powder bed regions and parts close to the gas flow inlet.

The heat affected zone is also clearly apparent on the zoomed image, figure 5.16 (b), with coloration close to the edges of the cubic specimen. Colored particles are noticeable with orange regions inside the 1 mm (and maybe even 300-500 µm) square around the part. These powder bed scans confirm the assumption that colored-oxidized particles can be present near the vicinity of melt pool tracks and solidified specimens. Colored particles were also observed surrounding large ejecta redeposited on the powder bed, even far from the printed parts. As mentioned earlier, these large ejecta can fall back in a semi-liquid state as it was observed with numerous satellites attached to the large spatters in the sieved residues, and their heat content is sufficient to lead to an oxide film growth on the nearby particles.

5.4.3 Crystallographic phases

X-ray diffraction was conducted on the samples from the L-PBF prints with 300 ppm of residual oxygen. As for the analysis of the impact of melted volume fraction, the results did not show any difference in crystallographic phases, with only standard austenite peaks. This is not necessarily surprising, as the magnetic particles should be small spatters that were ejected from the melt pool at high speed, or vapor entrained particles with high velocities leading to fast cooling rates. The small powder bed spacings do not have a high probability of ejecta fallout and therefore of any increase in ferritic content, and only one printing cycle is not expected to produce significant variations.

5.4.4 Parts surface roughness

Measurements of areal average surface roughness Sa (in µm) were carried out on the side surfaces of printed parts of 50 mm high (H50), for four spacings (S1, S3, S15 and S30). Three different zones were analyzed per spacing according to the height of fabrication, as schematized in figure 5.17, to study a potential variation of surface roughness along the L-PBF process. Figure 5.17 (a) shows analyzed cross sections in a print with large spacings, highlighted in green, and figure 5.17 (b) presents a truncated view with the different zones analyzed with three measurements per zone (schematized by black crosses). Zone A is close to the substrate, zone B is in the middle of the part and zone C is close to the surface.

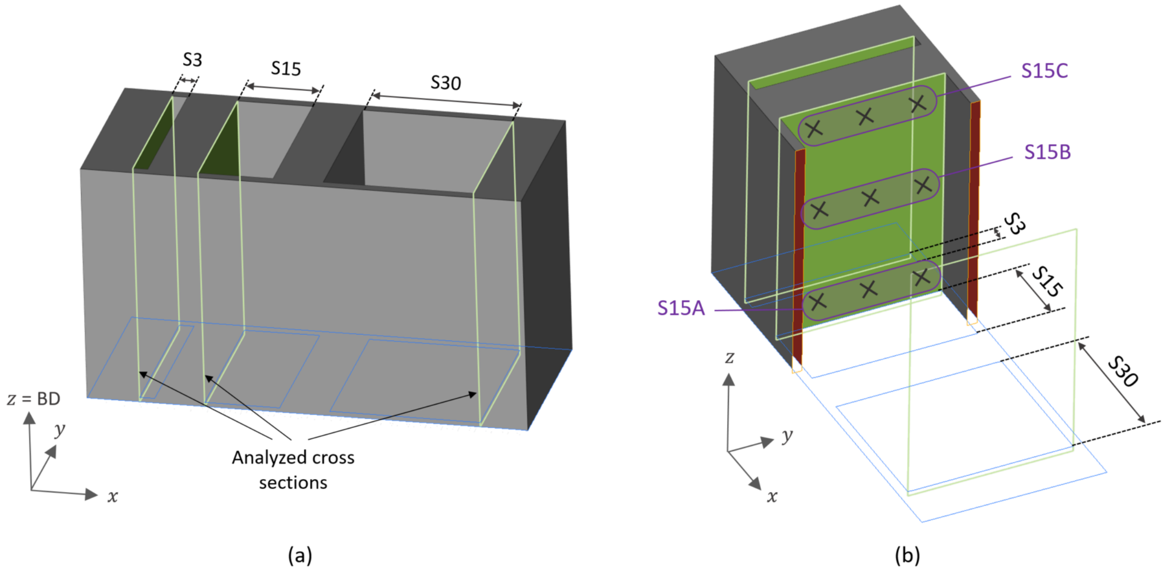

Figure 5.17 – (a) Schematic representation of analyzed cross sections for surface roughness measurement, (b) Truncated view with indication of analyzed zones on the cross sections as a function of the height.

Different spacings (S30, S15, S3 and S1) were analyzed for the prints with an oxygen level of 1000 ppm, in each of the three height zones. The arithmetic mean roughness (Sa) depending on all these conditions is presented in figure 5.18.

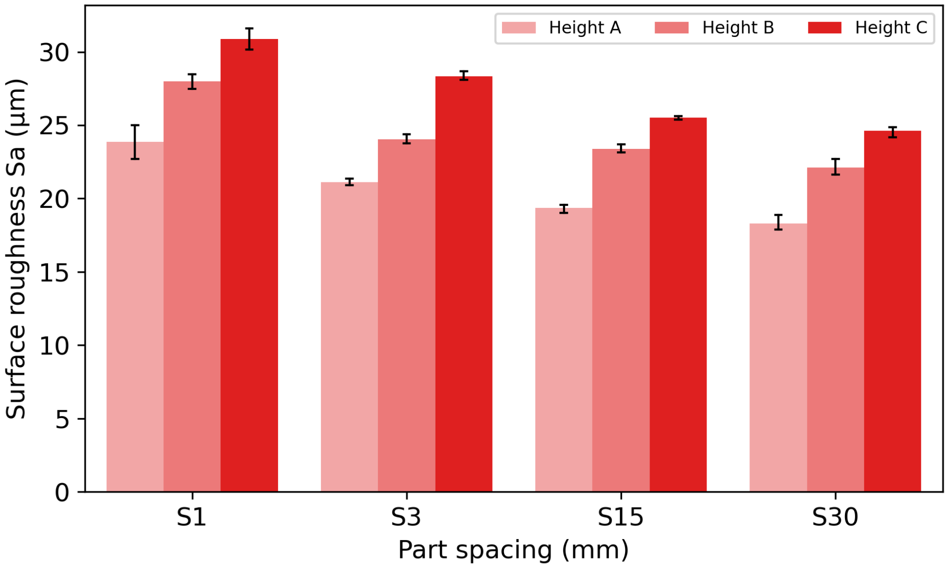

Figure 5.18 – Roughness of the printed parts side surface in function of part spacing and part height.

The position of the measurements regarding the part height strongly influences the surface roughness. For each spacing, roughness values are gradually larger with increasing height. The mean Sa of zones A, close to the substrate (approximately equal to 10 mm high), are the smaller ones. Mean values are increased by 18 % in zone B at a height about 25 mm, and zone C measurements (conducted just bellow the surface, at about 45 mm high) are increased by 32 % in average compared to the values of zone A, which represents an Sa increase around 7 µm for a fixed spacing.

In addition to fabrication height, part spacing also has a significant impact. The maximum roughness is observed for the smaller spacing tested (1 mm), and an increase to 3, 15 and 30 mm reduces the roughness. As for the results of oxygen content in function of part spacing, the increase of roughness with a lowering of the spacing between parts is not totally gradual when observed with a linear scale axis. The rise of Sa is rather progressive from 30 mm to 3 mm, with a gain of about 3 µm averaged over the 3 heights, then it is quite abrupt, with a similar increase with a reduction of the spacing by only 2 mm (to S1). It has been observed previously, in recovered powder by SEM and by powder bed scanning during L-PBF process that many ejecta are found at very close distances from solidified parts. This could influence the parts surface roughness with sintering of spatter particles to the scanned parts, altering the flatness of the surface.

Analysis of the local side surface relief maps of each spacing condition in function of the altitude within the parts were carried out. Figure 5.19 shows the outcomes for the spacings S1 and S30 and the three height zones A, B and C. It reveals that the increase of roughness along the height is mainly due to the sintering of more particles and potentially larger ones to the side surface. Spatter can be found in all conditions as they can fall back on the powder bed in a semi-liquid state. However, it can be assumed that the overall increase of part temperature with repeated laser scanning allows the sintering of more numerous particles surrounding the part during melting and solidification. Spatter can also fall back in a cold state [109] and sinter to the surface because of the part elevated temperature, which might not have provoked this effect at relatively lower temperature at the beginning of the process where the heat sink effect of the fabrication plate is expected to be stronger.

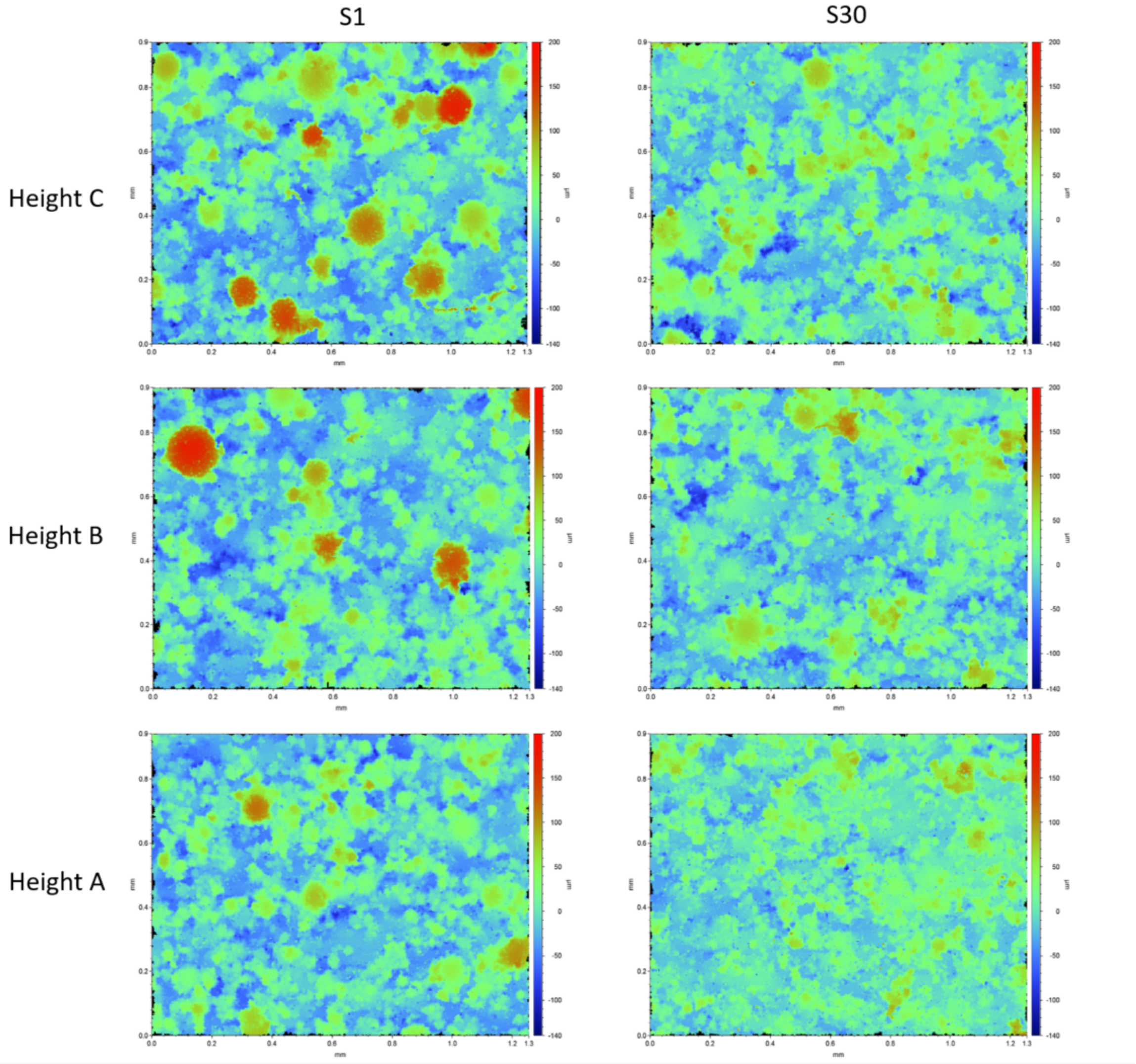

Figure 5.19 – Surface height maps of S1 and S30 side surfaces for the three height zones.

5.5 Summary

This chapter focused on studying the effects of several L-PBF process and build parameters on powder degradation, with the purpose of minimizing feedstock alteration during its reuse. Numerous prints were carried out to investigate the impact on powder with different melted volume fractions in the prints, part spacings, fabrication heights and build chamber oxygen contents. The main findings are summarized as follows.

Larger fractions of melted volume during L-PBF fabrications lead to an increase of the fraction of sieved material in relation to the total amount of recovered powder on the build platform at the end of the process. After sieving, the oxygen content of recovered powder is roughly proportional to the melted volume fraction in the print. Slightly more numerous colored particles are observed with larger solidified areas, likely resulting from longer perimeters on the surface of each layer, *i.e.* larger heat-affected zones. More spatters with selective oxidation of Mn and Si are also present after sieving, because of the greater distances covered by the laser beam and complex interactions with the powder resulting in more material ejecta. There is a slight trend regarding the particle size as a function of the melted volume during the manufacturing process. The values of D_{10}, D_{50}, and especially D_{90} tend to slightly increase with an increase of consolidated volume.

A reduction of part spacing also results in an elevation of the oxygen content in recovered powders, with a drastic rise between 1 mm and 0.5 mm, characterized by larger proportions of colored particles. The heat affected zone around printed parts was evidenced with these color particles in the very small spacings, and by imaging of the powder bed during processing. Moreover, a large amount of spatter particles with selective oxidation on the surface are also present in such narrow grooves, which also contributes to the oxygen pickup. A distance of 30 mm between printed parts on the build platform strongly limits powder degradation, with powder oxygen concentration and attributes really close to the ones of virgin powder.

For large spacings, fabrication height has an impact on the recovered powder, with more color-oxidized particles and higher oxygen contents. Higher parts imply longer printing times, leading to an increase of part temperature with the addition of layers and repeated laser scanning. This results in thicker oxides films for the particles in the vicinity of the parts. For smaller spacings (1 mm or 500 µm), the effect of fabrication height seems less important, and the oxygen content of powders might be governed by the really short distance between the solidified specimens, reaching a plateau. The build height also greatly influences the parts side surface roughness, regardless of the spacing. The flatness of the parts is strongly deteriorated along the build direction, with more numerous and larger particles sintered during melting and solidification close to the surface. A reduction of part spacing also gradually increases the surface roughness.

All these phenomena are accentuated when L-PBF processing occurs with a higher residual oxygen concentration in the build chamber (1000 ppm compared to 300 ppm). A greater oxygen level lead to an increase fraction of large particles and agglomerates. Besides, the spatters found in the sieved residues present more coalesced oxide nodules. Severely oxidized particles with a rough surface and dendrite-shape structure in addition to oxide patches were also observed for the first time. In addition, the oxygen contents of recovered and sieved powders from the melted volume and spacing studies systematically present higher values in fabrications carried out with the highest partial pressure of oxygen in the chamber.

No changes in crystallographic phases are found in recovered powder as a function of all parameters (part spacing, height, melted volume, chamber oxygen content). A few magnetic particles are still noticeable in the feedstocks but in line with the findings of chapter 3 a single recycling step does not lead to any significant phase fraction modifications.

To conclude, the degradation of the powder and mainly its oxidation is inevitable during the L-PBF process. However, some parameters and manufacturing characteristics allow to strongly limit the kinetics of alteration. Smaller melted volumes in the build platform, associated with large enough space distance between parts can greatly contribute to minimize the effects after one printing cycle. Moreover, the chamber oxygen concentration plays a very crucial role, and its restriction to levels well below the 1000 ppm often found in industrial machines enables to limit powder degradation, with less ejecta, agglomerates and a slower oxidation.

General conclusions

This thesis has been focused on the study of powder degradation in the laser powder bed fusion technology, in order to enhance the understanding of the phenomena, and to make recycling more reliable and robust by means of the monitoring of the raw material quality and the minimization of powder degradation through appropriate manufacturing conditions.

In a first approach, a study was conducted with a methodology based on the successive recycling of stainless steel 316L powder, consisting in the recovery of the un-melted powder, its sieving and reintroduction in the machine. It led to the production of 15 consecutive printing cycles without addition of virgin material, thus allowing powder and part characterization. Regarding the recovered powder, the results show that a certain level of degradation is inevitable. Most important, the oxygen content of the powder increases gradually with each reuse cycle, leading to an increase of 40 % after 15 prints, despite the relatively low oxygen concentration fixed in the build chamber atmosphere (300 wppm). Recycled powder is altered by the presence of partially oxidized particles, *i.e.* melt pool spatters or particles entrained by vapor recoil pressure, presenting oxides nodules rich in Mn and Si on their surface. A progressive increase of the number of colored particles (yellow/brown/blue) is also noticeable, due to the presence of particles in the vicinity of solidified parts (HAZ), resulting in a longer and more uniform oxidation and in a continuous film responsible for the observed colors according to its thickness. These colored particles can also account for the oxygen pickup in reused powders.

Furthermore, there is a slight increase in particle size with successive powder recycling. The flowability of the powders is not negatively impacted and is on the contrary improved with this size increase and the presence of oxides on the particles surface which reduce adhesion and inter-particles frictions. On the other hand, more magnetic particles are present in the recycled feedstocks, with a significant increase in the proportion of δ-ferrite phase, up to 4 wt.% after 15 fabrications. This could be detrimental to the L-PBF process due the magnetic attraction and resulting clustering during powder layer spreading.

A conclusion of this first approach is that a sieving step is absolutely crucial to limit powder degradation and allow its reuse, the characteristics of sieved residues being far too different than those of conventional powders. Indeed, a number of particles are extremely large, irregular, composed of agglomerates and satellites. Their oxygen content is more than three times higher as compared to the virgin powder. In addition, sieving allow to slow down the increase of the number of magnetic particles. Indeed, even though the majority of the latter is smaller than the selected mesh, they are nevertheless at sieving because of their clustering.

Regarding the effect of powder recycling on stainless steel 316L elaborated specimens, the findings are rather positive. Parts microstructure is typical of L-PBF features with visible melt pool tracks, elongated grains along the building direction and cellular substructure. A limited but significant grain refinement is noticeable with more numerous and finer grains with intensive recycling, that could be due to increased oxygen contents in the powder. Nevertheless, there is no significant difference in samples microhardness and tensile properties with recycling. The specimens show consistent and satisfactory values well above the required standards, with hardness of 212 HV, YS of 580 MPa, UTS of 670 MPa and elongation at break of 40 %, showing that at least with such simple characterizations, SS316L powder can be used up to 15 times with the L-PBF process without significantly compromising these mechanical properties of printed parts.

However, the density of the elaborated components is slightly impacted. The latter is stable for 5-6 printing cycles with reused powder, around 99.6 % measured by Archimedes method. Then, relative density is reduced progressively to a final value slightly over 98 % after 15 builds, which could potentially affect mechanical performance under dynamic load. In addition, oxygen content of manufactured samples is also increasing gradually with successive powder reuse, ranging from 405 to 545 wppm. The extend of such an increase likely depends on to the conditions of elaboration and materials processed, and could be critical for Ti-based or Ni-based alloys for example, that present a stringent maximum oxygen level in their standards specifications.

In view of these results and observations, combined with the findings present in the literature, the oxygen content of the powder appears to be a good indicator for monitoring the quality of the powder as it is reused in the L-PBF process. The idea implemented in the frame of the present thesis was to take advantage of the layer-by-layer spreading of the powder during the process, to perform in-line control of the raw material at a layerwise level. A recoater based scanner was implemented on a customized L-PBF platform, allowing to acquire in-line scans of the entire powder bed area resolving single powder particles (5.3 µm × 5.3 µm / pixel).

A new methodology was developed, using the colors of oxidized particles to determine their oxygen content. The approach is based on a preliminary calibration consisting of an ex-situ oxidation of powder samples in furnace and measurements of corresponding oxygen content by conventional chemical analysis. Then, powder bed scanning of these colored powder samples enabled to correlate the color of the particles, defined on the scan images by the R, G and B channel values, to their oxygen concentration. This calibration leads to the determination of an oxygen prediction function for the SS316L powder, taking R, G and B pixel values as arguments.

Once calibrated, this in-line scanning technique allows to accurately measure the oxygen content in an unknown powder layer, after powder bed scanning and a fast image analysis consisting only of calculating the average RGB colors and applying the oxygen prediction function. This system and methodology have been validated with numerous case studies using degraded powders of different states. In-situ measurements of powder bed oxygen content of layers composed of degraded powders from the recycling study were demonstrated to be in accordance with ex-situ measurements carried out by inert gas fusion.

One of the advantages of this solution is that powder attributes can be evaluated in-line on large quantities that are directly representative of the material to be used in the L-PBF process. As opposed to ex-situ measurements that are time consuming, conducted on small amounts of powder and require a sample collection inside the printer, this method is suitable for industrial machines operating in powder circuit closed loops and as such offers perspectives for automation of this in-situ monitoring technique. However, a limiting factor remains the long acquisition time to provide such high spatial resolution, but alternatives could be explored and will be discussed afterwards.

An additional finding from this study is that the oxygen results are consistent, using a technique accounting only the colored particles, which was a priori not obvious given the multitude of altered particles observed in the recycled powders, notably with partially oxidized particles. This suggests that the oxygen pickup of the recycled powders may be primarily related to the color-oxidized particles in the HAZs rather than the oxide nodules on spatters surface.

Finally, with the aim of minimizing the alteration of powder characteristics during the process in order to extend the feedstock durability during powder recycling, a study of the influence of process parameters and build characteristics in L-PBF was carried out. Numerous fabrications were conducted with various melted volume fractions, parts spacings, fabrication heights and build chamber oxygen concentrations.

The solidification of larger volume as parts during processing leads to an increase of the fraction of sieved residues with respect to the total amount of recovered powder at the end of the manufacturing. In the powder recovered after sieving, the oxygen content is roughly proportional to the melted volume in the print. However, it should be stated that such a result may only be valid for plain parts, such as the cubes used in the present thesis. As observed within the recycling study, spatter particles with selective oxidation can be small enough to pass through the sieve mesh, and were found to me more numerous with increased melted volume. A slight increase in particles size is also observed with greater consolidated volume.

A reduction of part spacing also results in an increase of the oxygen content in the recovered powder. A major pickup is noticeable for powders close to the printed specimens, especially at distances of 500 µm or 1 mm. In such small intervals, many colored particles are observable, but also many ejecta that must fall relatively close to the laser tracks. A distance of 30 mm between adjacent parts on the build platform greatly minimizes powder degradation, with oxygen contents values close to the one the virgin powder.

Fabrication height, related to printing time has an impact on powder oxygen concentration for the large spacings, with higher contents and slightly more colored particles. However, it should be recalled that these observations were made on recovered powders from batches processed without heating plate. Indeed, the use of an heated substrate could certainly influence the kinetics of powder degradation. Fabrication height resulting in progressive increase of part temperature with repeated laser scanning also affects significantly the surface roughness of the parts, with more numerous and larger particles sintered to the side surfaces. A reduction of part spacing also negatively impacts surface roughness.

Last but no least, a higher oxygen concentration in the build chamber during processing accentuates all the previously described phenomena. Processing with 1000 wppm of residual oxygen compared to 300 wppm leads to an increase of sieved residues, ejecta in the sieved powders, colored particles, and overall oxygen contents in all comparable conditions. This showed that the 0.1 wt.% of residual oxygen concentration that is often used in industrial printers is probably not suitable enough in view of the objective of repeated powder reuse, and that lower oxygen contents, say of the order of 300 wppm or less, should be favored to minimize powder oxidation in L-PBF.

Perspectives

Several perspectives can be suggested on the three main work lines addressed in this thesis.

The recycling study could be extended with further investigations on the effect of powder reuse on other properties of the printed parts. For example, corrosion resistance in various environments could be evaluated, which is important especially in the nuclear field for stainless steel 316L components. Complementary mechanical tests in fatigue should be implemented to truly validate the performances stability of the material elaborated with recycled powder.

Given the observed grains modification in parts manufactured with recycled powders, the potential of grain refinement using powders with higher oxygen contents could be explored.

As for the increase in ferritic content observed in the recycling study, it could be interesting to develop a process of magnetic separation in addition to conventional vibrating sieving performed on powder batches between each reuse. This would minimize the risk of process alteration and defect formation with poor uniformity of powder bed layers due to the clustering of ferritic particles in recycled powders.

In view of the slight decrease in the density of printed parts as powder is recycled, it would be useful to try to optimize the standard and most influential processing parameters such as laser power and scanning speed, as the manufacturing cycles are repeated. This could allow to counter the effects linked to the presence of oxides on the particles surface. Further investigation on more sophisticated characterization techniques (e.g. XCT) should be pursued to identify the defects causing this density decrease.

Finally, a similar extensive campaign on the effects of recycling on powders and printed parts could be carried out with a refreshing strategy, *i.e.* by adding different amounts of virgin powder to the reused feedstock after several iterations, to assess the influence of the blending on the extension of powder reuse in the L-PBF process.

This refreshing strategy for powder recycling could be assisted and enhanced by in-situ monitoring of the powder bed. A potentially interesting strategy could consist in using the in-line monitoring of powder bed oxygen content at the end of each production run, and to set one or more threshold values that would determine an addition of new powder to the current powder batch. Figure 6.1 illustrates schematically this solution for powder refreshing strategy coupled with in-situ moniroting of the powder bed.

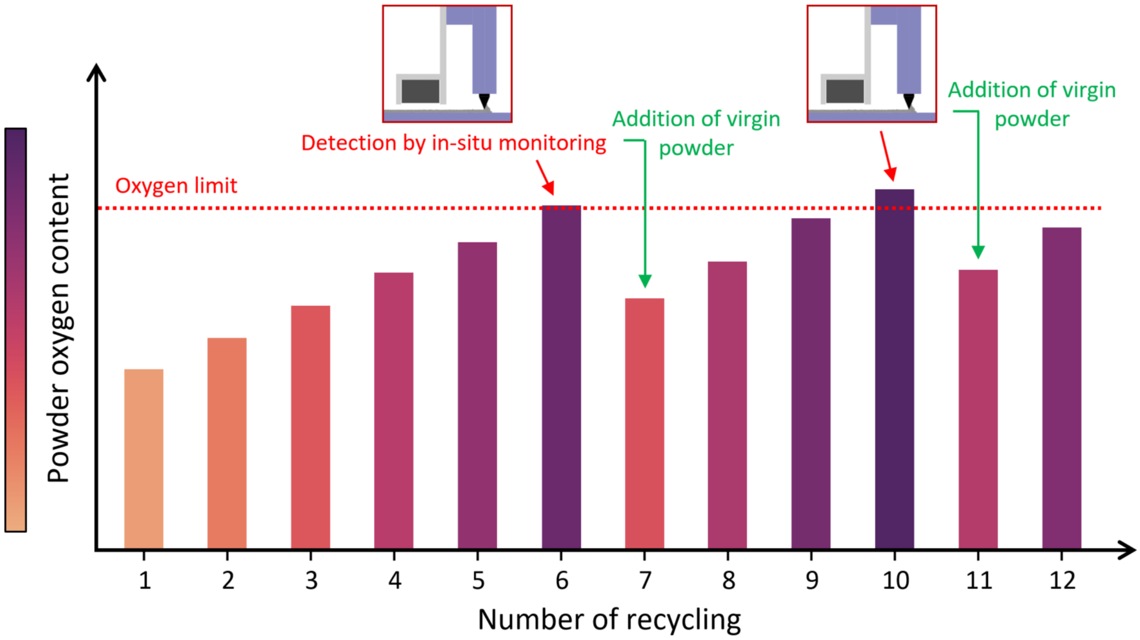

Figure 6.1 – Schematic illustration of refreshing strategy using powder bed monitoring.

On a different line of thought, a detection by in-line scanning of a too important oxygen concentration in the powder feedstock could lead to corrective actions with an adaptation of process parameters to be in accordance with the attributes of the powder. Such an approach could also be beneficial for the in-line determination of other powder characteristics, such as particle size or surface density of the powder bed layer. Alternative image analysis methods for the determination of oxygen concentration could also be proposed, *e.g.* with particle detection and removal of the edges in order to only analyze the central pixels.

Regarding the limitations related to the long acquisition time of the scans for such high spatial resolution, several solutions can be discussed. The use of other types of more efficient scanners could accelerate the acquisition speed, although gains of an order of magnitude cannot be expected using currently available technology. A method using multiple high speed cameras mounted on the recoater could also be considered, taking into account the space issues in the build chambers of L-PBF printers. Keeping the same scanner technology, the feasibility and repeatability of the results should also be evaluated by acquiring lower resolution scans, which would allow a very significant time gain (see table 2.2). Given the completely satisfactory results of the scan method based on the averaging of the colors on the powder bed before applying the oxygen prediction function, one could assume that a lower resolution acquisition (thus larger pixel size) already performs a similar averaging during the image acquisition and could result in reliable outcomes.

In any case, even with long scanning time, it is possible to implement in-situ powder bed monitoring with minimal impact on the process productivity. One could think of conducting the powder bed scans only at specific time locations, *e.g.* before the start of the process during injection of inert gas in the build chamber, and at the end of the fabrication while the solidified specimens are cooling down. This would ensure quality control between each production batch. Such an approach seems to be one of the most viable solution for closed loop systems where the powder is not removed for sieving but circulates autonomously through a sieve while being mixed between recovered powder and still virgin un-used powder from the machine hopper.

The methodology for in-line measurement of powder bed oxygen content was performed with stainless steel 316L powders, but this approach could easily be transposed to other metallic materials. Future work could be focused on performing the calibration with ex-situ oxidation leading to the identification of a correlation function O = f(R,G,B) for titanium alloys and nickel-based alloys.

From the material science standpoint, another perspective concerns the ex-situ powder oxidation study. Experiments with other combinations of heating temperature and exposure time to complement the database composed of 300, 400 and 500 °C oxidations, coupled with further theoretical modeling of the oxidation phenomena could allow to better understand the oxidation mechanisms of powder occurring during processing in L-PBF.

In addition to the parameters and build characteristics studied in this work, other factors could be explored regarding the alteration of the recovered powder. The use of a heating plate during the manufacturing process, useful in particular to reduce the residual stresses of the parts, must certainly have a strong impact on the powders remaining on the powder bed.

On the same line of thought, it would be interesting to assess as well complex geometries such as lattices structures which are of interest in additive manufacturing. Such geometries present high surface/volume ratio, therefore larger numbers of particles in heat affected zones in the vicinity of the laser tracks. This could lead to significantly different results as compared to those obtained in the present study using plain parts.

A preliminary look at the effect on the printed parts has been presented with surface roughness analysis. This study should be supplemented with additional characterizations, in order to understand the impact of volume occupied by the parts on the build area, part spacing and build chamber oxygen concentration on the density and mechanical properties of the elaborated components.

Finally, an interesting prospect as regards powder degradation would be to investigate even lower oxygen concentrations in the build chamber, say under 100 or 50 ppm, as it has been done occasionally in the literature or in other processes such as laser metal deposition for example.

All the results presented in this thesis, as well as the opened perspectives show that powder recycling in laser powder bed fusion has the strong potential to become a game changer in the years to come. Further work is of course required, with adjustments of recycling strategies according to the materials, machines and applications, but the methodologies proposed in the present work can be taken as first steps in this direction.

Appendix

Appendix A:
Preliminary process parameters optimization

Prior to conducting the recycling study, a short optimization of the process parameters was performed on the Trumpf TruPrint 1000 machine with the virgin SS316L powder used in this thesis.

Process parameters optimization was conducted regarding three variables that were varied in the following ranges:

- Laser powder P: [80 W ; 180 W]
- Scanning speed v: [550 mm/s ; 1400 mm/s]
- Hatch distance h: [0.05 mm; 0.11 mm]

For a reminder of the meaning of these parameters, one can refer to figure 1.18 in section 1.2.2. All the other parameters were fixed, such as the layer thickness of 30 µm, a maximum oxygen content of 300 wppm in the build chamber, or the scanning strategy as described in part 2.1.1, figure 2.2.

A statistical design of experiments (DOE) (Latin Hypercube Sampling, LHS) was generated using Python programming in order to reduce the number of tests and to uniformly distribute the processing conditions over the investigated ranges. Cubic specimens were manufactured according the different combinations of parameters, and were analyzed by metallographic observation to determine the resulting densities. This approach was repeated incrementally by narrowing down the process window, until optimized parameters were obtained.

Figure 6.2 (a) shows the entire DOE with the density of the parts (in color) in function of the laser power, scanning speed and hatch distance. Figure 6.2 (b) displays a narrowed area of interest and for samples presenting a density above 99.9 %, in order to differentiate these very good parameters combinations.

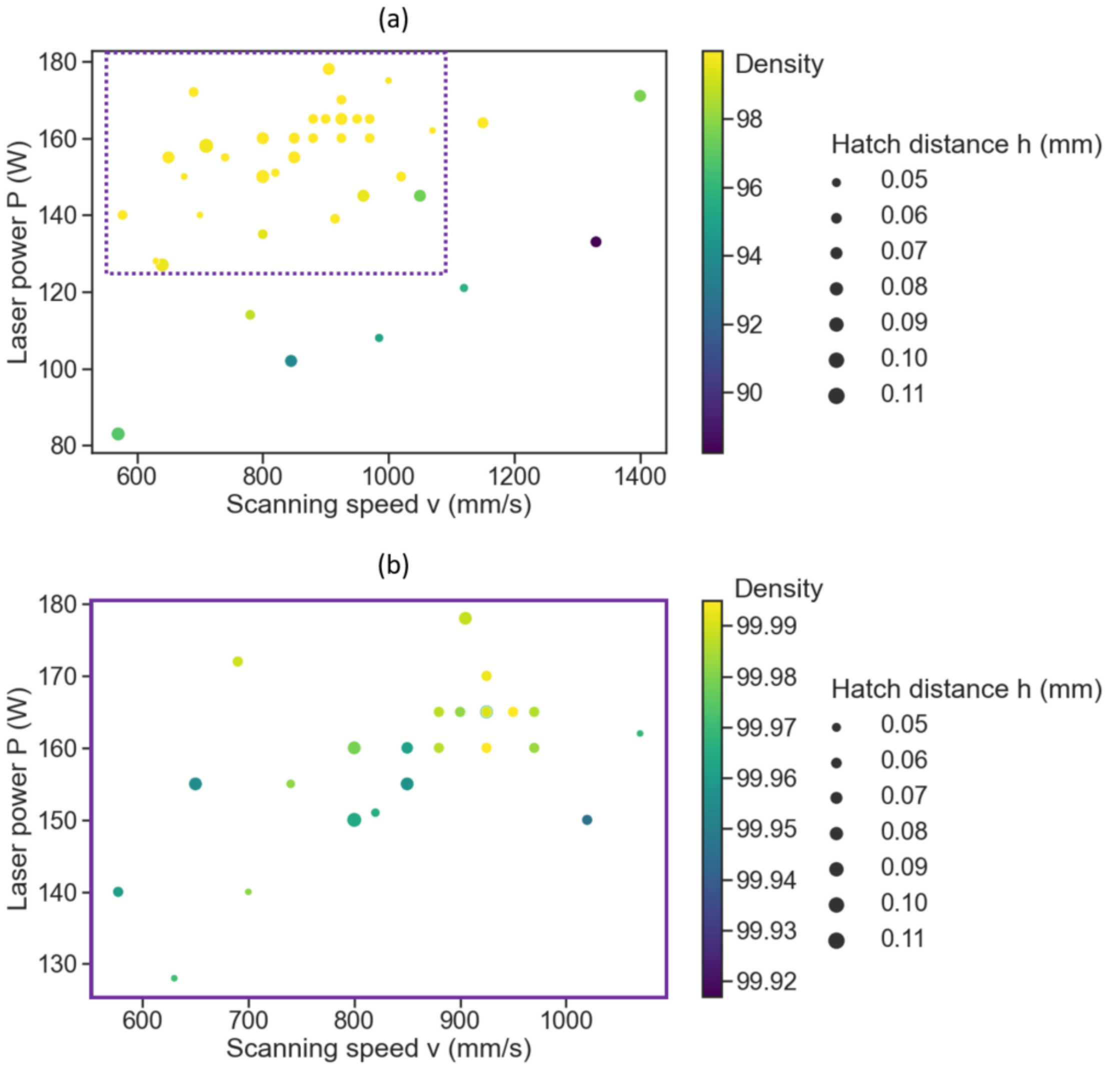

Figure 6.2 – Parts density in function of laser power, scanning speed and hatch distance: (a) Entire DOE, (b) Zoom on samples with density over 99.9 %.

This preliminary study led to the choice of the following optimized parameters: $P = 165$ W, $v = 950$ mm/s and $h = 0.05$ mm, for a layer thickness of 30 µm. These parameters produced specimens with a density consistently above 99.9% when measured by cross section examination, and over 99.5% by the Archimedes method. The parameters set was used for all the L-PBF prints carried out during this work.

Résumé étendu français

La fabrication additive métallique à base de poudre s'est imposée comme une technologie compétitive alternative aux procédés métallurgiques classiques tels que la fonderie ou le forgeage pour la production de pièces utilisées dans différents secteurs industriels comme l'aérospatial, l'automobile, le biomédical ou les énergies. Ce succès est attribué aux possibilités de conception presque illimitées pour la fabrication de composants proche des cotes. Cette liberté géométrique permet de faire de l'allègement de matière avec de l'optimisation topologique, de remplacer la production de nombreuses pièces autrefois soudées entre elles par un assemblage intégré, ou encore de fonctionnaliser des pièces avec des structures lattices complexes. D'autres avantages s'ajoutent à cela, à savoir des propriétés mécaniques excellentes, un temps d'industrialisation rapide, une production directe sans outillage, ou encore un faible nombre d'opérations de post-traitement nécessaires. De plus, un des points les plus différenciant par rapport aux procédés soustractifs classiques est le fait que la fabrication additive nécessite énormément moins de matière pour fabriquer les pièces.

Le procédé de fusion laser sur lit de poudre (Laser Powder Bed Fusion, L-PBF) est l'un des procédés de fabrication additive le plus mature et est déjà utilisé industriellement. Comme tout procédé de fabrication additive, il permet de fabriquer les pièces par ajout successif de matière, couche par couche, à partir d'un fichier numérique. En L-PBF, la fabrication est réalisée par l'étalement de fines couches de poudre métallique les unes au-dessus des autres, avec une étape de consolidation de la matière par un ou plusieurs faisceaux laser entre chaque étalement de couche. De ce fait, lors des fabrications, seule une petite fraction du volume de poudre utilisé est consolidée en tant que pièces, et les coûts et le rendement économique et écologique du procédé L-PBF dépendent fortement de la capacité à réutiliser efficacement la poudre non fondue (aussi appelé recyclage de la poudre).

Cependant, les poudres récupérées à la fin d'une fabrication, bien que non solidifiées en tant que pièces, peuvent subir une dégradation de leurs attributs. Lorsque le laser interagit avec le lit de poudre, un bain liquide est créé et des interactions et phénomènes complexes mènent à des instabilités et éjections de matière qui contaminent le lit de poudre adjacent. Par ailleurs, le lit de poudre est exposé à de hautes températures lors des passages successifs du laser, et ce dans une atmosphère imparfaitement contrôlée avec des teneurs résiduelles en oxygène suffisantes pour promouvoir leur oxydation. Ces modifications des attributs des particules de poudre ajoutent de l'incertitude vis-à-vis du procédé et des résultantes propriétés des pièces élaborées. Une autre problématique concerne la dégradation de la poudre qui n'est pas homogène, avec la présence de particules altérées présentant différents états de dégradation réparties aléatoirement dans le lot de poudre récupéré à la fin d'une fabrication.

De plus, de nombreux facteurs tels que les paramètres opératoires du procédé, mais aussi les caractéristiques topologiques des pièces élaborées, influencent la cinétique de dégradation de la matière première non fusionnée.

Ce travail de thèse se concentre sur la compréhension des phénomènes et conditions de dégradation de la poudre durant le procédé et lors de la réutilisation successive de la poudre, ainsi que l'impact sur les pièces élaborées. Ces connaissances, combinées à un meilleur contrôle et suivi de la qualité de la poudre lors du procédé, pourraient permettre d'assurer une implémentation fiable du processus de réutilisation de la poudre dans le procédé L-PBF. Les objectifs de la thèse cherchent à répondre aux questions de recherche suivantes :

- Comment la réutilisation de la poudre en L-PBF affecte-t-elle la qualité de la matière première et les propriétés des pièces élaborées ?
- Comment la dégradation de la poudre peut-elle être suivie lors de sa réutilisation successive en L-PBF ?
- Comment la teneur en oxygène dans la chambre de fabrication et les caractéristiques géométriques des pièces influencent-elles la dégradation de la poudre, dans le but de la minimiser ?

Les travaux ont été réalisé avec un matériau communément utilisé en fabrication additive métallique et dans l'industrie de l'énergie, à savoir l'acier inoxydable 316L. Ils sont divisés en trois études traitant chacune de ces trois questions, avec des objectifs de compréhension du recyclage de la poudre en L-PBF, d'implémentation d'un système de monitoring de la dégradation de la poudre, et de minimisation de cette dégradation avec une optimisation des paramètres. L'approche scientifique est résumée par la figure 6.3, avec ces objectifs regroupés dans les cadres *Analysis*, *Monitoring* et *Optimization*.

La thèse est divisée en 5 chapitres, incluant ces trois études en trois chapitres de résultats. Le premier chapitre présente une revue de la littérature, décrivant tout d'abord le domaine de la fabrication additive et le procédé de fusion laser sur lit de poudre, ainsi que le matériau d'acier inoxydable 316L. Ensuite, le procédé est présenté en plus grand détail, avec notamment les paramètres influençant sur ce dernier, en se concentrant sur les effets de la poudre et des paramètre opératoires. S'en suit un état de l'art sur le recyclage de la poudre en L-PBF, avec les différentes études traitant de l'influence sur les poudres et les pièces fabriquées. Enfin, le monitoring du procédé L-PBF implémenté dans la littérature est évoqué, vis-à-vis des différentes caractéristiques contrôlées.

Le deuxième chapitre décrit les différentes techniques expérimentales et méthodes employées pour produire et caractériser les échantillons. Les caractéristiques et conditions d'opération de la machine de fusion laser sur lit de poudre utilisée pour cette thèse sont d'abord détaillées. Ensuite, les techniques utilisées pour la caractérisation des matériaux sont présentées, incluant les techniques d'analyses microstructurales communes aux poudres et aux pièces, ainsi que les techniques spécifiques pour la caractérisation des poudres et de pièces massives. Enfin, le dispositif de banc instrumental utilisé pour le développement de la méthodologie de monitoring de la poudre est introduit.

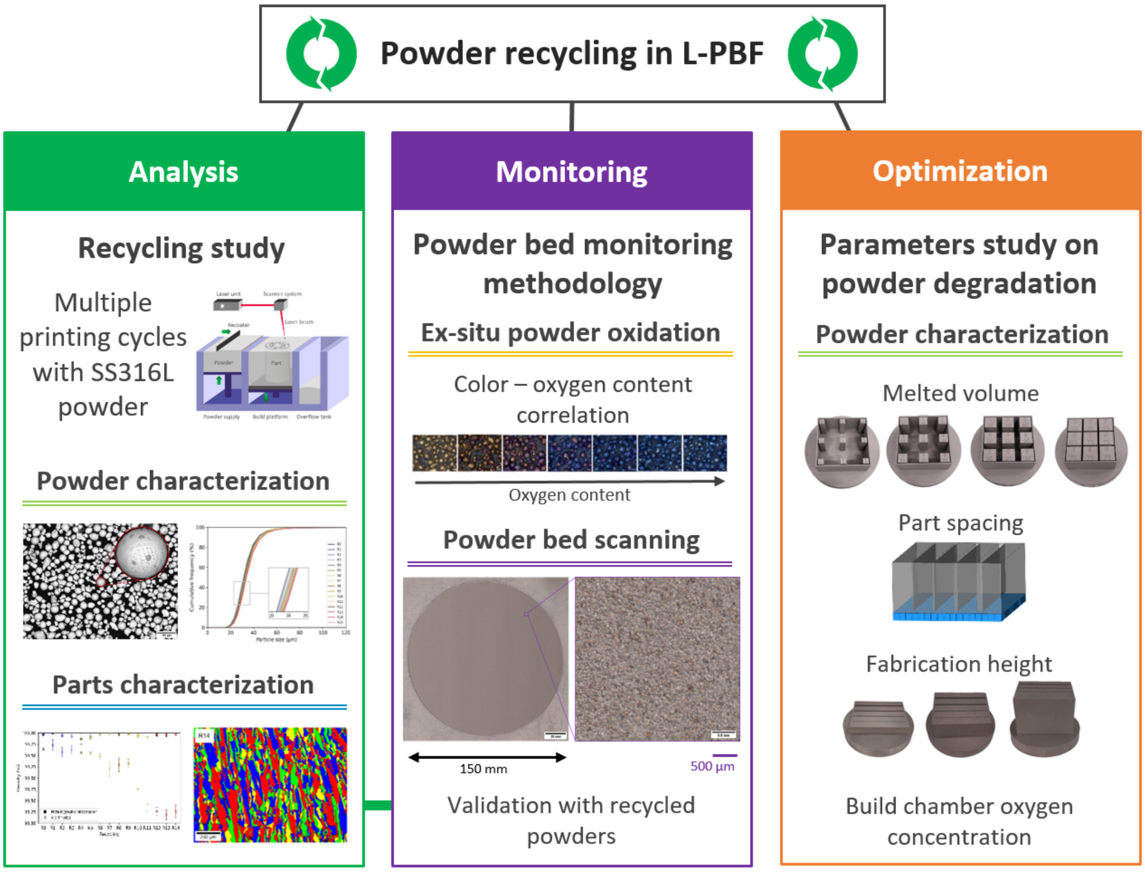

Figure 6.3 – Représentation schématique de l'approche scientifique et des études de la thèse.

Le chapitre 3 se focalise sur l'étude du recyclage de la poudre. La méthodologie entreprise est schématisée en figure 6.4. Un plateau comportant les même pièces (des cylindres pour des essais de traction et des cubes pour évaluer la densité, la microdureté, la teneur en oxygène et les phases) est fabriqué de nombreuses fois, à partir d'un lot de poudre neuve puis de celle récupérée après chaque fabrication. Entre chaque cycle, la poudre est tamisée afin de retirer les particules plus grandes que 50 µm, et un suivi de la poudre est réalisé, avec le prélèvement d'échantillons pour une caractérisation extensive. Cette étude a permis la fabrication de 15 plateaux successifs sans ajout de poudre neuve, et le suivi des attributs des poudres et des propriétés des pièces fabriquées à chaque itération.

Les résultats des caractérisations montrent une dégradation inévitable des attributs des particules avec la réutilisation successive dans le procédé L-PBF. Le changement le plus significatif concerne la teneur en oxygène, qui augmente graduellement au cours des 15 recyclages. Cela représente une prise d'oxygène de 40%, représentant presque 200 ppm massique de plus pour la poudre recyclée de nombreuse fois par rapport à la poudre neuve (mesurée à 474 ppm). Cette augmentation de la teneur en oxygène se traduit par la présence de particules altérées dans les échantillons de poudres réutilisées. Cela inclut des particules partiellement oxydées, présentant des nodules d'oxydes riches en Si et Mn. Ces dernières sont significatives des éjectas de matière provenant du bain liquide ou des environs de ce dernier, s'étant oxydées partiellement en vol, avec des temps de refroidissement très rapide ne permettant pas la coalescence des nodules d'oxyde en une couche continue. Des poudres colorées sont également visibles, ces dernières présentant des teneurs locales en oxygènes

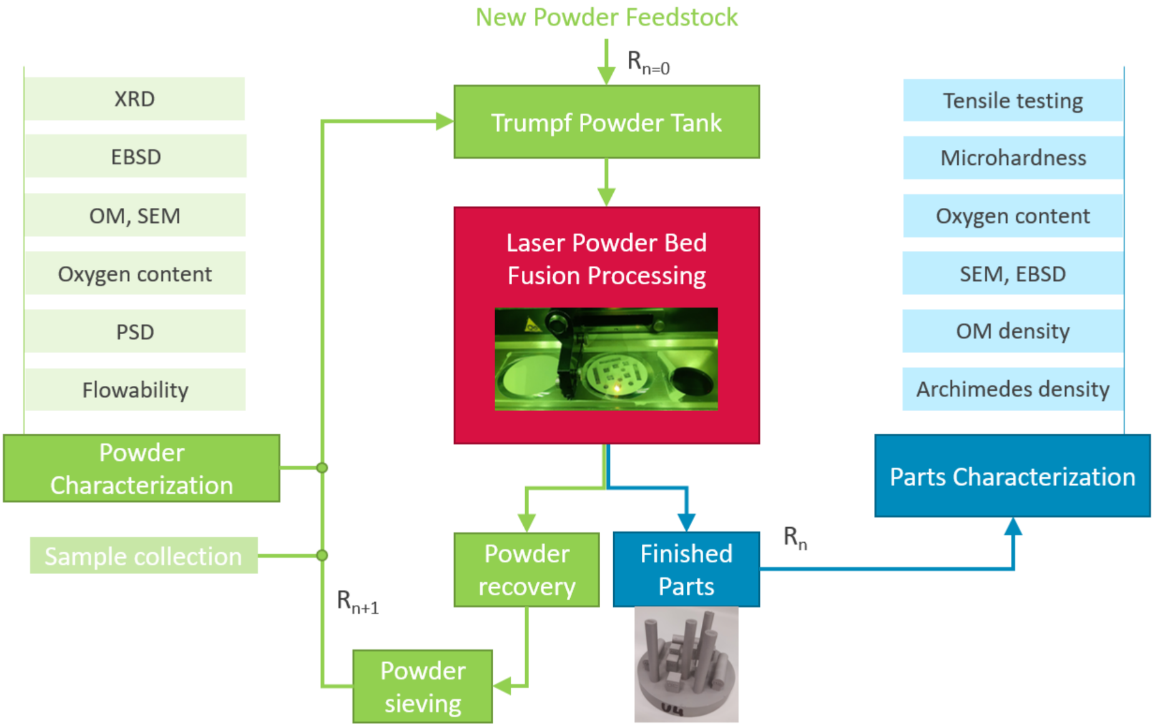

Figure 6.4 – Méthodologie de l'étude de recyclage de la poudre.

plus faibles que celles des nodules d'oxyde des éjectas, mais une couche d'oxyde uniforme et continue en surface. Ces particules oxydées colorées sont susceptibles de provenir des zones affectées thermiquement, proche des pièces qui sont des sources chaudes avec les passages successifs du laser, et qui subissent une oxydation à l'état solide plus longue permettant la croissance continue d'un film d'oxyde.

D'autres changements des caractéristiques des poudres ont également été observés. La distribution en taille des particules se décale légèrement vers de plus grandes valeurs au fur et à mesure des réutilisations. La coulabilité, quant à elle, est légèrement améliorée, du fait de ces tailles légèrement plus grandes mais aussi de la présence d'oxydes en surface qui réduit la cohésion inter-particules. Des particules magnétiques, très sphériques, lisses et brillantes ont également été observées par microscopie optique, et identifiées par EBSD comme étant des monocristaux de ferrite. Une quantification par DRX a permis d'identifier une augmentation de la fraction de phase de δ-ferrite qui se porte à 4 % massique après 15 recyclages, comparé à une poudre neuve quasiment totalement austénitique (0-1% de ferrite). Ces particules magnétiques sont retrouvées en plus grand nombre dans les résidus de tamis, bien que leur taille n'excède jamais 70-80 µm. Il est considéré que ces particules ferritiques sont des particules de relativement petites tailles éjectées du bain ou entrainées par les pressions alentours à de grandes vélocités, donnant lieu à des vitesses de refroidissement très rapide et une solidification métastable en ferrite δ. Ces particules ferritiques sont nuisibles au procédé L-PBF du fait de leur attraction magnétique qui va engendrer des clusters et irrégularités lors de l'étalement des couches de poudre.

Les résidus de tamis ont été identifiés comme présentant des caractéristiques non appropriées pour le procédé et très loin de celles des particules communément utilisées. En plus de la grande proportion de particules magnétiques, les résidus sont très grands en taille, allant souvent jusqu'à 100 – 150 µm de diamètre. Les formes sont irrégulières, avec la présence de nombreux satellites, et la teneur en oxygène est trois fois supérieure à celle de la poudre initiale. Cette étape de tamisage est donc vraiment cruciale pour limiter la dégradation de la poudre et favoriser une durée de vie prolongée d'utilisation de la poudre en L-PBF.

Concernant les propriétés des pièces, la densité de ces dernières diminue légèrement au cours des fabrications, passant de 99.6 % à légèrement au-dessus de 98%, mesuré par la méthode d'Archimède. D'un point de vue microstructure, la taille des grains allongés dans le sens de fabrication a tendance à diminuer, avec des grains plus fins et nombreux au fur et à mesure des réutilisations de la poudre. Ces changements peuvent être connectées aux différences de caractéristiques de la matière première, avec notamment la prise d'oxygène et présence de couches d'oxydes, qui vont influencer la stabilité du bain de fusion et la solidification. Une augmentation de la teneur en oxygène dans les pièces fabriquées est également relevée. Malgré ces différences, les propriétés mécaniques des pièces fabriquées restent stables en termes de résistance à la traction et microdureté. Les valeurs obtenues sont satisfaisantes et au-dessus des standards requis par les normes pour l'acier inoxydable en fabrication additive, avec une dureté moyenne de 212 HV, une limite élastique Re de 580 MPa, une résistance Rm de 670 MPa et un allongement à rupture de 40 %.

Le chapitre 4 de la thèse présente le développement d'une nouvelle méthode de suivi de la dégradation de la poudre in-situ. En vue des résultats de l'étude de recyclage, la teneur en oxygène des poudres est apparue comme un bon indicateur du vieillissement de la poudre au cours de son utilisation et sa réutilisation dans le procédé de fusion laser sur lit de poudre. La méthodologie mise en place dans le cadre de cette étude utilise l'avantage de la fabrication couche par couche du procédé avec l'étalement successif de couches de poudre pour permettre à contrôle en ligne de la matière première au niveau du lit de poudre. Un scanner installé sur le système d'étalement de poudre d'un banc instrumenté de L-PBF a permis d'acquérir des images en ligne du lit de poudre. En synchronisant la vitesse de déplacement du racleur avec la vitesse d'acquisition d'image du scanner, il est possible de capturer l'entièreté du lit de poudre avec une résolution allant jusqu'à 4800 dpi (dots-per-inch), ce qui correspond à 5.3 µm par pixel. Une telle résolution permets de résoudre chaque particule individuelle.

Une nouvelle méthodologie a été développée, utilisant les couleurs des particules pour déterminer leur concentration en oxygène. L'approche est basée sur des étapes de calibrations préliminaires permettant de faire cette corrélation entre couleur et oxygène. Des échantillons de poudres ont été chauffés en four à différentes combinaisons de temps et température afin d'obtenir différents états d'oxydation. La teneur en oxygène de chaque échantillon a été mesurée par analyse chimique conventionnelle de fusion sous gaz inerte. Ensuite, tous ces échantillons de poudres oxydées sont scannés en ligne après étalement sur lit de poudre à l'aide du dispositif mis en place sur le banc instrumenté. La couleur moyenne de chaque lit de poudre est déterminée par une simple identification des valeurs caractéristiques qui définissent les couleurs sur les images numériques, à savoir les valeurs des quantités RGB (Red, Green, Blue). En combinant ces valeurs de couleur moyenne aux concentrations en oxygènes correspondantes mesurées précédemment, il a été possible de modéliser l'oxygène en tant que fonction des valeurs RGB, O = f(R,G,B). Cette fonction de calibration permet donc ensuite de calculer l'oxygène de la poudre d'acier inoxydable 316L par analyse d'image, en fonction des couleurs présentes sur cette dernière. La méthodologie développée et décrite précédemment est résumée en figure 6.5.

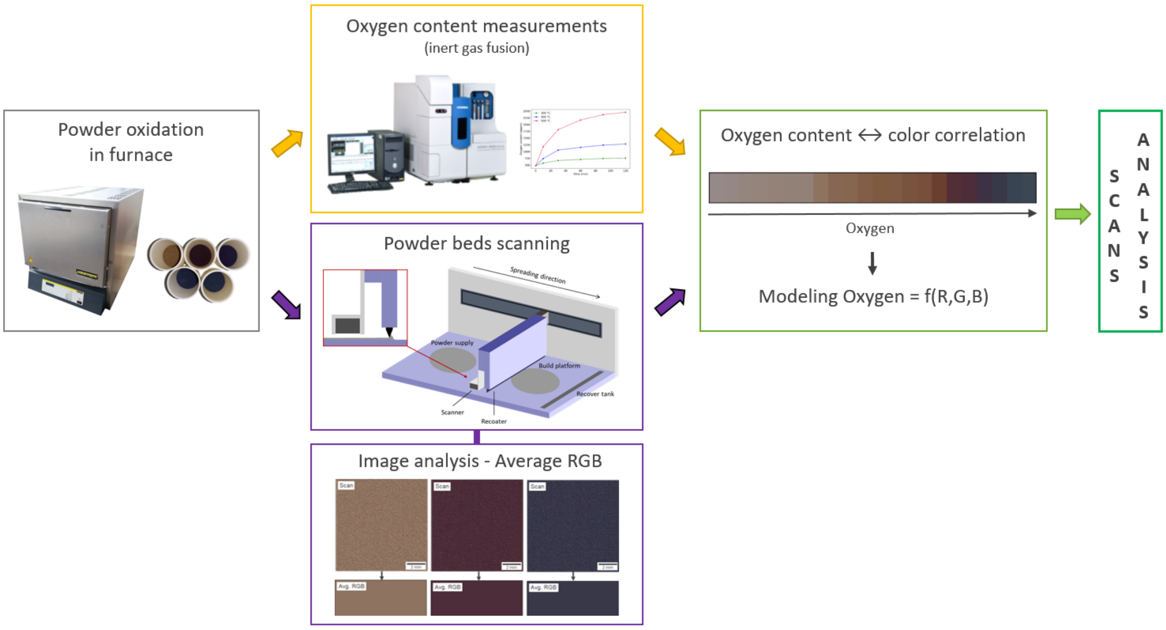

Figure 6.5 – Résumé de la méthodologie développée pour le monitoring de la poudre.

Une fois ce calibrage effectué, cette technique d'analyse en ligne de la qualité de la poudre a été testée et validée en utilisant différents échantillons de poudre dégradés. Des poudres recyclées, collectées lors de l'étude précédente ont été analysées in-situ par scan et analyse d'image, et les résultats se sont révélés conformes aux mesures ex-situ par analyse chimique. D'autres analyses ont validé la méthode, avec la mesure en ligne de la teneur en oxygène de poudre dégradées ≪ artificiellement ≫, avec différentes fractions et teneurs de poudre oxydées en four mélangées à de la poudre de neuve, mais aussi avec des poudres non tamisées, ou encore des résidus de tamis.

Un des avantages de la solution développée est le fait que la matière première est analysée sur de grandes quantités qui sont directement représentatif du matériau dans la machine. Contrairement aux mesures ex-situ conventionnelles qui sont onéreuses, prennent beaucoup de tempes et qui sont réalisées sur de faibles quantités, cette méthode est adaptée pour les machines L-PBF qui fonctionnent avec un circuit de poudre en boucle fermée, et offre des perspectives pour une automatisation de cette technique de monitoring in-situ. Cependant, un facteur limitant à ce jour reste de très longs tempes d'acquisition d'images avec de telles résolutions spatiales.

Une autre conclusion provenant des résultats de cette étude concerne l'apport des particules colorées dans la prise d'oxygène des poudres recyclées. Du fait des résultats très satisfaisants et en accord avec les mesures par fusion sous gaz inerte de cette méthode, qui est basée uniquement sur le calcul de l'oxygène en prenant en compte les couleurs des particules, il peut en être déduit que ces particules oxydées dans les zones affectées thermiquement jouent un rôle significatif dans la prise d'oxygène des poudres réutilisées, comparées aux éjectas présentant des nodules d'oxydes.

Le dernier chapitre de cette thèse présente l'étude sur l'influence de paramètres du procédé et géométriques des pièces sur la dégradation de la poudre en L-PBF. Pour cela, de nombreuses fabrications par L-PBF sont réalisées avec différentes fractions de volume fusionné et solidifié en tant que pièce, différents espacements entre les pièces et des hauteurs de fabrication varié. De plus, toutes les fabrications sont produites en double, avec deux conditions de concentration d'oxygène résiduel dans l'atmosphère au sein de la chambre de fabrication, de 300 ppm et 1000 ppm massique. La poudre non fusionnée à la fin de la fabrication est récupérée dans les zones d'intérêt, à savoir sur le plateau de fabrication pour les différents volumes de pièces, et directement dans des rainures de différentes largeurs pour étudier l'espacement des pièces et les changements locaux au plus proche des zones fusionnées par le laser. Ces échantillons sont tamisés de manière identique à la procédure de réutilisation successive de la poudre, et caractérisés après ce premier et unique cycle de fabrication, avec une attention particulière à l'oxydation de la poudre qui s'est montrée comme le principal changement observé avec le recyclage de la poudre.

L'étude montre que la solidification de plus grands volumes en tant que pièces lors du procédé donne lieu à une augmentation de la fraction de résidus de tamis par rapport à la quantité totale de poudre récupérée sur le plateau de fabrication. Dans la poudre récupérée après tamisage, la teneur en oxygène est globalement proportionnelle à la fraction de volume fusionné sur le plateau, pour des pièces pleines. Comme observé lors de l'étude du chapitre 3, des éjectas avec une oxydation sélective peuvent être de tailles similaires à la poudre neuve et retrouver dans la poudre tamisée, et ont été retrouvés en plus grand nombre avec une fraction de volume fusionné plus grande. Une légère augmentation de la taille des particules est également détectée avec ces plus grands volumes de pièces.

Une réduction de l'espacement des pièces provoque une augmentation de la concentration en oxygène dans les poudres non-utilisées. Une prise d'oxygène significative est mesurée dans la poudre pour un espacement entre les pièces de 500 µm, montrant les effets importants des zones affectées thermiquement proche des pièces qui sont des sources chaudes. Dans ces rainures, on retrouve de nombreuses particules colorées, ainsi qu'un nombre important d'éjectas. A l'opposé, une distance de 30 mm entre les pièces permet de grandement minimiser la dégradation de la poudre, avec des attributs et teneurs en oxygène proches de ceux de la poudre neuve.

La hauteur des pièces et donc de fabrication, qui est reliée au temps de fabrication a également un effet sur la concentration en oxygène des poudres récupérées, principalement pour les grands espacements de pièces, avec de plus grandes teneurs pour des pièces plus hautes. Cela s'explique par le fait qu'aucun plateau chauffant n'a été utilisé, et la température des pièces augmente au fur et à mesure de la fabrication avec les passages successifs du laser. En plus de cela, la rugosité de surface des pièces augmente également de manière significative le long de la direction de fabrication, avec des particules plus nombreuses et plus grandes frittées à la surface. Une réduction de l'espacement des pièces impacte également négativement la rugosité.

Enfin, le paramètre de concentration d'oxygène résiduelle dans la chambre de fabrication joue un rôle crucial dans la cinétique de dégradation et principalement d'oxydation de la poudre. Une pression partielle d'oxygène plus grande accentue tous les phénomènes précédemment décrits. Des fabrications avec 1000 ppm d'oxygène dans l'enceinte comparé à 300 ppm massique conduit à une augmentation de la quantité de résidus de tamis, d'éjectas dans les poudres, et de teneurs en oxygènes pour toutes conditions comparables. Cela montre que la concentration de 0.1% d'oxygène qui est souvent utilisée dans les machines de L-PBF industrielles ne sont pas adaptés pour une réutilisation optimale de la poudre, et des teneurs les plus faibles possibles doivent être privilégiées.

Un résumé schématique de cette étude et des résultats principaux est présenté en figure 6.6.

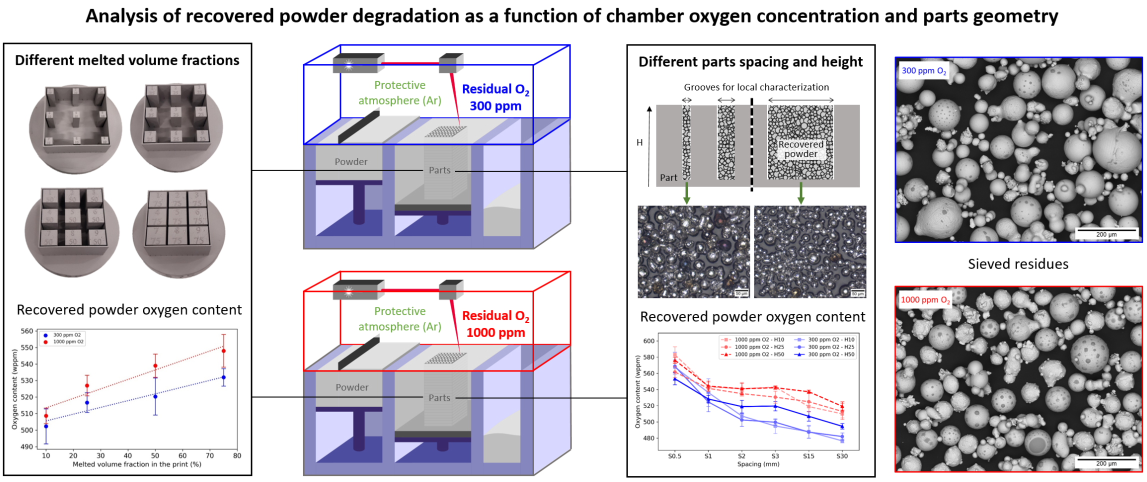

Figure 6.6 – Résumé graphique de l'étude de dégradation de la poudre.

Tous les résultats présentés dans cette thèse montrent que la réutilisation de la poudre dans le procédé de fusion laser sur lit de poudre a un fort potentiel pour devenir de plus en plus robuste dans les années à venir. Une extension de la durée de vie de la poudre non fusionnée lors du procédé, grâce à des connaissances étendues et un suivi du vieillissement fiable, pourra changer la donne vis-à-vis durabilité du procédé. Des travaux complémentaires sont bien sûr nécessaires, avec des ajustements des stratégies de recyclage en fonction des matériaux, machines et applications, mais les méthodologies proposées dans le cadre de cette thèse peuvent être considérées comme des premiers pas dans cette direction.

References

[1] C. Barlier and A. Bernard, *Fabrication additive.* Dunod, Aug. 2015.

[2] A.-F. Obaton, “Fabrication additive : contrôles,” *Techniques de l’ingénieur Procédés de fabrication additive*, vol. base documentaire : TIB633DUO., no. ref. article : bm7950, 2017.

[3] Y. Huang, M. C. Leu, J. Mazumder, and A. Donmez, “Additive Manufacturing: Current State, Future Potential, Gaps and Needs, and Recommendations,” *Journal of Manufacturing Science and Engineering*, vol. 137, Feb. 2015.

[4] Q. Shi, D. Gu, M. Xia, S. Cao, and T. Rong, “Effects of laser processing parameters on thermal behavior and melting/solidification mechanism during selective laser melting of TiC/Inconel 718 composites,” *Optics & Laser Technology*, vol. 84, pp. 9–22, Oct. 2016.

[5] C. Pauzon, E. Hryha, P. Forêt, and L. Nyborg, “Effect of argon and nitrogen atmospheres on the properties of stainless steel 316 L parts produced by laser-powder bed fusion,” *Materials & Design*, vol. 179, p. 107873, Oct. 2019.

[6] F. Yan, W. Xiong, E. Faierson, and G. B. Olson, “Characterization of nano-scale oxides in austenitic stainless steel processed by powder bed fusion,” *Scripta Materialia*, vol. 155, pp. 104–108, Oct. 2018.

[7] A. Leicht, M. Rashidi, U. Klement, and E. Hryha, “Effect of process parameters on the microstructure, tensile strength and productivity of 316L parts produced by laser powder bed fusion,” *Materials Characterization*, p. 110016, Nov. 2019.

[8] Y. M. Wang, T. Voisin, J. T. McKeown, J. Ye, N. P. Calta, Z. Li, Z. Zeng, Y. Zhang, W. Chen, T. T. Roehling, R. T. Ott, M. K. Santala, P. J. Depond, M. J. Matthews, A. V. Hamza, and T. Zhu, “Additively manufactured hierarchical stainless steels with high strength and ductility,” *Nature Materials*, vol. 17, pp. 63–71, Jan. 2018.

[9] M. Randall, *Powder metallurgy science.* Princeton, N.J.: Metal Powder Industries Federation, 1994.

[10] S. Wallner, “Powder Production Technologies,” *BHM Berg- und Hüttenmännische Monatshefte*, vol. 164, pp. 108–111, Mar. 2019.

[11] J. M. Benson and E. Snyders, “The need for powder characterisation in the additive manufacturing industry and the establishment of a national facility,” *The South African Journal of Industrial Engineering*, vol. 26, pp. 104–114, Aug. 2015.

[12] J. H. Tan, W. L. E. Wong, and K. W. Dalgarno, “An overview of powder granulometry on feedstock and part performance in the selective laser melting process,” *Additive Manufacturing*, vol. 18, pp. 228–255, Dec. 2017.

[13] K. Abd-Elghany and D. L. Bourell, “Property evaluation of 304L stainless steel fabricated by selective laser melting,” *Rapid Prototyping Journal*, July 2012.

[14] S. Kou, *Welding Metallurgy*. Hoboken, NJ, USA: John Wiley & Sons, Inc., Oct. 2002.

[15] J. Kruth, L. Froyen, J. Van Vaerenbergh, P. Mercelis, M. Rombouts, and B. Lauwers, “Selective laser melting of iron-based powder,” *Journal of Materials Processing Technology*, vol. 149, pp. 616–622, June 2004.

[16] D. Wang, S. Wu, F. Fu, S. Mai, Y. Yang, Y. Liu, and C. Song, “Mechanisms and characteristics of spatter generation in SLM processing and its effect on the properties,” *Materials & Design*, vol. 117, pp. 121–130, Mar. 2017.

[17] S. Ly, A. M. Rubenchik, S. A. Khairallah, G. Guss, and M. J. Matthews, “Metal vapor micro-jet controls material redistribution in laser powder bed fusion additive manufacturing,” *Scientific Reports*, vol. 7, pp. 1–12, June 2017.

[18] M. Taheri Andani, R. Dehghani, M. R. Karamooz-Ravari, R. Mirzaeifar, and J. Ni, “A study on the effect of energy input on spatter particles creation during selective laser melting process,” *Additive Manufacturing*, vol. 20, pp. 33–43, Mar. 2018.

[19] W. J. Sames, F. A. List, S. Pannala, R. R. Dehoff, and S. S. Babu, “The metallurgy and processing science of metal additive manufacturing,” *International Materials Reviews*, vol. 61, pp. 315–360, July 2016.

[20] W. E. King, H. D. Barth, V. M. Castillo, G. F. Gallegos, J. W. Gibbs, D. E. Hahn, C. Kamath, and A. M. Rubenchik, “Observation of keyhole-mode laser melting in laser powder-bed fusion additive manufacturing,” *Journal of Materials Processing Technology*, vol. 214, pp. 2915–2925, Dec. 2014.

[21] M. Yakout, M. A. Elbestawi, and S. C. Veldhuis, “Density and mechanical properties in selective laser melting of Invar 36 and stainless steel 316L,” *Journal of Materials Processing Technology*, vol. 266, pp. 397–420, Apr. 2019.

[22] C. Kamath, B. El-dasher, G. F. Gallegos, W. E. King, and A. Sisto, “Density of additively-manufactured, 316L SS parts using laser powder-bed fusion at powers up to 400 W,” *The International Journal of Advanced Manufacturing Technology*, vol. 74, pp. 65–78, Sept. 2014.

[23] Y. Bai, Y. Yang, D. Wang, and M. Zhang, “Influence mechanism of parameters process and mechanical properties evolution mechanism of maraging steel 300 by selective laser melting,” *Materials Science and Engineering a-Structural Materials Properties Microstructure and Processing*, vol. 703, pp. 116–123, Aug. 2017.

[24] R. Li, J. Liu, Y. Shi, L. Wang, and W. Jiang, “Balling behavior of stainless steel and nickel powder during selective laser melting process,” *The International Journal of Advanced Manufacturing Technology*, vol. 59, pp. 1025–1035, Apr. 2012.

[25] F. Pinto, I. Souza Filho, M. Sandim, and H. Sandim, “Defects in parts manufactured by selective laser melting caused by delta-ferrite in reused 316L steel powder feedstock,” *Additive Manufacturing*, vol. 31, p. 100979, Jan. 2020.

[26] F. Ahmed, U. Ali, D. Sarker, E. Marzbanrad, K. Choi, Y. Mahmoodkhani, and E. Toyserkani, “Study of powder recycling and its effect on printed parts during laser powder-bed fusion of 17-4 PH stainless steel,” *Journal of Materials Processing Technology*, p. 116522, Nov. 2019.

[27] V. Seyda, N. Kaufmann, and C. Emmelmann, “Investigation of Aging Processes of Ti-6Al-4 V Powder Material in Laser Melting,” *Physics Procedia*, vol. 39, pp. 425–431, 2012.

[28] P. E. Carrion, A. Soltani-Tehrani, N. Phan, and N. Shamsaei, “Powder Recycling Effects on the Tensile and Fatigue Behavior of Additively Manufactured Ti-6Al-4V Parts,” *JOM*, vol. 71, pp. 963–973, Nov. 2018.

[29] G. Jacob, C. U. Brown, M. A. Donmez, S. S. Watson, and J. Slotwinski, “Effects of powder recycling on stainless steel powder and built material properties in metal powder bed fusion processes,” Tech. Rep. NIST AMS 100-6, National Institute of Standards and Technology, Gaithersburg, MD, Feb. 2017.

[30] A. T. Sutton, C. S. Kriewall, S. Karnati, M. C. Leu, and J. W. Newkirk, “Characterization of AISI 304L stainless steel powder recycled in the laser powder-bed fusion process,” *Additive Manufacturing*, vol. 32, p. 100981, Mar. 2020.

[31] H. P. Tang, M. Qian, N. Liu, X. Z. Zhang, G. Y. Yang, and J. Wang, “Effect of Powder Reuse Times on Additive Manufacturing of Ti-6Al-4V by Selective Electron Beam Melting,” *JOM*, vol. 67, pp. 555–563, Mar. 2015.

[32] M. J. Heiden, L. A. Deibler, J. M. Rodelas, J. R. Koepke, D. J. Tung, D. J. Saiz, and B. H. Jared, “Evolution of 316L stainless steel feedstock due to laser powder bed fusion process,” *Additive Manufacturing*, vol. 25, pp. 84–103, Jan. 2019.

[33] A. T. Sutton, C. S. Kriewall, M. C. Leu, J. W. Newkirk, and B. Brown, “Characterization of laser spatter and condensate generated during the selective laser melting of 304L stainless steel powder,” *Additive Manufacturing*, vol. 31, p. 100904, Jan. 2020.

[34] M. Simonelli, C. Tuck, N. T. Aboulkhair, I. Maskery, I. Ashcroft, R. D. Wildman, and R. Hague, “A Study on the Laser Spatter and the Oxidation Reactions During Selective Laser Melting of 316L Stainless Steel, Al-Si10-Mg, and Ti-6Al-4V,” *Metallurgical and Materials Transactions A*, vol. 46, pp. 3842–3851, Sept. 2015.

[35] B. Sartin, T. Pond, B. Griffith, W. Everhart, L. Elder, E. Wenski, C. Cook, D. Wieliczka, W. King, A. Rubenchik, S. Wu, B. Brown, C. Johnson, and J. Crow, “316L powder reuse for metal additive manufacturing,” *Solid Freeform Fabr. Symp. Proc.*, vol. 2017, pp. 351–364, 2017.

[36] V. Contaldi, F. Del Re, B. Palumbo, A. Squillace, P. Corrado, and P. Di Petta, “Mechanical characterisation of stainless steel parts produced by direct metal laser

sintering with virgin and reused powder," *The International Journal of Advanced Manufacturing Technology*, vol. 105, pp. 3337–3351, Dec. 2019.

[37] Q. Guo, C. Zhao, M. Qu, L. Xiong, L. Escano, S. M. H. Hojjatzadeh, N. D. Parab, K. Fezzaa, W. Everhart, T. Sun, and L. Chen, "In-situ characterization and quantification of melt pool variation under constant input energy density in laser powder bed fusion additive manufacturing process," *Additive Manufacturing*, vol. 28, pp. 600–609, Aug. 2019.

[38] J. zur Jacobsmühlen, G. Witt, S. Kleszczynski, and D. Merhof, "Elevated Region Area Measurement for Quantitative Analysis of Laser Beam Melting Process Stability," *26th Annual International Solid Freeform Fabrication Symposium, SFF 2015*, 2015.

[39] L. Scime and J. Beuth, "A multi-scale convolutional neural network for autonomous anomaly detection and classification in a laser powder bed fusion additive manufacturing process," *Additive Manufacturing*, vol. 24, pp. 273–286, Dec. 2018.

[40] L. Tan Phuc and M. Seita, "A high-resolution and large field-of-view scanner for in-line characterization of powder bed defects during additive manufacturing," *Materials & Design*, vol. 164, p. 107562, Feb. 2019.

[41] Horiba Group, "Partica LA-950 Brochure," 2020.

[42] A. T. Sutton, C. S. Kriewall, M. C. Leu, and J. W. Newkirk, "Powder characterisation techniques and effects of powder characteristics on part properties in powder-bed fusion processes," *Virtual and Physical Prototyping*, vol. 12, pp. 3–29, Jan. 2017.

[43] D. Kotecki and T. Siewert, "WRC-1992 constitution diagram for stainless steel weld metals : a modification of the WRC-1988 diagram," *Welding Journal*, vol. 71, 1992.

[44] T. de Terris, O. Andreau, P. Peyre, F. Adamski, I. Koutiri, C. Gorny, and C. Dupuy, "Optimization and comparison of porosity rate measurement methods of Selective Laser Melted metallic parts," *Additive Manufacturing*, vol. 28, pp. 802–813, Aug. 2019.

[45] P. S. Korinko and S. H. Malene, "Considerations for the weldability of types 304L and 316L stainless steel," *Practical Failure Analysis*, vol. 1, pp. 61–68, Aug. 2001.

[46] Wohlers Associates, *Wohlers Report 2022: 3D printing and Additive Manufacturing Global State of the Industry.* 2022.

[47] AMPOWER GmbH & Co. KG., *AMPOWER Report 2022.* 2022.

[48] ISO/ASTM, "52900:2021, Additive Manufacturing – General Principles – Fundamentals and Vocabulary," tech. rep., ASTM International, West Conshohocken, PA, 2021.

[49] C. Kriewall, A. Sutton, S. Karnati, J. Newkirk, and M.-C. Leu, "Effects of Area Fraction and Part Spacing on Degradation of 304L Stainless Steel Powder in Selective Laser Melting," *Proceedings of the 28th Solid Freeform Fabrication Symposium (2017, Austin, TX)*, pp. 277–288, Aug. 2017.

[50] M. Barclift, S. Joshi, T. W. Simpson, and C. J. Dickman, "Cost Modeling and Depreciation for Reused Powder Feedstocks in Powder Bed Fusion Additive Manufacturing," *Proceedings of the 27th Annual International Solid Freeform Fabrication Symposium, SFF 2016*, pp. 2007–2028, 2016.

[51] D. Bourell, J. Beaman, M. Leu, and D. Rosen, “A brief history of additive manufacturing and the 2009 roadmap for additive manufacturing: Looking back and looking ahead,” *Proceedings of RapidTech*, pp. 24–25, 01 2009.

[52] P. Ciraud, “Process and method for the manufacture of any objects desired from any meltable material,” French Patent FR2166526, 1971.

[53] R. F. Housholder, “Molding process,” US Patent US4247508, 1979.

[54] H. Kodama, “A scheme for three-dimensional display by automatic fabrication of three-dimensional model,” *IEICE Transactions on Electronics*, vol. J64-C, pp. 237–241, Apr. 1981.

[55] H. Kodama, “Automatic method for fabricating a three-dimensional plastic model with photo-hardening polymer,” *Review of Scientific Instruments*, vol. 52, pp. 1770–1773, Nov. 1981.

[56] J.-C. André, A. Le Mehauté, and O. De Witte, “Device for producing a model of an industrial part,” French Patent FR2567668, 1984.

[57] T. Wohlers and T. Gornet, “History of additive manufacturing,” *Wohlers report*, vol. 24, 2016.

[58] C. Hull, “Apparatus for production of three-dimensional objects by stereolithography,” US Patent US4575330, 1984.

[59] P. Kocovic, *3D Printing and Its Impact on the Production of Fully Functional Components: Emerging Research and Opportunities.* Advances in Chemical and Materials Engineering, IGI Global, 2017.

[60] J. Kruth, “Material Incress Manufacturing by Rapid Prototyping Techniques,” *CIRP Annals*, vol. 40, no. 2, pp. 603–614, 1991.

[61] D. Kochan, “Solid freeform manufacturing—Possibilities and restrictions,” *Computers in Industry*, vol. 20, pp. 133–140, Jan. 1992.

[62] F. Laverne, F. Segonds, and P. Dubois, “Fabrication additive - principes généraux,” *Techniques de l’ingénieur Procédés de fabrication additive*, vol. base documentaire : TIB633DUO., no. ref. article : bm7017, 2016.

[63] NF EN ISO 17296-2, “Fabrication additive - Principes généraux - Partie 2 : vue d’ensemble des catégories de procédés et des matières premières,” Dec. 2016.

[64] ASTM International, “Standard terminology for additive manufacturing technologies: designation F2792-12a,” tech. rep., West Conshohocken, PA, 2012.

[65] J. P. Kruth, M. C. Leu, and T. Nakagawa, *Progress in additive manufacturing and rapid prototyping.* 3001 Bern: Hallwag Publishers, 1998. WOS:000078773100006.

[66] N. Guo and M. C. Leu, “Additive manufacturing: technology, applications and research needs,” *Frontiers of Mechanical Engineering*, vol. 8, pp. 215–243, Sept. 2013.

[67] G. N. Levy, R. Schindel, and J. P. Kruth, “Rapid manufacturing and rapid tooling with layer manufacturing (LM) technologies, state of the art and future perspectives,” *CIRP Annals*, vol. 52, pp. 589–609, Jan. 2003.

[68] B. K. Paul and S. Baskaran, “Issues in fabricating manufacturing tooling using powder-based additive freeform fabrication,” *Journal of Materials Processing Technology*, vol. 61, pp. 168–172, Aug. 1996.

[69] Wohlers Associates, *Wohlers Report 2019: 3D printing and additive manufacturing state of the industry.* 2019.

[70] Pôle interministériel de prospective et d’anticipation des mutations économiques, Direction générale des entreprises, and Commissariat général à l’égalité des territoires, *Futur de la fabrication additive.* Paris: DGE, 2017.

[71] W. E. Frazier, “Metal Additive Manufacturing: A Review,” *Journal of Materials Engineering and Performance*, vol. 23, pp. 1917–1928, June 2014.

[72] S. Pillot, “Fusion laser sélective de lit de poudres métalliques,” *Techniques de l’ingénieur Procédés de fabrication additive*, vol. base documentaire : TIB633DUO., no. ref. article : bm7900, 2016.

[73] D. D. Gu, W. Meiners, K. Wissenbach, and R. Poprawe, “Laser additive manufacturing of metallic components: materials, processes and mechanisms,” *International Materials Reviews*, vol. 57, pp. 133–164, May 2012.

[74] S. L. Sing, J. An, W. Y. Yeong, and F. E. Wiria, “Laser and electron-beam powder-bed additive manufacturing of metallic implants: A review on processes, materials and designs,” *Journal of Orthopaedic Research*, vol. 34, pp. 369–385, Mar. 2016.

[75] J. Zhang, B. Song, Q. Wei, D. Bourell, and Y. Shi, “A review of selective laser melting of aluminum alloys: Processing, microstructure, property and developing trends,” *Journal of Materials Science & Technology*, vol. 35, pp. 270–284, Feb. 2019.

[76] B. Song, S. Dong, P. Coddet, H. Liao, and C. Coddet, “Fabrication of NiCr alloy parts by selective laser melting: Columnar microstructure and anisotropic mechanical behavior,” *Materials & Design*, vol. 53, pp. 1–7, Jan. 2014.

[77] Pôle interministériel de prospective et d’anticipation des mutations économiques, Direction générale des entreprises, and Commissariat général à l’égalité des territoires, *Futur de la fabrication additive - Focus sur les alliages d’aluminium.* Paris: DGE, 2017.

[78] A. Khorasani, I. Gibson, J. K. Veetil, and A. H. Ghasemi, “A review of technological improvements in laser-based powder bed fusion of metal printers,” *The International Journal of Advanced Manufacturing Technology*, vol. 108, pp. 191–209, May 2020.

[79] E. Atzeni and A. Salmi, “Economics of additive manufacturing for end-usable metal parts,” *The International Journal of Advanced Manufacturing Technology*, vol. 62, pp. 1147–1155, Oct. 2012.

[80] G. Strano, L. Hao, R. M. Everson, and K. E. Evans, “A new approach to the design and optimisation of support structures in additive manufacturing,” *The International Journal of Advanced Manufacturing Technology*, vol. 66, pp. 1247–1254, June 2013.

[81] C. Galy, E. Le Guen, E. Lacoste, and C. Arvieu, “Main defects observed in aluminum alloy parts produced by SLM: From causes to consequences,” *Additive Manufacturing*, vol. 22, pp. 165–175, Aug. 2018.

[82] L. Dowling, J. Kennedy, S. O’Shaughnessy, and D. Trimble, “A review of critical repeatability and reproducibility issues in powder bed fusion,” *Materials & Design*, vol. 186, p. 108346, Jan. 2020.

[83] M. Colombié, “Aciers inoxydables,” *Techniques de l’ingénieur Aciers inoxydables*, no. ref. article : M320A, 1991.

[84] ASTM International, “ASTM F3184-16: Standard Specification for Additive Manufacturing Stainless Steel Alloy (UNS S31603) with Powder Bed Fusion,” tech. rep., ASTM International, West Conshohocken, PA, 2016.

[85] S. David, J. Vitek, R. Reed, and T. Hebble, “Effect of rapid solidification on stainless steel weld metal microstructures and its implications on the Schaeffler diagram,” Tech. Rep. ORNL/TM-10487, 5957599, Sept. 1987.

[86] Y. Zhong, L. Liu, S. Wikman, D. Cui, and Z. Shen, “Intragranular cellular segregation network structure strengthening 316L stainless steel prepared by selective laser melting,” *Journal of Nuclear Materials*, vol. 470, pp. 170–178, Mar. 2016.

[87] M. Ma, Z. Wang, and X. Zeng, “A comparison on metallurgical behaviors of 316L stainless steel by selective laser melting and laser cladding deposition,” *Materials Science and Engineering: A*, vol. 685, pp. 265–273, Feb. 2017.

[88] A. Leicht, U. Klement, and E. Hryha, “Effect of build geometry on the microstructural development of 316L parts produced by additive manufacturing,” *Materials Characterization*, vol. 143, pp. 137–143, Sept. 2018.

[89] K. V. Yang, P. Rometsch, C. Davies, A. Huang, and X. Wu, “Effect of heat treatment on the microstructure and anisotropy in mechanical properties of A357 alloy produced by selective laser melting,” *Materials & Design*, vol. 154, pp. 275–290, Sept. 2018.

[90] K. Saeidi, X. Gao, Y. Zhong, and Z. J. Shen, “Hardened austenite steel with columnar sub-grain structure formed by laser melting,” *Materials Science and Engineering: A*, vol. 625, pp. 221–229, Feb. 2015.

[91] J. Suryawanshi, K. G. Prashanth, and U. Ramamurty, “Mechanical behavior of selective laser melted 316l stainless steel,” *Materials Science and Engineering: A*, vol. 696, pp. 113–121, June 2017.

[92] F. Bartolomeu, M. Buciumeanu, E. Pinto, N. Alves, O. Carvalho, F. S. Silva, and G. Miranda, “316L stainless steel mechanical and tribological behavior-A comparison between selective laser melting, hot pressing and conventional casting,” *Additive Manufacturing*, vol. 16, pp. 81–89, Aug. 2017.

[93] B. Song, X. Zhao, S. Li, C. Han, Q. Wei, S. Wen, J. Liu, and Y. Shi, “Differences in microstructure and properties between selective laser melting and traditional manufacturing for fabrication of metal parts: A review,” *Frontiers of Mechanical Engineering*, vol. 10, pp. 111–125, July 2015.

[94] I. Tolosa, F. Garciandía, F. Zubiri, F. Zapirain, and A. Esnaola, "Study of mechanical properties of AISI 316 stainless steel processed by "selective laser melting", following different manufacturing strategies," *The International Journal of Advanced Manufacturing Technology*, vol. 51, pp. 639–647, Apr. 2010.

[95] A. Riemer, S. Leuders, M. Thoene, H. A. Richard, T. Troester, and T. Niendorf, "On the fatigue crack growth behavior in 316L stainless steel manufactured by selective laser melting," *Engineering Fracture Mechanics*, vol. 120, pp. 15–25, Apr. 2014.

[96] T. G. Spears and S. A. Gold, "In-process sensing in selective laser melting (SLM) additive manufacturing," *Integrating Materials and Manufacturing Innovation*, vol. 5, pp. 16–40, Dec. 2016.

[97] L. V. M. Antony and R. G. Reddy, "Processes for production of high-purity metal powders," *JOM*, vol. 55, pp. 14–18, Mar. 2003.

[98] K. Kassym and A. Perveen, "Atomization processes of metal powders for 3D printing," *Materials Today: Proceedings*, Mar. 2020.

[99] S. Lagutkin, L. Achelis, S. Sheikhaliev, V. Uhlenwinkel, and V. Srivastava, "Atomization process for metal powder," *Materials Science and Engineering: A*, vol. 383, pp. 1–6, Oct. 2004.

[100] D. Bourell, J. P. Kruth, M. Leu, G. Levy, D. Rosen, A. M. Beese, and A. Clare, "Materials for additive manufacturing," *CIRP Annals*, vol. 66, no. 2, pp. 659–681, 2017.

[101] ASTM International, "ASTM F3049-14: Standard Guide for Characterizing Properties of Metal Powders Used for Additive Manufacturing Processes," tech. rep., ASTM International, West Conshohocken, PA, 2014.

[102] A. B. Spierings, M. Voegtlin, T. Bauer, and K. Wegener, "Powder flowability characterisation methodology for powder-bed-based metal additive manufacturing," *Progress in Additive Manufacturing*, vol. 1, pp. 9–20, June 2016.

[103] R. Li, Y. Shi, Z. Wang, L. Wang, J. Liu, and W. Jiang, "Densification behavior of gas and water atomized 316L stainless steel powder during selective laser melting," *Applied Surface Science*, vol. 256, pp. 4350–4356, Apr. 2010.

[104] S. Cacace, A. G. Demir, and Q. Semeraro, "Densification Mechanism for Different Types of Stainless Steel Powders in Selective Laser Melting," *Procedia CIRP*, vol. 62, pp. 475–480, Jan. 2017.

[105] N. P. Karapatis, G. Egger, P. E. Gygax, and R. Glardon, "Optimization of Powder Layer Density in Selective Laser Sintering," *1999 International Solid Freeform Fabrication Symposium*, 1999.

[106] S. E. Brika, M. Letenneur, C. A. Dion, and V. Brailovski, "Influence of particle morphology and size distribution on the powder flowability and laser powder bed fusion manufacturability of Ti-6Al-4V alloy," *Additive Manufacturing*, vol. 31, p. 100929, Jan. 2020.

[107] A. Rogalsky, I. Rishmawi, L. Brock, and M. Vlasea, “Low cost irregular feed stock for laser powder bed fusion,” *Journal of Manufacturing Processes*, vol. 35, pp. 446–456, Oct. 2018.

[108] H. Gu, H. Gong, J. J. S. Dilip, D. Pal, A. J. Hicks, H. Doak, and B. E. Stucker, “Effects of Powder Variation on the Microstructure and Tensile Strength of Ti-6Al-4V Parts Fabricated by Selective Laser Melting,” *Proceedings of the 25th Annual International Solid Freeform Fabrication Symposium, SFF 2014*, 2014.

[109] U. V. Shah, V. Karde, C. Ghoroi, and J. Y. Heng, “Influence of particle properties on powder bulk behaviour and processability,” *International Journal of Pharmaceutics*, vol. 518, pp. 138–154, Feb. 2017.

[110] A. Spierings and G. Levy, “Comparison of density of stainless steel 316L parts produced with Selective Laser Melting using different powder grades,” *20th Annual International Solid Freeform Fabrication Symposium, SFF 2009*, pp. 342–353, 2009.

[111] R. Engeli, T. Etter, S. Hoevel, and K. Wegener, “Processability of different IN738LC powder batches by selective laser melting,” *Journal of Materials Processing Technology*, vol. 229, pp. 484–491, Mar. 2016.

[112] B. Liu, R. Wildman, C. Tuck, I. Ashcroft, and R. J. M. Hague, “Investigation the Effect of Particle Size Distribution on Processing Parameters Optimisation in Selective Laser Melting Process,” *22nd Annual International Solid Freeform Fabrication Symposium, SFF 2011*, pp. 227–238, 2011.

[113] H. Irrinki, M. Dexter, B. Barmore, R. Enneti, S. Pasebani, S. Badwe, J. Stitzel, R. Malhotra, and S. V. Atre, “Effects of Powder Attributes and Laser Powder Bed Fusion (L-PBF) Process Conditions on the Densification and Mechanical Properties of 17-4 PH Stainless Steel,” *JOM*, vol. 68, pp. 860–868, Mar. 2016.

[114] A. Simchi, “The role of particle size on the laser sintering of iron powder,” *Metallurgical and Materials Transactions B*, vol. 35, pp. 937–948, Oct. 2004.

[115] N. T. Aboulkhair, M. Simonelli, L. Parry, I. Ashcroft, C. Tuck, and R. Hague, “3D printing of Aluminium alloys: Additive Manufacturing of Aluminium alloys using selective laser melting,” *Progress in Materials Science*, vol. 106, p. 100578, Dec. 2019.

[116] M. J. Heiden, S. C. Jensen, J. R. Koepke, D. J. Saiz, S. M. Dickens, and B. H. Jared, “Process and feedstock driven microstructure for laser powder bed fusion of 316L stainless steel,” *Materialia*, vol. 21, p. 101356, Mar. 2022.

[117] S. Yim, H. Bian, K. Aoyagi, K. Yamanaka, and A. Chiba, “Spreading behavior of Ti48Al2Cr2Nb powders in powder bed fusion additive manufacturing process: Experimental and discrete element method study,” *Additive Manufacturing*, p. 102489, Nov. 2021.

[118] G. Jacob, C. Brown, and A. Donmez, “The influence of spreading metal powders with different particle size distributions on the powder bed density in laser-based powder bed fusion processes,” *Advanced Manufacturing Series (NIST AMS), National Institute of Standards and Technology, Gaithersburg, MD*, Mar. 2018.

[119] H. Fayazfar, M. Salarian, A. Rogalsky, D. Sarker, P. Russo, V. Paserin, and E. Toyserkani, “A critical review of powder-based additive manufacturing of ferrous alloys: Process parameters, microstructure and mechanical properties,” *Materials & Design*, vol. 144, pp. 98–128, Apr. 2018.

[120] N. Read, W. Wang, K. Essa, and M. M. Attallah, “Selective laser melting of AlSi10Mg alloy: Process optimisation and mechanical properties development,” *Materials & Design*, vol. 65, pp. 417–424, Jan. 2015.

[121] K. G. Prashanth, S. Scudino, T. Maity, J. Das, and J. Eckert, “Is the energy density a reliable parameter for materials synthesis by selective laser melting?,” *Materials Research Letters*, vol. 5, pp. 386–390, Nov. 2017.

[122] Y. Liu, Y. Yang, S. Mai, D. Wang, and C. Song, “Investigation into spatter behavior during selective laser melting of AISI 316L stainless steel powder,” *Materials & Design*, vol. 87, pp. 797–806, Dec. 2015.

[123] V. Gunenthiram, P. Peyre, M. Schneider, M. Dal, F. Coste, I. Koutiri, and R. Fabbro, “Experimental analysis of spatter generation and melt-pool behavior during the powder bed laser beam melting process,” *Journal of Materials Processing Technology*, vol. 251, pp. 376–386, Jan. 2018.

[124] M. C. Sow, T. De Terris, O. Castelnau, Z. Hamouche, F. Coste, R. Fabbro, and P. Peyre, “Influence of beam diameter on Laser Powder Bed Fusion (L-PBF) process,” *Additive Manufacturing*, vol. 36, p. 101532, Dec. 2020.

[125] P. Fischer, V. Romano, H. P. Weber, N. P. Karapatis, E. Boillat, and R. Glardon, “Sintering of commercially pure titanium powder with a Nd : YAG laser source,” *Acta Materialia*, vol. 51, pp. 1651–1662, Apr. 2003.

[126] C. D. Boley, S. A. Khairallah, and A. M. Rubenchik, “Calculation of laser absorption by metal powders in additive manufacturing,” *Applied Optics*, vol. 54, pp. 2477–2482, Mar. 2015.

[127] T. DebRoy, H. Wei, J. Zuback, T. Mukherjee, J. Elmer, J. Milewski, A. Beese, A. Wilson-Heid, A. De, and W. Zhang, “Additive manufacturing of metallic components – Process, structure and properties,” *Progress in Materials Science*, vol. 92, pp. 112–224, Mar. 2018.

[128] J.-P. Kruth, G. Levy, F. Klocke, and T. H. C. Childs, “Consolidation phenomena in laser and powder-bed based layered manufacturing,” *Cirp Annals-Manufacturing Technology*, vol. 56, no. 2, pp. 730–759, 2007.

[129] N. K. Tolochko, S. E. Mozzharov, I. A. Yadroitsev, T. Laoui, L. Froyen, V. I. Titov, and M. B. Ignatiev, “Balling processes during selective laser treatment of powders,” *Rapid Prototyping Journal*, vol. 10, no. 2, pp. 78–87, 2004.

[130] V. Gunenthiram, *Compréhension de la formation de porosités en fabrication additive (LBM). Analyse expérimentale de l’interaction laser – lit de poudre – bain liquide.* PhD thesis, Paris, ENSAM, July 2018.

[131] I. Yadroitsev, A. Gusarov, I. Yadroitsava, and I. Smurov, “Single track formation in selective laser melting of metal powders,” *Journal of Materials Processing Technology*, vol. 210, pp. 1624–1631, Sept. 2010.

[132] D. Gu and Y. Shen, “Balling phenomena in direct laser sintering of stainless steel powder: Metallurgical mechanisms and control methods,” *Materials & Design*, vol. 30, pp. 2903–2910, Sept. 2009.

[133] K. Antony, N. Arivazhagan, and K. Senthilkumaran, “Studies on wettability of stainless steel 316L powder in laser melting process,” *Journal of Engineering Science and Technology*, vol. 9, no. 5, pp. 533–540, 2014.

[134] S. A. Khairallah, A. T. Anderson, A. Rubenchik, and W. E. King, “Laser powder-bed fusion additive manufacturing: Physics of complex melt flow and formation mechanisms of pores, spatter, and denudation zones,” *Acta Materialia*, vol. 108, pp. 36–45, Apr. 2016.

[135] M. Lutter-Günther, M. Bröker, T. Mayer, S. Lizak, C. Seidel, and G. Reinhart, “Spatter formation during laser beam melting of AlSi10Mg and effects on powder quality,” *Procedia CIRP*, vol. 74, pp. 33–38, 2018.

[136] J.-P. Kruth, M. Badrossamay, E. Yasa, J. Deckers, L. Thijs, and J. Van Humbeeck, “Part and material properties in selective laser melting of metals,” *16th International Symposium on Electromachining, ISEM 2010*, pp. 3–14, 2010.

[137] E. Liverani, S. Toschi, L. Ceschini, and A. Fortunato, “Effect of selective laser melting (SLM) process parameters on microstructure and mechanical properties of 316L austenitic stainless steel,” *Journal of Materials Processing Technology*, vol. 249, pp. 255–263, Nov. 2017.

[138] H.-Z. Jiang, Z.-Y. Li, T. Feng, P.-Y. Wu, Q.-S. Chen, Y.-L. Fen, S.-W. Li, H. Gao, and H.-J. Xu, “Factor analysis of selective laser melting process parameters with normalised quantities and Taguchi method,” *Optics and Laser Technology*, vol. 119, p. 105592, Nov. 2019.

[139] M. L. Montero-Sistiaga, M. Godino-Martinez, K. Boschmans, J.-P. Kruth, J. Van Humbeeck, and K. Vanmeensel, “Microstructure evolution of 316L produced by HP-SLM (high power selective laser melting),” *Additive Manufacturing*, vol. 23, pp. 402–410, Oct. 2018.

[140] W. M. Tucho, V. H. Lysne, H. Austbo, A. Sjolyst-Kverneland, and V. Hansen, “Investigation of effects of process parameters on microstructure and hardness of SLM manufactured SS316L,” *Journal of Alloys and Compounds*, vol. 740, pp. 910–925, Apr. 2018.

[141] C. Qiu, C. Panwisawas, M. Ward, H. C. Basoalto, J. W. Brooks, and M. M. Attallah, “On the role of melt flow into the surface structure and porosity development during selective laser melting,” *Acta Materialia*, vol. 96, pp. 72–79, Sept. 2015.

[142] X. Liu, C. Zhao, X. Zhou, Z. Shen, and W. Liu, “Microstructure of selective laser melted AlSi10Mg alloy,” *Materials & Design*, vol. 168, p. 107677, Apr. 2019.

[143] C. A. Biffi, J. Fiocchi, P. Bassani, D. S. Paolino, A. Tridello, G. Chiandussi, M. Rossetto, and A. Tuissi, “Microstructure and preliminary fatigue analysis on AlSi10Mg samples manufactured by SLM,” *Procedia Structural Integrity*, vol. 7, pp. 50–57, Jan. 2017.

[144] J. L. Bartlett and X. Li, “An overview of residual stresses in metal powder bed fusion,” *Additive Manufacturing*, vol. 27, pp. 131–149, May 2019.

[145] B. Zhang, L. Dembinski, and C. Coddet, “The study of the laser parameters and environment variables effect on mechanical properties of high compact parts elaborated by selective laser melting 316L powder,” *Materials Science and Engineering: A*, vol. 584, pp. 21–31, Nov. 2013.

[146] A. Masmoudi, R. Bolot, and C. Coddet, “Investigation of the laser-powder-atmosphere interaction zone during the selective laser melting process,” *Journal of Materials Processing Technology*, vol. 225, pp. 122–132, Nov. 2015.

[147] A. Ladewig, G. Schlick, M. Fisser, V. Schulze, and U. Glatzel, “Influence of the shielding gas flow on the removal of process by-products in the selective laser melting process,” *Additive Manufacturing*, vol. 10, pp. 1–9, Apr. 2016.

[148] J. Reijonen, A. Revuelta, T. Riipinen, K. Ruusuvuori, and P. Puukko, “On the effect of shielding gas flow on porosity and melt pool geometry in laser powder bed fusion additive manufacturing,” *Additive Manufacturing*, vol. 32, p. 101030, Mar. 2020.

[149] A. Gasper, B. Szost, X. Wang, D. Johns, S. Sharma, A. Clare, and I. Ashcroft, “Spatter and oxide formation in laser powder bed fusion of Inconel 718,” *Additive Manufacturing*, vol. 24, pp. 446–456, Dec. 2018.

[150] C. L. A. Leung, S. Marussi, M. Towrie, R. C. Atwood, P. J. Withers, and P. D. Lee, “The effect of powder oxidation on defect formation in laser additive manufacturing,” *Acta Materialia*, vol. 166, pp. 294–305, Mar. 2019.

[151] N. Emminghaus, C. Hoff, J. Hermsdorf, and S. Kaierle, “Residual oxygen content and powder recycling: Effects on surface roughness and porosity of additively manufactured Ti-6Al-4V,” *Additive Manufacturing*, vol. 46, p. 102093, Oct. 2021.

[152] K. Dietrich, J. Diller, S. Dubiez-Le Goff, D. Bauer, P. Forêt, and G. Witt, “The influence of oxygen on the chemical composition and mechanical properties of Ti-6Al-4V during laser powder bed fusion (L-PBF),” *Additive Manufacturing*, vol. 32, p. 100980, Mar. 2020.

[153] E. Hryha, R. Shvab, M. Bram, M. Bitzer, and L. Nyborg, “Surface chemical state of Ti powders and its alloys: Effect of storage conditions and alloy composition,” *Applied Surface Science*, vol. 388, pp. 294–303, Dec. 2016.

[154] M. Baumers, C. Tuck, R. Wildman, I. Ashcroft, E. Rosamond, and R. Hague, “Combined build-time, energy consumption and cost estimation for direct metal laser sintering,” *23rd Annual International Solid Freeform Fabrication Symposium - An Additive Manufacturing Conference, SFF 2012*, pp. 932–944, Jan. 2012.

[155] J. Teubler, S. Weber, P. Suski, I. Peschke, and C. Liedtke, “Critical evaluation of the material characteristics and environmental potential of laser beam melting processes for

the additive manufacturing of metallic components," *Journal of Cleaner Production*, vol. 237, p. 117775, Nov. 2019.

[156] J. Slotwinski, E. Garboczi, P. Stutzman, C. Ferraris, S. Watson, and M. Peltz, "Characterization of Metal Powders Used for Additive Manufacturing," *Journal of Research of the National Institute of Standards and Technology*, vol. 119, pp. 460–493, Sept. 2014.

[157] B. K. Barnhart, *Characterization of Powder and the Effects of Powder Reuse in Selective Laser Melting.* PhD thesis, Case Western Reserve University, 2017.

[158] X. He, D. Kong, Y. Zhou, L. Wang, X. Ni, L. Zhang, W. Wu, R. Li, X. Li, and C. Dong, "Powder recycling effects on porosity development and mechanical properties of Hastelloy X alloy during laser powder bed fusion process," *Additive Manufacturing*, p. 102840, Apr. 2022.

[159] Y. Sun, M. Aindow, and R. J. Hebert, "The effect of recycling on the oxygen distribution in Ti-6Al-4V powder for additive manufacturing," *Materials at High Temperatures*, vol. 35, pp. 217–224, May 2018.

[160] A. Strondl, O. Lyckfeldt, H. Brodin, and U. Ackelid, "Characterization and Control of Powder Properties for Additive Manufacturing," *JOM*, vol. 67, pp. 549–554, Mar. 2015.

[161] L. Cordova, M. Campos, and T. Tinga, "Revealing the Effects of Powder Reuse for Selective Laser Melting by Powder Characterization," *JOM*, vol. 71, pp. 1062–1072, Mar. 2019.

[162] L. Marchetti and C. Hulme-Smith, "Flowability of steel and tool steel powders: A comparison between testing methods," *Powder Technology*, vol. 384, pp. 402–413, May 2021.

[163] L. Ardila, F. Garciandia, J. González-Díaz, P. Álvarez, A. Echeverria, M. Petite, R. Deffley, and J. Ochoa, "Effect of IN718 Recycled Powder Reuse on Properties of Parts Manufactured by Means of Selective Laser Melting," *Physics Procedia*, vol. 56, pp. 99–107, 2014.

[164] H. Asgari, C. Baxter, K. Hosseinkhani, and M. Mohammadi, "On microstructure and mechanical properties of additively manufactured AlSi10Mg_200c using recycled powder," *Materials Science and Engineering: A*, vol. 707, pp. 148–158, Nov. 2017.

[165] M. Hilzenthaler, L. Bifano, F. Scherm, G. Fischerauer, A. Seemann, and U. Glatzel, "Characterization of recycled AISI 904L superaustenitic steel powder and influence on selective laser melted parts," *Powder Technology*, vol. 391, pp. 57–68, Oct. 2021.

[166] E. Jelis, M. Clemente, S. Kerwien, N. M. Ravindra, and M. R. Hespos, "Metallurgical and Mechanical Evaluation of 4340 Steel Produced by Direct Metal Laser Sintering," *JOM*, vol. 67, pp. 582–589, Jan. 2015.

[167] P. Nandwana, W. H. Peter, R. R. Dehoff, L. E. Lowe, M. M. Kirka, F. Medina, and S. S. Babu, "Recyclability Study on Inconel 718 and Ti-6Al-4V Powders for Use in Electron Beam Melting," *Metallurgical and Materials Transactions B*, vol. 47, pp. 754–762, Feb. 2016.

[168] C. Lu, R. Zhang, M. Xiao, X. Wei, Y. Yin, Y. Qu, H. Li, P. Liu, X. Qiu, and T. Guo, “A comprehensive characterization of virgin and recycled 316L powders during laser powder bed fusion,” *Journal of Materials Research and Technology*, vol. 18, pp. 2292–2309, May 2022.

[169] O. A. Quintana, J. Alvarez, R. Mcmillan, W. Tong, and C. Tomonto, “Effects of Reusing Ti-6Al-4V Powder in a Selective Laser Melting Additive System Operated in an Industrial Setting,” *JOM*, vol. 70, pp. 1863–1869, Sept. 2018.

[170] N. E. Gorji, R. O’Connor, A. Mussatto, M. Snelgrove, P. M. González, and D. Brabazon, “Recyclability of stainless steel (316 L) powder within the additive manufacturing process,” *Materialia*, vol. 8, p. 100489, Dec. 2019.

[171] N. E. Gorji, P. Saxena, M. Corfield, A. Clare, J.-P. Rueff, J. Bogan, P. G. M. González, M. Snelgrove, G. Hughes, R. O’Connor, R. Raghavendra, and D. Brabazon, “A new method for assessing the recyclability of powders within Powder Bed Fusion process,” *Materials Characterization*, vol. 161, p. 110167, Mar. 2020.

[172] D. Galicki, F. List, S. S. Babu, A. Plotkowski, H. M. Meyer, R. Seals, and C. Hayes, “Localized Changes of Stainless Steel Powder Characteristics During Selective Laser Melting Additive Manufacturing,” *Metallurgical and Materials Transactions A*, vol. 50, pp. 1582–1605, Mar. 2019.

[173] P. Zapico, S. Giganto, J. Barreiro, and S. Martínez-Pellitero, “Characterisation of 17-4PH metallic powder recycling to optimise the performance of the selective laser melting process,” *Journal of Materials Research and Technology*, Dec. 2019.

[174] C. Lu, R. Zhang, X. Wei, M. Xiao, Y. Yin, Y. Qu, H. Li, P. Liu, X. Qiu, and T. Guo, “An investigation on the oxidation behavior of spatters generated during the laser powder bed fusion of 316L stainless steel,” *Applied Surface Science*, vol. 586, p. 152796, June 2022.

[175] N. Derimow and N. Hrabe, “Oxidation in Reused Powder Bed Fusion Additive Manufacturing Ti-6Al-4V Feedstock: A Brief Review,” *JOM*, vol. 73, pp. 3618–3638, Nov. 2021.

[176] F. J. Alamos, J. Schiltz, K. Kozlovsky, R. Attardo, C. Tomonto, T. Pelletiers, and S. R. Schmid, “Effect of powder reuse on mechanical properties of Ti-6Al-4V produced through selective laser melting,” *International Journal of Refractory Metals and Hard Materials*, vol. 91, p. 105273, Sept. 2020.

[177] V. V. Popov, A. Katz-Demyanetz, A. Garkun, and M. Bamberger, “The effect of powder recycling on the mechanical properties and microstructure of electron beam melted Ti-6Al-4 V specimens,” *Additive Manufacturing*, vol. 22, pp. 834–843, Aug. 2018.

[178] A. T. Sutton, C. S. Kriewall, S. Karnati, M. C. Leu, J. W. Newkirk, W. Everhart, and B. Brown, “Evolution of AISI 304L stainless steel part properties due to powder recycling in laser powder-bed fusion,” *Additive Manufacturing*, vol. 36, p. 101439, Dec. 2020.

[179] C. Wei, X. Ma, X. Yang, M. Zhou, C. Wang, Y. Zheng, W. Zhang, and Z. Li, “Microstructural and property evolution of Ti6Al4V powders with the number of usage

in additive manufacturing by electron beam melting," *Materials Letters*, vol. 221, pp. 111–114, June 2018.

[180] S. Giganto, S. Martínez-Pellitero, J. Barreiro, and P. Zapico, "Influence of 17-4 PH stainless steel powder recycling on properties of SLM additive manufactured parts," *Journal of Materials Research and Technology*, vol. 16, pp. 1647–1658, Jan. 2022.

[181] F. Del Re, V. Contaldi, A. Astarita, B. Palumbo, A. Squillace, P. Corrado, and P. Di Petta, "Statistical approach for assessing the effect of powder reuse on the final quality of AlSi10Mg parts produced by laser powder bed fusion additive manufacturing," *The International Journal of Advanced Manufacturing Technology*, vol. 97, pp. 2231–2240, July 2018.

[182] T. Purtonen, A. Kalliosaari, and A. Salminen, "Monitoring and Adaptive Control of Laser Processes," *Physics Procedia*, vol. 56, pp. 1218–1231, Jan. 2014.

[183] M. L. Grasso and B. M. Colosimo, "Process defects and in situ monitoring methods in metal powder bed fusion: A review," *Measurement Science and Technology*, vol. 28, p. 044005, Feb. 2017.

[184] I. A. Okaro, S. Jayasinghe, C. Sutcliffe, K. Black, P. Paoletti, and P. L. Green, "Automatic fault detection for laser powder-bed fusion using semi-supervised machine learning," *Additive Manufacturing*, vol. 27, pp. 42–53, May 2019.

[185] G. Tapia and A. Elwany, "A Review on Process Monitoring and Control in Metal-Based Additive Manufacturing," *Journal of Manufacturing Science and Engineering*, vol. 136, Oct. 2014.

[186] J.-P. Kruth, J. R. Duflou, P. Mercelis, J. V. Vaerenbergh, T. Craeghs, and J. D. Keuster, "On-line monitoring and process control in selective laser melting and laser cutting," *Proceedings of the 5th Lane Conference, Laser Assisted Net Shape Engineering*, pp. 23–37, 2007.

[187] T. Craeghs, F. Bechmann, S. Berumen, and J.-P. Kruth, "Feedback control of Layerwise Laser Melting using optical sensors," *Physics Procedia*, vol. 5, pp. 505–514, Jan. 2010.

[188] T. Craeghs, S. Clijsters, E. Yasa, and J.-P. Kruth, "Online quality control of selective laser melting," *22nd Annual International Solid Freeform Fabrication Symposium - An Additive Manufacturing Conference, SFF 2011*, Jan. 2011.

[189] S. Clijsters, T. Craeghs, S. Buls, K. Kempen, and J.-P. Kruth, "In situ quality control of the selective laser melting process using a high-speed, real-time melt pool monitoring system," *The International Journal of Advanced Manufacturing Technology*, vol. 75, pp. 1089–1101, Nov. 2014.

[190] P. Lott, H. Schleifenbaum, W. Meiners, K. Wissenbach, C. Hinke, and J. Bültmann, "Design of an Optical system for the In Situ Process Monitoring of Selective Laser Melting (SLM)," *Physics Procedia*, vol. 12, pp. 683–690, Jan. 2011.

[191] M. Doubenskaia, M. Pavlov, and Y. Chivel, "Optical System for On-Line Monitoring and Temperature Control in Selective Laser Melting Technology," *Key Engineering Materials*, vol. 437, pp. 458–461, May 2010.

[192] Y. Chivel and I. Smurov, "On-line temperature monitoring in selective laser sintering/melting," *Physics Procedia*, vol. 5, pp. 515–521, Jan. 2010.

[193] F. Bayle and M. Doubenskaia, "Selective laser melting process monitoring with high speed infrared camera and pyrometer. Fundamentals of laser assisted micro- and nanotechnologies," *SPIE*, pp. 1–8, Jan. 2008.

[194] C. L. A. Leung, S. Marussi, M. Towrie, J. del Val Garcia, R. C. Atwood, A. J. Bodey, J. R. Jones, P. J. Withers, and P. D. Lee, "Laser-matter interactions in additive manufacturing of stainless steel SS316L and 13-93 bioactive glass revealed by in situ X-ray imaging," *Additive Manufacturing*, vol. 24, pp. 647–657, Dec. 2018.

[195] A. Bobel, L. G. Hector, I. Chelladurai, A. K. Sachdev, T. Brown, W. A. Poling, R. Kubic, B. Gould, C. Zhao, N. Parab, A. Greco, and T. Sun, "In situ synchrotron X-ray imaging of 4140 steel laser powder bed fusion," *Materialia*, vol. 6, p. 100306, June 2019.

[196] B. J. Simonds, J. Tanner, A. Artusio-Glimpse, P. A. Williams, N. Parab, C. Zhao, and T. Sun, "Simultaneous high-speed x-ray transmission imaging and absolute dynamic absorptance measurements during high-power laser-metal processing," *Procedia CIRP*, vol. 94, pp. 775–779, Jan. 2020.

[197] N. Derimow, E. J. Schwalbach, J. T. Benzing, J. P. Killgore, A. B. Artusio-Glimpse, N. Hrabe, and B. J. Simonds, "In situ absorption synchrotron measurements, predictive modeling, microstructural analysis, and scanning probe measurements of laser melted Ti-6Al-4V single tracks for additive manufacturing applications," *Journal of Alloys and Compounds*, vol. 900, p. 163494, Apr. 2022.

[198] Y. Huang, T. G. Fleming, S. J. Clark, S. Marussi, K. Fezzaa, J. Thiyagalingam, C. L. A. Leung, and P. D. Lee, "Keyhole fluctuation and pore formation mechanisms during laser powder bed fusion additive manufacturing," *Nature Communications*, vol. 13, p. 1170, Mar. 2022.

[199] S. A. Khairallah, T. Sun, and B. J. Simonds, "Onset of periodic oscillations as a precursor of a transition to pore-generating turbulence in laser melting," *Additive Manufacturing Letters*, vol. 1, p. 100002, Dec. 2021.

[200] M. J. Matthews, G. Guss, S. A. Khairallah, A. M. Rubenchik, P. J. Depond, and W. E. King, "Denudation of metal powder layers in laser powder bed fusion processes," *Acta Materialia*, vol. 114, pp. 33–42, Aug. 2016.

[201] S. K. Everton, M. Hirsch, P. Stravroulakis, R. K. Leach, and A. T. Clare, "Review of in-situ process monitoring and in-situ metrology for metal additive manufacturing," *Materials & Design*, vol. 95, pp. 431–445, Apr. 2016.

[202] M. Grasso, A. Remani, A. Dickins, B. M. Colosimo, and R. K. Leach, "In-situ measurement and monitoring methods for metal powder bed fusion: an updated review," *Measurement Science and Technology*, vol. 32, p. 112001, July 2021.

[203] S. Kleszczynski, J. z. Jacobsmühlen, G. Witt, and J. Sehrt, "Error detection in laser beam melting systems by high resolution imaging," *23rd Annual International Solid Freeform Fabrication Symposium - An Additive Manufacturing Conference, SFF 2012*, Aug. 2012.

[204] S. Kleszczynski, J. z. Jacobsmühlen, B. Reinarz, and J. Sehrt, “Improving Process Stability of Laser Beam Melting Systems,” *Fraunhofer Direct Digital Manufacturing Conference (DDMC) 2014*, Jan. 2014.

[205] J. zur Jacobsmühlen, S. Kleszczynski, D. Schneider, and G. Witt, “High resolution imaging for inspection of Laser Beam Melting systems,” *2013 IEEE International Instrumentation and Measurement Technology Conference (I2MTC)*, 2013.

[206] W. S. Land, B. Zhang, J. Ziegert, and A. Davies, “In-Situ Metrology System for Laser Powder Bed Fusion Additive Process,” *Procedia Manufacturing*, vol. 1, pp. 393–403, 2015.

[207] B. Zhang, J. Ziegert, F. Farahi, and A. Davies, “In situ surface topography of laser powder bed fusion using fringe projection,” *Additive Manufacturing*, vol. 12, pp. 100–107, Oct. 2016.

[208] M. G. Guerra, V. Errico, A. Fusco, F. Lavecchia, S. L. Campanelli, and L. M. Galantucci, “High resolution-optical tomography for in-process layerwise monitoring of a laser-powder bed fusion technology,” *Additive Manufacturing*, vol. 55, p. 102850, July 2022.

[209] K. Foster, W. Reutzel, R. Nassar, T. Hall, W. Brown, and C. Dickman, “Optical, layerwise monitoring of powder bed fusion,” *Solid Free. Fabr. Symp. Proc.*, pp. 295–307, 2015.

[210] M. Abdelrahman, E. W. Reutzel, A. R. Nassar, and T. L. Starr, “Flaw detection in powder bed fusion using optical imaging,” *Additive Manufacturing*, vol. 15, pp. 1–11, May 2017.

[211] F. Caltanissetta, M. Grasso, S. Petrò, and B. M. Colosimo, “Characterization of in-situ measurements based on layerwise imaging in laser powder bed fusion,” *Additive Manufacturing*, vol. 24, pp. 183–199, Dec. 2018.

[212] C. Gobert, E. W. Reutzel, J. Petrich, A. R. Nassar, and S. Phoha, “Application of supervised machine learning for defect detection during metallic powder bed fusion additive manufacturing using high resolution imaging.,” *Additive Manufacturing*, vol. 21, pp. 517–528, May 2018.

[213] J. L. Bartlett, F. M. Heim, Y. V. Murty, and X. Li, “In situ defect detection in selective laser melting via full-field infrared thermography,” *Additive Manufacturing*, vol. 24, pp. 595–605, Dec. 2018.

[214] M. A. Spurek, V. H. Luong, A. B. Spierings, M. Lany, G. Santi, B. Revaz, and K. Wegener, “Relative Density Measurement of PBF-Manufactured 316L and AlSi10Mg Samples via Eddy Current Testing,” *Metals*, vol. 11, p. 1376, Sept. 2021.

[215] L. Scime and J. Beuth, “Anomaly detection and classification in a laser powder bed additive manufacturing process using a trained computer vision algorithm,” *Additive Manufacturing*, vol. 19, pp. 114–126, Jan. 2018.

[216] L. Scime, D. Siddel, S. Baird, and V. Paquit, “Layer-wise anomaly detection and classification for powder bed additive manufacturing processes: A machine-agnostic algorithm for real-time pixel-wise semantic segmentation,” *Additive Manufacturing*, vol. 36, p. 101453, Dec. 2020.

[217] D. B. Pedersen, E. R. Eiriksson, H. Aanaes, and H. N. Hansen, “In-Situ Monitoring in Additive Manufacturing Using Contact Image Sensors,” *ASPE/euspen 2016 Summer Topical Meeting on Dimensional Accuracy and Surface Finish in Additive Manufacturing*, June 2016.

[218] EOS GmbH Electro Optical Systems, “Method and recoater for a device for the production of a three-dimensional object,” European patent EP3362262B1, 2016.

[219] T.-P. Le, X. Wang, K. P. Davidson, J. E. Fronda, and M. Seita, “Experimental analysis of powder layer quality as a function of feedstock and recoating strategies,” *Additive Manufacturing*, vol. 39, p. 101890, Mar. 2021.

[220] C. Barrett, E. MacDonald, B. Conner, and F. Persi, “Micron-Level Layer-Wise Surface Profilometry to Detect Porosity Defects in Powder Bed Fusion of Inconel 718,” *JOM*, vol. 70, pp. 1844–1852, Sept. 2018.

[221] F. G. Fischer, N. Birk, L. Rooney, L. Jauer, and J. H. Schleifenbaum, “Optical process monitoring in Laser Powder Bed Fusion using a recoater-based line camera,” *Additive Manufacturing*, vol. 47, p. 102218, Nov. 2021.

[222] M. Bugatti and B. M. Colosimo, “The intelligent recoater: A new solution for in-situ monitoring of geometric and surface defects in powder bed fusion,” *Additive Manufacturing Letters*, vol. 3, p. 100048, Dec. 2022.

[223] L. Lutterotti, “Maud Version 2.94,” 2020.

[224] ASTM International, “ASTM B213-20: Standard Test Methods for Flow Rate of Metal Powders Using the Hall, Flowmeter Funnel,” tech. rep., ASTM International, West Conshohocken, PA, 2020.

[225] A. Spierings, M. Schneider, and R. Eggenberger, “Comparison of density measurement techniques for additive manufactured metallic parts,” *Rapid Prototyping Journal*, vol. 17, pp. 380–386, Jan. 2011.

[226] International Organization for Standardization, “ISO 6892-1, Metallic materials - Tensile testing - Part 1: Method of test at room temperature,” tech. rep., 2019.

[227] R. Yavari, Z. Smoqi, A. Riensche, B. Bevans, H. Kobir, H. Mendoza, H. Song, K. Cole, and P. Rao, “Part-scale thermal simulation of laser powder bed fusion using graph theory: Effect of thermal history on porosity, microstructure evolution, and recoater crash,” *Materials & Design*, vol. 204, p. 109685, June 2021.

[228] D. Riabov, E. Hryha, M. Rashidi, S. Bengtsson, and L. Nyborg, “Effect of atomization on surface oxide composition in 316L stainless steel powders for additive manufacturing,” *Surface and Interface Analysis*, vol. 52, no. 11, pp. 694–706, 2020.

[229] A. Raza, T. Fiegl, I. Hanif, A. MarkstrÖm, M. Franke, C. Körner, and E. Hryha, “Degradation of AlSi10Mg powder during laser based powder bed fusion processing,” *Materials & Design*, vol. 198, p. 109358, Jan. 2021.

[230] Z. A. Young, Q. Guo, N. D. Parab, C. Zhao, M. Qu, L. I. Escano, K. Fezzaa, W. Everhart, T. Sun, and L. Chen, “Types of spatter and their features and formation

mechanisms in laser powder bed fusion additive manufacturing process,” *Additive Manufacturing*, vol. 36, p. 101438, Dec. 2020.

[231] Q. Lu, M. Grasso, T.-P. Le, and M. Seita, “Predicting build density in L-PBF through in-situ analysis of surface topography using powder bed scanner technology,” *Additive Manufacturing*, vol. 51, p. 102626, Mar. 2022.

[232] Q. Chao, V. Cruz, S. Thomas, N. Birbilis, P. Collins, A. Taylor, P. D. Hodgson, and D. Fabijanic, “On the enhanced corrosion resistance of a selective laser melted austenitic stainless steel,” *Scripta Materialia*, vol. 141, pp. 94–98, Dec. 2017.

[233] P. Deng, M. Karadge, R. B. Rebak, V. K. Gupta, B. C. Prorok, and X. Lou, “The origin and formation of oxygen inclusions in austenitic stainless steels manufactured by laser powder bed fusion,” *Additive Manufacturing*, vol. 35, p. 101334, Oct. 2020.

[234] y. Grong, L. Kolbeinsen, C. v. d. Eijk, and G. Tranell, “Microstructure Control of Steels through Dispersoid Metallurgy Using Novel Grain Refining Alloys,” *ISIJ International*, vol. 46, no. 6, pp. 824–831, 2006.

[235] X. Lou, P. L. Andresen, and R. B. Rebak, “Oxide inclusions in laser additive manufactured stainless steel and their effects on impact toughness and stress corrosion cracking behavior,” *Journal of Nuclear Materials*, vol. 499, pp. 182–190, Feb. 2018.

[236] M. Moyle, C. Ledermueller, Z. Zou, S. Primig, and N. Haghdadi, “Multi-scale characterisation of microstructure and texture of 316L stainless steel manufactured by laser powder bed fusion,” *Materials Characterization*, vol. 184, p. 111663, Feb. 2022.

[237] T. Kurzynowski, K. Gruber, W. Stopyra, B. Kuźnicka, and E. Chlebus, “Correlation between process parameters, microstructure and properties of 316 L stainless steel processed by selective laser melting,” *Materials Science and Engineering: A*, vol. 718, pp. 64–73, Mar. 2018.

[238] N. Ahmed, I. Barsoum, G. Haidemenopoulos, and R. K. A. Al-Rub, “Process parameter selection and optimization of laser powder bed fusion for 316L stainless steel: A review,” *Journal of Manufacturing Processes*, vol. 75, pp. 415–434, Mar. 2022.

[239] A. Leicht, C. H. Yu, V. Luzin, U. Klement, and E. Hryha, “Effect of scan rotation on the microstructure development and mechanical properties of 316L parts produced by laser powder bed fusion,” *Materials Characterization*, vol. 163, p. 110309, May 2020.

[240] H. Hindam and D. P. Whittle, “Microstructure, adhesion and growth kinetics of protective scales on metals and alloys,” *Oxidation of Metals*, vol. 18, pp. 245–284, Dec. 1982.

[241] P. Moulin, A. Huntz, and P. Lacombe, “Influence des phenomenes diffusionnels sur le mecanisme d'oxydation des alliages NiCr,” *Acta Metallurgica*, vol. 28, no. 6, pp. 745–756, 1980.

[242] A. M. Huntz, A. Reckmann, C. Haut, C. Sévérac, M. Herbst, F. C. T. Resende, and A. C. S. Sabioni, “Oxidation of AISI 304 and AISI 439 stainless steels,” *Materials Science and Engineering: A*, vol. 447, pp. 266–276, Feb. 2007.

[243] A. C. S. Sabioni, R. P. B. Ramos, V. Ji, and F. Jomard, "Oxygen Diffusion Study in Oxidation Films of the AISI 304 Austenitic Stainless Steel," *Defect and Diffusion Forum*, vol. 323-325, pp. 345–351, 2012.

[244] J. Karczewski, T. Brylewski, T. Miruszewski, K. B. Andersen, P. Z. Jasinski, and S. Molin, "High-temperature kinetics study of 430L steel powder oxidized in air at 600–850 °C," *Corrosion Science*, vol. 149, pp. 100–107, Apr. 2019.

[245] D. Mortimer and M. L. Post, "The oxidation of Cr and an Fe-50% Cr alloy," *Corrosion Science*, vol. 8, pp. 499–512, Jan. 1968.

[246] E. J. Felten, "High-Temperature Oxidation of Fe-Cr Base Alloys with Particular Reference to Fe-Cr-Y Alloys," *Journal of The Electrochemical Society*, vol. 108, p. 490, June 1961.

[247] E. Hryha, R. Shvab, H. Gruber, A. Leicht, and L. Nyborg, "Surface Oxide State on Metal Powder and its Changes during Additive Manufacturing: an Overview," *Metallurgia Italiana*, pp. 34–39, 2018.

[248] G. Salomonsen, N. Norman, O. Lønsjø, and T. G. Finstad, "Kinetics and mechanism of oxide formation on titanium, vanadium and chromium thin films," *Journal of the Less Common Metals*, vol. 158, pp. 251–265, Mar. 1990.

[249] H. S. Fairman, M. H. Brill, and H. Hemmendinger, "How the CIE 1931 color-matching functions were derived from Wright-Guild data," *Color Research & Application*, vol. 22, no. 1, pp. 11–23, 1997.

[250] T. Delacroix, F. Lomello, F. Schuster, H. Maskrot, and J.-P. Garandet, "Influence of powder recycling on 316L stainless steel feedstocks and printed parts in laser powder bed fusion," *Additive Manufacturing*, vol. 50, p. 102553, Feb. 2022.

[251] P. Moghimian, T. Poirié, M. Habibnejad-Korayem, J. A. Zavala, J. Kroeger, F. Marion, and F. Larouche, "Metal powders in additive manufacturing: A review on reusability and recyclability of common titanium, nickel and aluminum alloys," *Additive Manufacturing*, vol. 43, p. 102017, July 2021.

[252] H. Amano, Y. Yamaguchi, T. Ishimoto, and T. Nakano, "Reduction of Spatter Generation Using Atmospheric Gas in Laser Powder Bed Fusion of Ti–6Al–4V," *Materials Transactions*, vol. 62, pp. 1225–1230, Aug. 2021.

[253] G. Chebil, P. Lapouge, Y. Renollet, C. Davoine, M. Thomas, V. Favier, and M. Schneider, "Study of spatter ejections during laser-powder bed fusion process for aluminum alloys," *Journal of Laser Applications*, vol. 33, p. 042047, Nov. 2021.

[254] S. Lu, H. Fujii, K. Nogi, and T. Sato, "Effect of oxygen content in He–O2 shielding gas on weld shape in ultra deep penetration TIG," *Science and Technology of Welding and Joining*, vol. 12, pp. 689–695, Nov. 2007.

[255] A. Raza, C. Pauzon, E. Hryha, A. Markström, and P. Forêt, "Spatter oxidation during laser powder bed fusion of Alloy 718: Dependence on oxygen content in the process atmosphere," *Additive Manufacturing*, vol. 48, p. 102369, Dec. 2021.

[256] C. L. A. Leung, S. Marussi, R. C. Atwood, M. Towrie, P. J. Withers, and P. D. Lee, "In situ X-ray imaging of defect and molten pool dynamics in laser additive manufacturing," *Nature Communications*, vol. 9, p. 1355, Apr. 2018.

[257] Q. Guo, C. Zhao, L. I. Escano, Z. Young, L. Xiong, K. Fezzaa, W. Everhart, B. Brown, T. Sun, and L. Chen, "Transient dynamics of powder spattering in laser powder bed fusion additive manufacturing process revealed by in-situ high-speed high-energy x-ray imaging," *Acta Materialia*, vol. 151, pp. 169–180, June 2018.

[258] C. Schwerz, A. Raza, X. Lei, L. Nyborg, E. Hryha, and H. Wirdelius, "In-situ detection of redeposited spatter and its influence on the formation of internal flaws in laser powder bed fusion," *Additive Manufacturing*, vol. 47, p. 102370, Nov. 2021.